

**PROGRAMMABLE NANOMATERIALS DEVELOPMENT
VIA KINETICALLY CONTROLLED SELF-ASSEMBLY OF
COMPUTATIONALLY DESIGNED PEPTIDES**

by

Yu Tian

A dissertation submitted to the Faculty of the University of Delaware in partial fulfillment of the requirements for the degree of Doctor of Philosophy in Materials Science and Engineering

Fall 2018

© 2018 Yu Tian
All Rights Reserved

**PROGRAMMABLE NANOMATERIALS DEVELOPMENT
VIA KINETICALLY CONTROLLED SELF-ASSEMBLY OF
COMPUTATIONALLY DESIGNED PEPTIDES**

by

Yu Tian

Approved:

Darrin J. Pochan, Ph.D.
Chair of the Department of Materials Science and Engineering

Approved:

Levi T. Thompson, Ph.D.
Dean of the College of Engineering

Approved:

Douglas J. Doren, Ph.D.
Interim Vice Provost for the Office of Graduate and Professional
Education

I certify that I have read this dissertation and that in my opinion it meets the academic and professional standard required by the University as a dissertation for the degree of Doctor of Philosophy.

Signed:

Darrin J. Pochan, Ph.D.
Professor in charge of dissertation

I certify that I have read this dissertation and that in my opinion it meets the academic and professional standard required by the University as a dissertation for the degree of Doctor of Philosophy.

Signed:

Kristi L. Kiick, Ph.D.
Professor in charge of dissertation

I certify that I have read this dissertation and that in my opinion it meets the academic and professional standard required by the University as a dissertation for the degree of Doctor of Philosophy.

Signed:

Christopher J. Kloxin, Ph.D.
Member of dissertation committee

I certify that I have read this dissertation and that in my opinion it meets the academic and professional standard required by the University as a dissertation for the degree of Doctor of Philosophy.

Signed:

Jeffery G. Saven, Ph.D.
Member of dissertation committee

ACKNOWLEDGMENTS

Time flies the fastest when it has the most delightful moments. My journey at the University of Delaware must come to an end with the memory of my first entering DuPont Hall still as fresh as it happened this morning. With all my sincerity, I wrote this ceremonious acknowledgement to appreciate my experience.

With the completion of this dissertation, I would truly want to thank my advisors Professor Darrin Pochan and Professor Kristi Kiick. Having two advisors means I need to attend the doubled amount of group meetings than others; but it also gives me the doubled resource to the greatness. Their intelligence and achievement have set the goal of my career. I thank Professor Jeffery Saven for his essential computational work in this Ph.D. project. I thank Professor Christopher Kloxin for the constructive suggestion and discussion to the project.

I thank my previous colleagues, Dr. Frank Polzer and Dr. Dongdong Wu, for the practical guidance in research and showing me the standard of a self-motivated, professional, young scientist. Alles ist gute!

I thank the members in the Saven group for the collaboration in this project, particularly Dr. Huixi Violet Zhang and Dr. Matthew Ebling, for the computational design work and the peptide crystallization work. I thank dear colleague Michael Haider for the successful completion of this project together with me. I thank the Pochan group members and Kiick group members for the discussion and help. I also thank fellow classmates and friends in Delaware. You make science more fun. I thank all the MSEG department staff members Charles Garbini, Christine Williamson,

Robin Buccos, Kathy Forwood and Judy Allarey. I also thank Keck Lab staff members, Professor Chaoying Ni, Dr. Jennifer Sloppy, Dr. Fei Deng, Dr. Yong Zhao and Frank Kriss.

The funding resources NSF DMREF (DMR-1234161 and DMR-1235084), NSF CHE1213728 and NIH (RO1 EB006006) are appreciated.

Most importantly, I thank my family, my parents and Yiran Shang, for the support and love.

In the end, I would like to thank science for bringing me such a great journey. It shall continue.

TABLE OF CONTENTS

LIST OF TABLES	x
LIST OF FIGURES	xi
ABSTRACT	xxvii
Chapter	
1 INTRODUCTION	1
1.1 Materials Construction via Self-assembly and the Kinetic Control	1
1.2 Chemical Structure- and Shape-specific Assembly Building Block	5
1.3 Designed Peptides for Self-assembly	8
1.4 <i>De novo</i> Designed Peptide Coil-coiled Bundles and Assemblies	16
1.5 Dissertation Content Summary	20
REFERENCES	22
2 KINETICALLY CONTROLLED PEPTIDE SELF-ASSEMBLY PROCESS FOR THE FORMATION OF TWO-DIMENSIONAL NANOSTRUCTURES	38
2.1 Introduction	38
2.2 Materials and Methods	41
2.2.1 Peptide Synthesis	41
2.2.2 Peptide Purification	42
2.2.3 Circular Dichroism Spectroscopy Measurement	45
2.2.4 Peptide Solution Self-assembly Experiments	46
2.2.5 Transmission Electron Microscopy Measurement	47
2.2.6 Atomic Force Microscopy Measurement	47
2.2.7 Small Angle X-ray Scattering (SAXS)	48
2.3 Peptide Sequences and Design	48
2.4 pH-dependent Assembly Kinetic Process	50
2.4.1 Kinetic Trap at pH 8 and pH 7 of Room Temperature	56
2.4.2 Accelerated Lattice Formation by Thermal Annealing at pH 8 and pH 7	57
2.4.3 N-terminus Charge Effect on Assembly Kinetic	70

2.5	Irregularly Assembled P422 ₂ Sequence.....	74
2.6	Conclusion.....	77
REFERENCES.....		79
3	NANOTUBES, PLATES, AND NEEDLES: PATHWAY-DEPENDENT SELF-ASSEMBLY PROCESS OF COMPUTATIONALLY DESIGNED PEPTIDES.....	88
3.1	Introduction.....	88
3.2	Materials and Methods.....	89
3.2.1	Peptide Synthesis.....	89
3.2.2	Peptide Purification.....	90
3.2.3	Peptide Solution Self-assembly Experiments.....	91
3.2.4	Transmission Electron Microscopy.....	92
3.2.5	Cryogenic TEM (Cryo-TEM).....	92
3.2.6	Scanning Transmission Electron Microscopy Mass-mapping Measurement.....	92
3.2.7	Atomic Force Microscopy.....	93
3.2.8	Circular Dichroism.....	94
3.2.9	Small Angle X-ray scattering.....	94
3.3	Peptide Sequence.....	95
3.4	Different Morphology Structures at Different pH Condition.....	96
3.5	Nanotube Structure Analysis.....	102
3.5.1	TEM and SAXS Result and Analysis.....	102
3.5.2	STEM Mass-Mapping Analysis.....	107
3.5.3	Tube Formation Discussion.....	111
3.6	Needle-like Structure Analysis.....	118
3.7	Conclusion.....	120
REFERENCES.....		122
4	PEPTIDE-GOLD HYBRID MATERIALS DEVELOPMENT.....	126
4.1	Introduction.....	126
4.2	Materials and Methods.....	129
4.2.1	Peptide Synthesis.....	129
4.2.2	Peptide Purification.....	130
4.2.3	Peptide Solution Self-assembly Experiments.....	132
4.2.4	Templating of Gold Nanoparticles.....	133
4.2.5	Transmission Electron Microscopy.....	133

4.2.6	Cryogenic TEM (Cryo-TEM).....	134
4.2.7	Circular Dichroism	134
4.2.8	Gold Nanowires Deposition	134
4.2.9	Atomic Force Microscopy	134
4.2.10	Wide and Small Angle X-ray scattering.....	135
4.2.11	Ultraviolet-visible Spectroscopy (UV-vis).....	135
4.3	Peptide-mediated Gold Nanoparticle Structures	136
4.3.1	Cysteine-modified Peptide Assemblies	136
4.3.2	One-dimensional and Two-dimensional Gold Nanoparticle Arrays Templated by Peptide Assembly	137
4.3.3	Optical Property of Templated One-Dimensional Gold Nanoparticle Chain	142
4.3.4	Peptide Assembly Kinetic-Control of Gold Nanoparticle Organization	146
4.4	Fabrication of Gold Nanowires	153
4.5	Conclusion.....	155
	REFERENCES	157
5	INTERACTIONS BETWEEN GOLD PRECURSOR ANIONS AND POSITIVELY CHARGED CYSTEINE CONTAINING PEPTIDE SCAFFOLDS DURING THE TEMPLATED AQUEOUS SYNTHESIS.....	167
5.1	Introduction	167
5.2	Materials and Methods	170
5.2.1	Peptide Synthesis.....	170
5.2.2	Peptide Purification	170
5.2.3	Peptide Solution Self-assembly Experiments.....	170
5.2.4	Templating of Gold Nanoparticles	170
5.2.5	Transmission Electron Microscopy	170
5.2.6	Cryogenic TEM (Cryo-TEM).....	171
5.2.7	Wide and Small Angle X-ray scattering.....	171
5.3	Stoichiometry Effect.....	171
5.4	Addition Order Effect of Precursor Molecules	175
5.5	Binding Selectivity to inorganic Species.....	181
5.6	Conclusion.....	187
	REFERENCES	188
6	CONCLUSIONS AND PERSPECTIVE	195

6.1	Conclusions	195
6.2	Prospective	199
6.2.1	Co-assembly of multiple peptides	199
6.2.2	Novel materials development	206
6.2.3	Conclusion	208
REFERENCES		209
Appendix		
PERMISSION LETTERS		212
A.	American Chemical Society Publications License	212
B.	Royal Society of Chemistry License	213

LIST OF TABLES

Table 2.1	The theoretically predicted P422 lattice former candidates and the acetylated variants. The underlined letters indicate the interior residues. IEP (iso-electric point) is estimated from a web-calculator http://www.bachem.com/service-support/peptide-calculator/	49
Table 2.2	Estimated net charge of each Ac-P422_1 peptide bundle at different pH values.	56
Table 2.3	Estimated net charge of each H-P422_1 peptide bundle at different pH values.	72
Table 3.1	The modified H-P222_9 sequences. AC is the original sequence with acetylated N-terminus. R3K is the original sequence with arginine in position 3 being substituted by lysine. E5Q is the original sequence with glutamic acid in position 5 being substituted by glutamine.	113

LIST OF FIGURES

- Figure 1.1** The structure model of peptide dimeric coiled-coil. **Top:** the wheel diagram with the viewing direction that is parallel to the coiled-coil axis. The *abcdefg* heptad pattern is used to depict the amino acid residue position arrangement. The *a* and *d* positions occupied by hydrophobic amino acid residues are buried between the two peptide helical chains. **Bottom:** the coiled-coil structure model viewing from the direction perpendicular to the coiled-coil axis, depicted by ribbon-drawing. (Figure adapted with permission from reference 137, copyright 2004 American Chemical Society) 14
- Figure 1.2** The design of the helical-motif building block by sampling 5 parameters (*R*: super-helical radius; θ : minor-helical phase; α : super-helical phase; *Z*: super-helical axis; *P*: super-helical pitch) associated with the size and geometry of the bundle using Monte Carlo simulated annealing (left): N terminus is depicted in blue and C terminus in red; side and top view of the selected low-energy motif with the most probable amino acids at the interior sites shown in space-filling representations (right)..... 17
- Figure 1.3** Computationally designed, α -helical, homotetrameric assemblies. **A-D:** Models of peptides forming distinct nanostructures using a *de novo* designed helical homotetrameric bundle, which comprises both the backbone coordinates of the D2 symmetric tetramer and interior hydrophobic residues. In the left of each panel, designed exterior residues are colored according to chemical properties: positively charged (red), negatively charged (blue), polar (green) and hydrophobic (gray). On the right of each panel, the targeted assemblies are rendered along with symmetry axes (C2 oval, C3 triangle, C4 square, C6 hexagon) and the unique dimensions of the unit cell, *a* and *b*. **A:** D2 symmetric tetramer designed in isolation and targeted to remain in solution. The exterior residues of the remaining proteins were designed in the context of the corresponding space groups: **(B)** P622; **(C)** P422; **(D)** P222..... 19

Figure 2.1	Representative ESI-mass spectrometry data for Ac-P422_1 peptide. Designed molecular weight: [M] 3614 Da. The accordingly calculated mass is: [M+2H ⁺] 3616 Da, [M+3H ⁺] 3617 Da, [M+4H ⁺] 3618 Da, [M+5H ⁺] 3619 Da, [M+6H ⁺] 3620 Da. The experimental measured mass is: [M+2H ⁺] 3616 Da, [M+3H ⁺] 3618 Da, [M+4H ⁺] 3620 Da, [M+5H ⁺] 3620 Da, [M+6H ⁺] 3624 Da.	44
Figure 2.2	Representative analytical HPLC chromatographic data for Ac-P422_1 peptide. The single elution peak indicates the high purity of the peptide products.	45
Figure 2.3	A: The peptide homotetrameric coiled-coil bundle building block with exterior residues coloured according to amino acid properties: blue indicates positively charged residues, red indicates negatively charged residues, green indicates polar residues, and yellow indicates hydrophobic residues. Interior residues are coloured grey. B: Rendering of one layer from a lattice with P422 symmetry, viewed from the top of the two-dimensional assembly.	50
Figure 2.4	Circular dichroism spectroscopy data for Ac-P422_1 measured at 20°C in four different buffer conditions as shown in the figure legend. The ratios of [MRE] _{222nm} /[MRE] _{208nm} are 1.06, 1.12, 1.62 and 1.16 for pH 4.5, 7, 8 and 10, respectively. The ratios at pH4.5 and pH10 are close to 1 indicating the stabilized coiled-coil formation. While for pH7 and pH8, due to the fast assembly process, peptides already started to precipitate, causing the loss of CD signal for this measurement. Formation of lattices is consistent with stable coil-coils at the pH 7 and pH 8 conditions.	51
Figure 2.5	Transmission electron microscopy images of Ac-P422_1 peptide assembled at RT with concentration of 0.1 mM. and observed at different time periods. A-C: Peptides assembled at RT pH 8 for 2 days, 1 week and 8 weeks, respectively. D-F: Peptides assembled at RT pH 7 for 2 days, 1 week and 8 weeks, respectively. Both cases show disordered aggregates that formed at earlier time points and then transformed into ordered two-dimensional plates after aging.	52
Figure 2.6	Dry state transmission electron microscopy high magnification images of Ac-P422_1 peptide assembled at room temperature show the symmetry of lattices is the same. Images were taken with 2% wt. phosphotungstic acid negative staining to enhance the contrast. Scale bars are all in 20nm. A-B: Peptides assembled at RT pH8 for 1 week and 8 weeks, respectively. C-D: Peptides assembled at RT pH7 for 1 week and 8 weeks, respectively.	53

- Figure 2.7** SAXS result measured from Ac-P422_1 peptide assembly solution at pH 10 with concentration of 1 mM and different aging time. The black plot is the sample solution aged for 8 days, no distinctive peaks. The red plot is the sample solution aged for 22 days; the distinctive peaks indicate the existence of ordered lattice structures..... 54
- Figure 2.8** TEM images of Ac-P422_1 peptide assembled at 50°C with concentration of 0.1 mM and observed after incubation for 24 hours. **A:** pH8 after 24 hours. **B:** pH7 after 24 hours. Assembly of mature plates several micrometres in size was observed for both conditions. Images were taken without staining. 58
- Figure 2.9** TEM images of Ac-P422_1 peptide assembled at 40°C with concentration of 0.1 mM. **A:** Peptides assembled at 40°C pH8 for 24 hours. **B:** Peptides assembled at 40°C pH7 for 24 hours. Compared to the assemblies formed at 50°C, irregular aggregates are observed around the peptide plates. 59
- Figure 2.10** Circular dichroism spectroscopy data for Ac-P422_1 peptide sample quenched to 50 °C. **A:** 0.1mM peptide at 50 °C pH8, CD spectra measured as peptide solution quenched from 95 °C to 50 °C. The ratio of $[\theta]_{222\text{nm}}/[\theta]_{208\text{nm}}$ at time 0 is 1.00, indicating the coiled-coil formation. The gradual loss of signal is because of larger assemblies precipitating from of solution. **B:** 0.1mM peptide at 50 °C pH7, CD spectra were measured as peptide solution quenched from 95 °C to 50 °C. The ratio of $[\theta]_{222\text{nm}}/[\theta]_{208\text{nm}}$ at time 0 is 0.98, indicating the coiled-coil formation. 60
- Figure 2.11** Temperature-dependent circular dichroism spectroscopy data for Ac-P422_1 peptide. 0.1mM peptide in 10mM pH7 phosphate buffer was measured upon heating. Left: wavelength scan at different temperatures on heating. Right: MRE at 222nm with increasing temperature, showing the melting temperature of approximately 60°C.. 61
- Figure 2.12** TEM images of Ac-P422_1 peptide assembled at 50°C with concentration of 0.1 mM and observed at different time points. Insets are higher magnification images of individual peptide plates present at each time point. **A-C:** Peptides assembled at 50°C, pH8 for 15 min, 30 min and 6 hours, respectively. **D-F:** Peptides assembled at 50°C pH7 for 15 min, 30 min and 6 hours, respectively. All the images were observed with 2 wt% phosphotungstic acid negative staining to enhance the contrast. 63

- Figure 2.13** TEM high magnification images of Ac-P422_1 peptide assembled at 50°C and observed at different time point show the symmetry of lattices is the same. Images were taken with 2% wt. phosphotungstic acid negative staining to enhance the contrast. Scale bars are all in 20nm. **A-C**: Peptides assembled at 50°C pH8 for 15 min, 30 min and 6 hours, respectively. **D-F**: Peptides assembled at 50°C pH7 for 15 min, 30 min and 6 hours, respectively..... 64
- Figure 2.14** Atomic force microscopy images of Ac-P422_1 peptides assembled at 50°C. The white lines in the AFM images indicate the section height analysis trace. The positions of coloured cross markers are indicated by the dash lines in the height plots at right with corresponding colours in the height plots on the left. **A**: 50°C pH 8 for 48 hours. **B**: 50°C pH 7 for 48 hours..... 67
- Figure 2.15** TEM images of Ac-P422_1 peptides assembled at 50°C pH 7 at different time points showing the defects in assembly structures. Images were taken with 2% wt. phosphotungstic acid negative staining. **A**: High magnification image of 50°C pH 7 assemblies to show grain boundary defect highlighted by red dash line. Two sets of lattices with different orientations are highlighted with red meshes. **B**: High magnification image of peptides assembled at 50°C pH 7 for 48 hours to show grain boundary highlighted by red dash line. **C**: High magnification of peptides assembled at 50°C pH 7 for 6 hours. The red dash line is indicating the grain boundary. There is developed crack following the grain boundary. The plates usually will crack upon drying after casting film on TEM grids..... 68
- Figure 2.16** **A**: SAXS result measured from H-P422_1 peptide assembly solution at pH 10 with concentration of 1 mM and different aging time. The black plot is the sample solution aged for 8 days, no distinctive peaks. The red plot is the sample solution aged for 22 days; the distinctive peaks indicate the existence of ordered lattice structures. **B**: TEM image of H-P422_1 peptide assembly solution at pH 10 with concentration of 1 mM aged for 2 months. Left is the low magnification image showing the two-dimensional assembly structures. Right is the high magnification image showing the lattice structure. 71

- Figure 2.17** **A:** TEM image of H-P422_1 peptide assembled at room temperature with concentration of 0.1 mM pH 7 and observed after incubation for 30 days. **B:** TEM image of H-P422_1 peptide assembled at 30°C with concentration of 0.1 mM pH 7 and observed after incubation for 24 hours. **C:** TEM image of H-P422_1 peptide assembled at 50°C with concentration of 0.1 mM pH 7 and observed after incubation for 24 hours. **D:** SAXS result measured from H-P422_1 peptide assembly solution at pH 7 with concentration of 1 mM treated with different temperature and different aging time; the distinctive peaks indicate the existence of ordered lattice structures. 74
- Figure 2.18** Analysis of the crystal structure of H-P422_1. **Top:** Two asymmetric units each containing three helical bundles, presented by ribbon drawing. Within each bundle-bundle interface, sidechains of critical stabilizing interactions are rendered as sticks and colored by atom type: C (white), N (blue), O (red) and S (yellow). Colored dash boxes correspond to the enlarged and reoriented regions of the interfaces on the bottoms. **Bottom left:** Two example Met-Trp-Met motifs at the bundle-bundle interface are shown in sticks and electron density map. Dashed black lines between Trp10 and Met21, and Trp10 and Met17 label two consistent distances across twelve motifs in three bundle-bundle interfaces. The packing of the motifs (spheres) on the top is shown in the bottom box. **Bottom right:** The hydrogen bonds between Lys13 and Gln16 are shown (black dashed lines) with distance between donors and acceptors labeled. Outline colors correspond to the boxes on the twisted ribbon structure. 76
- Figure 3.1** Representative ESI-mass spectrometry data for H-P222_9 peptides. Designed molecular weight: [M] 3168 Da. The accordingly calculated mass is: [M+2H⁺] 3170 Da, [M+3H⁺] 3171 Da, [M+4H⁺] 3172 Da. The experimental measured mass is: [M+2H⁺] 3170 Da, [M+3H⁺] 3171 Da, [M+4H⁺] 3172 Da. 90
- Figure 3.2** Representative analytical HPLC chromatographic data for H-P222_9 peptide. The single elution peak indicates the high purity of the peptide products. 91

- Figure 3.3** Designed H-P222_9 peptide coiled-coil bundle model and the TEM images of designed peptide assembled in aqueous solution with different pH values. **A:** The assembly building block is a cylinder-like homotetrameric coiled-coil bundle, with that is approximately 4 nm in length and 2 nm in diameter. The α -helices of designed sequence DGRIEGM AEAIKKM AYNIADM AGRIWGE A-NH₂ are represented by ribbon drawings (the exterior residues are colored according to amino acid properties: blue indicates basic residues, red indicates acidic residues, green indicates polar residues, and yellow indicates hydrophobic residues. Interior residues are colored grey). **B:** TEM image of 0.25 mM peptide assembled in 10 mM pH 4.5 sodium acetate buffer; observed are flattened assembled peptide nanotubes. **C:** TEM image of 1 mM peptide assembled in 10 mM pH 7 phosphate buffer; observed are 2D platelets. **D:** TEM image of 1 mM peptide assembled in 10 mM pH 10 borate buffer; observed are elongated, micrometer-long, needle-like structures..... 97
- Figure 3.4** Circular dichroism spectroscopy data for H-P222_9 peptide measured at 20°C in pH 4.5 sodium acetate buffer and pH 10 borate buffer. Data is plotted with buffer background subtracted. Both spectrum show typical α -helical conformation. And at pH 4.5, the ratio of two ellipticity minima $[MRE]_{225nm}/[MRE]_{210nm} = 1.11$; at pH 10, the ratio of two ellipticity minima $[MRE]_{222nm}/[MRE]_{208nm} = 0.99$. The ratios are close to 1 indicating the stabilized coiled-coil formation in both pH conditions. 99
- Figure 3.5** AFM of H-P222_9 peptide assembled in aqueous solution with different pH values. **A:** 0.25 mM peptide assembled in 10 mM pH 4.5 sodium acetate buffer. **B:** 1 mM peptide assembled in 10 mM pH 7 phosphate buffer. **C:** 1mM peptide assembled in 10mM pH 10 borate buffer. **D:** The corresponding height analysis histogram of the nanoribbon assemblies. **E:** The height scans of the platelet assemblies. **F:** The height scans of the needle-like assemblies. 101
- Figure 3.6** **A:** Cryo-TEM images of 0.2mM H-P222_9 peptide assembled in 10mM pH 4.5 sodium acetate buffer showing hollow nanotubes. Inset is higher magnification image showing tubes with tube diameter $13.3 \text{ nm} \pm 0.7 \text{ nm}$ and tube wall thickness $3.1 \text{ nm} \pm 0.5 \text{ nm}$. **B:** SAXS result measured from H-P222_9 peptide assembly solution at pH 4.5. The experimental data is plotted in blue, and the calculated curve using a hollow tube model is plotted in red..... 102

- Figure 3.7** H-P222_9 peptide nanotube diameter and wall thickness measurement distribution. 10 different cryo-TEM images taken from the same samples were used for measurement in ImageJ. **Left:** The tube diameter was measured from wall center to wall center across the tube diameter. Total 119 different areas were measured giving the mean tube diameter value of 13.3 nm and standard deviation of 0.7 nm. **Right:** For nanotube wall thickness, total 146 different areas were measured giving the mean thickness value of 3.1 nm and standard deviation of 0.5 nm..... 103
- Figure 3.8** Possible structure models for peptide nanotubes formed at pH 4.5. **A,** **B:** Tilted single bundle-layered tube model. The tube wall is a single layer of peptide bundle. The cross-section schematic (**B**) reveals the bundles to be packed in a tilted angle to the tube wall. The tilted angle can be calculated as 40° . The corresponding central angle can be calculated as 30.3° . A single slice contains approximately 11 bundles. **C:** Perpendicular-packing tube model. Bundles are proposed as being packed perpendicularly to the tube wall. The wall thickness is approximately 3 nm according to TEM and SAXS results. The bundle length is approximately 4 nm according to design. A single cross-section contains approximately 16 bundles..... 105
- Figure 3.9** Negatively stained protein microtubules used as standard sample in STEM mass-mapping measurement. The microtubules are formed by the tubulin proteins (from Cytoskeleton, Inc.). Tubulin is composed of a heterodimer of two 55 kDa proteins. The microtubules formed from tubulin proteins have the mean diameter of 25 nm, and each micrometer of microtubule containing 1650 heterodimers (more information seen in Cytoskeleton, Inc. <https://www.cytoskeleton.com/tubulins/microtubules>). Therefore, the mass-per-length value of protein microtubules can be calculated as: $55 \times 2 \times 1650 \div 1000 = 181.5 \text{ kDa/nm}$ 108
- Figure 3.10** STEM mass-mapping results of peptide nanotubes with the use of protein microtubules as standard samples. **A:** As indicated, the relatively brighter 1D ribbon-like structures are the protein microtubules, while the relatively darker and more abundant 1D ribbon-like structures are the peptide nanotubes. In ImageJ, a box with dimension of $a \text{ nm} \times b \text{ nm}$ was drawn to include whole section of protein microtubules to obtain the intensity. A series of boxes with dimension of $c \text{ nm} \times d \text{ nm}$ was drawn to include whole section of peptide nanotube to obtain the intensity. **B:** Mass-per-length of peptide nanotube histogram obtained from STEM measurement, fitted to a single Gaussian peak (red curve) at 50.1 kDa/nm, with 32.8 kDa/nm full width at half maximum (FWHM). 110

- Figure 3.11** Cryo-TEM micrograph of modified sequences assembly structures. **A:** 0.2 mM **AC** sequence in 10 mM pH 4.5 sodium acetate buffer, assembled at room temperature for 24 hours. A mixture of two-dimensional plates and nanotubes can be observed. **B:** 0.2 mM **R3K** sequence in 10 mM pH 4.5 sodium acetate buffer, assembled at room temperature for 24 hours. Nanotubes are observed with width of 11.7 ± 1.1 nm and wall thickness of 4.0 ± 0.7 nm. 114
- Figure 3.12** **R3K** peptide nanotube diameter and wall thickness measurement distribution for **Figure 3.11B**. 10 different cryo-TEM images taken from the same samples were used for measurement in ImageJ. Left: **R3K** peptide nanotube diameter distribution. The tube diameter was measured from wall center to wall center across the tube diameter. Total 296 different areas were measured giving the mean diameter value of 11.7 nm and standard deviation of 1.1 nm. Right: **R3K** peptide nanotube wall thickness distribution. Total 304 different areas were measured giving the mean thickness value of 4.0 nm and standard deviation of 0.7 nm. 115
- Figure 3.13** Comparison between nanotube structure models between un-modified H-P222_9 peptides and **R3K** modified peptides. **A:** The original tilted-bundle model of un-modified H-P222_9 peptide nanotubes, same as in **Figure 3.8B**, depicting the hollow tube with diameter $13.3 \text{ nm} \pm 0.7 \text{ nm}$ and tube wall thickness $3.1 \text{ nm} \pm 0.5 \text{ nm}$. **B:** The less tilted-bundle model of **R3K** modified peptide nanotubes, depicting the tube with diameter $11.7 \pm 1.1 \text{ nm}$ and wall thickness of 4.0 ± 0.7 . The bundles are less tilted, and packed more towards center, resulting in the thicker wall thickness and smaller tube diameter. 116
- Figure 3.14** Circular dichroism spectroscopy data for the modified sequence **E5Q** measured at 20°C at pH 4.5. 0.1 mM concentration peptide in pH 4.5 10 mM sodium acetate buffer. Data is plotted with buffer background subtracted. The spectrum shows typical α -helical conformation. The ratio of two ellipticity minima $[\text{MRE}]_{222\text{nm}}/[\text{MRE}]_{208\text{nm}} = 1.18$. The ratio is close to 1 indicating the stabilized coiled-coil formation. 117
- Figure 3.15** TEM image of 0.25 mM H-P222_9 peptide assembled in 10 mM pH 4.5 sodium acetate buffer, same condition as in **Figure 3.3B**, but with longer aging time (several months). Platelets can be observed. Image was taken under high defocused condition to reveal the tubes structure in background. 118

- Figure 3.16** Schematic of needle-like structure formation process at pH 10. **A:** High-magnification TEM image of needle-like structure revealing the details of orderly spaced strands. Inset is the HRTEM showing the lattices superimposed with designed lattice model, viewing from coiled-coil bundle axis. Red dashed lines indicate the two bundle-bundle interfaces. **B:** At pH 7, at interface 2, lysine can form a salt bridge with aspartic acid. At pH 10, due to the partial deprotonation, salt bridge was weakened, partially destabilizing the designed bundle-bundle interface 2. **C:** The original design is for bundles to organize into two-dimensional lattices in both x- and y-directions, which is the case at pH 7. Two-dimensional plates were formed, even stacking in the z-direction. At pH 10, the partially destabilized interface 2 caused the assembly to preferentially form needle-like structures with preferential growth in x-direction..... 120
- Figure 4.1** **A:** Time-of-flight mass chromatograph for Ac-C-P222 peptide. Peptides were eluted during the gradient of 95% solvent A to 5% solvent A in 5 min with first 0.5 min elution uncollected, in which solvent A is Milli-Q water containing 0.1%-vol TFA, solvent B is acetonitrile containing 0.1%-vol TFA. **B:** Combined mass spectrum of the major peak in mass chromatograph showing the m/z values. Designed molecular weight: [M] 3313 Da. The accordingly calculated mass is: [M+3H⁺] 3316 Da, [M+4H⁺] 3317 Da. The experimental measured mass is: [M+3H⁺] 3315 Da, [M+4H⁺] 3316 Da..... 131
- Figure 4.2** **A:** Time-of-flight mass chromatograph for Ac-C-P422 peptide. Peptides were eluted during the gradient of 95% solvent A to 5% solvent A in 5 min with first 0.5 min elution uncollected, in which solvent A is Milli-Q water containing 0.1%-vol TFA, solvent B is acetonitrile containing 0.1%-vol TFA. **B:** Combined mass spectrum of the major peak in mass chromatograph showing the m/z values. Designed molecular weight: [M] 3717 Da. The accordingly calculated mass is: [M+4H⁺] 3721 Da, [M+5H⁺] 3722 Da, [M+6H⁺] 3723 Da. The experimental measured mass is: [M+4H⁺] 3720 Da, [M+5H⁺] 3720 Da, [M+6H⁺] 3726 Da..... 132
- Figure 4.3** TEM micrographs of cysteine-modified peptide assemblies. **A:** Ac-C-P222 with 0.2 mM concentration, in 50 mM pH 4.5 buffer with 0.5 mM TCEP, assembled at room temperature for 18 hours. Hollow nanotubes can be observed under cryo-TEM. **B:** Ac-C-P422 with 0.5 mM concentration, in 50 mM pH 7 buffer with 1.25 mM TCEP, assembled at 50°C for 7 hours. Inset is the HRTEM image showing the lattice structures..... 137

- Figure 4.4** TEM images show the nanostructures of solution synthesized gold nanoparticles templated by cysteine-modified peptides. **A:** One-dimensional gold nanoparticle chains templated by peptide nanotubes in 50 mM pH 4.5 buffer with 0.2 mM Ac-C-P222 peptides, 0.4 mM HAuCl₄ and 0.4 mM NaBH₄, and incubated at room temperature for 2 hours. **B:** High magnification image showing individual gold nanoparticles. **C:** HAADF image with bright dots showing the inorganic nanoparticles. **D:** Two-dimensional gold nanoparticle arrays templated by peptide plates in 50 mM pH 7 buffer with 0.5 mM Ac-C-P422 peptides, 5 mM HAuCl₄, 5 mM NaBH₄ and 2.5 mM bis(*p*-sulfonatophenyl)phenylphosphane dehydrate and incubated at room temperature for 24 hours. **E:** High magnification image showing individual gold nanoparticles. **F:** HAADF image with bright dots showing the inorganic nanoparticles. 139
- Figure 4.5** TEM images show the nanostructures of solution synthesized gold nanoparticles templated by non-cysteine peptides. **A:** Gold nanoparticles templated by peptide nanotubes in 50 mM pH 4.5 buffer with 0.2 mM P222_9, 0.4 mM HAuCl₄ and 0.4 mM NaBH₄. Image was taken under high defocus condition to reveal peptide nanotubes. The formed gold nanoparticles exhibit no templating effect. **B:** Gold nanoparticles templated by peptide plates in 50 mM pH 7 buffer with 0.5 mM P422_1, 5 mM HAuCl₄, 5 mM NaBH₄ and 2.5 mM bis(*p*-sulfonatophenyl)phenylphosphane dehydrate. Inset is the zoom-in image showing individual nanoparticles. The formed gold nanoparticles exhibit no templating effect. 140
- Figure 4.6** TEM images show the morphologies of un-templated growth of gold materials in solution. **A:** 1 mM HAuCl₄ in 50 mM pH 4.5 buffer and reduced by the same molar ratio of NaBH₄ and examined at 5 min time point. Inset is the electron diffraction pattern showing the crystalline gold. **B:** 1 mM HAuCl₄ in 50 mM pH 7 buffer and reduced by the same molar ratio of NaBH₄ and examined at 5 min time point. Inset is the electron diffraction pattern showing the crystalline gold.... 141
- Figure 4.7** TEM images show the nanostructure of templated, pre-made 5 nm AuNPs. **A:** Two-dimensional 5 nm AuNP arrays templated by Ac-C-P422 peptide plates in 50 mM pH 7 buffer. The peptide plate solution and pre-made 5 nm AuNP solution were mixed and incubated at room temperature for 24 hours for examination. **B:** High magnification image showing individual 5 nm AuNPs. 142

- Figure 4.8** **A:** TEM image of peptide nanotube-templated growth of gold nanoparticle-chains (0.2 mM Ac-C-P222 nanotubes with 2eqv H_{Au}Cl₄ and 2eqv NaBH₄ with respect to the amount of peptides) after 4 days, inset is the gold nanoparticle diameter distribution width diameter of 6.4 nm ± 3.4 nm. **B:** UV-Vis spectra recorded during gold nanoparticle growth process using 18 hour-assembled Ac-C-P222 peptide nanotubes as templates with 2eqv. H_{Au}Cl₄ and 2eqv. NaBH₄ with respect to the amount of peptides. The SPR peak at about 528 nm started to emerge at about 12 hours of gold nanoparticle growth. 144
- Figure 4.9** UV-Vis spectra recorded during gold nanoparticle synthesis process only using 0.4 mM H_{Au}Cl₄ and 0.4 mM NaBH₄, without peptide nanotubes as templates. No distinctive SPR peak is observed. Only an absorption shoulder appears in the wavelength region of 500nm-550nm. 145
- Figure 4.10** Circular dichroism spectroscopy data for Ac-C-P222 peptide with 0.1mM concentration measured at different temperatures in pH4.5 buffer condition containing 0.5mM TCEP. Data is plotted with buffer background subtracted. The spectrum measured at room temperature show typical α -helical conformation. The spectrum measured from 85°C-30min incubated the solution shows the melting of α -helical structures. The α -helical conformation can be recovered immediately once the solution is cooled, as shown by the spectrum measured from the solution cooled from 85°C to 20°C in time 0 point. 147
- Figure 4.11** **A:** The schematic of the kinetic assembly process of Ac-C-P222. In stage 1, peptides exist as denatured random coils. In stage 2, peptides mainly exist as folded coiled-coil bundles, depicted by cylindrical ribbon-drawings. In stage 3, peptides mainly exist as assembled nanotube morphologies. **B:** TEM image showing the nanostructures formed from 2 eqv. gold precursor solution added at stage 1 of the peptide assembly process. The structure was examined 2 hours after mixing. **C:** TEM image showing the nanostructures formed from 2 eqv. gold precursor solution added at stage 2 of the peptide assembly process. The structure was examined after 24 hours from the point of mixing. Inset is the HR-TEM of an individual gold nanoparticle. **D:** TEM image showing the nanostructures formed from 2 eqv. gold precursor solution added at stage 3 of the peptide assembly process. The structure was examined after 2 hours from the point of mixing. **E:** The corresponding structure models illustrating the nanostructures formed in **B-D**, respectively. The sizes of objects are not in scale. After the attachment of gold nanoparticles, the peptide nanotubes exhibit more flexibility. 148

- Figure 4.12** Cryo-TEM images show the morphology of Ac-C-P222 peptide assembly structures formed after 20 min of room temperature incubation. **A** and **B** were taken from different areas indicating the existence of only short peptide nanotubes. Individual un-assembled peptide coiled-coil bundles cannot be directly detected under TEM due to the small size and low electron density. 150
- Figure 4.13** Circular dichroism spectroscopy data for Ac-C-P422 peptide with 0.1mM concentration measured at different temperatures in pH7 buffer condition containing 0.5mM TCEP. Data is plotted with buffer background subtracted. The spectrum measured at room temperature show typical α -helical conformation. The spectrum measured from 85°C-30min incubated the solution shows the melting of α -helical structures. The α -helical conformation can be recovered immediately once the solution is cooled, as shown by the spectrum measured from the solution cooled from 85°C to 20°C in time 0 point. 151
- Figure 4.14** TEM images show the nanostructures of pre-made 5 nm AuNPs templated with Ac-C-P422 peptide assembled at different stages at 50°C in pH 7 buffer. **A**: 5 nm AuNP solution mixed with peptides in denatured state and examined after 24 hours from the mixing. **B**: High magnification image of indicated **area 1** in **A** showing disordered, aggregated 5 nm AuNPs. **C**: High magnification image of indicated **area 2** in **A** showing hexagonally packed 5 nm AuNP. **D**: 5 nm AuNP mixed with peptide solution after 6 hours of peptide plate-assembly at 50°C and evaluated after 24 hours from the mixing; two-dimensional 5 nm AuNP arrays can be observed. Inset is the high magnification image from plates showing the individual 5 nm AuNPs. 153
- Figure 4.15** Gold nanowire deposition process. **A**: Three different baths including peptide solution, HAuCl₄, and NaBH₄ solution were exposed to a mica substrate successively for gold nanowires fabrication. **B**: AFM micrograph of the deposited gold nanowires on mica sheet. **C**: Height analysis reveals the average height as 8.8 nm with a standard deviation of 1.3 nm. 155

- Figure 5.1** TEM images of Ac-C-P222 peptide nanotube templated solution synthesis of gold nanoparticles with different precursor molecule ratio. **A:** 0.2 mM peptide nanotubes with 0.5 mM TCEP, 0.2 mM HAuCl₄ and 0.2 mM NaBH₄ in 50 mM pH 4.5 buffer were used as growth solution and incubated for 2 hours. (Molar ratio of peptide: HAuCl₄: NaBH₄=1: 1: 1). **B:** 0.2 mM peptide nanotubes with 0.5 mM TCEP, 0.4 mM HAuCl₄ and 0.4 mM NaBH₄ in 50 mM pH 4.5 buffer were used as growth solution and incubated for 2 hours. (Molar ratio of peptide: HAuCl₄: NaBH₄=1: 2: 2). Inset is HR-TEM of individual gold nanoparticle showing gold (111) crystal plane with 2.3 Å spacing. **C:** 0.2 mM peptide nanotubes with 0.5 mM TCEP, 0.6 mM HAuCl₄ and 0.6 mM NaBH₄ in 50 mM pH 4.5 buffer were used as growth solution and incubated for 2 hours. (Molar ratio of peptide: HAuCl₄: NaBH₄=1: 3: 3)..... 172
- Figure 5.2** TEM image shows the formation of continuous gold nanowire structures from the solution condition containing 0.2 mM Ac-C-P222 peptide nanotubes, 0.5 mM TCEP, 1 mM HAuCl₄ and 1 mM NaBH₄, and incubated for growth for 2 hours. (Molar ratio of peptide: HAuCl₄: NaBH₄=1: 5: 5)..... 173
- Figure 5.3** HAADF image of UV photo-induced formation of gold nanoparticles. In 0.2 mM Ac-C-P222 peptide nanotube solution with 0.5 mM TCEP, 1eqv. of HAuCl₄ (20 mM in DI water) and 1eqv. of NaBH₄ (20 mM in DI water) were added successively, to reach the final concentration of 0.2 mM for each precursor molecule. The solution was then radiated under UV lamp with wavelength of 365 nm, 20.1 mW/cm² for 7 hours. Bright particles in the image indicate the existence of inorganic gold nanoparticles..... 175
- Figure 5.4** TEM images show the gold nanoparticle growth on Ac-C-P222 peptide tubes with precursor molecules in the addition order of NaBH₄ as the first and HAuCl₄ as the second added. **A:** In 0.2 mM peptide nanotube solution containing 0.5 mM TCEP, NaBH₄ and HAuCl₄ were successively added to reach the final concentration of 0.4 mM for each precursor molecules. The solution was incubated for 7 hours. **B:** In 0.2 mM peptide nanotube solution containing 0.5 mM TCEP, NaBH₄ and HAuCl₄ were successively added to reach the final concentration of 0.4 mM for each precursor molecules. The solution was then radiated under UV lamp with wavelength of 365 nm, 20.1 mW/cm² for 7 hours. Gold nanoparticles were formed in one-dimensional organization. 176

- Figure 5.5** TEM images show the gold nanoparticle growth on Ac-C-P222 peptide tubes with precursor molecules in the addition order of NaBH₄ as the first and HAuCl₄ as the second. **A:** In 0.2 mM peptide nanotube solution containing 0.5 mM TCEP, NaBH₄ and HAuCl₄ were successively added to reach the final concentration of 1 mM for each precursor molecule. The solution was then incubated for growth for 2 hours. Spherical clusters are observed along with peptide nanotubes. Inset is the high magnification image of spherical clusters revealing the clustered structures. **B:** To the same solution shown in **A**, extra 5eqv. of NaBH₄ with respect to peptide concentration was added and incubated for 2 hours. Spherical clusters disappeared after the extra addition of NaBH₄. Gold nanoparticles formed. Inset is the high magnification image showing the individual gold nanoparticles organized into one-dimensional structures templated by peptide nanotubes. 178
- Figure 5.6** TEM images show the time-dependent growth process of gold nanoparticles on Ac-C-P222 peptide tubes in 5-equivalent condition. 0.2mM cysteine modified peptide solution was firstly assembled in 50mM pH 4.5 buffer with 2 eqv. TCEP for 18hours. 5 eqv. of HAuCl₄ solution and 5 eqv. of NaBH₄ with respect to peptide concentration were successively added to the solution for the growth of gold nanomaterials. **A:** After 5min of growth, some gold nanoparticles organized in one-dimension were observed. Spherical salt clusters from not yet reacted HAuCl₄ were observed as well. Inset is the high magnification image of cluster structure. **B:** After 15min of growth, more gold nanoparticles organized in one-dimension were observed. Spherical salt clusters were reduced. Inset is high magnification image showing the cluster structure and the templated gold nanoparticles. **C:** After 1h of growth, all the salt clusters disappeared, forming gold nanoparticles. 179
- Figure 5.7** TEM images show the gold nanoparticle growth result on Ac-C-P222 peptide nanotubes through a multi-step addition procedure of precursor molecules. **A:** In 0.2 mM peptide nanotube solution containing 0.5 mM TCEP, 1eqv. of NaBH₄ and 5eqv. of HAuCl₄ with respect to peptide concentration were added successively and incubated for growth for 2 hours. (Molar ratio of peptide: NaBH₄: HAuCl₄=1: 1: 5) Salt clusters are observed along with peptide nanotubes. **B:** To the same solution, extra 4eqv. of NaBH₄ with respect to peptide concentration was added, and incubated for 5 min. One-dimensional gold nanoparticle arrays can be observed. 181

- Figure 5.8** Cryo-TEM images of Ac-C-P222 peptide nanotube templated solution synthesis of gold nanoparticles. 0.2 mM cysteine-modified peptide nanotubes with 0.5 mM TCEP, 0.4 mM HAuCl₄ and 0.4 mM NaBH₄ were used as growth solution and incubated for 4 days for imaging. **A** and **B** are taken from the same sample in different areas, showing the peptide nanotubes attached with gold nanoparticles. This confirms the one-dimensional organization of gold nanoparticles is from the bonding between cysteine and peptides, not due to drying accumulation effect. 182
- Figure 5.9** TEM images show the growth of gold nanoparticles on non-cysteine containing H-P222 peptide tubes and the growth of silver nanoparticles on cysteine containing Ac-C-P222 peptide tubes. **A**: In 0.2 mM H-P222 peptide nanotube solution, 5eqv. of HAuCl₄ and 5eqv. of NaBH₄ with respect to peptide concentration were added successively and incubated for 2 hours. **B**: In 0.2 mM Ac-C-P222 peptide nanotube solution containing 0.5 mM TCEP, 5eqv. of AgNO₃ and 5eqv. of NaBH₄ with respect to peptide concentration were added successively and incubated for 2 hours. Both images were taken under highly defocused condition to reveal the tubes. Therefore, the observed widths of tubes are not accurate..... 183
- Figure 5.10** The loading percentage calculation of Ag nanoparticles on peptide nanotubes. **A**: The original TEM image of Ag nanoparticles synthesized with Ac-C-P222 nanotubes as templates. The image was taken from the same sample shown in **Figure 5.9**. **B**: The image with particle area information extracted from **A** using ImageJ. The red outlines indicate the areas of Ag nanoparticles. The blue outline indicates the area of the peptide nanotube, which can be calculated in ImageJ as A_{tube} . Within the nanotube area, the area summation of the silver nanoparticles can be calculated as A_{particle} . Therefore, the loading percentage can be calculated as $A_{\text{particle}}/A_{\text{tube}}*100\%$ 185
- Figure 5.11** The loading percentage calculation of Au nanoparticles on peptide nanotubes. **A**: The original TEM image of Au nanoparticles synthesized with Ac-C-P222 nanotubes as templates. The image was taken from the same sample shown in **Figure 4.4B** in **Chapter 4**. **B**: The image with particle area information extracted from **A** using ImageJ. The red outlines indicate the areas of Au nanoparticles. The blue outline indicates the area of the peptide nanotube, which can be calculated in ImageJ as A_{tube} . Within the nanotube area, the area summation of the silver nanoparticles can be calculated as A_{particle} . Therefore, the loading percentage can be calculated as $A_{\text{particle}}/A_{\text{tube}}*100\%$ 186

Figure 6.1	A: Cryo-TEM images of 0.2mM H-P222_9 peptide assembled in 10mM pH 4.5 buffer at room temperature for 18 hours. The tube diameter measured from wall center to wall center in TEM images is $13.3 \text{ nm} \pm 0.7 \text{ nm}$. The wall thickness measured from TEM images is $3.1 \text{ nm} \pm 0.5 \text{ nm}$. B: Cryo-TEM images of 0.2mM Ac-C-P222 peptide assembled in 50 mM pH 4.5 buffer with additional 2.5 TCEP at room temperature for 18 hours. The tube diameter measured from TEM is $13.0 \pm 0.8 \text{ nm}$, and wall thickness is $3.2 \pm 0.4 \text{ nm}$	200
Figure 6.2	Cryo-TEM images of branched nanotubes co-assembled from H-P222_9 and Ac-C-P222 peptides. 0.2 mM H-P222_9 and 0.2 mM Ac-C-P222 peptides firstly were allowed to self-assemble in pH 4.5 buffer individually. After 5 min of separate assembly, solutions were mixed for co-assembly. Nanostructures were examined after 18 hours of co-assembly.	201
Figure 6.3	Cryo-TEM images of branched nanotubes co-assembled from H-P222_9 and Ac-C-P222 peptides. 0.2 mM H-P222_9 and 0.2 mM Ac-C-P222 peptides firstly were allowed to self-assemble in pH 4.5 buffer individually. After 30 min of separate assembly, solutions were mixed for co-assembly. Nanostructures were examined after 18 hours of co-assembly.	202
Figure 6.4	Cryo-TEM images of branched nanotubes co-assembled from H-P222_9 and Ac-C-P222 peptides. 0.2 mM H-P222_9 and 0.2 mM Ac-C-P222 peptides firstly were allowed to self-assemble in pH 4.5 buffer individually. After 3 hours of separate assembly, solutions were mixed for co-assembly. Nanostructures were examined after 18 hours of co-assembly.	203
Figure 6.5	TEM images of glutaraldehyde cross-linked H-P222_9 nanotubes. A: Peptide nanotubes assembled from H-P222_9 and cross-linked by glutaraldehyde in pH 4.5 buffer. B: The cross-linked nanotubes from A mixed with DMF. The morphology is showing the nanotube structures are able to maintain themselves in the polar solvent.	207

ABSTRACT

Self-assembly is a spontaneous organization process of components into patterns and structures driven by weak, non-covalent interactions. Well-studied examples are amphiphilic molecules such as surfactants and amphiphilic block copolymers. Although a significant number of successful examples have been demonstrated for the production of self-assembled materials with various morphologies, the intrinsic polydispersity in chemical structures and chain conformation limits the complexity that can be achieved via the self-assembly of these types of molecules. Therefore, sequence- and shape-specific biomacromolecules, such as polypeptides and polynucleotides, provide a better opportunity to produce complex nanoarchitectures with programmability.

In the collaborative work presented in this Ph.D. dissertation, a computational design method is established by Saven group (University of Pennsylvania) to generate a group of 29-mer peptide sequences that were predicted to form robust, antiparallel, α -helical homotetrameric coiled-coil bundles as materials building blocks. The designed peptide coiled-coil bundles share the same interior bundle composition consisting of complementary hydrophobic amino acids for bundle stability in aqueous solution. The bundle exterior composition was varied to implement directional interactions at bundle-bundle interfaces on the basis of various predetermined space groups (P622, P422 and P222) to achieve two-dimensional, self-assembled lattices with programmability. Peptides were synthesized via solid-phase peptide synthesis

method and the successful programmable self-assembly behavior are experimentally confirmed. Moreover, the solution condition-dependent self-assembly behavior and the related kinetically controlled assembly pathways for two-dimensional sheet formation were investigated for two groups of designed peptides, including P422 and P222 sequences. The designed hydrophobic bundle core ensures the structure stability to tolerate non-physiological conditions which were applied in the kinetic manipulation processes. Specifically, the solution pH was used to control the charged state of amino acid residues in the exterior part of the coiled-coil bundles thus tuning the inter-bundle interactions. A general pI (isoelectric point)-dependent rule is introduced that peptides exhibit fast assembly kinetics in the pH conditions that are close to the pI values at which peptides carry the least charge. Classic thermal annealing methods can be applied to overcome the possible kinetic traps existing during the assembly process. In the pH conditions that are deviated from the pI values of the sequences, more diverse nanoarchitectures with controllable morphologies, other than the originally designed 2D nano-lattices, were successfully produced, triggered by the differently charged states of peptide bundles in these conditions. Moreover, the self-assembled peptide nanoarchitectures were applied as scaffolds to template the growth of gold nanomaterials. Due to the specific peptide templates, the synthesized gold nanoparticles are organized into 1D or 2D nanostructures exhibiting enhanced surface plasmon resonance properties. Future research should dive into the detailed processing study of the templated synthesis of gold nanoparticles for the development of functional devices as well as co-assembly study with the use of multiple peptide sequences for the production of multi-component, complex nanoarchitectures.

Chapter 1

INTRODUCTION

1.1 Materials Construction via Self-assembly and the Kinetic Control

Self-assembly is a spontaneous organization process of components into patterns or structures driven by weak, non-covalent interactions, such as hydrogen bonding, van der Waals forces, and π - π interactions.¹ It is a ubiquitous phenomenon in the fields of chemistry, physics and biology. For example, crystals are the self-assembled structures of atoms or molecules, living organisms are the self-assembled systems of numerous living cells. Within the living cells, functional proteins are self-assembled from peptides via secondary-, tertiary-, and quaternary structures. Self-assembly covers a large scale of objects of interest, connecting small building blocks and large ensembles. To materials scientists, the self-assembly technique makes it possible to manufacture functional (nano)materials in a fast and easy manner;¹ and it has the essential importance in nanotechnology. There are two general strategies in for nanomaterials fabrication. One is “top-down” strategy that uses the lithography technique to reduce the dimensions of bulk materials to nm-scale.² Another is “bottom-up” strategy represented by self-assembly using basic atom/molecule building blocks.³ Currently, the top-down method has been extensively applied in the large scale manufacturing of materials and devices in the semiconductor industry. However, the intrinsic disadvantage is the dimension resolution limitation. Therefore, the self-assembly technique can serve as a great complementary method to the top-down strategy. There already are processes that have been developed combining the

techniques of self-assembly and lithography for the fabrication of patterned structures.^{2,4} The process includes formation of a thin film of block co-polymers with self-assembled patterns followed by lithography for the creation of ordered structures. Nevertheless, the ordered nanomaterials can be directly created solely through self-assembly process, and have been largely applied in the polymer industry during emulsion polymerization and as delivery systems for drug payloads and carriers in the pharmaceutical and consumer goods industry.^{5,6} But, large-scale industrialization of self-assembly in the nanofabrication field still remains to be developed.

With the above-mentioned significance, massive efforts have been devoted in the research of self-assembly using various building blocks to understand the thermodynamic and kinetic factors involved during this process. Amphiphilic molecules such as surfactant and amphiphilic block co-polymers, which are composed of a hydrophilic (charged or polar) domain and a hydrophobic (nonpolar) domain are found can self-organize into certain large aggregated structures (micelles) when the concentration is above the critical micelle concentration.⁶⁻¹¹ The mechanism of this process can be described based on thermodynamic theory that the micelles formation is driven by hydrophobic interaction to minimize free energy in dilute solution. The molecular packing parameter controls the size and shape of micelles.¹² The packing parameter is determined by factors including the molecular composition, the interactions between solvent environment and hydrophilic/hydrophobic domains, and the interactions among hydrophilic domains, such as steric effects and repulsive electrostatic interactions. Through the controlling of the molecular composition (block ratio and the degree of polymerization for block co-polymers) and the molecule-solvent interaction (temperature, pH, ionic strength, additives), controllable

construction of various shapes of micelles have been achieved⁷ such as spherical,^{13,14} worm-like,¹⁵ disk-like,¹⁶ bilayer vesicle,¹¹ toroidal,¹⁷ and hybrid shape.^{18,19}

While a self-assembly system is intended to reach the thermodynamic stable state, the method of kinetic manipulation can be applied to restrict or trap the system at certain kinetic states thereby creating different pathways between the initial assembly stage and the final assembly stage. Therefore, the kinetic control method is especially productive in the generation of complex assembly architectures without having to change the chemistry of the building block molecules.

In the Pochan group (University of Delaware), the method of kinetic manipulation has been largely explored in the block co-polymer assembly system. Cui *et al.* have reported by inducing rapid solvent change, poly(acrylic acid)-*block*-poly(methyl acrylate)-*block*-polystyrene (PAA-*b*-PMA-*b*-PS) micelles can be trapped in the non-equilibrium state with anisotropic shape. Combined with inter-micelle electrostatic interaction, complex one-dimensional structures can be built.¹⁶ Zhong *et al.* have reported that by applying extra electrostatic interaction with the addition of counter-ions, PAA-*b*-PMA-*b*-PS cylindrical micelles can be forced into helical coils with tunable structures.¹⁵ Zhu *et al.* have reported the slow kinetics of the hydrophobic core phase separation process in PAA-*b*-PMMA and PAA-*b*-PS co-assembly system and utilized this kinetic feature to create complex multicompetent structures.²⁰

Manners (University of Bristol), Winnik (University of Toronto) and their co-workers incorporated crystalline chain domains in the block co-polymers to force the fast domain separation within the micelles and trap the micelle in anisotropic shape, developing the so-called crystallization-driven living self-assembly method.²¹ Wang *et al.* have reported that the polyferrocenylsilane (PFS) crystalline domain-containing

block co-polymers with a core-corona block ratio between about 1:6 and 1:20 can undergo an epitaxial growth process after the nucleation of PFS domains under the melting temperature to form cylindrical micelles. Moreover, the co-assembly of different PFS-containing block co-polymers can produce cylindrical micelles with different patches like a “living polymerization” process.²² Qiu *et al.* further reported that the interactions among these patchy cylindrical micelles can be utilized to create multidimensional hierarchical structures.²³ Different PFS-containing platelet-forming co-polymer with core-corona block ratio $\geq 1:1$ can also be applied in the same crystallization-drive living self-assembly method to create two dimensional multi-patchy structures.^{24,25}

Besides the examples of block co-polymers, the studies of conjugated molecules, such as π -conjugates,^{26–28} or polymer-peptide conjugates^{29–32} also reveal a common kinetic structural transition when different intermolecular interaction modes are involved during the assembly process. For example, strong interactions such as hydrophobic interactions and π - π stacking occur and initially define a nanostructure. Then, subsequent, intermolecular reorganization can occur, modulated by weak interactions such as steric effects, that produces, for example, more ordered intermolecular stacking^{26,29} or different types of curved surfaces.^{15,27,30,32–34} Similarly, due to the combination of hydrogen-bonding and chirality, peptides with β -sheet domains firstly fold and assemble into intermolecular β -sheet structures such as one-dimensional ribbons or two-dimensional laminates directed by hydrogen-bonding. Then, further driven by the minimization of hydrophobic nanostructure faces exposed to aqueous solution, various types of curved surface such as twisted, helical, and even

closed, tubular structures can form subsequently, even converting between each other in a kinetic manner.^{35,36}

As can be seen from these reported examples, the kinetically manipulated self-assembly method is proven to be productive in creating complex, hierarchical nanostructures. Therefore, the kinetic study of the self-assembly process is a focus of this Ph.D. project to create controllable self-assembled structures.

1.2 Chemical Structure- and Shape-specific Assembly Building Block

The ultimate goal and challenge of self-assembly study is the achievement of structural complexity and programmability.^{37,38} In the above section, the examples of kinetic manipulation in block co-polymers and small surfactant molecule systems have demonstrated effectiveness in the production of higher order complex assembly structures. However, the sizes and the shapes of secondary building blocks, e.g. micelles, are generally restricted beyond certain limits, e.g. by certain symmetries of nanostructures. This is limiting the ultimate dimensions and the complexity that can be achieved by these assembly systems. Also, the intrinsic limitations of the block co-polymers during the self-assembly are molecular polydispersity and the lack of definition and persistence of molecular conformation in solution.

Therefore, the idea of designing and using chemical structure- and shape-specific assembly building blocks has emerged. Recent examples are studies about the synthesis of new and more precisely determined molecules,³⁹⁻⁴² such as so called “giant surfactants”^{41,43-45} or peptoids.^{42,46-49} In the Cheng group (University of Akron), a series of complex, conjugated molecules, supramolecular giant surfactants, have been precisely synthesized with specific shapes and specific spatial displaying of chemical groups. Huang *et al.* have reported to use tetrakis(4-aminophenyl)methane as

a rigid tetrahedral core to link differently modified silsesquioxane (POSS) molecules via click chemistry. The shape of this type of conjugated molecule is determined by the shape of core molecular frame while the chemical structure is determined by the choice of different POSS molecules “clicked” in different positions.⁴⁵ Therefore, this strategy is effective in the assembly of programmable structures, such as double-layer lamellae⁴³ and ordered lattices.⁴⁵ However, this approach requires elaborate and multi-step syntheses.

Another type of structure-specific molecules is the peptoid, or poly-*N*-substituted glycines. This is a type of peptide-like synthetic molecules with the backbone lacking hydrogen bonding but the same sequence controllability. The synthesis process is simpler comparing to block co-polymers and can be conducted using an automated synthesizer. The Zuckermann group (Lawrence Berkeley National Laboratory) and De Yoreo group (Pacific Northwest National Laboratory) have conducted extensive work using peptoids to construct nanostructures.^{42,43,45-51} Manniges *et al.* have reported that peptoids adopt a zigzag-like secondary structure that is not seen in the nature and enables the formation of nanosheets, and potentially other organizations.⁵⁰ Jiao *et al.* have reported that through the choice of peptoids sequences, patterned, two-dimensional membrane-like materials can be assembled.⁴⁸ Ma *et al.* also reported to control the crystallization behavior of peptoids materials by the sequence engineering method.⁴⁹ For this type of biomimetic molecules, the chemical structure is precisely determined by the sequences while the shape is generally fixed as zig-zag due to backbone rotation. The self-assembled materials can thus be rationally designed and tuned.

The best examples of structure- and shape-specific assembly building blocks are from naturally existing, self-assembled supramolecular structures based on polynucleotides and polypeptides. These biomolecules are composed of nucleotides and amino acids, respectively, with precise sequences. Moreover, the shapes (chain conformations) of the molecules are determined by the molecular sequences. Due to the precise molecular sequences, the shapes of these biomolecules, such as DNA double helices, peptide helices or β -sheets, can be ensured with certain spatial display of chemical groups. With these primary building blocks, nature exhibits an enormous library of molecular self-assembled structures. By the date of writing, only counting the solved assembled and folded natural structures, there are 130,599 biological macromolecular structures according to RCSB PDB.⁵² Those structures are not only large in number but also diverse and complex in architectures. Taking natural proteins for example, the structures vary from one-dimensional, such as collagen fibrils, to two-dimensional, such as DNA clamps, and to very complex three-dimensional structures, such as viral capsids and ferritins.^{53–55} These protein structures are self-assembled from assembly subunits, namely peptides with tertiary-structures. For example, the maxi-ferritin protein has a hollow spherical structure which is composed of 24 helix-bundle subunits.⁵³ The assembly subunits have quite simple symmetries, such as D2 or D4 symmetries,^{56,57} and by orderly repeating and arranging these simple oligomers directed by well-evolved local interactions, various proteins with distinct quaternary-structures can be built with biological functions.^{53,54,56} Inspired from nature, the structure and shape features of these biomacromolecules have been studied and used extensively to fabricate novel self-assembled nanomaterials, for example, DNA RNA nanoarchitectures,^{58–60} DNA origami,^{38,61,62} even DNA machines and robots.^{63–67}

These complex nanodevices are formed by base-pairing interactions or complementary shapes with designed polynucleotide sequences.⁶⁰ Polypeptides/proteins with the same programmability, but more chemical versatility and robustness, have also been applied in self-assembly studies. A series of nanomaterials, from simple to higher order hierarchical structures, such as, but not limited to, peptide β -hairpin fibrils, surfactant-like peptide fibers, peptide coiled-coil bundles,^{68,69} coiled-coil barrels,^{70,71} coiled-coil fibers,⁷²⁻⁷⁵ coiled-coil tubes,⁷⁶ coiled-coil cages,⁷⁷ protein-fused two-dimensional sheets,^{56,78-82} and protein polyhedron structures,⁸³⁻⁸⁸ have been reported. And these peptide/protein-based self-assembled materials have shown great advantages and potential in practical applications. For example, peptide hydrogels have been used in drug delivery and cell culture.^{74,89-93} The engineered natural protein cages have shown capability in drug and enzyme encapsulation.^{94,95} Porous materials fabricated based on protein crystals have the potential to be used as catalyst carriers,⁹⁶ filtering materials,^{97,98} and templates to further grow other species materials.⁹⁹⁻¹⁰¹

1.3 Designed Peptides for Self-assembly

The naturally existing, self-assembled structures show tremendous sophistication above that of any of the above-mentioned synthetic molecules. A complex programmability needs the self-assembly information to be encoded within individual self-assembly units. This can be accomplished generally in two approaches, puzzle and folding approaches,³⁷ which both are used by natural self-assembled biomacromolecules. First of all, polynucleotides and polypeptides have well-defined sequences where the molecular structures are precise with little dispersity. These biomolecules can, therefore, adopt certain secondary structures with well-defined spatial display of chemical groups with, the information required for proper secondary

structure formation encoded within the primary sequence. In this way, nature ensures the correct folding of biomacromolecules during the assembly process. For example, polypeptides can fold into helices or β -sheets.¹⁰² Then, the assembly subunits, peptide helices or β -sheets, can interact through inter-component interactions determined by well-defined display of the chemical groups, to go through a puzzle-recognizing process to assemble into hierarchical structures.¹⁰³ This precisely controlled bottom-up assembly feature of biomacromolecules affords the opportunity to produce programmable, arbitrary structures, particularly when a system is based on proper computational design of biomacromolecules.

As mentioned previously, great work has been conducted in the design and self-assembly of DNA and RNA molecules with the achievement of tremendously beautiful structures and devices. Due to the peptide-focus of this Ph.D. project, the elaborate list and description of the excellent DNA/RNA work conducted by other researchers will not be given here. A recent review from the Mirkin group (Northwestern University) summarizes the designing strategies in the DNA-based programmable nanomaterials.¹⁰⁴ In the work presented in this dissertation, polypeptide molecules with similar programmability are designed and self-assembled for the construction of nanomaterials. It is worthy to note that the invention of solid-phase synthesis method makes it relatively easy to synthesize sequence-controlled peptides with length up to 100 residues.¹⁰⁵ Nevertheless, large polypeptides can be synthesized through biological genetic engineering method¹⁰⁶ and ring-opening polymerization.¹⁰⁷

Taking use of the different ionization properties of amino acids side chain groups, short surfactant-like peptides, composed of a hydrophobic amino acid domain and hydrophilic domain, have been rationally designed and studied. For example, the

Zhang group (MIT) reported a series of surfactant-like peptides composed of a hydrophilic head and a hydrophobic tail, such as G₄D₂, G₆D₂, G₈D₂, G₁₀D₂ (glycine as G, aspartic acid as D).¹⁰⁸⁻¹¹¹ Because of the molecular composition (short hydrophilic domain and long hydrophobic domain), these short peptides behave similarly as lipids, especially in the formation of bilayer structures, such as bilayer vesicles and bilayer nanotubes. In earlier work by Zhang, peptides containing alternating hydrophobic and hydrophilic amino acid residues were rationally designed with respect to charge distribution control. A series of ionic self-complementary peptides with the designed charge arrangements such as - + - + - + - + and - - + + - - + +, have been studied.^{112,113} These peptides exhibit strong tendency to form β -sheet structures in water due to the alternating hydrophobic/hydrophilic sequence. And further because of the specific charge distribution along the molecular chains, molecules can assemble in a self-complementary way via ionic interactions. Therefore, high order assembly structures, such as ordered two-dimensional membranes, can be observed from these assembled molecules. In their peptide design conclusion, specific sequences are not required for certain nanostructures formation. But, the general hydrophobicity of amino acid residues is the important underlying self-assembly driving force. The work shed light on the design principles of peptide-based materials. However, the lack of discussion of more delicate differences among the amino acid residues, such as differences between amino acids with similar hydrophobicity, such as side chain size, secondary-structure propensity, limited the more precise control of the self-assembled structures.

Originated from the studies of amyloid fibrils, certain domains within natural peptides involved in the formation of amyloid fibrils have been identified as the key factors in the molecular recognition and self-assembly process. These fragments of

amyloid peptides have been extensively studied for the self-assembly of designed nanomaterials, including mostly nanotubes and nanofibers. For example, aromatic amino acid residues are suggested by the work in the Gazit group (Tel Aviv University) as the core recognition motif in amyloid fibrils. They reported the efficient formation of hollow tubes from diphenylalanines, and the nanosphere formation from diphenylglycines driven by π - π stacking.¹¹⁴⁻¹¹⁷ Self-assembled fibrils, nanotubes and sheets are not only from amyloid peptides.¹¹⁶ As described earlier, peptide sequences containing alternating hydrophobic/polar residues (*HPHPHP* pattern, H-hydrophobic, P-polar) have been proven to have strong tendency in β -sheet structure formation, with the possibility of forming higher order structures, such as nanofibers, nanotubes and sheets.¹⁰² This provides more design opportunities. In the Boden group (University of Cambridge), a 11-residue peptide QQRFQWQFEQQ (glutamine as Q, arginine as R, phenylalanine as F, tryptophan as W, glutamate as E) was rationally designed with the consideration of certain assembly interactions, such as π - π stacking, complementary ionic interactions and chirality of molecules.¹¹⁸ This system has demonstrated the hierarchical self-assembly process into β -sheet tapes, ribbons, fibrils and fibers.^{35,118} In the Pochan group and Schneider group (National Cancer Institute, NIH), the MAX-series peptides containing β -rich domains (alternating valine/proline) connected by specific folding domains (valine-^Dproline-^Lproline-threonine or valine-^Lproline-^Lproline-threonine) have been de novo designed to study the sequence-dependent folding and assembly behavior.¹¹⁹⁻¹²¹ Only the domain with ^Dproline exhibited the pH and temperature-dependent folding behavior, coupled with β -rich domains, resulting in the stimuli-responsive β -hairpin hydrogel composed of physically entangled fibrils.

While the peptides contained only L-prolines, only the un-folded molecular conformation was found resulting in the straight filaments and laminates formation.

Conjugated, amphiphilic molecules composed of a peptide domain and a carbohydrate domain have also been designed and assembled for various controllable nanomaterials. In the Stupp group (Northwestern University), hydrophilic peptide domains with β -sheet formation propensity were conjugated with hydrophobic carbohydrate chains.^{30,31,122–124} These conjugated molecules exhibit effective self-assembly of one-dimensional nanofibers analogous to the worm-like micelles assembled from amphiphile block co-polymers and surfactants. Because of the β -sheet formation propensity of the peptide-domain, the formation of spherical micelles can be excluded. Furthermore, the peptide domains allow more design opportunities in the potential functionalities of these nanofibers. Certain residues can be added in the sequence for the purpose of templated biomineralization, with a series of hybrid nanomaterials being developed.^{99,125–127} Examples from other research groups have demonstrated other nanostructures construction using rationally designed, conjugated peptides, such twisted ribbons,¹²⁸ nanotubes and virus-like particles.¹²⁹

Other types of designed peptides, such as cyclic peptides, which possibly are the first examples of the pioneering work in peptide engineering, have exhibited a strong correlation between the structural designing and the assembly behavior, ultimately forming hollow nanotubes.^{130,131} This Ph.D. dissertation work is focused on the self-assembly with the use of α -helical rich, coiled-coil peptides. Although the understanding of coiled-coil folding and organization is still not complete, with dedicated efforts, “there are now sufficient rules to allow confident design attempts of coiled-coil motifs”.¹³²

The research of self-assembled materials using designed coiled-coils started based on the leucine-zipper model.¹³² In the structure of leucine-zipper α -helical coiled-coils, an α -helical peptide chain contains 3.6 residues per turn and is stabilized by hydrogen bonds parallel to the axis of helix. The *HPPHPPP* or *abcdefg* heptad pattern can be used to describe the sequence composition. From the view that is parallel to the axis of helix, a wheel diagram with *abcdefg* heptad pattern is commonly used to depict the amino acid residue position arrangement, as shown in **Figure 1.1**. The wheel diagram is convenient in the rational design of sequence composition with regard to different coiled-coil structures. For example, in the dimeric coiled-coil structure shown in **Figure 1.1**, driven by hydrophobic interactions, the hydrophobic amino acid residues occupying the *a* and *d* positions are buried between the two peptide helical chains, forming the hydrophobic core of the coiled-coils. The rest of the positions are not strictly restricted to certain types of amino acids, therefore, allowing flexibility during the designing process. For example, the amino acid residues occupying the *e* and *g* positions are usually chosen to be ionizable, which play important role in determining and stabilizing different coiled-coil organizations, from dimer to higher oligomer states.¹³³ The peripheral positions are generally further designed to allow specific inter-bundle interactions to take place to determine the higher order assembled structures based on the coiled-coils.^{134–136}

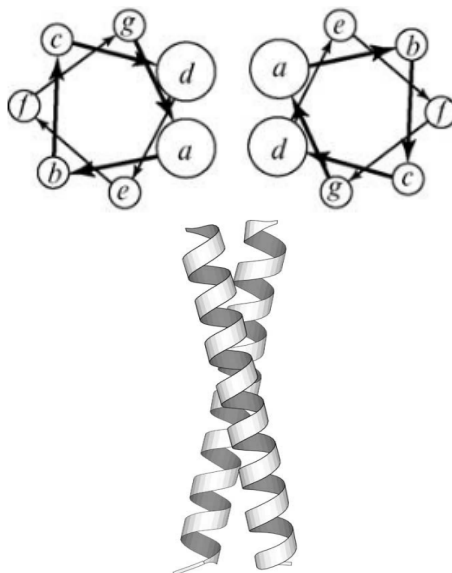


Figure 1.1 The structure model of peptide dimeric coiled-coil. **Top:** the wheel diagram with the viewing direction that is parallel to the coiled-coil axis. The *abcdefg* heptad pattern is used to depict the amino acid residue position arrangement. The *a* and *d* positions occupied by hydrophobic amino acid residues are buried between the two peptide helical chains. **Bottom:** the coiled-coil structure model viewing from the direction perpendicular to the coiled-coil axis, depicted by ribbon-drawing. (Figure adapted with permission from reference 137, copyright 2004 American Chemical Society)

The Tirrell group (California Institute of Technology) reported the design and utilization of the leucine zipper coiled-coil structure for the development of artificial protein hydrogels. And they proposed the dynamic assembly nature of the designed leucine zipper aggregation is responsible for the mechanical property of the self-assembled hydrogels.^{138,139}

In the Woolfson group (University of Bristol), the rational design of peptide α -helical coiled-coils has been largely explored for the development of a series of SAF (self-assembling fiber) peptides. Through the choice of certain amino acids for the

peripheral positions other than *a* and *d*, coiled-coil structures with different oligomer states are reported assembled from the synthetic α -helical peptides.¹³³ Based on the successful establishment of basic coiled-coil bundle structures, more complicated inter-bundle interactions are introduced into the system for the production of higher order assembly structures. For example, the charge distribution within the coiled-coil bundles is specifically designed to produce sticky-ended bundles, which have opposite charges on two ends, forming the self-assembled, elongated nanofibers, nanoribbons and nanotubes.¹⁴⁰ Strong, functional hydrogels are reported assembled from these coiled-coil nanofibers due to enhanced inter-fiber interactions by introducing oppositely charged amino acid residues in the exterior part of the individual nanofibers.¹³⁴ Branched nanofibers are reported assembled from the deliberately designed branched α -helical peptide chains.¹⁴¹ Inter-bundle crosslinking with disulfide bonds is reported as anchor points for the formation of ordered network structures and the closed cages from the connected coiled-coil bundles.⁷⁷ Furthermore, guided by the same inter-bundle interaction principle, the reverse designing process is also reported to disassociate the assembled structures to single fibrils or individual bundles.⁷⁵

In the Conticello group (Emory University), the rational designing of coiled-coil bundles is also extensively studied such as by implementing complementary interactions among the bundles to form nanofibers, nanosheets, and superlattices.^{73,142} Furthermore, assembly solution conditions were utilized to control the intra- and inter-bundle interactions. By changing the charged state of amino acid residues via pH adjustment, the pH-sensitive assembly behavior of coiled-coils can be observed.¹⁴³

Taking advantage of the metal-coordination property of certain amino acid residues, such as histidine and ionizable amino acid residues, metal coordination

interactions have been used, to drive the formation of coiled-coil structures,^{72,144} and higher order assembly structures¹⁴⁵ such as spheres or fibrils.^{146–150} These metal coordination interactions are also further utilized for the construction of artificial ion-transporting membranes^{151,152} and coiled-coil structures with catalytic activity.¹⁵³

Although such mentioned successes have been accomplished with computationally designed peptide/protein assembly systems, significant improvements still need to be made. For example, in the above mentioned coiled-coil designs,^{73,133} the design process is generally rational, while not precise; therefore, the higher order self-assembled lattices formed by the densely packed coiled-coil bundles are generally not programmable. Although protein-protein interface designing can give the programmable structures/lattices, naturally existing structures are needed as design templates, and the efficiency in successful design of new assembled states is low.^{85,86} Therefore, if peptide-based building blocks, such as coiled-coil bundles, are used, the self-assembled nanostructures with much smaller sizes can be achieved comparing to protein-based lattices.⁸¹ An entirely *de novo* designed protein crystal reported by Lanci *et al.* in Saven group (University of Pennsylvania) demonstrates a promising peptide design, strategy to achieve the programmability and complexity in the self-assembled nanoarchitectures while not relying on the naturally existing protein structure templates.¹⁵⁴ This work sets the tone of the Ph.D. project presented in this dissertation.

1.4 *De novo* Designed Peptide Coil-coiled Bundles and Assemblies

In this Ph.D. dissertation work, our collaborators in the Saven Group take the use of the computational design to generate *de novo* designed sequences that can adopt desired secondary-structure and quaternary structure and to form higher order supramolecular structures. Fundamentally, the self-assembly study of computationally

designed peptides can not only broaden the self-assembly library but also provide better understanding of sequence-to-structure relationship of peptide/protein system.^{102,132}

The detailed computational design process is elaborated in the Ph.D. dissertation of Dr. Violet Huixi Zhang (Department of Chemistry, University of Pennsylvania, 2016); only a brief description is given here. Firstly, the structure of an α -helical, antiparallel homotetrameric coiled-coil bundle is selected as the building block. Each constituent peptide sequence contains 29 amino acid residues. The backbone structure of the coiled-coil tetramer bundle is identified using a mathematical model for coiled-coils with a small number of geometric parameters including the super-helical radius R , the super-helical phase α , the relative displacement of the ends of the helices parallel to the super-helical axis Z , the minor-helical phase θ (rotation of the alpha helix about its axis), and the super-helical pitch P (as shown in **Figure 1.2**).¹⁵⁵

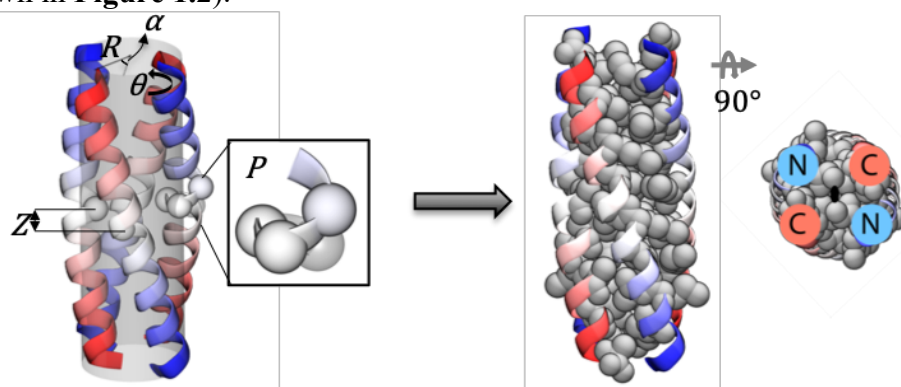


Figure 1.2 The design of the helical-motif building block by sampling 5 parameters (R : super-helical radius; θ : minor-helical phase; α : super-helical phase; Z : super-helical axis; P : super-helical pitch) associated with the size and geometry of the bundle using Monte Carlo simulated annealing (left): N terminus is depicted in blue and C terminus in red; side and top view of the selected low-energy motif with the most probable amino acids at the interior sites shown in space-filling representations (right).

Monte-Carlo simulated annealing (MCSA) is used to sample parameters and identify helical bundle sequences and structures that produce local energy minima. Each generated coiled-coil bundle structure contains 11 interior residues that are specified as hydrophobic amino acids to ensure the structure stability in aqueous solution. A statistical sequence design methodology is used to calculate the probabilities of hydrophobic amino acids at interior residue positions and also with respect to variation of the rest exterior amino acid residues. For each sequence, an average internal energy is calculated using the site-specific probabilities of the amino acids. The sequence scored with the lowest energy is selected for the subsequent designs targeting higher order assembly structures such as 2D sheets with predetermined nanolattices.

The exterior amino acid residue positions of the coiled-coil bundles are designed in context of these 2D monolayer lattices with predetermined symmetries including the space groups of P222, P422 and P622, as shown in **Figure 1.3**.

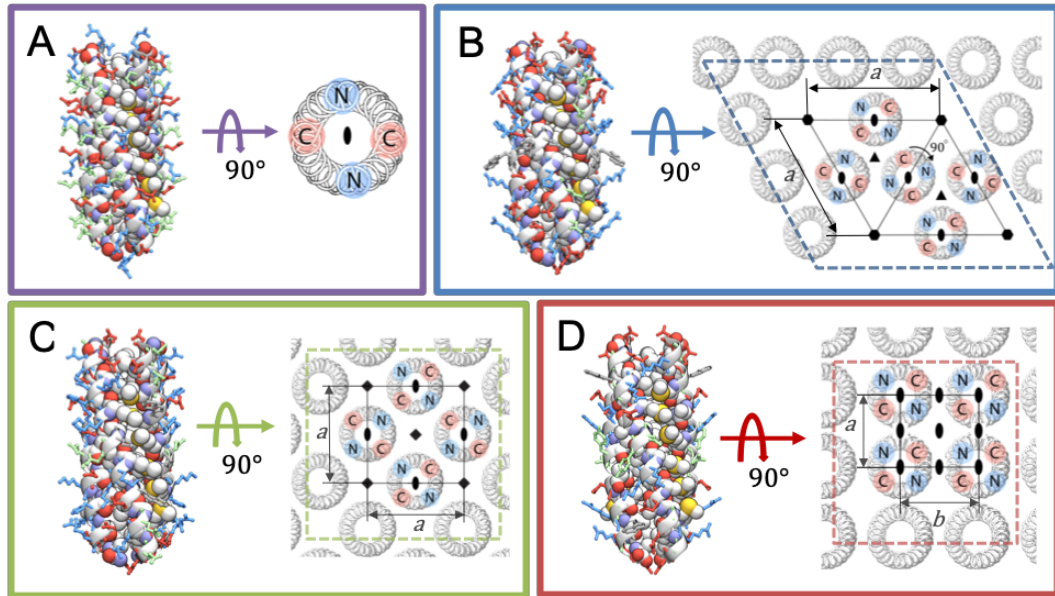


Figure 1.3 Computationally designed, α -helical, homotetrameric assemblies. **A-D**: Models of peptides forming distinct nanostructures using a *de novo* designed helical homotetrameric bundle, which comprises both the backbone coordinates of the D2 symmetric tetramer and interior hydrophobic residues. In the left of each panel, designed exterior residues are colored according to chemical properties: positively charged (red), negatively charged (blue), polar (green) and hydrophobic (gray). On the right of each panel, the targeted assemblies are rendered along with symmetry axes (C2 oval, C3 triangle, C4 square, C6 hexagon) and the unique dimensions of the unit cell, a and b . **A**: D2 symmetric tetramer designed in isolation and targeted to remain in solution. The exterior residues of the remaining proteins were designed in the context of the corresponding space groups: **(B)** P622; **(C)** P422; **(D)** P222.

For each lattice symmetry, 18 natural amino acid residues, excluding proline and cysteine, are allowed in the exterior positions of the coiled-coiled bundle. Unit cell parameters are varied to search for the low-energy lattice structures. For each predetermined lattice symmetry, an energy landscape with respect to the sequence-structure is calculated from which sequences are selected with local energy minima. In the final step, a PDB-based, macromolecule interface designing tool, PDBePISA is

used to evaluate the interactions at the bundle-bundle interfaces for each predetermined lattice symmetry. This generates the final list of peptide sequences. The full list can be seen in reference 135. In this Ph.D. dissertation, the self-assembly behavior and assembled nanostructures of P422 and P222 sequences are experimentally investigated. The experimental study of the individual coiled-coil bundles and P622 sequence peptides is described in the Ph.D. dissertation of Dr. Michael Haider (Department of Materials Science and Engineering, University of Delaware, 2018).

1.5 Dissertation Content Summary

In most commonly reported self-assembly research work based on computationally-designed peptides/proteins, the kinetic control of the self-assembly process remains largely unexploited and unexplored. Because the kinetic products from different assembly pathways are in non-equilibrium and occur only as a result of certain assembly solution conditions, a priori, computational prediction and design of kinetically trapped products is difficult. Therefore, based on the computational design work of Saven group, the work presented in this Ph.D. dissertation is focused on the kinetic manipulation of the self-assembly process for the production of various nanoarchitectures with controllable morphologies.

In **Chapter 2**, the assembly behavior of P422 sequences is investigated under a variety of solution conditions (pH = 4.5, 7, 8, 10, temperature = room temperature, 30 °C, 40 °C, 50 °C, 60 °C). A sequence and pI-based assembly guide rule is demonstrated that peptides generally exhibit fast assembly kinetics at the pH near the pI of the sequence. Moreover, thermal annealing can be readily applied to overcome the kinetic traps during the assembly process with fast kinetics. In **Chapter 3**,

different pH conditions (pH = 4.5, 7, 10) are applied to demonstrate different pH-dependent self-assembly pathways of the P222 sequence for the production of various nanoarchitectures including nanotubes, platelets and needles at each specific pH, driven by differently charged amino acid residues. The unique and homogenous nanotube structures assembled from coiled-coil bundles are studied in detail with the proposed structural models based on cryo-TEM, small-angle X-ray scattering, STEM mass-mapping and site-specific amino acid modification analyses. In **Chapter 4**, the assembled nanoarchitectures established in **Chapters 2** and **3** are utilized as scaffolds for the templated synthesis of inorganic nanoparticles through the incorporation of cysteine residues in the peptide sequences. One- and two-dimensional ordered gold nanoparticle arrays are successfully fabricated based on self-assembled 1D nanotubes of cysteine-modified P222 sequence and 2D platelets of cysteine-modified P422 sequence, respectively. The 1D gold nanoparticle arrays exhibit enhanced surface plasmon resonance properties and, thus is further explored for the fabrication of solid-state gold nanowires. In **Chapter 5**, a detailed formulation study is presented for the optimized inorganic nanoparticle templating process. It is discovered that the electrostatic interactions between positively charged peptide templates and inorganic precursor anions, and the thiol-gold bonding between cysteine residues and gold nanoparticles, play important roles during the in-situ synthesis process of gold nanoparticles with peptide templates. In the last **Chapter 6**, conclusion and future work is presented.

REFERENCES

1. Whitesides, G. M.; Grzybowski, B. Self-Assembly at All Scales. *Science* **2002**, *295* (5564), 2418–2421.
2. Biswas, A.; Bayer, I. S.; Biris, A. S.; Wang, T.; Dervishi, E.; Faupel, F. Advances in Top-down and Bottom-up Surface Nanofabrication: Techniques, Applications & Future Prospects. *Adv. Colloid Interface Sci.* **2012**, *170* (1–2), 2–27.
3. Whitesides, G. M.; Kriebel, J. K.; Mayers, B. T. In *Nanoscale Assembly*; Springer, New York, **2013**, p 217–239.
4. Mijatovic, D.; Eijkel, J. C. T.; van den Berg, A. Technologies for Nanofluidic Systems: Top-down vs. Bottom-up—a Review. *Lab Chip* **2005**, *5* (5), 492.
5. Drummond, C. J.; Fong, C. Surfactant Self-Assembly Objects as Novel Drug Delivery Vehicles. *Curr. Opin. Colloid Interface Sci.* **1999**, *4* (6), 449–456.
6. Rösler, A.; Vandermeulen, G. W. M.; Klok, H. A. Advanced Drug Delivery Devices via Self-Assembly of Amphiphilic Block Copolymers. *Adv. Drug Deliv. Rev.* **2012**, *64*, 270–279.
7. Vinson, P. K.; Bellare, J. R.; Davis, H. T.; Miller, W. G.; Scriven, L. E. Direct Imaging of Surfactant Micelles, Vesicles, Discs, and Ripple Phase Structures by Cryo-Transmission Electron Microscopy. *J. Colloid Interface Sci.* **1991**, *142* (1), 74–91.
8. Jonkheijm, P.; Schoot, P. van der; Schenning, A. P. H. J.; Meijer, E. W. Probing the Solvent-Assisted Nucleation Pathway in Chemical Self-Assembly. *Science* **2006**, *313* (5783), 80–83.
9. Klok, H. A.; Lecommandoux, S. Supramolecular Materials via Block Copolymer Self-Assembly. *Adv. Mater.* **2001**, *13* (16), 1217–1229.

10. Discher, D. E.; Ortiz, V.; Srinivas, G.; Klein, M. L.; Kim, Y.; Christian, D.; Cai, S.; Photos, P.; Ahmed, F. Emerging Applications of Polymersomes in Delivery: From Molecular Dynamics to Shrinkage of Tumors. *Prog. Polym. Sci.* **2007**, *32* (8–9), 838–857.
11. Brinkhuis, R. P.-; Rutjes, F. P. J. T.-; van Hest, J. C. M.-. Polymeric Vesicles in Biomedical Applications. *Polym. Chem.* **2011**, *2*, 1449–1462.
12. Leibler, L.; Orland, H.; Wheeler, J. C. Theory of Critical Micelle Concentration for Solutions of Block Copolymers. *J. Chem. Phys.* **1983**, *79* (7), 3550–3557.
13. Kelley, E. G.; Murphy, R. P.; Seppala, J. E.; Smart, T. P.; Hann, S. D.; Sullivan, M. O.; Epps, T. H. Size Evolution of Highly Amphiphilic Macromolecular Solution Assemblies via a Distinct Bimodal Pathway. *Nat. Commun.* **2014**, *5*, 1–10.
14. Lee, S.; Leighton, C.; Bates, F. S. Sphericity and Symmetry Breaking in the Formation of Frank–Kasper Phases from One Component Materials. *Proc. Natl. Acad. Sci.* **2014**, *111* (50), 17723–17731.
15. Zhong, S.; Cui, H.; Chen, Z.; Wooley, K. L.; Pochan, D. J. Helix Self-Assembly through the Coiling of Cylindrical Micelles. *Soft Matter* **2008**, *4* (1), 90–93.
16. Cui, H.; Chen, Z.; Zhong, S.; Wooley, K. L.; Pochan, D. J. Block Copolymer Assembly via Kinetic Control. *Science* **2007**, *317* (5838), 647–650.
17. Pochan, D. J.; Chen, Z.; Cui, H.; Hales, K.; Qi, K.; Wooley, K. L. Toroidal Triblock Copolymer Assemblies. *Science* **2004**, *306* (5693), 94–97.
18. Chen, Y.; Zhang, K.; Wang, X.; Zhang, F.; Zhu, J.; Mays, J. W.; Wooley, K. L.; Pochan, D. J. Multigeometry Nanoparticles: Hybrid Vesicle/Cylinder Nanoparticles Constructed with Block Copolymer Solution Assembly and Kinetic Control. *Macromolecules* **2015**, *48* (16), 5621–5631.
19. Danino, D.; Abezgauz, L.; Portnaya, I.; Dan, N. From Discs to Ribbons Networks: The Second Critical Micelle Concentration in Nonionic Sterol Solutions. *J. Phys. Chem. Lett.* **2016**, *7* (8), 1434–1439.

20. Zhu, J.; Zhang, S.; Zhang, F.; Wooley, K. L.; Pochan, D. J. Hierarchical Assembly of Complex Block Copolymer Nanoparticles into Multicompartment Superstructures through Tunable Interparticle Associations. *Adv. Funct. Mater.* **2013**, *23* (14), 1767–1773.
21. Massey, J. A.; Temple, K.; Cao, L.; Rharbi, Y.; Raez, J.; Winnik, M. A.; Manners, I. Self-Assembly of Organometallic Block Copolymers: The Role of Crystallinity of the Core-Forming Polyferrocene Block in the Micellar Morphologies Formed by Poly(Ferrocenylsilane-*b*-Dimethylsiloxane) in *n*-Alkane Solvents. *J. Am. Chem. Soc.* **2000**, *122* (47), 11577–11584.
22. Wang, X.; Guerin, G.; Wang, H.; Wang, Y.; Manners, I.; Winnik, M. A. Cylindrical Block Copolymer Micelles and Co-Micelles of Controlled Length and Architecture. *Science* **2007**, *317* (5838), 644–647.
23. Qiu, H.; Hudson, Z. M.; Winnik, M. A.; Manners, I. Multidimensional Hierarchical Self-Assembly of Amphiphilic Cylindrical Block Copolymers. *Science* **2015**, *347* (6228), 1329–1332.
24. Hudson, Z. M.; Boott, C. E.; Robinson, M. E.; Rupar, P. A.; Winnik, M. A.; Manners, I. Tailored Hierarchical Micelle Architectures Using Living Crystallization-Driven Self-Assembly in Two Dimensions. *Nat. Chem.* **2014**, *6* (10), 893–898.
25. Qiu, H.; Gao, Y.; Boott, C. E.; Gould, Oliver E. C.; Harniman, R. L.; Miles, M. J.; Webb, S. E. D.; Winnik, M. A.; Manners, I. Uniform Patchy and Hollow Rectangular Platelet Micelles from Crystallizable Polymer Blends. *Science* **2016**, *352* (6286), 697–701.
26. Lohr, A.; Lysetska, M.; Würthner, F. Supramolecular Stereomutation in Kinetic and Thermodynamic Self-Assembly of Helical Merocyanine Dye Nanorods. *Angew. Chemie - Int. Ed.* **2005**, *44* (32), 5071–5074.
27. Tidhar, Y.; Weissman, H.; Wolf, S. G.; Gulino, A.; Rybtchinski, B. Pathway-Dependent Self-Assembly of Perylene Diimide/Peptide Conjugates in Aqueous Medium. *Chem. - A Eur. J.* **2011**, *17* (22), 6068–6075.
28. Hoeben, F. J. M.; Jonkheijm, P.; Meijer, E. W.; Albertus P. H. J. Schenning. About Supramolecular Assemblies of π -Conjugated Systems. *Angew. Chem. Int. Ed. Engl.* **2014**, *53* (46), 12537–12541.

29. Kühnle, H.; Börner, H. G. Biotransformation on Polymer-Peptide Conjugates: A Versatile Tool to Trigger Microstructure Formation. *Angew. Chemie - Int. Ed.* **2009**, *48* (35), 6431–6434.
30. Cui, H.; Cheetham, A. G.; Pashuck, E. T.; Stupp, S. I. Amino Acid Sequence in Constitutionally Isomeric Tetrapeptide Amphiphiles Dictates Architecture of One-Dimensional Nanostructures. *J. Am. Chem. Soc.* **2014**, *136*, 12461–12468.
31. Yu, Z.; Tantakitti, F.; Yu, T.; Palmer, L. C.; Schatz, G. C.; Stupp, S. I. Simultaneous Covalent and Noncovalent Hybrid Polymerizations. *Science* **2016**, *351* (6272), 497–502.
32. Merg, A. D.; Boatz, J. C.; Mandal, A.; Zhao, G.; Mokashi-Punekar, S.; Liu, C.; Wang, X.; Zhang, P.; van der Wel, P. C. A.; Rosi, N. L. Peptide-Directed Assembly of Single-Helical Gold Nanoparticle Superstructures Exhibiting Intense Chiroptical Activity. *J. Am. Chem. Soc.* **2016**, *138* (41), 13655–13663.
33. Yan, X.; Cui, Y.; He, Q.; Wang, K.; Li, J.; Mu, W.; Wang, B.; Ou-yang, Z. C. Reversible Transitions between Peptide Nanotubes and Vesicle-like Structures Including Theoretical Modeling Studies. *Chem. - A Eur. J.* **2008**, *14* (19), 5974–5980.
34. Pashuck, E. T.; Stupp, S. I. Direct Observation of Morphological Transformation from Twisted Ribbons into Helical Ribbons. *J. Am. Chem. Soc.* **2010**, *132* (26), 8819–8821.
35. Aggeli, A.; Nyrkova, I. A.; Bell, M.; Harding, R.; Carrick, L.; McLeish, T. C. B.; Semenov, A. N.; Boden, N. Hierarchical Self-Assembly of Chiral Rod-like Molecules as a Model for Peptide β -Sheet Tapes, Ribbons, Fibrils, and Fibers. *Proc. Natl. Acad. Sci.* **2001**, *98* (21), 11857–11862.
36. Morris, K. L.; Zibae, S.; Chen, L.; Goedert, M.; Sikorski, P.; Serpell, L. C. The Structure of Cross- β Tapes and Tubes Formed by an Octapeptide, AS β 1. *Angew. Chemie - Int. Ed.* **2013**, *52* (8), 2279–2283.
37. Cademartiri, L.; Bishop, K. J. M. Programmable Self-Assembly. *Nat. Mater.* **2015**, *14* (1), 2–9.
38. Jacobs, W. M.; Frenkel, D. Self-Assembly of Structures with Addressable Complexity. *J. Am. Chem. Soc.* **2016**, *138* (8), 2457–2467.

39. Rettig, H.; Krause, E.; Börner, H. G. Atom Transfer Radical Polymerization with Polypeptide Initiators: A General Approach to Block Copolymers of Sequence-Defined Polypeptides and Synthetic Polymers. *Macromol. Rapid Commun.* **2004**, *25* (13), 1251–1256.
40. Zhu, M.-Q.; Wei, L.-H.; Du, F.-S.; Li, Z.-C.; Li, F.-M.; Li, M.; Jiang, L. A Unique Synthesis of a Well-Defined Block Copolymer Having Alternating Segments Constituted by Maleic Anhydride and Styrene and the Self-Assembly Aggregating Behavior Thereof. *Chem. Commun.* **2001**, *0*, 365–366.
41. Chu, Y.; Zhang, W.; Lu, X.; Mu, G.; Zhang, B.; Li, Y.; Cheng, S. Z. D.; Liu, T. Rational Controlled Morphological Transitions in the Self-Assembled Multi-Headed Giant Surfactants in Solution. *Chem. Commun.* **2016**, *52* (56), 8687–8690.
42. Knight, A. S.; Zhou, E. Y.; Francis, M. B.; Zuckermann, R. N. Sequence Programmable Peptoid Polymers for Diverse Materials Applications. *Adv. Mater.* **2015**, *27* (38), 5665–5691.
43. Wang, C. L.; Zhang, W. Bin; Van Horn, R. M.; Tu, Y.; Gong, X.; Cheng, S. Z. D.; Sun, Y.; Tong, M.; Seo, J.; Hsu, B. B. Y.; et al. A Porphyrin-Fullerene Dyad with a Supramolecular “Double-Cable” Structure as a Novel Electron Acceptor for Bulk Heterojunction Polymer Solar Cells. *Adv. Mater.* **2011**, *23* (26), 2951–2956.
44. Yu, X.; Yue, K.; Hsieh, I.-F.; Li, Y.; Dong, X.-H.; Liu, C.; Xin, Y.; Wang, H.-F.; Shi, A.-C.; Newkome, G. R.; et al. Giant Surfactants Provide a Versatile Platform for Sub-10-Nm Nanostructure Engineering. *Proc. Natl. Acad. Sci. U. S. A.* **2013**, *110* (25), 10078–10083.
45. Huang, M.; Hsu, C.; Wang, J.; Mei, S.; Dong, X.; Li, Y.; Li, M.; Liu, H.; Zhang, W.; Aida, T.; et al. Selective Assemblies of Giant Tetrahedra via Precisely Controlled Positional Interactions. *Science* **2015**, *348* (6233), 424–428.
46. Robertson, E. J.; Olivier, G. K.; Qian, M.; Proulx, C.; Zuckermann, R. N.; Richmond, G. L. Assembly and Molecular Order of Two-Dimensional Peptoid Nanosheets through the Oil–Water Interface. *Proc. Natl. Acad. Sci.* **2014**, *111* (37), 13284.
47. Sun, J.; Jiang, X.; Lund, R.; Downing, K. H.; Balsara, N. P.; Zuckermann, R. N. Self-Assembly of Crystalline Nanotubes from Monodisperse Amphiphilic Diblock Copolypeptoid Tiles. *Proc. Natl. Acad. Sci.* **2016**, *113* (15), 3954–3959.

48. Jiao, F.; Chen, Y.; Jin, H.; He, P.; Chen, C.-L.; De Yoreo, J. J. Self-Repair and Patterning of 2D Membrane-Like Peptoid Materials. *Adv. Funct. Mater.* **2016**, *26* (48), 8960–8967.
49. Ma, X.; Zhang, S.; Jiao, F.; Newcomb, C. J.; Zhang, Y.; Prakash, A.; Liao, Z.; Baer, M. D.; Mundy, C. J.; Pfaendtner, J.; et al. Tuning Crystallization Pathways through Sequence Engineering of Biomimetic Polymers. *Nat. Mater.* **2017**, *16*, 767–774.
50. Mannige, R. V.; Haxton, T. K.; Proulx, C.; Robertson, E. J.; Battigelli, A.; Butterfoss, G. L.; Zuckermann, R. N.; Whitlam, S. Peptoid Nanosheets Exhibit a New Secondary-Structure Motif. *Nature* **2015**, *526* (7573), 415–420.
51. Flood, D.; Proulx, C.; Battagelli, A.; Robertson, E.; Wang, S.; Schwartzberg, A.; Zuckermann, R. N. Improved Chemical and Mechanical Stability of Peptoid Nanosheets by Photo-Crosslinking the Hydrophobic Core. *Chem. Commun.* **2016**, *52*, 4753–4756.
52. Berman, H. M.; Westbrook, J.; Feng, Z.; Gilliland, G.; Bhat, T. N.; Weissig, H.; Shindyalov, I. N.; Bourne, P. E. The Protein Data Bank. *Nucleic Acids Res.* **2000**, *28* (1), 235–242.
53. Pieters, B. J. G. E.; van Eldijk, M. B.; Nolte, R. J. M.; Mecinović, J. Natural Supramolecular Protein Assemblies. *Chem. Soc. Rev.* **2016**, *45*, 24–39.
54. Bai, Y.; Luo, Q.; Liu, J. Protein Self-Assembly via Supramolecular Strategies. *Chem. Soc. Rev.* **2016**, *3*, 2756–2767.
55. Rother, M.; Nussbaumer, M. G.; Renggli, K.; Bruns, N. Protein Cages and Synthetic Polymers: A Fruitful Symbiosis for Drug Delivery Applications, Bionanotechnology and Materials Science. *Chem. Soc. Rev.* **2016**, *105*, 1445–1489.
56. Padilla, J. E.; Colovos, C.; Yeates, T. O. Nanohedra: Using Symmetry to Design Self Assembling Protein Cages, Layers, Crystals, and Filaments. *Proc. Natl. Acad. Sci. U. S. A.* **2001**, *98* (5), 2217–2221.
57. Lai, Y. T.; King, N. P.; Yeates, T. O. Principles for Designing Ordered Protein Assemblies. *Trends Cell Biol.* **2012**, *22* (12), 653–661.

58. Zheng, J.; Birktoft, J. J.; Chen, Y.; Wang, T.; Sha, R.; Constantinou, P. E.; Ginell, S. L.; Mao, C.; Seeman, N. C. From Molecular to Macroscopic via the Rational Design of a Self-Assembled 3D DNA Crystal. *Nature* **2009**, *461* (7260), 74–77.
59. Boerneke, M. A.; Dibrov, S. M.; Hermann, T. Crystal-Structure-Guided Design of Self-Assembling RNA Nanotriangles. *Angew. Chemie Int. Ed.* **2016**, *55* (12), 4097–4100.
60. Veneziano, R.; Ratanalert, S.; Zhang, K.; Zhang, F.; Yan, H.; Chiu, W.; Bathe, M. Designer Nanoscale DNA Assemblies Programmed from the Top Down. *Science* **2016**, *352* (6293), 1534.
61. Suzuki, Y.; Endo, M.; Sugiyama, H. Lipid-Bilayer-Assisted Two-Dimensional Self-Assembly of DNA Origami Nanostructures. *Nat. Commun.* **2015**, *6*, 8052.
62. Hong, F.; Jiang, S.; Wang, T.; Liu, Y.; Yan, H. 3D Framework DNA Origami with Layered Crossovers. *Angew. Chemie Int. Ed.* **2016**, *55* (41), 12832–12835.
63. Benenson, Y.; Paz-Elizur, T.; Adar, R.; Keinan, E.; Livneh, Z.; Shapiro, E. Programmable and Autonomous Computing Machine Made of Biomolecules. *Nature* **2001**, *414* (6862), 430–434.
64. Elbaz, J.; Lioubashevski, O.; Wang, F.; Remacle, F.; Levine, R. D.; Willner, I. DNA Computing Circuits Using Libraries of DNAzyme Subunits. *Nat. Nanotechnol.* **2010**, *5* (6), 417–422.
65. Seelig, G.; Soloveichik, D.; Zhang, D. Y.; Winfree, E. Enzyme-Free Nucleic Acid Logic Circuits. *Science* **2006**, *314* (5805), 1585–1589.
66. Hao, Y.; Kristiansen, M.; Sha, R.; Birktoft, J. J.; Hernandez, C.; Mao, C.; Seeman, N. C. A Device That Operates within a Self-Assembled 3D DNA Crystal. *Nat. Chem.* **2017**, *9*, 824–827.
67. Gerling, T.; Wagenbauer, K. F.; Neuner, A. M.; Dietz, H. Dynamic DNA Devices and Assemblies Formed by Shape-Complementary, Non – Base Pairing 3D Components. *Science* **2015**, *347* (6229), 1446–1452.
68. Lupas, A. N.; Gruber, M. The Structure of α -Helical Coiled Coils. *Adv. Protein Chem.* **2005**, *70*, 37–78.
69. Moutevelis, E.; Woolfson, D. N. A Periodic Table of Coiled-Coil Protein Structures. *J. Mol. Biol.* **2009**, *385* (3), 726–732.

70. Thomson, A. R.; Wood, C. W.; Burton, A. J.; Bartlett, G. J.; Sessions, R. B.; Brady, R. L.; Woolfson, D. N. Computational Design of Water-Soluble α -Helical Barrels. *Science* **2014**, *346* (6208), 485–488.
71. Mahendran, K. R.; Niitsu, A.; Kong, L.; Thomson, A. R.; Sessions, R. B.; Woolfson, D. N.; Bayley, H. A Monodisperse Transmembrane α -Helical Peptide Barrel. *Nat. Chem.* **2017**, *9*, 411–419.
72. Dublin, S. N.; Conticello, V. P. Design of a Selective Metal Ion Switch for Self-Assembly of Peptide-Based Fibrils. *J. Am. Chem. Soc.* **2008**, *130* (1), 49–51.
73. Xu, C.; Liu, R.; Mehta, A. K.; Guerrero-Ferreira, R. C.; Wright, E. R.; Dunin-Horkawicz, S.; Morris, K.; Serpell, L. C.; Zuo, X.; Wall, J. S.; et al. Rational Design of Helical Nanotubes from Self-Assembly of Coiled-Coil Lock Washers. *J. Am. Chem. Soc.* **2013**, *135* (41), 15565–15578.
74. Mehrban, N.; Zhu, B.; Tamagnini, F.; Young, F. I.; Wasmuth, A.; Hudson, K. L.; Thomson, A. R.; Birchall, M. a.; Randall, A. D.; Song, B.; et al. Functionalized α -Helical Peptide Hydrogels for Neural Tissue Engineering. *ACS Biomater. Sci. Eng.* **2015**, *1* (6), 431–439.
75. Thomas, F.; Burgess, N. C.; Thomson, A. R.; Woolfson, D. N. Controlling the Assembly of Coiled-Coil Peptide Nanotubes. *Angew. Chemie - Int. Ed.* **2016**, *128* (3), 999–1003.
76. Egelman, E. H.; Xu, C.; DiMaio, F.; Magnotti, E.; Modlin, C.; Yu, X.; Wright, E.; Baker, D.; Conticello, V. P. Structural Plasticity of Helical Nanotubes Based on Coiled-Coil Assemblies. *Structure* **2015**, *23* (2), 280–289.
77. Fletcher, J. M.; Harniman, R. L.; Barnes, F. R. H.; Boyle, A. L.; Collins, A.; Mantell, J.; Sharp, T. H.; Antognozzi, M.; Booth, P. J.; Linden, N.; et al. Self-Assembling Cages from Coiled-Coil Peptide Modules. *Science* **2013**, *340* (6132), 595–600.
78. Ringler, P.; Schulz, G. E. Self-Assembly of Proteins into Designed Networks. *Science* **2003**, *302* (5642), 106–109.
79. Sinclair, J. C.; Davies, K. M.; Vénien-Bryan, C.; Noble, M. E. M. Generation of Protein Lattices by Fusing Proteins with Matching Rotational Symmetry. *Nat. Nanotechnol.* **2011**, *6* (9), 558–562.

80. Brodin, J. D.; Carr, J. R.; Sontz, P. A.; Tezcan, F. A. Exceptionally Stable, Redox-Active Supramolecular Protein Assemblies with Emergent Properties. *Proc. Natl. Acad. Sci. U. S. A.* **2014**, *111* (8), 2897–2902.
81. Gonen, S.; Dimairo, F.; Gonen, T.; Baker, D. Design of Ordered Two-Dimensional Arrays Mediated by Noncovalent Protein-Protein Interfaces. *Science* **2015**, *348* (6241), 1365–1368.
82. Suzuki, Y.; Cardone, G.; Restrepo, D.; Zavattieri, P. D.; Baker, T. S.; Tezcan, F. A. Self-Assembly of Coherently Dynamic, Auxetic, Two-Dimensional Protein Crystals. *Nature* **2016**, *533* (7603), 369.
83. Lai, Y.; Cascio, D.; Yeates, T. O. Structure of a 16-Nm Cage Designed by Using Protein Oligomers. *Science* **2012**, *336* (6085), 1129.
84. Sciore, A.; Su, M.; Koldewey, P.; Eschweiler, J. D.; Diffley, K. A.; Linhares, B. M.; Ruotolo, B. T.; Bardwell, J. C. A.; Skiniotis, G.; Marsh, E. N. G. Flexible, Symmetry-Directed Approach to Assembling Protein Cages. *Proc. Natl. Acad. Sci.* **2016**, *113* (31), 8681–8686.
85. King, N. P.; Sheffler, W.; Sawaya, M. R.; Vollmar, B. S.; Sumida, J. P.; André, I.; Gonen, T.; Yeates, T. O.; Baker, D. Computational Design of Self-Assembling Protein Nanomaterials with Atomic Level Accuracy. *Science* **2012**, *336* (6085), 1171–1174.
86. King, N. P.; Bale, J. B.; Sheffler, W.; McNamara, D. E.; Gonen, S.; Gonen, T.; Yeates, T. O.; Baker, D.; Methods, S. Accurate Design of Co-Assembling Multi-Component Protein Nanomaterials. *Nature* **2014**, *510* (7503), 103–108.
87. Hsia, Y.; Bale, J. B.; Gonen, S.; Shi, D.; Sheffler, W.; Fong, K. K.; Nattermann, U.; Xu, C.; Huang, P.-S.; Ravichandran, R.; Yi, S.; Davis, T. N.; Gonen, T.; King, N. P.; Baker, D.; Design of a Hyperstable 60-Subunit Protein Icosahedron. *Nature* **2016**, *535* (7610), 136–139.
88. Bale, J. B.; Gonen, S.; Liu, Y.; Sheffler, W.; Ellis, D.; Thomas, C.; Cascio, D.; Yeates, T. O.; Gonen, T.; King, N. P.; et al. Accurate Design of Megadalton-Scale Two-Component Icosahedral Protein Complexes. *Science* **2016**, *353* (6297), 389–394.
89. Lindsey, S.; Piatt, J. H.; Worthington, P.; Sönmez, C.; Satheye, S.; Schneider, J. P.; Pochan, D. J.; Langhans, S. A. Beta Hairpin Peptide Hydrogels as an Injectable Solid Vehicle for Neurotrophic Growth Factor Delivery. *Biomacromolecules* **2015**, *16* (9), 2672–2683.

90. Worthington, P.; Pochan, D. J.; Langhans, S. A. Peptide Hydrogels – Versatile Matrices for 3D Cell Culture in Cancer Medicine. *Front. Oncol.* **2015**, *5*, 92.
91. King, P. J. S.; Giovanna Lizio, M.; Booth, A.; Collins, R. F.; Gough, J. E.; Miller, A. F.; Webb, S. J. A Modular Self-Assembly Approach to Functionalised β -Sheet Peptide Hydrogel Biomaterials. *Soft Matter* **2016**, *12*, 1915–1923.
92. Sun, J. E. P.; Stewart, B.; Litan, A.; Lee, S. J.; Schneider, J. P.; Langhans, S. A.; Pochan, D. J. Sustained Release of Active Chemotherapeutics from Injectable-Solid β -Hairpin Peptide Hydrogel. *Biomater. Sci.* **2016**, *4* (5), 839–848.
93. Worthington, P.; Langhans, S.; Pochan, D. Beta-Hairpin Peptide Hydrogels for Package Delivery. *Adv. Drug Deliv. Rev.* **2016**, 1–10.
94. Lu, Y.; Chan, W.; Ko, B. Y.; VanLang, C. C.; Swartz, J. R. Assessing Sequence Plasticity of a Virus-like Nanoparticle by Evolution toward a Versatile Scaffold for Vaccines and Drug Delivery. *Proc. Natl. Acad. Sci.* **2015**, *112* (20), 12360–12365.
95. Azuma, Y.; Zschoche, R.; Tinzl, M.; Hilvert, D. Quantitative Packaging of Active Enzymes into a Protein Cage. *Angew. Chemie - Int. Ed.* **2016**, *55*, 1531–1534.
96. Clair, N. L. St.; Navia, M. A. Cross-Linked Enzyme Crystals as Robust Biocatalysts. *J. Am. Chem. Soc.* **1992**, *114* (18), 7314–7316.
97. Vilenchik, L. Z.; Griffith, J. P.; Clair, N. St.; Navia, M. A.; Margolin, A. L. Protein Crystals as Novel Microporous Materials. *J. Am. Chem. Soc.* **1998**, *120* (18), 4290–4294.
98. Häring, D.; Schreier, P. Cross-Linked Enzyme Crystals. *Curr. Opin. Chem. Biol.* **1999**, *3* (1), 35–38.
99. Hartgerink, J. D.; Beniash, E.; Stupp, S. I. Self-Assembly and Mineralization of Peptide-Amphiphile Nanofibers. *Science* **2001**, *294* (5547), 1684–1688.
100. Sharma, N.; Top, A.; Kiick, K. L.; Pochan, D. J. One-Dimensional Gold Nanoparticle Arrays by Electrostatically Directed Organization Using Polypeptide Self-Assembly. *Angew. Chemie* **2009**, *121*, 7212–7216.

101. Lee, J.; Bhak, G.; Lee, J.; Park, W.; Lee, M.; Lee, D.; Jeon, L.; Jeong, D. H.; Char, K.; Paik, S. R. Free-Standing Gold-Nanoparticle Monolayer Film Fabricated by Protein Self-Assembly of α -Synuclein. *Angew. Chemie - Int. Ed.* **2015**, *54* (15), 4571–4576.
102. Boyle, A. L.; Woolfson, D. N. Rational Design of Peptide-Based Biosupramolecular Systems. In *Supramolecular Chemistry: From Molecules to Nanomaterials*; John Wiley & Sons, Ltd: New York, 2012.
103. Benner, S. A.; Sismour, A. M. Synthetic Biology. *Nat. Rev. Genet.* **2005**, *6* (7), 533–543.
104. Jones, M. R.; Seeman, N. C.; Mirkin, C. A. Programmable Materials and the Nature of the DNA Bond. *Science* **2015**, *347* (6224), 840.
105. Fields, G. B.; Noble, R. L. Solid Phase Peptide Synthesis Utilizing 9-Fluorenylmethoxycarbonyl Amino Acids. *Int. J. Pept. Protein Res.* **1990**, *35* (3), 161–214.
106. Maude, S.; Tai, L. R.; Davies, R. P. W.; Liu, B.; Harris, S. A.; Kocienski, P. J.; Aggeli, A. Peptide Synthesis and Self-Assembly. *Pept. Mater.* **2012**, *310*, 27–69.
107. Deming, T. J. Facile Synthesis of Block Copolypeptides of Defined Architecture. *Nature* **1997**, *390* (6658), 386–389.
108. Vauthey, S.; Santoso, S.; Gong, H.; Watson, N.; Zhang, S. Molecular Self-Assembly of Surfactant-like Peptides to Form Nanotubes and Nanovesicles. *Proc. Natl. Acad. Sci.* **2002**, *99* (8), 5355–5360.
109. Santoso, S.; Hwang, W.; Hartman, H.; Zhang, S. Self-Assembly of Surfactant-like Peptides with Variable Glycine Tails to Form Nanotubes and Nanovesicles. *Nano Lett.* **2002**, *2* (7), 687–691.
110. Zhang, S. Fabrication of Novel Biomaterials through Molecular Self-Assembly. *Nat. Biotechnol.* **2003**, *21* (10), 1171–1178.
111. Loo, Y.; Zhang, S.; Hauser, C. a E. From Short Peptides to Nanofibers to Macromolecular Assemblies in Biomedicine. *Biotechnol. Adv.* **2012**, *30* (3), 593–603.
112. Zhang, S.; Holmes, T.; Lockshin, C.; Rich, A. Spontaneous Assembly of a Self-Complementary Oligopeptide to Form a Stable Macroscopic Membrane. *Proc. Natl. Acad. Sci.* **1993**, *90* (8), 3334–3338.

113. Zhang, S.; Holmes, T. C.; DiPersio, C. M.; Hynes, R. O.; Su, X.; Rich, A. Self-Complementary Oligopeptide Matrices Support Mammalian Cell Attachment. *Biomaterials* **1995**, *16* (18), 1385–1393.
114. Reches, M.; Gazit, E. Casting Metal Nanowires Within Discrete Self-Assembled Peptide Nanotubes. *Science* **2003**, *300* (5619), 625–627.
115. Reches, M.; Gazit, E. Controlled Patterning of Aligned Self-Assembled Peptide Nanotubes. *Nat. Nanotechnol.* **2006**, *1* (3), 195–200.
116. Gazit, E. Self-Assembled Peptide Nanostructures: The Design of Molecular Building Blocks and Their Technological Utilization. *Chem. Soc. Rev.* **2007**, *36* (8), 1263–1269.
117. Adler-Abramovich, L.; Aronov, D.; Beker, P.; Yevnin, M.; Stempler, S.; Buzhansky, L.; Rosenman, G.; Gazit, E. Self-Assembled Arrays of Peptide Nanotubes by Vapour Deposition. *Nat. Nanotechnol.* **2009**, *4* (12), 849–854.
118. Aggeli, A.; Bell, M.; Boden, N.; Keen, J. N.; McLeish, T. C. B.; Nyrkova, I.; Radford, S. E.; Semenov, A. Engineering of Peptide Beta-Sheet Nanotapes. *J. Mater. Chem.* **1997**, *7* (7), 1135–1145.
119. Schneider, J. P.; Pochan, D. J.; Ozbas, B.; Rajagopal, K.; Pakstis, L.; Kretsinger, J. Responsive Hydrogels from the Intramolecular Folding and Self-Assembly of a Designed Peptide. *J. Am. Chem. Soc.* **2002**, *124* (50), 15030–15037.
120. Ozbas, B.; Kretsinger, J.; Rajagopal, K.; Schneider, J. P.; Pochan, D. J. Salt-Triggered Peptide Folding and Consequent Self-Assembly into Hydrogels with Tunable Modulus. *Macromolecules* **2004**, *37*, 7331–7337.
121. Lamm, M. S.; Rajagopal, K.; Schneider, J. P.; Pochan, D. J. Laminated Morphology of Nontwisting β -Sheet Fibrils Constructed via Peptide Self-Assembly. *J. Am. Chem. Soc.* **2005**, *127* (47), 16692–16700.
122. Moyer, T. J.; Finbloom, J. A.; Chen, F.; Toft, D. J.; Cryns, V. L.; Stupp, S. I. PH and Amphiphilic Structure Direct Supramolecular Behavior in Biofunctional Assemblies. *J. Am. Chem. Soc.* **2014**, *136* (42), 14746–14752.
123. Palmer, L. C.; Leung, C.-Y.; Kewalramani, S.; Kumthekar, R.; Newcomb, C. J.; Olvera De La Cruz, M.; Bedzyk, M. J.; Stupp, S. I. Long-Range Ordering of Highly Charged Self-Assembled Nanofilaments. *J. Am. Chem. Soc.* **2014**, *136* (41), 14377–14380.

124. Korevaar, P. A.; Newcomb, C. J.; Meijer, E. W.; Stupp, S. I. Pathway Selection in Peptide Amphiphile Assembly. *J. Am. Chem. Soc.* **2014**, *136* (24), 8540–8543.
125. Li, L. S.; Stupp, S. I. One-Dimensional Assembly of Lipophilic Inorganic Nanoparticles Templated by Peptide-Based Nanofibers with Binding Functionalities. *Angew. Chemie - Int. Ed.* **2005**, *44* (12), 1833–1836.
126. Sone, E. D.; Stupp, S. I. Bioinspired Magnetite Mineralization of Peptide-Amphiphile Nanofibers. *Chem. Mater.* **2011**, *23* (8), 2005–2007.
127. Pazos, E.; Sleep, E.; Rubert Pérez, C. M.; Lee, S. S.; Tantakitti, F.; Stupp, S. I. Nucleation and Growth of Ordered Arrays of Silver Nanoparticles on Peptide Nanofibers: Hybrid Nanostructures with Antimicrobial Properties. *J. Am. Chem. Soc.* **2016**, *138* (17), 5507–5510.
128. Lim, Y.; Lee, E.; Yoon, Y.-R.; Lee, M. M. S. Filamentous Artificial Virus from a Self-Assembled Discrete Nanoribbon. *Angew. Chem. Int. Ed. Engl.* **2008**, *47* (24), 4525–4528.
129. Boato, F.; Thomas, R. M.; Ghasparian, A.; Freund-renard, A.; Robinson, J. A.; Moehle, K. Synthetic Virus-like Particles from Self-Assembling Coiled-Coil Lipopeptides and Their Use in Antigen Display to the Immune System. *Angew. Chem. Int. Ed. Engl.* **2007**, *46* (47), 9015–9018.
130. Ghadiri, M. R.; Granja, J. R.; Milligan, R. A.; McRee, D. E.; Khazanovich, N. Self-Assembling Organic Nanotubes Based on a Cyclic Peptide Architecture. *Nature* **1993**, *366* (6453), 324–327.
131. Ghadiri, M. R.; Granja, J. R.; Buehler, L. K. Artificial Transmembrane Ion Channels from Self-Assembling Peptide Nanotubes. *Nature* **1994**, *369* (6478), 301–304.
132. Woolfson, D. N. The Design of Coiled-Coil Structures and Assemblies. *Adv. Protein Chem.* **2005**, *70*, 79–112.
133. Burgess, N. C.; Sharp, T. H.; Thomas, F.; Wood, C. W.; Thomson, A. R.; Zaccai, N.; Brady, R. L.; Serpell, L. C.; Woolfson, D. N. Modular Design of Self-Assembling Peptide-Based Nanotubes. *J. Am. Chem. Soc.* **2015**, *137* (33), 10554–10562.
134. Banwell, E. F.; Abelardo, E. S.; Adams, D. J.; Birchall, M. a; Corrigan, A.; Donald, A. M.; Kirkland, M.; Serpell, L. C.; Butler, M. F.; Woolfson, D. N. Rational Design and Application of Responsive Alpha-Helical Peptide Hydrogels. *Nat. Mater.* **2009**, *8* (7), 596–600.

135. Zhang, H. V.; Polzer, F.; Haider, M. J.; Tian, Y.; Villegas, J. A.; Kiick, K. L.; Pochan, D. J.; Saven, J. G. Computationally Designed Peptides for Self-Assembly of Nanostructured Lattices. *Sci. Adv.* **2016**, *2* (9), e1600307.
136. Schnarr, N. A.; Kennan, A. J. Specific Control of Peptide Assembly with Combined Hydrophilic and Hydrophobic Interfaces. *J. Am. Chem. Soc.* **2003**, *125* (3), 667–671.
137. Pandya, M. J.; Cerasoli, E.; Joseph, A.; Stoneman, R. G.; Waite, E.; Woolfson, D. N. Sequence and Structural Duality: Designing Peptides to Adopt Two Stable Conformations. *J. Am. Chem. Soc.* **2004**, *126* (51), 17016–17024.
138. Shen, W.; Lammertink, R. G. H.; Sakata, J. K.; Kornfield, J. A.; Tirrell, D. A. Assembly of an Artificial Protein Hydrogel through Leucine Zipper Aggregation and Bisulfide Bond Formation. *Macromolecules* **2005**, *38* (9), 3909–3916.
139. Shen, W.; Kornfield, J. A.; Tirrell, D. A. Dynamic Properties of Artificial Protein Hydrogels Assembled through Aggregation of Leucine Zipper Peptide Domains. *Macromolecules* **2007**, *40* (3), 689–692.
140. Pandya, M. J.; Spooner, G. M.; Sunde, M.; Thorpe, J. R.; Rodger, A.; Woolfson, D. N. Sticky-End Assembly of a Designed Peptide Fiber Provides Insight into Protein Fibrillogenesis. *Biochemistry* **2000**, *39* (30), 8728–8734.
141. Ryadnov, M. G.; Woolfson, D. N.; Chem, A.; Ed, I. Introducing Branches into a Self-Assembling Peptide Fiber. *Angew. Chem. Int. Ed. Engl.* **2003**, *42* (26), 3021–3023.
142. Magnotti, E. L.; Hughes, S. A.; Dillard, R. S.; Wang, S.; Hough, L.; Karumbamkandathil, A.; Lian, T.; Wall, J. S.; Zuo, X.; Wright, E. R.; et al. Self-Assembly of an α -Helical Peptide into a Crystalline Two-Dimensional Nanoporous Framework. *J. Am. Chem. Soc.* **2016**, *138* (50), 16274–16282.
143. Zimenkov, Y.; Dublin, S. N.; Ni, R.; Tu, R. S.; Breedveld, V.; Apkarian, R. P.; Conticello, V. P. Rational Design of a Reversible PH-Responsive Switch for Peptide Self-Assembly. *J. Am. Chem. Soc.* **2006**, *128*, 6770–6771.
144. Ghadiri, M. R.; Soares, C.; Choi, C. A Convergent Approach to Protein Design - Metal Ion-Assisted Spontaneous Self-Assembly of a Polypeptide into a Triple-Helix Bundle Protein. *J. Am. Chem. Soc.* **1992**, *114* (3), 825–831.

145. Tavenor, N. A.; Murnin, M. J.; Horne, W. S. Supramolecular Metal-Coordination Polymers, Nets, and Frameworks from Synthetic Coiled-Coil Peptides. *J. Am. Chem. Soc.* **2017**, *139* (6), 2212–2215.
146. Tsurkan, M. V.; Ogawa, M. Y. Formation of Peptide Nanospheres and Nanofibrils by Metal Coordination. *Biomacromolecules* **2007**, *8* (12), 3908–3913.
147. Pires, M. M.; Chmielewski, J. Self-Assembly of Collagen Peptides into Microflorettes via Metal Coordination. *J. Am. Chem. Soc.* **2009**, *131* (7), 2706–2712.
148. Przybyla, D. E.; Chmielewski, J. Metal-Triggered Radial Self-Assembly of Collagen Peptide Fibers. *J. Am. Chem. Soc.* **2008**, *130* (38), 12610–12611.
149. Pires, M. M.; Przybyla, D. E.; Rubert Pérez, C. M.; Chmielewski, J. Metal-Mediated Tandem Coassembly of Collagen Peptides into Banded Microstructures. *J. Am. Chem. Soc.* **2011**, *133* (37), 14469–14471.
150. Przybyla, D. E.; Rubert Pérez, C. M.; Gleaton, J.; Nandwana, V.; Chmielewski, J. Hierarchical Assembly of Collagen Peptide Triple Helices into Curved Disks and Metal Ion-Promoted Hollow Spheres. *J. Am. Chem. Soc.* **2013**, *135* (9), 3418–3422.
151. Cochran, F. V.; Wu, S. P.; Wang, W.; Nanda, V.; Saven, J. G.; Therien, M. J.; DeGrado, W. F. Computational de Novo Design and Characterization of a Four-Helix Bundle Protein That Selectively Binds a Nonbiological Cofactor. *J. Am. Chem. Soc.* **2005**, *127* (5), 1346–1347.
152. Joh, N. H.; Wang, T.; Bhate, M. P.; Acharya, R.; Wu, Y.; Grabe, M.; Hong, M.; Grigoryan, G.; Degrado, W. F. De Novo Design of a Transmembrane Zn²⁺-Transporting Four-Helix Bundle. *Science* **2014**, *346* (6216), 1520–1524.
153. Protease, S.; Aldrich, S.; Fos-choline, C. M. C.; Gfp, T.; Sepharose, B.; Trio, T.; Bio-, A.; Biosystems, A.; Jensen, B.-; Tegoni, M.; et al. Designing a Functional Type 2 Copper Center That Has Nitrite Reductase Activity within α -Helical Coiled Coils. *Proc. Natl. Acad. Sci. U. S. A.* **2012**, *109* (13), 21234–21239.
154. Lanci, C.; MacDermaid, C.; Kang, S.; Acharya, R.; North, B.; Yang, X.; Qiu, X. J.; Degrado, W. F.; Saven, J. G. Computational Design of a Protein Crystal. *Proc. Natl. Acad. Sci. U. S. A.* **2012**, *109* (19), 7304–7309.

155. Crick, F. H. C. The Fourier Transform of a Coiled-Coil. *Acta Crystallogr.* **1953**, 6 (8), 685–689.

Chapter 2

KINETICALLY CONTROLLED PEPTIDE SELF-ASSEMBLY PROCESS FOR THE FORMATION OF TWO-DIMENSIONAL NANOSTRUCTURES

2.1 Introduction

Efforts in nanomaterial construction via solution-phase self-assembly recently have focused on nanostructure complexity and controllability.^{1,2,11–19,3–10} For example, block copolymer assembly has been successfully employed to yield controlled complexity of nanoparticle shape and size via hierarchical assembly mechanisms.^{17,20–24} The application of a kinetic assembly pathway and/or chemical modification of assembling molecules can trigger desired interactions between block copolymers^{21,22} or can induce crystallization-driven self-assembly with crystalline-coil di-block copolymers to produce targeted, kinetically-defined morphologies.^{16,18,24} Molecules with specific architectures and desired display of chemical groups have also been used to control intermolecular assembly. For example, by placing different silsesquioxane molecules onto rigid carbon frameworks, the resultant molecules can self-assemble into highly ordered superlattices.^{2,3} With control of biomimetic polymer sequence, designed peptoid molecules can produce ordered structures such as nano-sheets or porous nano-networks.^{25–29} Biomolecules represent an exceptionally versatile set of building blocks that can yield complex assembled nanostructures, including nucleic acids (DNA and RNA), peptides and proteins. The folded states of these biopolymers allow inherent specificity of local chemical functionality and its display due to exact primary, secondary, tertiary and intermolecular quaternary structures. The specific

base-pairing interactions of nucleic acids, which drive their natural hierarchical organization, allow computational design to create new, non-natural sequences and resultant nanostructure after solution assembly.^{7,8,30} Self-assembled DNA/RNA nanostructures can be controlled at the nanoscale exclusively through the proper design of complementary base pairing, which has enabled the production of complex structures,^{7,8} the templating of other molecules onto the nucleic acid-based nanostructure,^{31–34} and the performance of simple computational functions.^{35–38}

Peptides and proteins share similar features with polymeric nucleic acids in that they can form well-defined molecular conformations containing regular secondary structures defined by the primary sequence of monomers – a stark difference in conformational properties when compared with the random coil conformations of most synthetic polymers.^{39,40} Peptide or protein molecular shape can be considered as a key parameter in the design of intermolecular assemblies, both on the basis of geometric considerations and also by virtue of the installation of directed, local covalent or physical interactions that allow the construction of nanostructures in a controllable fashion. Moreover, the 20 naturally occurring amino acids provide a variety of different side-chain functional groups making peptides/proteins much more versatile chemically when compared with nucleic acids. This versatility becomes almost limitless when considering designs that incorporate non-natural, synthetic amino acids.^{41–44} The advent of computational design is quickly advancing the creation of new peptide or protein-based nanostructures. Examples include the alteration of natural proteins for desired intermolecular assembly such as protein nanohedra,^{45–47} periodic assemblies of helical proteins,^{48–52} and fibers, lattices and cages produced by redesigning natural protein interfaces.^{10,14,53,54}

Different assembly products can be kinetically trapped in reproducible fashion with different assembly pathways. In block copolymer systems, kinetic trapping is due to slow or non-existent chain exchange between aggregates and solvent.^{20,21,55} Other examples include π -conjugated systems, such as oligo(p-phenylenevinylene) derivatives, for which a hierarchical nucleation pathway, assisted by solvent, dictated final assembled structures.⁵⁶ Additionally, small molecules, such as self-assembled bis(merocyanine) nanorods, exhibit a time-dependent stereomutation from a product of a fast kinetic pathway of formation to a more stable product.⁵⁷ Kinetically-defined assembly pathways have clear effects in peptide- and protein-based assemblies such as the slow morphology transition from ribbons to β -helices in myeloid-derived peptide segments, driven in part by reorganization of molecular packing.⁵⁸ Thermal pathways can drive nanofibers formed by peptide amphiphiles to fuse into stronger plaque-like structures.⁵⁹ A variety of protein assembly products with different morphologies can result from different nucleation rates affected by pH and metal/protein ratios.⁶⁰

In this **Chapter 2**, the two-dimensional nanostructures are presented, and produced by the assembly of peptide building blocks that are entirely computationally designed⁵⁰ rather than derived from existing, natural protein-based motifs or templates. This approach provides design flexibility for the creation of non-natural, arbitrary nanostructures. As described in **Chapter 1**, our assembly system uses a homotetrameric, antiparallel coiled-coil peptide bundle as the building block for hierarchical solution assembly.⁶¹ The interior of the bundle consists primarily of complementary hydrophobic amino acids that provide for high stability of the bundle. Using the stable hydrophobic core as a basis for additional design, the amino acids on the exterior of the bundle were computationally designed to stabilize a two-

dimensional lattice formed by inter-bundle solution assembly.⁶¹ Due to the robust design, the peptide building blocks are able to maintain the α -helical secondary structure and coiled-coil quaternary structure in solutions very different from common physiological conditions. Therefore, a significantly larger range of solution conditions can be employed to explore the effects of different intermolecular assembly pathways on nanostructure formation. Kinetic pathways may be designed and used in the self-assembly process to create complex assemblies.^{21,56,57,59,60,62}

As mentioned, our designed peptide tetrameric bundle need not be constrained to assemble in physiological solution conditions but can tolerate variation of pH and temperature. Therefore, a variety of solution condition parameters (pH = 4.5, 7, 8 or 10; T = room temperature, 40°C or 50°C) were applied as assembly solution conditions to investigate the formation of the tetrameric bundle building block and resultant inter-bundle structures. This control includes the ability to control regular inter-bundle assembly and the reorganization of disordered aggregates into ordered plate-like nanomaterials, where the rate of re-organization is dictated by solution temperature. With the use of computationally designed, non-natural peptide bundles, the control of kinetic pathways through manipulation of non-biological solution conditions offers new opportunities to process and anneal nanostructures into a desired assembly state.

2.2 Materials and Methods

2.2.1 Peptide Synthesis

Peptides were synthesized at a 0.25 mmol scale on Rink Amide resin using an AAPPTec Focus XC synthesizer (AAPPTec, Louisville, KY). Standard room

temperature Fmoc-based protocols were employed.⁶³ Peptides were deprotected for 5 min and then 10 min with 20% piperidine in dimethylformamide (DMF). The coupling reaction was conducted for 40 min with 4 eq. of the appropriate amino acid dissolved in N-methyl-2-pyrrolidone (NMP) (5 mL), 3.8 eq. HCTU dissolved in DMF (2.5 ml), and 8 eq. diisopropylethylamine (DIEA) dissolved in NMP (1 ml). Five washes were performed in between steps with 50:50 (v:v) DMF:methylene chloride (12 mL) for the first two washes and DMF (10 mL) for the last three. Amino acids, resin and activator were purchased from ChemPep (Wellington, FL) and used as received. All solvents were analytical grade (Fisher Scientific). After the last deprotection step, peptide acetylation was achieved as needed by incubation with a solution of (by volume) 80% DMF and 20% acetic anhydride with additional 3% DIEA for 30 min (repeated twice).

Peptide cleavage was achieved by shaking peptide solutions for 2 hours in a cleavage cocktail comprising (by volume) 95% trifluoroacetic acid (TFA), 2.5% triisopropylsilane, and 2.5% Milli-Q water. The final peptide was precipitated by adding the cleavage cocktail and cleaved peptide to diethyl ether. The mixture was centrifuged and the supernatant discarded. The process of suspension in diethyl ether, centrifugation, and supernatant disposal was repeated a total of three times. The resulting peptide was then dissolved in water and lyophilized.

2.2.2 Peptide Purification

Purification was performed via reverse-phase HPLC using a BEH130 Prep C18 10 μ m column (XBridge, Waters Corporation, Milford, MA). Crude peptides were dissolved in Milli-Q water containing 0.1%-vol TFA and were filtered (0.20 μ m filter, Corning, Inc., Corning, NY) before HPLC injection. Products were subjected to

an elution gradient (Quaternary Gradient Module (Waters 2545), Waters Corporation) of 100% solvent A (Milli-Q water with 0.1%-vol TFA) to 30% solvent A within 60 min; the composition of solvent B was acetonitrile with 0.1%-vol TFA. Fractions were detected using UV-Vis detection at 214nm (Waters 2489, Waters Corporation) and collected (Waters Fraction Collector III, Waters Corporation). The collected fractions were examined by ESI-mass spectrometry (LCQ Advantage Mass Spectrometer System, Thermo Finnigan, San Jose, CA) with an auto sampler system (Surveyor Autosampler, Thermo Finnigan). Pure fractions were combined and lyophilized.

The purity of the resulting products was assessed via reverse-phase Analytical scale HPLC using a BEH C4 3.5 μm column (XBridge, Waters Corporation, Milford, MA). Peptides were dissolved in 80/20-vol Milli-Q water/ACN containing 0.1%-vol TFA, and filtered with 0.20 μm filter (Corning, Inc., Corning, NY) before injection. Products were subjected to a linear elution gradient (Waters 600 Controller, Waters Corporation, Milford, MA) of 80% solvent A (Milli-Q water with 0.1%-vol TFA) to 5% solvent A in 70 min. The composition of solvent B was acetonitrile with 0.1%-vol TFA. Fractions were detected using a photodiode array detector (Waters 2996, Waters Corporation, Milford, MA) tuned at 214 nm.

Representative mass spectroscopy and chromatographic data are shown in **Figure 2.1** and **Figure 2.2**.

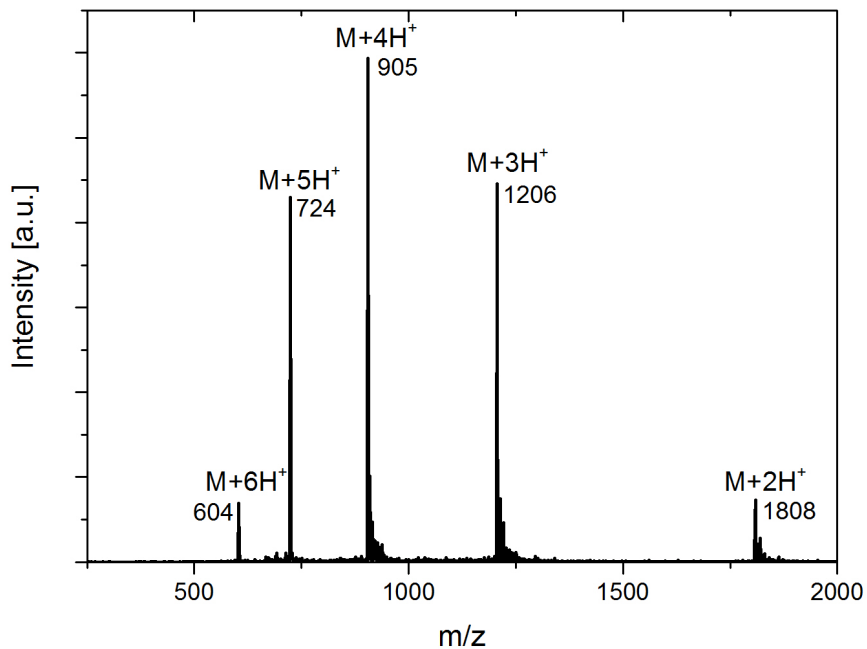


Figure 2.1 Representative ESI-mass spectrometry data for Ac-P422_1 peptide. Designed molecular weight: [M] 3614 Da. The accordingly calculated mass is: [M+2H⁺] 3616 Da, [M+3H⁺] 3617 Da, [M+4H⁺] 3618 Da, [M+5H⁺] 3619 Da, [M+6H⁺] 3620 Da. The experimental measured mass is: [M+2H⁺] 3616 Da, [M+3H⁺] 3618 Da, [M+4H⁺] 3620 Da, [M+5H⁺] 3620 Da, [M+6H⁺] 3624 Da.

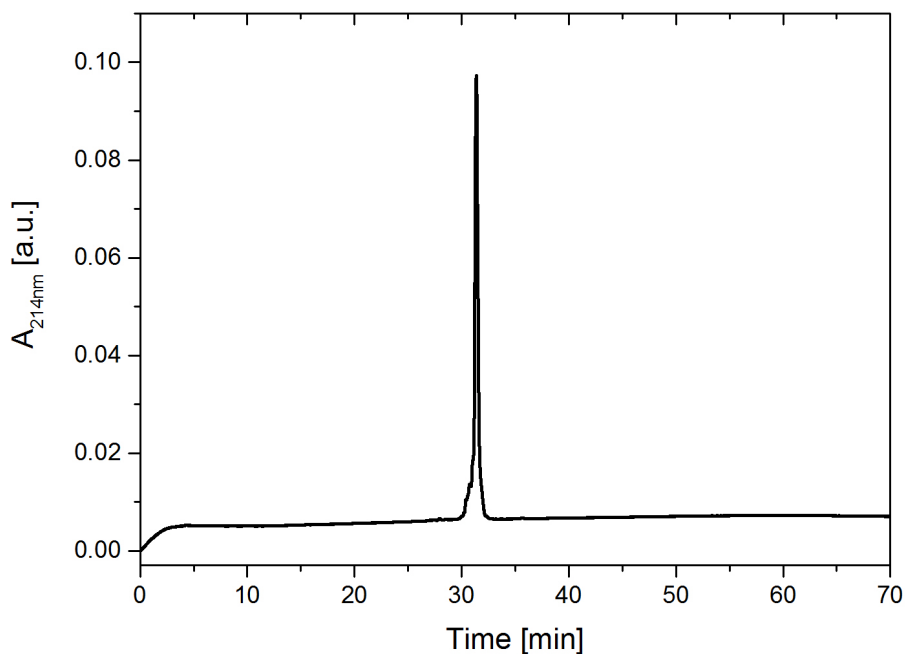


Figure 2.2 Representative analytical HPLC chromatographic data for Ac-P422_1 peptide. The single elution peak indicates the high purity of the peptide products.

2.2.3 Circular Dichroism Spectroscopy Measurement

Secondary structure and coiled-coils were analyzed using a CD spectropolarimeter (J-820, JASCO Corporation). Sample solutions were prepared at 0.1 mM concentration in buffers and transferred into an absorption cuvette with 1 mm path length (110-QS, Hellma, Inc.). Pure buffer solutions were used for the background correction. Unless otherwise specified, for full wavelength scans, sample spectra were recorded from 190-250 nm at desired temperatures, with scanning rate of 20 nm/min and averaged over three wavelength scans. Data points for the wavelength-dependent CD spectra were recorded at every nanometer with a 1 nm bandwidth and a

4-second response time for each data point. The CD data were converted to mean residue ellipticity, $[\theta]$ ($\text{deg cm}^2 \text{ dmol}^{-1}$) using the formula:

$$[\theta] (\text{deg} \cdot \text{cm}^2 \cdot \text{dmol}^{-1}) = \frac{\theta (\text{millidegree})}{L (\text{mm}) \times c (\text{M}) \times N}$$

in which, θ is the measured ellipticity in millidegree, L is the pathway length of CD cuvette in millimetre, c is the peptide solution molar concentration in mol/L, N is the number of amino acid residues. The values of θ at 222 nm measured from 5 °C to 95 °C were used to monitor temperature-dependent behavior such as the possible denaturation of the α -helix. The θ values at 222nm, as well as full wavelength scans, were recorded at temperatures from 5 °C to 95 °C at 5 °C intervals. During the temperature-dependent measurement, the heating rate was 1 °C/min; and 10 min was allowed at each temperature point for sample equilibration.

2.2.4 Peptide Solution Self-assembly Experiments

Peptide solutions for assembly were prepared at 0.1 mM concentration by dissolving the lyophilized pure peptides into desired buffer solutions (no additional salts) including: 10 mM pH 4.5 sodium acetate buffer, 10 mM pH 7 phosphate buffer, 10 mM pH 8 phosphate buffer or 10 mM pH 10 borate buffer. Solutions were placed in 1.5 mL vials and subsequently placed in an incubator (Thermomixer®C, Eppendorf) and incubated at 95°C for 30 min in order to fully denature the peptide α -helices and coiled-coil bundles; the solutions appeared optically clear after heating. After the thermal denaturation step, for room temperature assembly, the solution was removed from incubator and permitted to equilibrate to room temperature under ambient conditions (approximately 5 min to equilibrium measured by thermometer) and then incubated at room temperature thereafter for inter-molecular assembly. For high temperature assembly, the solution was taken directly from the 95°C incubator to

either a 40°C or 50°C incubator. After approximately 3 min the samples equilibrated to the set temperature (measured by thermometer) and were subsequently kept at the desired temperature for assembly for desired amounts of time. The pH of all solutions during incubation was confirmed

2.2.5 Transmission Electron Microscopy Measurement

The carbon-coated 200 mesh copper grids (CF200-Cu, Electron Microscopy Sciences, Inc.) were freshly treated by glow discharge using a plasma cleaner (PDC-32G, Harrica Plasma, Inc.) before sample grid preparation. 5 μL of sample suspension was applied onto the grids. After 1 min, any remaining excess liquid was wicked away with filter paper. Then 5 μL of Milli-Q water was applied to the grids and also wicked away in order to remove excess buffer salts from the sample grid. The grids were incubated under ambient condition for another 30 min before TEM observation (Tecnai 12, FEI or TALOS, FEI) or subsequent staining. To negatively stain the grids, 5 μL phosphotungstic acid aqueous solution (2% wt.) was applied to the cast-film grids, retained for 20-30 seconds, and then blotted with filter paper. The stained grids were left undisturbed for at least 10 min before TEM observation.

2.2.6 Atomic Force Microscopy Measurement

Atomic force microscopy was performed on a Bruker Multimode using Bruker ScanAsyst Air ultra-sharp tips with a nominal tip radius of 2 nm and a spring constant of 0.4 N/m. Samples were prepared by casting 15 μL of assembly solution on a freshly cleaved mica disc, the solution retained for 5 min on the disk, excess liquid blotted from the substrate with filter paper, and any remaining solution dried with application of compressed air. The instrument was operated in contact mode. Micrographs were

recorded digitally using Bruker nanoscope software using 512 to 1024 lines at 0.5-1 Hz scan rate.

2.2.7 Small Angle X-ray Scattering (SAXS)

SAXS measurements were conducted at 18ID Bio-CAT beamline and DND-CAT beamline at the Advanced Photon Source (APS) of Argonne National Laboratory (Argonne, IL).⁶⁴ The beamline was operated at 12 keV corresponding to a wavelength of 1.033 Å. The scattering patterns were collected using a Pilatus 1M detector covering a q -range of $0.005 \text{ \AA}^{-1} < q < 0.48 \text{ \AA}^{-1}$. Two different sample environments were used. Static measurements were performed on 100 μL of peptide sample with a concentration between 0.1 to 1 mM in buffer that were transferred into quartz glass capillaries with a diameter of 0.1 cm. Measurements on samples during flow were performed on 400 μL of sample that were inserted into a flow cell set-up operating at a flow rate of 10 $\mu\text{L/s}$. 10 exposures of 0.5 to 1.0 sec were recorded. The single spectra were averaged and corrected for background using the ATSAS software package v2.6.1.⁶⁵ Background subtracted SAXS curve was fit using the SasView software (www.sasview.org).

2.3 Peptide Sequences and Design

Two sequences were designed; and the N-terminus acetylated and un-acetylated variants of each were synthesized and denoted as following:

H-P422_1 & H-P422_2 for the N-terminus un-acetylated P422_1 and P422_2 molecules;

Ac-P422_1 & Ac-P422_2 for the N-terminus acetylated P422_1 and P422_2 molecules; sequence details are listed in **Table 2.1**. The backbone structure of P422

tetramer is constructed using a mathematic model for coiled-coils.⁶⁶ There are eleven residues per helix interior of the tetramer that are designed as hydrophobic amino acids to achieve shape-complementary packing. The remaining, surface-exposed residues were designed in the context of a single layer of a P422 lattice, as shown in **Figure 2.3**. The probabilistic design method provides an average energy over sequences for a given structure,⁵⁰ and the designed peptide falls in a local energy minimum. The two sequences are predicted to make the same P422 lattice with lattice spacing *a* equals to *b* equals 31.2 Å.

Peptide	Space group	Sequence code	Σ AAs	IEP	Mw[Da]
H-P422_1	P422	DQE <u>I</u> R QMAEW <u>I</u> KK <u>M</u> A QM <u>I</u> DK <u>M</u> A <u>H</u> R <u>I</u> DRE <u>A</u> -NH ₂	29	9.84	3572
Ac-P422_1	P422	Ac-DQE <u>I</u> R QMAEW <u>I</u> KK <u>M</u> A QM <u>I</u> DK <u>M</u> A <u>H</u> R <u>I</u> DRE <u>A</u> -NH ₂	29	8.12	3614
H-P422_2	P422	DQE <u>I</u> R QMAEW <u>I</u> KK <u>M</u> A LM <u>I</u> DK <u>M</u> A <u>H</u> R <u>I</u> DRE <u>A</u> -NH ₂	29	9.84	3557
Ac-P422_2	P422	Ac-DQE <u>I</u> R QMAEW <u>I</u> KK <u>M</u> A LM <u>I</u> DK <u>M</u> A <u>H</u> R <u>I</u> DRE <u>A</u> -NH ₂	29	8.12	3599

Table 2.1 The theoretically predicted P422 lattice former candidates and the acetylated variants. The underlined letters indicate the interior residues. IEP (iso-electric point) is estimated from a web-calculator <http://www.bachem.com/service-support/peptide-calculator/>.

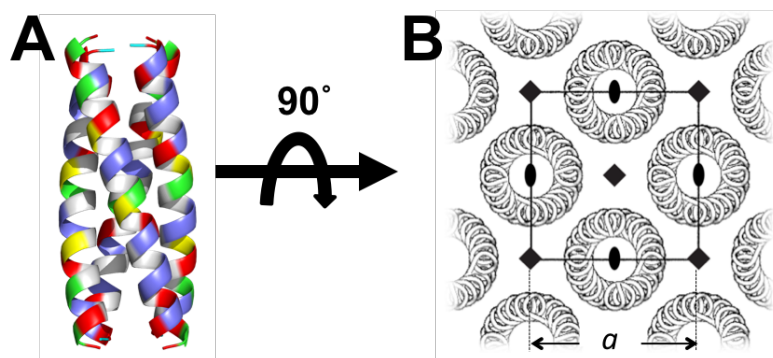


Figure 2.3 **A:** The peptide homotetrameric coiled-coil bundle building block with exterior residues coloured according to amino acid properties: blue indicates positively charged residues, red indicates negatively charged residues, green indicates polar residues, and yellow indicates hydrophobic residues. Interior residues are coloured grey. **B:** Rendering of one layer from a lattice with P422 symmetry, viewed from the top of the two-dimensional assembly.

2.4 pH-dependent Assembly Kinetic Process

Firstly, for Ac-P422_1 peptide, buffer systems with pH values of 4.5, 7, 8 and 10 were used to investigate the assembly behavior. From the circular dichroism spectra of peptides in buffers with these pH values, as shown in **Figure 2.4**, it is clear that the peptides maintained ellipticity minima consistent with those for α -helical structures (208 nm and 222 nm) for each pH condition. Furthermore, the measured ratios of $[\theta]_{222\text{nm}}/[\theta]_{208\text{nm}}$ for each of the peptide solutions are close to 1, consistent with reported values of stabilized coiled-coils.^{67,68}

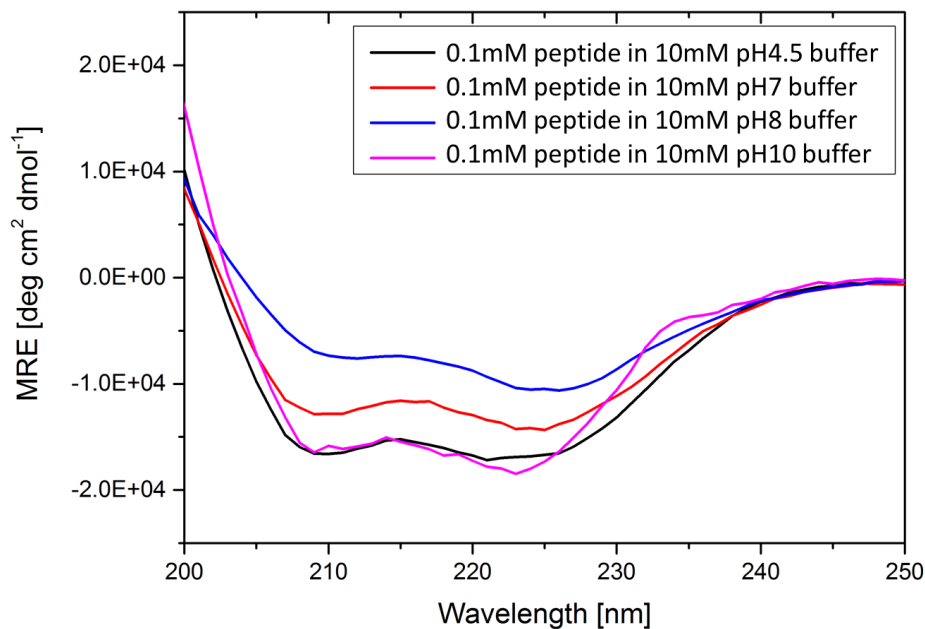


Figure 2.4 Circular dichroism spectroscopy data for Ac-P422_1 measured at 20°C in four different buffer conditions as shown in the figure legend. The ratios of $[MRE]_{222\text{nm}}/[MRE]_{208\text{nm}}$ are 1.06, 1.12, 1.62 and 1.16 for pH 4.5, 7, 8 and 10, respectively. The ratios at pH 4.5 and pH 10 are close to 1 indicating the stabilized coiled-coil formation. While for pH 7 and pH 8, due to the fast assembly process, peptides already started to precipitate, causing the loss of CD signal for this measurement. Formation of lattices is consistent with stable coil-coils at the pH 7 and pH 8 conditions.

These results reveal the tolerance of this tetrameric coiled-coil to a broad range of pH conditions, attributable to the robust computational design of a peptide with strong α -helix propensity and a stable hydrophobic coiled-coil core. Although the homotetrameric building blocks were formed, the hierarchical two-dimensional assembly observed under the different pH conditions varied considerably depending on the pH. The general rule is peptides assemble most rapidly at the pH value near its

IEP; whereas peptide would assemble more slowly as the solution pH value getting far away from the IEP, even would not assemble when the difference is big enough. When assembled at pH 4.5, the peptide coiled-coil bundles remained free in solution (peptide concentration from 0.1 mM to 1 mM) without any formation of aggregates or regular two-dimensional nanostructures (data not shown). At pH 7 and pH 8, peptide bundles aggregated rapidly and formed visible precipitates from solution within the first several hours, even at concentrations as low as 0.1 mM. After subsequent weeks of aging, these same solution conditions provided very regular assembled nanostructures (shown in **Figure 2.5** and **Figure 2.6**, discussed *vide infra*).

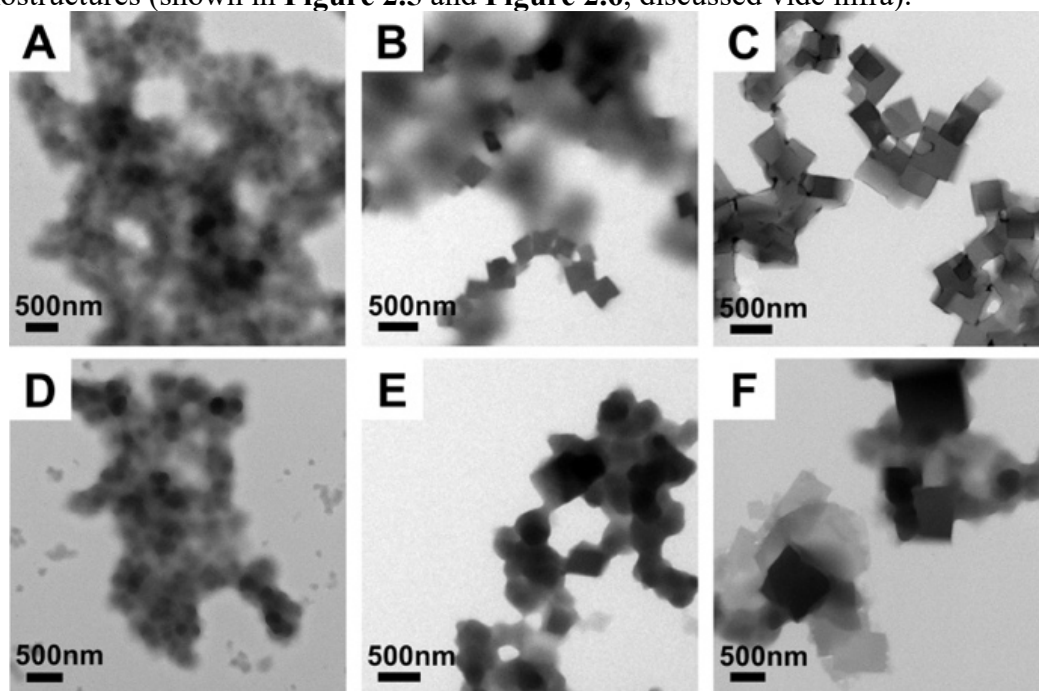


Figure 2.5 Transmission electron microscopy images of Ac-P422_1 peptide assembled at RT with concentration of 0.1 mM. and observed at different time periods. **A-C**: Peptides assembled at RT pH 8 for 2 days, 1 week and 8 weeks, respectively. **D-F**: Peptides assembled at RT pH 7 for 2 days, 1 week and 8 weeks, respectively. Both cases show disordered aggregates that formed at earlier time points and then transformed into ordered two-dimensional plates after aging.

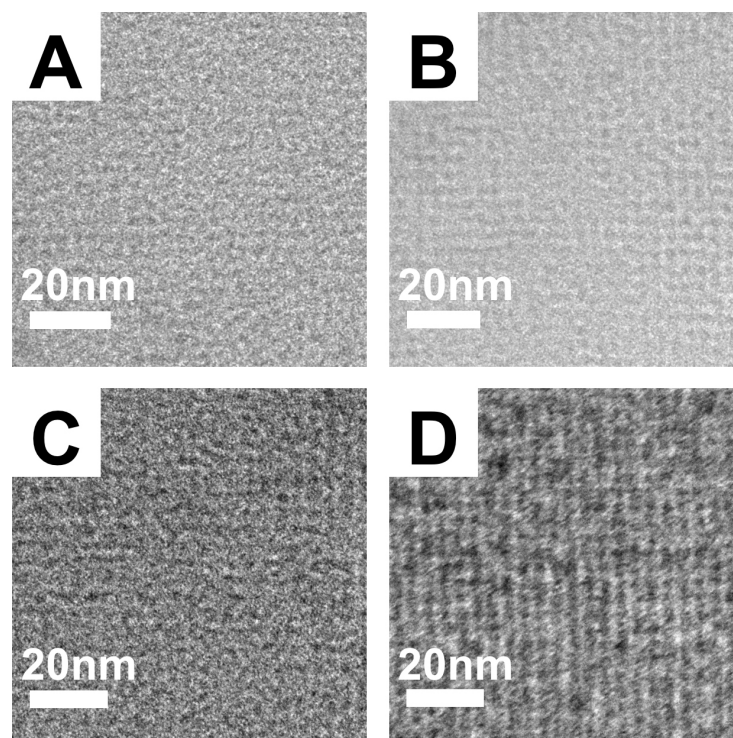


Figure 2.6 Dry state transmission electron microscopy high magnification images of Ac-P422_1 peptide assembled at room temperature show the symmetry of lattices is the same. Images were taken with 2% wt. phosphotungstic acid negative staining to enhance the contrast. Scale bars are all in 20nm. **A-B:** Peptides assembled at RT pH8 for 1 week and 8 weeks, respectively. **C-D:** Peptides assembled at RT pH7 for 1 week and 8 weeks, respectively.

At pH 10, in contrast, even at high concentration (1 mM), no solid precipitation was observed for solution; whereas, only a slightly denser, colloidal solution-like layer was formed in the bottom part. And only at this 1mM high concentration, after long-term aging (>2 weeks), distinctive SAX peaks can be observed from solution SAXS measurement, as shown in **Figure 2.7**. This is indicating the slow assembly kinetics at pH 10 condition; and the long-term aging is required for the formation of ordered lattice structures.

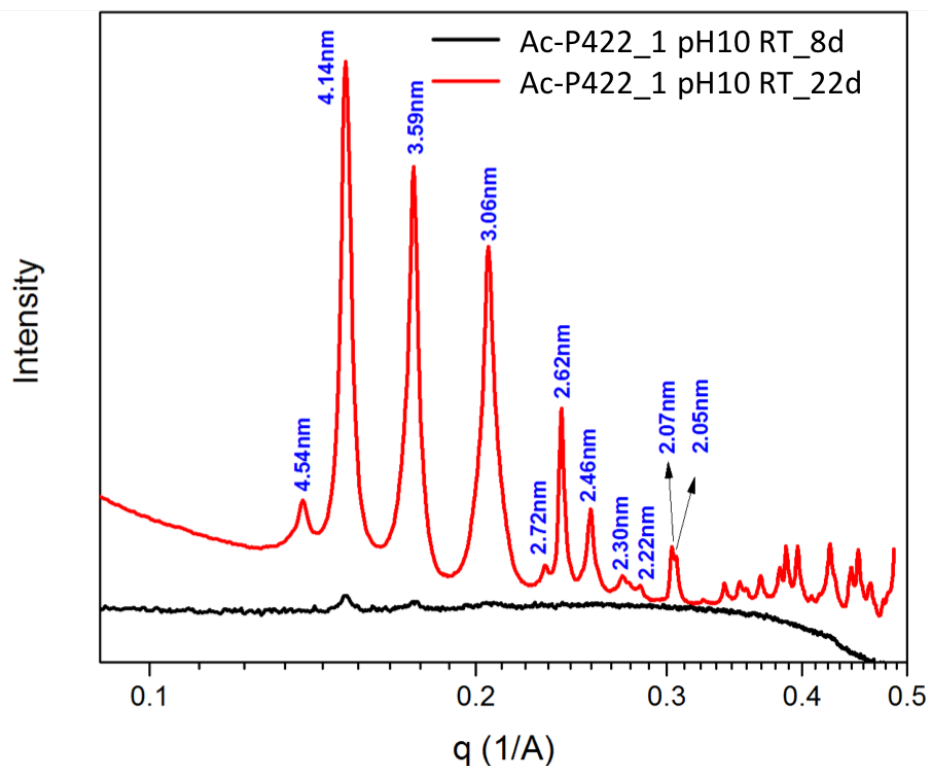


Figure 2.7 SAXS result measured from Ac-P422_1 peptide assembly solution at pH 10 with concentration of 1 mM and different aging time. The black plot is the sample solution aged for 8 days, no distinctive peaks. The red plot is the sample solution aged for 22 days; the distinctive peaks indicate the existence of ordered lattice structures.

As described earlier, the tetrameric coiled-coil bundle is mainly stabilized by the hydrophobic core while the hierarchical lattice assemblies are stabilized by the inter-bundle interactions through positioning of select amino acid residues at the exterior positions. This peptide sequence has 13 ionizable residues, and control of the charged states of these residues can be mediated by solution pH. This design affords control of the kinetics of the inter-bundle assembly process by tuning the inter-bundle interaction from repulsive to attractive (and more finely tuned to yield assembly or

aggregation) all while leaving the basic homotetrameric building block intact. Therefore, the observed assembly behaviour can be rationalized by the estimated charge per bundle at different pH values. The charge state is calculated from a web-calculator <http://www.bachem.com/service-support/peptide-calculator/>, based on individual amino acid side chain pKa values.⁶⁹ The approximate net charge of peptide at different pH values was obtained from the estimated net charge Z vs. pH titration curve, given as following:

$$Z = \sum_i N_i \frac{10^{pKa_i}}{10^{pH} + 10^{pKa_i}} - \sum_j N_j \frac{10^{pH}}{10^{pH} + 10^{pKa_j}}$$

In the algorithm, Z is the net charge and N is the number of amino acids. The first sum (i-index) is over positively charged groups: the N-terminus and the side-chains of arginine (pKa 12.48), lysine (pKa 10.53), and histidine (pKa 6.00). The second sum (j-index) is over negatively charged groups: the C-terminus and the side-chains of aspartic acid (pKa 3.65), glutamic acid (pKa 4.25). Amino acid residue pKa values are taken from Lehninger Principles of Biochemistry.⁶⁹ The estimated net charge of each peptide bundles at different pH values are listed in **Table 2.2**.

pH values	Calculated net charge of each peptide bundle (approximate values)
4.5	+12
7	+1
8	0
10	-2

Table 2.2 Estimated net charge of each Ac-P422_1 peptide bundle at different pH values.

At pH 4.5, each peptide carries a positive net charge of approximately $Z = +3$ with the tetrameric bundle having a net charge of approximately $Z = +12$. This strong electrostatic repulsive interaction disrupts inter-bundle assembly and precludes the formation of regular nanostructure. Importantly, the coiled-coil design is stable enough that bundles still formed at this pH (**Figure 2.4**) despite not undergoing further, hierarchical assembly. At pH 7 and pH 8, each bundle is expected to carry either a slightly positive charge (approximately $Z = +1$ at pH 7) or to be neutral ($Z = 0$ at pH 8). Due to the relatively small effective net charge, the peptides aggregated most rapidly in pH 7 and pH 8 buffer. At pH 10, each bundle has $Z = -2$, which destabilized the inter-bundle assembly to some extent relative to pH 7 or pH 8. At pH 10, inter-bundle assemblies could still be achieved, but the assembly process was significantly hindered, as supported by **Figure 2.7**.

2.4.1 Kinetic Trap at pH 8 and pH 7 of Room Temperature

As mentioned above, shown by **Figure 2.5**, Ac-P422_1 peptide room temperature (RT) assembled structures at pH 8 and pH 7, shown at different assembly time points, exhibited a morphology transition from disordered aggregates of coiled-

coil bundles to ordered platelets upon aging. After the shortest assembly period (2 days), disordered aggregates were primarily observed without well-defined structures at both pH 8 and pH 7, as shown by **Figures 2.5A** and **2.5D**. After 1 week of aging, there were ordered platelets growing from the disordered background, as shown by **Figure 2.5B** and **2.5E**. The platelet growth was quite slow; 8 weeks of aging at room temperature is required for the amorphous aggregates of bundles to transform into plates (**Figure 2.5C** and **2.5F**). The high magnification TEM images (**Figure 2.6**) confirmed the identical four-fold symmetry lattices of these platelets under different assembly conditions. This time-dependent morphology transition from disordered aggregates of bundles to the final ordered lattices shows that these disordered aggregates exist as a metastable kinetic product likely stabilized by localized inter-bundle complementary electrostatic interactions and hydrogen bonding. Our designed peptide bundle is primarily held together by the hydrophobic core. Therefore, there will be an immediate process through which bundle formation is driven by the hydrophobic interactions and a subsequent, slower kinetic process through which inter-bundle organization takes place through the inter-bundle interactions. A combination of these interactions created the disordered kinetic trap between initial and final assembly states.

2.4.2 Accelerated Lattice Formation by Thermal Annealing at pH 8 and pH 7

The disordered aggregation of the coiled coil bundles at earlier time points is reminiscent of disordered assemblies formed by many natural proteins involved in protein aggregation and fibril formation diseases. For example, unfolded soluble tau protein forms a disordered aggregate as a nucleus with an increase of β -sheet content, and then further assembles into paired helical filaments.⁷⁰ Other proteins can form

native-like states, but can still be amyloidogenic and cause fibrillation.^{71,72} However, these natural proteins require a disordered intermediate state prior to fibril formation. Our designed peptide lattice structures do not seem to populate such intermediate states if the assembly process proceeds along different assembly pathways. For example, elevated temperatures ($T = 50\text{ }^{\circ}\text{C}$ or $40\text{ }^{\circ}\text{C}$) were used to evaluate the effects of assembly pathway. Assemblies formed at $50\text{ }^{\circ}\text{C}$ in pH 8 and pH 7 are shown in **Figure 2.8A** and **2.8B**, respectively. Assemblies formed at $40\text{ }^{\circ}\text{C}$ in pH 8 and pH 7 are shown in **Figure 2.9A** and **2.9B**, respectively.

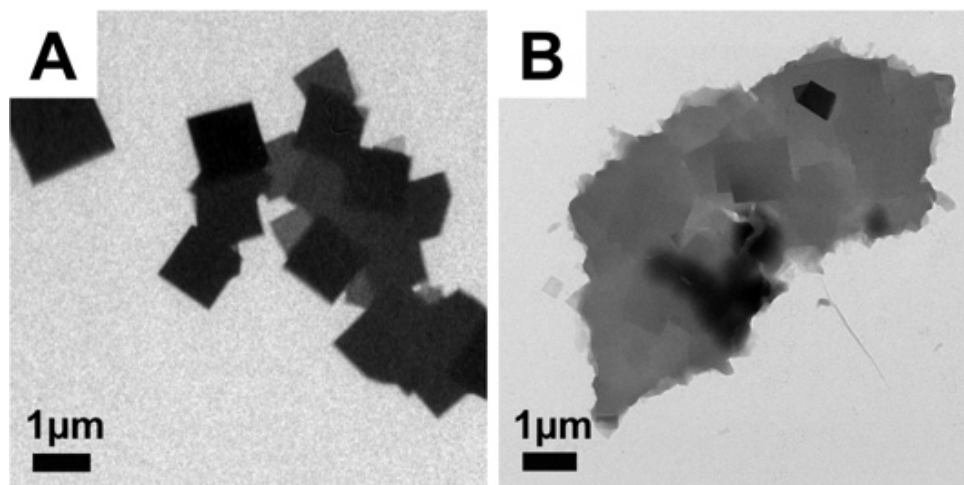


Figure 2.8 TEM images of Ac-P422_1 peptide assembled at 50°C with concentration of 0.1 mM and observed after incubation for 24 hours. **A:** pH8 after 24 hours. **B:** pH7 after 24 hours. Assembly of mature plates several micrometres in size was observed for both conditions. Images were taken without staining.

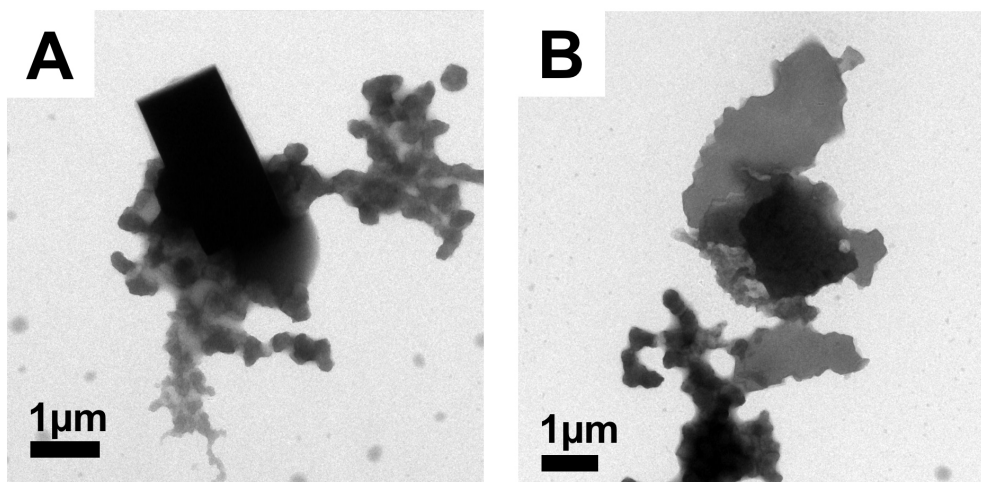


Figure 2.9 TEM images of Ac-P422_1 peptide assembled at 40°C with concentration of 0.1 mM. **A:** Peptides assembled at 40°C pH8 for 24 hours. **B:** Peptides assembled at 40°C pH7 for 24 hours. Compared to the assemblies formed at 50°C, irregular aggregates are observed around the peptide plates.

In **Figure 2.8A** and **2.8B**, mature plates (those having several microns in lateral dimension) are observed after assembly at 50 °C in both pH 8 and pH 7 within 24 hours, which is much faster when compared with RT conditions (assembly time is 1 week shown by **Figure 2.5B** and **2.5E**). The plates can grow even larger after being incubated for longer periods up to two days (data not shown, seen in supplementary information of ref ⁷³), and remain stable when the solution temperature is changed to RT (data not shown, seen in supplementary information of ref ⁷³) showing the stability of the assembled system. At relatively lower temperature of 40°C, after 24 hours, some extent of irregular aggregates still formed among regular plates, shown by **2.9A** and **2.9B**. The secondary structure information at elevated temperature is confirmed by circular dichroism spectra (**Figure 2.10**). Peptide solution was first denatured in an incubator at 95 °C, while CD chamber was pre-heated to 50 °C. Peptide solution was

then moved from incubator directly to CD chamber with measurements started immediately with fast scanning rate 50nm/min. The spectrum at 50°C confirmed an α -helical conformation. The ratio of $[\theta]_{222\text{nm}}/[\theta]_{208\text{nm}}$ at time 0 is 1.00 and 0.98, at pH 8 and pH 7, respectively. This value is close to 1, which is consistent with a coiled-coil helical structure.^{67,68} The temperature-dependence of $[\theta]_{222\text{nm}}$ (**Figure 2.11**) indicated an approximate melting temperature of $\sim 60^\circ\text{C}$.

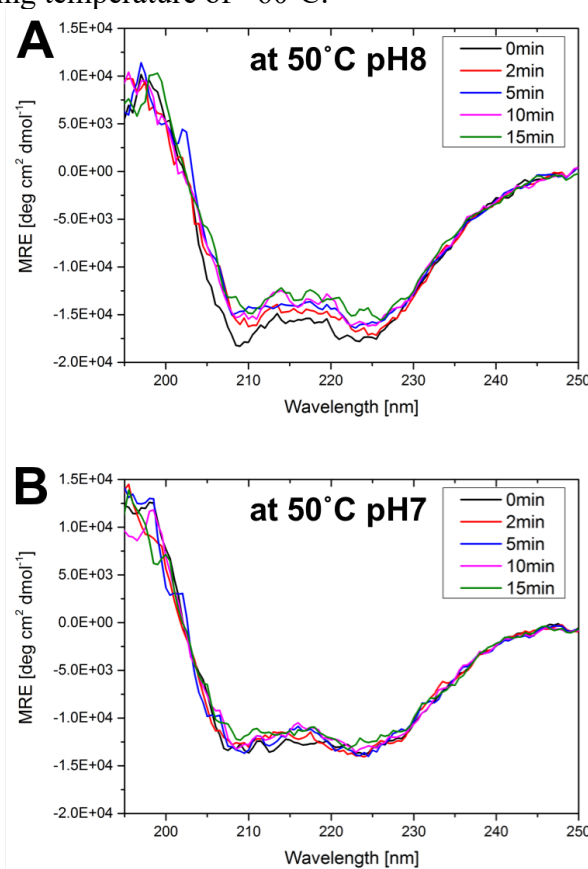


Figure 2.10 Circular dichroism spectroscopy data for Ac-P422_1 peptide sample quenched to 50 °C. **A:** 0.1mM peptide at 50 °C pH8, CD spectra measured as peptide solution quenched from 95 °C to 50 °C. The ratio of $[\theta]_{222\text{nm}}/[\theta]_{208\text{nm}}$ at time 0 is 1.00, indicating the coiled-coil formation. The gradual loss of signal is because of larger assemblies precipitating from of solution. **B:** 0.1mM peptide at 50 °C pH7, CD spectra were measured as peptide solution quenched from 95 °C to 50 °C. The ratio of $[\theta]_{222\text{nm}}/[\theta]_{208\text{nm}}$ at time 0 is 0.98, indicating the coiled-coil formation.

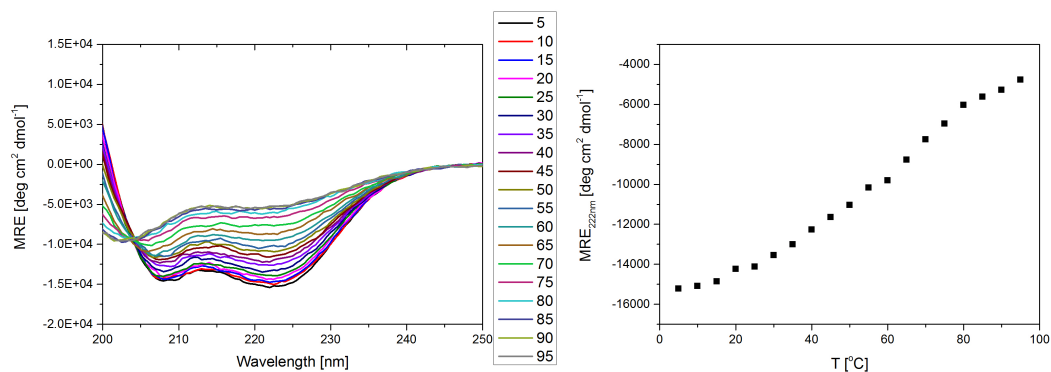


Figure 2.11 Temperature-dependent circular dichroism spectroscopy data for Ac-P422_1 peptide. 0.1mM peptide in 10mM pH7 phosphate buffer was measured upon heating. Left: wavelength scan at different temperatures on heating. Right: MRE at 222nm with increasing temperature, showing the melting temperature of approximately 60°C.

At the same pH conditions (pH = 8 or 7), elevated assembly temperature drives the peptide assembly toward mature plates relative to the smaller plate assemblies observed at lower temperature and much longer time of assembly. The temperature did not alter the stabilized coiled-coil bundles, which are maintained and act as the basic building blocks under all temperatures examined (T = room temperature, 40°C or 50°C). We propose that the extra energy provided by the higher assembly temperature conditions primarily affects inter-bundle interactions and helps to overcome kinetic traps formed at room temperature, allowing organization into the desired two-dimensional platelet nanostructure. At the lower temperature of 40°C, irregular aggregates remain among regular plates, while at the higher temperature of 50°C, only regular, two-dimensional plates were observed (**Figure 2.8A** and **2.8B**), further supporting the above proposed mechanism that an increase in thermal energy overcomes kinetically trapped disordered aggregates and allows more rapid reorganization into regular lattices. This temperature-controlled pathway is unlike

other peptide-based assembly kinetic studies, in which inter-monomer interactions are either screened or unscreened to drive the self-assembly process, and in general yielding only two states of the system, completely disassembled or assembled.^{74,75} In some cases, hierarchical assemblies within an almost completely assembled structure can be tuned slightly by adjusting interactions within the structure. For example, self-assembled nanofibers/ribbons with different widths or different extent of twist can be formed.^{4,58,76–78} In some cases, alterations in crystallization rate can be used to create different-sized assembled structures.⁶⁰ To the best of our knowledge, there are no reports of the intermediate disordered state in peptide assembly as observed here. The uniqueness lies in the ability to maintain the first-stage assembled structure, the fundamental coiled-coil bundles, under various solution conditions, a capability afforded by robust computational design. Subsequent control of inter-bundle interactions allows the capture of a disordered aggregated state or a higher-order hierarchical assembled state depending on the pathway of assembly.

In the formation of the highly ordered assemblies reported here, the possibility of reaching the final assembly state without going through the disordered intermediates can be achieved if the process occurs within a proper assembly window,^{29,79} which in our case is suggested to be near 50 °C as this temperature provided the most regularly structured inter-bundle assembly. In order to explore this possibility, bundle assembly at multiple time points at 50 °C was characterized. TEM observation was performed at short time intervals from very early bundle assembly, after 15 minutes and onward, in order to directly observe intermediate structures during the peptide and bundle assembly process. **Figure 2.12** shows the peptides assembled at 50 °C, at pH 8 and pH 7, respectively. Observations at 15 min, 30 min,

and 6 hours clearly show highly ordered structures early in the assembly process, and a complete absence of disordered aggregates; high magnification images (**Figure 2.13**) confirm the resultant lattices all display the same four-fold symmetry.

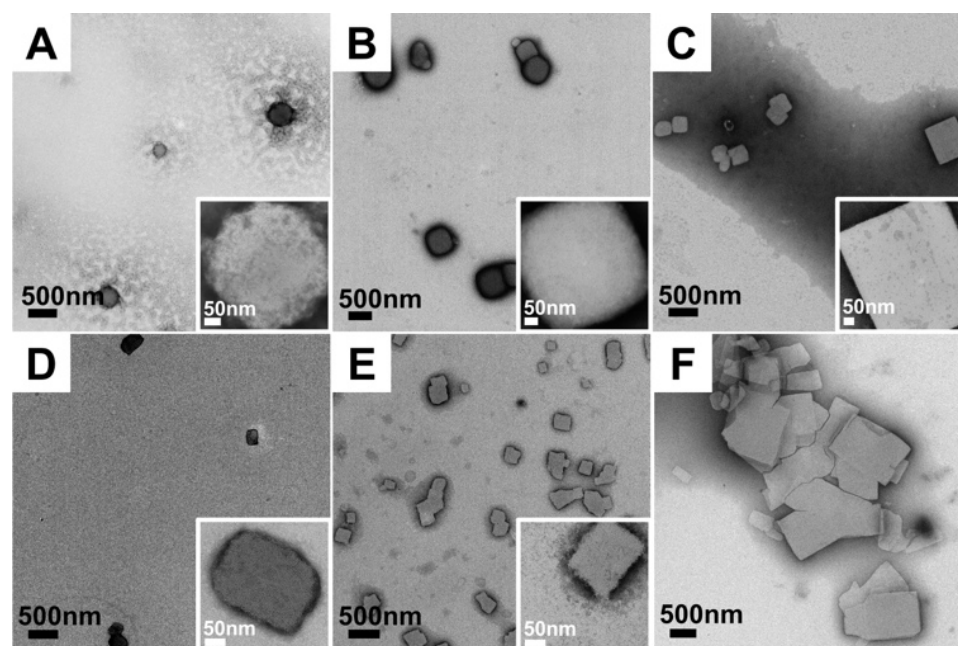


Figure 2.12 TEM images of Ac-P422_1 peptide assembled at 50°C with concentration of 0.1 mM and observed at different time points. Insets are higher magnification images of individual peptide plates present at each time point. **A-C**: Peptides assembled at 50°C, pH8 for 15 min, 30 min and 6 hours, respectively. **D-F**: Peptides assembled at 50°C pH7 for 15 min, 30 min and 6 hours, respectively. All the images were observed with 2 wt% phosphotungstic acid negative staining to enhance the contrast.

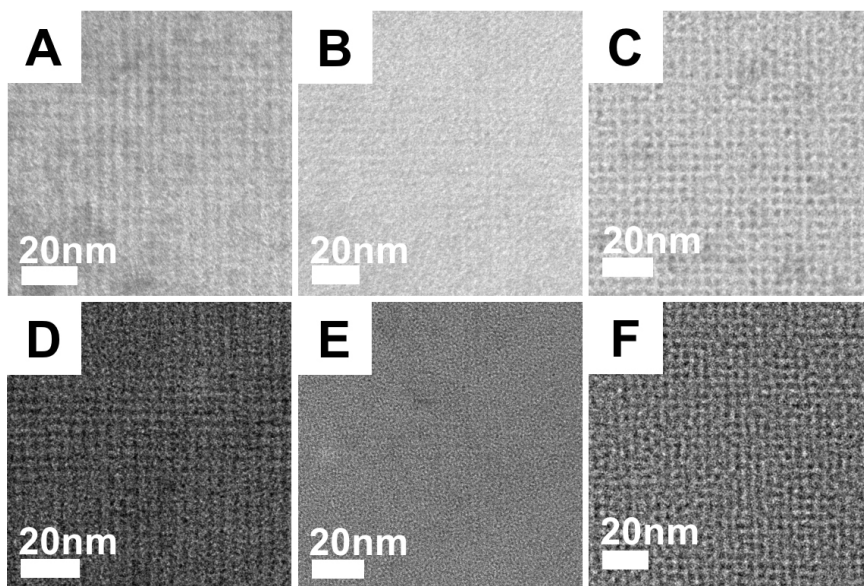


Figure 2.13 TEM high magnification images of Ac-P422_1 peptide assembled at 50°C and observed at different time point show the symmetry of lattices is the same. Images were taken with 2% wt. phosphotungstic acid negative staining to enhance the contrast. Scale bars are all in 20nm. **A-C**: Peptides assembled at 50°C pH8 for 15 min, 30 min and 6 hours, respectively. **D-F**: Peptides assembled at 50°C pH7 for 15 min, 30 min and 6 hours, respectively.

The representative TEM data in **Figure 2.12** shows that higher temperature assembly at pH 8 or pH 7 seems to prevent the formation of amorphous, disordered bundle aggregates at any time points. Small platelets around 300-500 nm in width formed rapidly within 15 min assembly time, as shown in **Figure 2.12A** and **2.12D**. Then, with longer assembly times, an increased number of plates of larger size were formed. Large fused plates can be observed at pH 7, as shown in **Figure 2.12B-C** and **2.12E-F**. The α -helix and coiled-coil bundle character of the peptide at 50°C was confirmed by the CD spectra measured of solution upon quenching from 95°C to 50°C (**Figure 2.10**). The initial measured $[\theta]_{222\text{nm}}/[\theta]_{208\text{nm}}$ ratios at time 0, at pH 8 and

pH 7 are 1.00 and 0.98, respectively, consistent with the immediate formation of the stabilized coiled-coil structure once the solution was cooled. Therefore, at earlier time points most of the coiled-coil bundles remained dispersed in solution and did not yet form visible aggregates as indicated by the clear background in **Figure 2.12A** and **2.12D**. The bundles that did undergo inter-bundle assembly after only 15 minutes seem to directly assemble into the two-dimensional lattice structures as indicated by the observed small platelets. This early assembly time point result suggests that if enough energy is provided, intermediate amorphous aggregate kinetic traps can be avoided.

With additional time, these small plates then served as seeds for continued bundle assembly resulting in plate growth in addition to the formation of new plates; more and larger plates formed at the later time points. As shown by the inset images of **Figure 2.12**, the morphology of assembled plates also changed from structures with slightly fuzzy, ill-defined edges to plates with well-defined, sharp edges as the assembly proceeded. These plates formed at elevated temperature can grow up to approximately 5 μ m in size after 48 hours (data not shown, seen in supplementary information of ref ⁷³). In comparison, at room temperature (**Figures 2.5C** and **2.5F**) plates did not grow significantly after 1 week of aging and remained smaller in size (several hundreds of nanometers). These observations are consistent with the temperature dependence of nucleation and growth mechanisms;⁸⁰ the increased number of nuclei initially formed at room temperature limited the ultimate size of the plates, while at elevated temperature fewer nuclei formed in the presence of plentiful unassembled bundles, providing for a larger size of the final plates after growth with slow incorporation of additional peptide bundles into the assembly plates.

Interesting and substantial morphology differences can be observed when comparing plates formed at room temperature and 50°C; differences in morphology are also apparent when comparing samples grown at pH 8 (**Figure 2.12A-C**) to those grown at pH 7 (**Figure 2.12D-F**). At early assembly times many regular plates are observed for both pH 7 and pH 8, as shown in **Figure 2.12A** and **2.12D**. However, at later times, the plates formed at pH 7 generally have a less regular shape compared with those at pH 8. This can be appreciated by comparison of **Figure 2.12B-C** and **2.12E-F**. This morphology difference, regular square plates for pH 8 vs complex two-dimensional plate-like structures at pH 7, can be explained through a mechanism in which smaller plates fuse together to form larger plate-like structures and final, irregular, compound plates at pH7. This mechanism did not happen at pH 8; even in later stages of assembly at pH 8 (**Figure 2.12C**), regular structures with sharp edges and angles are clearly visible. To better understand the difference in growth mechanism between pH8 and pH7, atomic force microscopy (AFM) was used to observe plate surface and thickness information for the mature plates, **Figure 2.14**.

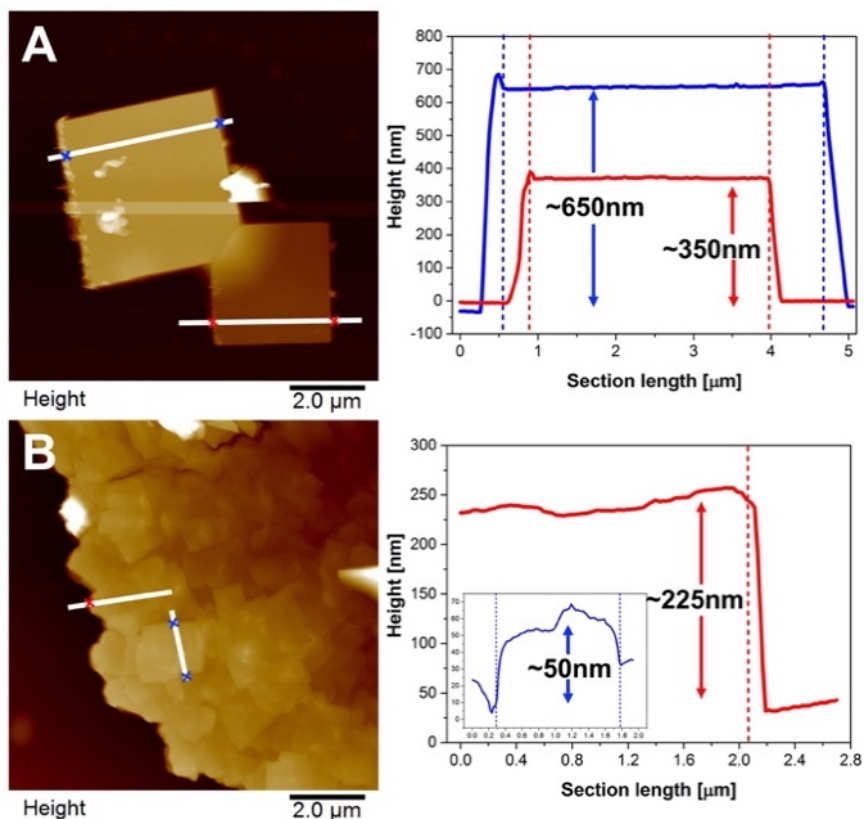


Figure 2.14 Atomic force microscopy images of Ac-P422_1 peptides assembled at 50°C. The white lines in the AFM images indicate the section height analysis trace. The positions of coloured cross markers are indicated by the dash lines in the height plots at right with corresponding colours in the height plots on the left. **A:** 50°C pH 8 for 48 hours. **B:** 50°C pH 7 for 48 hours.

The morphologies revealed by AFM in **Figure 2.14** are consistent with the TEM results. The section height analysis shows that the measured plates formed at pH 8 have approximate thickness of 350 nm and 650 nm respectively. There is a large difference in thickness between the two plates. However, within an individual plate the height remains nearly unchanged laterally across the assembled structure indicating the plate is a single, uniform structure. In contrast, the morphology at pH7

clearly shows a collection of smaller plates that have fused together to form the larger, compound structure. The measured, local thickness of a compound plate formed at pH 7 is approximately 225 nm, much thinner than the plates observed at pH 8. Also, within a mature pH7 plate there are significant thickness differences as one probes the surface moving from one smaller constituent plate to the next, clearly indicating that the mature plate consists of many smaller plates.

More morphology information of the large fused plates formed at pH 7 was revealed with detailed high magnification images taken at the boundaries between constituent, smaller plates, as shown in **Figure 2.15**.

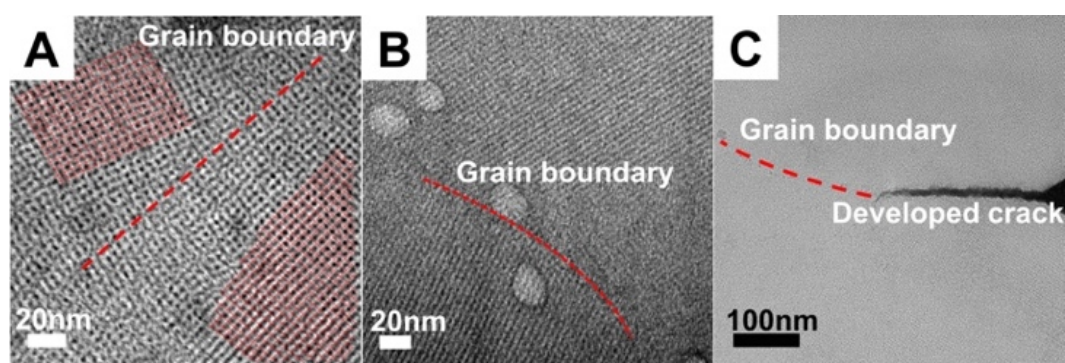


Figure 2.15 TEM images of Ac-P422_1 peptides assembled at 50°C pH 7 at different time points showing the defects in assembly structures. Images were taken with 2% wt. phosphotungstic acid negative staining. **A**: High magnification image of 50°C pH 7 assemblies to show grain boundary defect highlighted by red dash line. Two sets of lattices with different orientations are highlighted with red meshes. **B**: High magnification image of peptides assembled at 50°C pH 7 for 48 hours to show grain boundary highlighted by red dash line. **C**: High magnification of peptides assembled at 50°C pH 7 for 6 hours. The red dash line is indicating the grain boundary. There is developed crack following the grain boundary. The plates usually will crack upon drying after casting film on TEM grids.

The images in **Figure 2.15** were taken from the mature plates formed at pH 7 (with at least 6 hours of assembly time), and clearly show grain boundary-like structures (red dash line marked in **Figure 2.15**). These grain boundaries are only observed for the later-stage plates formed at pH 7. They also seem to be the weak part of plates; the grain boundaries sometimes are observed to develop into cracks (**Figure 2.15C**). The results support the hypothesis that thinner plates formed at pH 7 grow together to yield irregularly shaped, compound plates, consequently forming grain boundaries as observed by TEM. The reason for the formation of the fused plates and grain-boundaries at pH 7, and why the same fusing process did not happen at pH 8, can be explained by differences in assembly growth mechanisms at different pH values. The peptides assemble most ideally when the pH is near the estimated pI, pH 8. At the pI, the peptide bundles will quickly assemble laterally into the well-ordered nanostructures and two-dimensional plate morphology. However, the plate growth is not exclusively in two-dimensional, but with growth in thickness in the vertical direction as well. At pH8, when a new, additional layer nucleates, the lateral growth of a new assembly layer is immediate and commensurate with adjacent layers. This growth mechanism explains why there are plates with uniform thickness across their entire surface as opposed to plates with clear terraces due to unequal growth of adjacent layers.

Li *et al.* studied the attachment of molecular clusters and nanoparticles that happened during the crystal growth process of iron oxyhydroxide. They found that clusters or nanoparticles reoriented themselves until properly aligned to incorporate into the crystal. However, they also observed that grain-boundaries can still exist.⁸¹ This cluster/particle attachment crystal growth mechanism seems to be a good

analogue to our peptide plate growth process. The plates at pH 8 have a more developed vertical thickness. Therefore, it would require more perfect orientation for neighboring plates to reach the proper alignment position for fusion. This, in turn, makes it difficult/impossible for the fusion of separate plates. In contrast, at pH 7, although bundle assembly conditions are still good (as mentioned above, each bundle carries a slightly positive net charge $Z = +1$), the plates formed are significantly thinner. The thinner and more uniform thickness apparently provides for less of a mismatch in neighboring plate thickness and makes it easier to fuse at earlier assembly stages resulting in large, compound plates at later assembly stages. Even with the subtle pH change (from pH 8 to pH 7), significant plate morphology differences are observed. Therefore, with the same basic homotetrameric peptide building block, one can use pH to fine tune the inter-bundle interactions to control the growth of the desired nanostructures.

2.4.3 N-terminus Charge Effect on Assembly Kinetic

For the N-terminus un-acetylated variant, H-P422_1, buffer system with pH values of 4.5, 7 and 10 were used to investigate the pH-dependent assembly behavior. When assembled at pH 4.5, the peptide coiled-coil bundles remained soluble in solution (peptide concentration from 0.1 mM to 1 mM), without any formation of aggregates or regular two-dimensional nanostructures (data not shown). At pH 7, peptide bundles aggregated rapidly and formed visible precipitates in solution within the first several hours of solution assembly process, even at concentrations as low as 0.1 mM (details will be discussed *vide infra*). At pH 10, in contrast, even at high concentration (1 mM), no solid precipitates were observed for solution; whereas, only a slightly denser, colloidal solution-like layer was formed in the bottom. And only at

high concentration (1Mm), after long-term aging (>2 weeks), distinctive SAXS peaks can be observed from solution SAXS measurement, as shown in **Figure 2.16A**. After being aged for 2 months, the TEM images show the existence of two-dimensional assembly structures, as well as the underlying ordered lattices structures, as shown in **Figure 2.16B**. This is indicating the slow assembly kinetics at pH 10 condition; and long-term aging is required for the formation of ordered lattice structures.

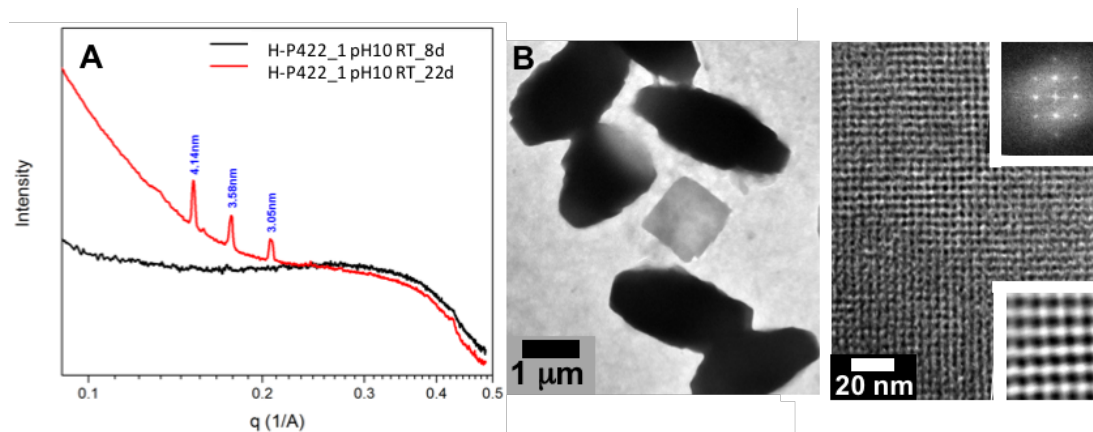


Figure 2.16 **A:** SAXS result measured from H-P422_1 peptide assembly solution at pH 10 with concentration of 1 mM and different aging time. The black plot is the sample solution aged for 8 days, no distinctive peaks. The red plot is the sample solution aged for 22 days; the distinctive peaks indicate the existence of ordered lattice structures. **B:** TEM image of H-P422_1 peptide assembly solution at pH 10 with concentration of 1 mM aged for 2 months. Left is the low magnification image showing the two-dimensional assembly structures. Right is the high magnification image showing the lattice structure.

The H-P422_1 shows the quite similar assembly kinetic behavior as the acetylated Ac-P422_1 under each pH condition. However, the un-capped N-terminus shifted the pI of peptide from around 8.2 (Ac-P422_1) to around 9.8 (H-P422_1). The

estimated net charge of each H-P422_1 peptide bundle at different pH values can be calculated use the same method in described above; the result is shown in **Table 2.3**.

pH values	Calculated net charge of each peptide bundle (approximate values)
4.5	+14
7	+5
10	-1

Table 2.3 Estimated net charge of each H-P422_1 peptide bundle at different pH values.

If considering the above-mentioned pI-dependent rule: peptides assemble faster in the pH condition near the pI, whereas slower when away from the pI, the H-P422_1 should assembly most rapidly at pH 10, instead of pH 7. However, the experimental observation suggested the different result. It seems that the extra ionizable group – free amine at N-terminus does not have significant effect on the assembly kinetic. This can be explained that during the assembly process of bundles into lattices, the inter-bundle contact occurs mostly along the side of the bundles. Therefore, the interactions located along the side of the bundles will play the key part in driving the inter-bundle assembly process, also the controlling of the assembly kinetics. The ionizable free amine groups of H-P422_1 are located at the N-terminus, which has the less important role among the interactions that determine the assembly process.

As mentioned above, H-P422_1 assembles rapidly at pH 7 forming visible precipitates; certain thermal annealing method also can be applied to control this fast-kinetic process. **Figure 2.17** is showing H-P422_1 peptide assembly result obtained

from the room temperature and elevated temperature conditions. It can be observed that H-P422_1 peptide mainly formed appeared disordered agglomerations at room temperature; however, these appeared disordered structures did not transform into regular platelets even after 30 days of aging (**Figure 2.17A**). Once the elevated solution assembly temperature was used (for example 30°C and 50°C, as shown by **Figure 2.17B** and **2.17C**), the two-dimensional plate-like structures formed quickly within 24 hours. More interestingly, the SAXS results (**Figure 2.17D**) obtained from either room temperature long-term aged samples, or elevated temperature short-term assembled samples exhibited the distinctive scattering peaks located in the same scattering angles. This is indicating the existence of ordered lattice structures for all of the samples, even for the sample appeared as disordered under TEM observation (**Figure 2.17A**). Therefore, those appeared disordered agglomerations should be the aggregation of lattice nuclei. The nucleation process of bundles into lattices is a relatively fast kinetic process for H-P422_1 at pH 7 room temperature, creating the aggregation of nuclei. According to classic nucleation theory, elevated temperature can slow down the nucleation process, but accelerate the growth process, to create larger crystals. This is the case for H-P422_1 at pH 7 as well. At elevated temperature, because of fewer nuclei formed, aggregation can be eliminated, while the growth of large, regular lattice plates can be promoted.

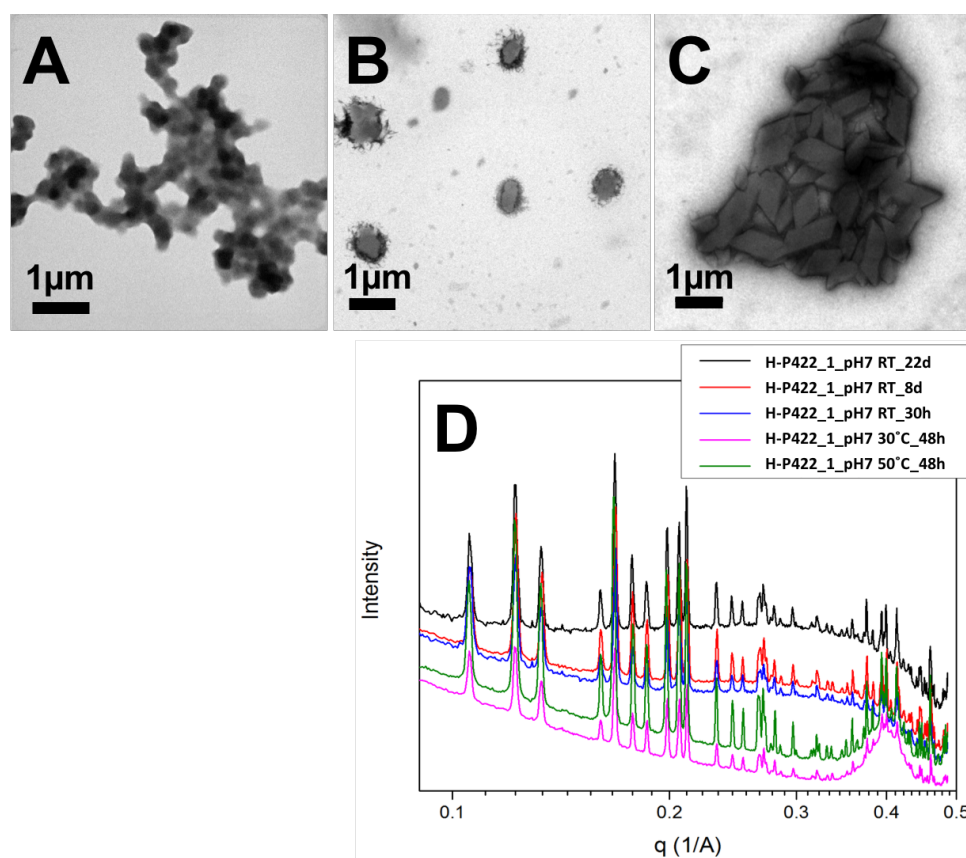


Figure 2.17 **A:** TEM image of H-P422_1 peptide assembled at room temperature with concentration of 0.1 mM pH 7 and observed after incubation for 30 days. **B:** TEM image of H-P422_1 peptide assembled at 30°C with concentration of 0.1 mM pH 7 and observed after incubation for 24 hours. **C:** TEM image of H-P422_1 peptide assembled at 50°C with concentration of 0.1 mM pH 7 and observed after incubation for 24 hours. **D:** SAXS result measured from H-P422_1 peptide assembly solution at pH 7 with concentration of 1 mM treated with different temperature and different aging time; the distinctive peaks indicate the existence of ordered lattice structures.

2.5 Irregularly Assembled P422_2 Sequence

Ac-P422_2 or H-P422_2 did not show evidence for the existence of ordered lattice structure by TEM or SAXS. The reason for the failure of P422_2 sequence will be discussed based on the solved crystal structure of H_P422_1.

Through the method of single crystal diffraction, Dr. Huixi Violet Zhang and Dr. Matthew Eilbling have solved the crystal structure of H-P422_1, which is important in the determination of the key interactions driving the assembly process. As shown in **Figure 2.18**, each asymmetric unit contains three helical bundles. And instead of the originally designed parallel packing, bundles are packed with a twisted angle in respect to each other. The reason for the discrepancy between designing and actual result still remains for the further investigation. The key information we can obtain here is the interactions stabilize the bundle-bundle interface, which will be helpful in explaining the failure of P422_2 sequence. Along the interfaces of H-P422_1 crystal, there are two pairs of hydrophobic interaction between Met17-Trp10-Met21 (black dashed box in **Figure 2.18**), and four pairs of hydrogen bonding interaction between Lys13-Gln16 (blue, red and purple dashed boxes in **Figure 2.18**). Therefore, from the solved crystal structure of H-P422_1, the hydrogen bonding between Lys13-Gln16 plays an important role in the interactions that stabilize the bundle-bundle interface. As comparison, P422_2 is very similar to P422_1 from the sequence designing aspect. Both molecules are designed to form the same P422 symmetry lattice with very close lattice parameter. The only difference is the in position 16 of the sequence: for P422_1, it is Gln in position 16, whereas, for P422_2, it is Leu. The side chain of Leu is hydrophobic and cannot form hydrogen bond with other side chains. Therefore, P422_2 peptide bundles lose the important hydrogen bonding interaction, which possibly causes the failure of P422_2 peptide lattice assembly.

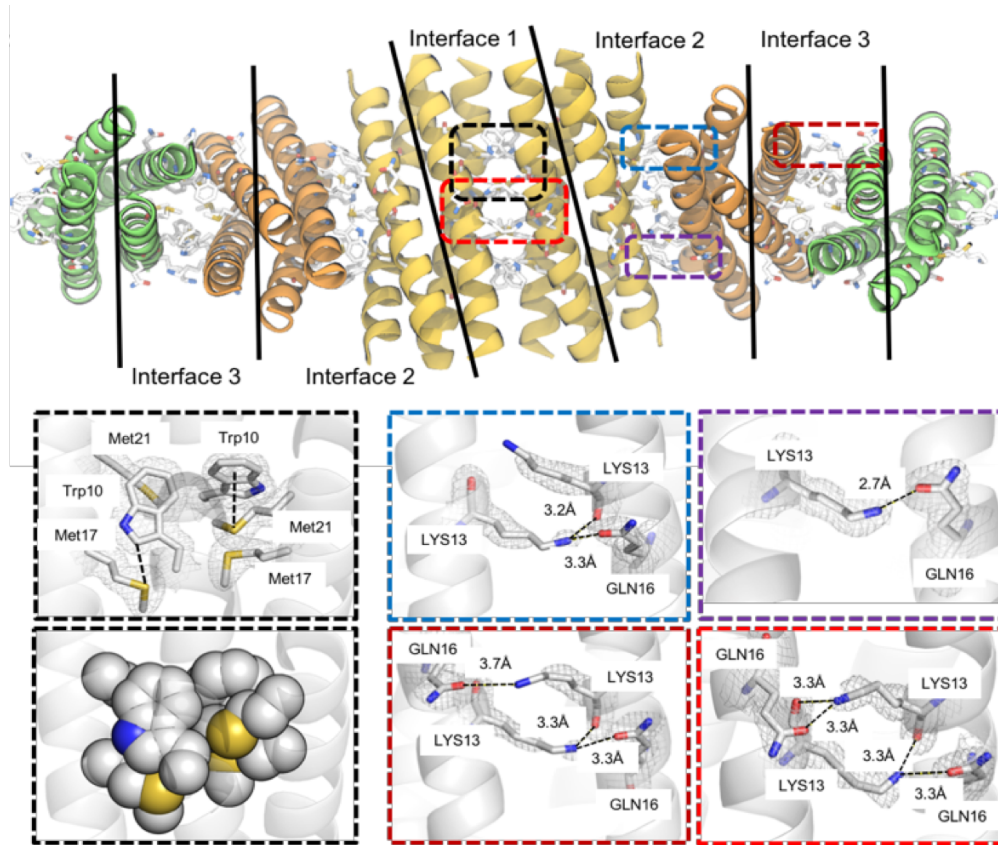


Figure 2.18 Analysis of the crystal structure of H-P422_1. **Top:** Two asymmetric units each containing three helical bundles, presented by ribbon drawing. Within each bundle-bundle interface, sidechains of critical stabilizing interactions are rendered as sticks and colored by atom type: C (white), N (blue), O (red) and S (yellow). Colored dash boxes correspond to the enlarged and reoriented regions of the interfaces on the bottoms. **Bottom left:** Two example Met-Trp-Met motifs at the bundle-bundle interface are shown in sticks and electron density map. Dashed black lines between Trp10 and Met21, and Trp10 and Met17 label two consistent distances across twelve motifs in three bundle-bundle interfaces. The packing of the motifs (spheres) on the top is shown in the bottom box. **Bottom right:** The hydrogen bonds between Lys13 and Gln16 are shown (black dashed lines) with distance between donors and acceptors labeled. Outline colors correspond to the boxes on the twisted ribbon structure.

2.6 Conclusion

In this **Chapter 2**, we investigated the assembly behavior of two designed peptide sequences P422_1 and P422_2 and their N-terminus acetylated and un-acetylated variants, totally four molecules. For P422_1 peptide, we have demonstrated that our synthetic peptide-based assembly system can tolerate various solution conditions and still assemble into a desired two-dimensional plate nanostructure with embedded lattice symmetry. Due to the design of the robust hydrophobic interior core, the stable, initial tetrameric bundle can form under different solution pH and temperatures. Given the charged state of the bundle exterior amino acids, variations in pH lead the bundles to repel each other or attract and aggregate, either slowly or rapidly. At room temperature when peptides are the least charged at pH 8 and pH 7, disordered aggregates are first formed then slowly transformed into the desired lattice structures over long periods of time (weeks). This is because the presence of disordered aggregate as kinetic traps that exist intermediately during plate formation. These aggregates are observable during slow inter-bundle assembly. At the same pH, elevating the temperature provides extra energy for bundle reorganization and a faster assembly process for peptide bundles to pack into two-dimensional lattices and to form plates, even at early assembly stages. Slight changes in solution conditions lead to significant morphological differences. At pH 8, quick plate growth leads to separate plates with intra-plate uniformity in thickness but large differences in thickness between individual plate structures. However, at pH 7, slower plate growth leads to the fusion of smaller plates with similar thickness into large, compound structures. This work clearly demonstrates the capacity to control the kinetics of the assembly process by simply changing inter-bundle interactions via temperatures and pH, while the computationally-designed tetrameric building blocks remain intact.

Expansion of these approaches will enable the construction of more complex nanostructures with simple building blocks.

REFERENCES

1. Wang, C. L.; Zhang, W. Bin; Van Horn, R. M.; Tu, Y.; Gong, X.; Cheng, S. Z. D.; Sun, Y.; Tong, M.; Seo, J.; Hsu, B. B. Y.; et al. A Porphyrin-Fullerene Dyad with a Supramolecular “Double-Cable” Structure as a Novel Electron Acceptor for Bulk Heterojunction Polymer Solar Cells. *Adv. Mater.* **2011**, *23* (26), 2951–2956.
2. Yu, X.; Yue, K.; Hsieh, I.-F.; Li, Y.; Dong, X.-H.; Liu, C.; Xin, Y.; Wang, H.-F.; Shi, A.-C.; Newkome, G. R.; et al. Giant Surfactants Provide a Versatile Platform for Sub-10-Nm Nanostructure Engineering. *Proc. Natl. Acad. Sci. U. S. A.* **2013**, *110* (25), 10078–10083.
3. Zhang, J.; Santos, P. J.; Gabrys, P. A.; Lee, S.; Liu, C.; Macfarlane, R. J. Self-Assembling Nanocomposite Tectons. *J. Am. Chem. Soc.* **2016**, *138* (50), 16228–16231.
4. Chen, C. L.; Zhang, P.; Rosi, N. L. A New Peptide-Based Method for the Design and Synthesis of Nanoparticle Superstructures: Construction of Highly Ordered Gold Nanoparticle Double Helices. *J. Am. Chem. Soc.* **2008**, *130* (41), 13555–13557.
5. Suzuki, Y.; Cardone, G.; Restrepo, D.; Zavattieri, P. D.; Baker, T. S.; Tezcan, F. A. Self-Assembly of Coherently Dynamic, Auxetic, Two-Dimensional Protein Crystals. *Nature* **2016**, *533* (7603), 369.
6. Bale, J. B.; Gonen, S.; Liu, Y.; Sheffler, W.; Ellis, D.; Thomas, C.; Cascio, D.; Yeates, T. O.; Gonen, T.; King, N. P.; et al. Accurate Design of Megadalton-Scale Two-Component Icosahedral Protein Complexes. *Science* **2016**, *353* (6297), 389–394.
7. Wang, X.; Guerin, G.; Wang, H.; Wang, Y.; Manners, I.; Winnik, M. A. Cylindrical Block Copolymer Micelles and Co-Micelles of Controlled Length and Architecture. *Science* **2007**, *317* (5838), 644–647.
8. Presa Soto, A.; Gilroy, J. B.; Winnik, M. A.; Manners, I. Pointed-Oval-Shaped Micelles from Crystalline-Coil Block Copolymers by Crystallization-Driven Living Self-Assembly. *Angew. Chemie - Int. Ed.* **2010**, *49* (44), 8220–8223.

9. Hudson, Z. M.; Boott, C. E.; Robinson, M. E.; Rupar, P. A.; Winnik, M. A.; Manners, I. Tailored Hierarchical Micelle Architectures Using Living Crystallization-Driven Self-Assembly in Two Dimensions. *Nat. Chem.* **2014**, *6* (10), 893–898.
10. Qiu, H.; Gao, Y.; Boott, C. E.; Gould, Oliver E C; Harniman, R. L.; Miles, M. J.; Webb, S. E. D.; Winnik, M. A.; Manners, I. Uniform Patchy and Hollow Rectangular Platelet Micelles from Crystallizable Polymer Blends. *Science* **2016**, *352* (6286), 697–701.
11. Zhang, H.; Dong, B.; Zhou, T.; Li, C. Directed Self-Assembly of Hetero-Nanoparticles Using Polymer Single Crystal Template. *Nanoscale* **2012**, *4* (24), 7641–7645.
12. Huang, M.; Hsu, C.; Wang, J.; Mei, S.; Dong, X.; Li, Y.; Li, M.; Liu, H.; Zhang, W.; Aida, T.; et al. Selective Assemblies of Giant Tetrahedra via Precisely Controlled Positional Interactions. *Science* **2015**, *348* (6233), 424–428.
13. Thomas, F.; Burgess, N. C.; Thomson, A. R.; Woolfson, D. N. Controlling the Assembly of Coiled-Coil Peptide Nanotubes. *Angew. Chemie - Int. Ed.* **2016**, *128* (3), 999–1003.
14. Sharma, N.; Top, A.; Kiick, K. L.; Pochan, D. J. One-Dimensional Gold Nanoparticle Arrays by Electrostatically Directed Organization Using Polypeptide Self-Assembly. *Angew. Chemie* **2009**, *121*, 7212–7216.
15. Lamm, M. S.; Sharma, N.; Rajagopal, K.; Beyer, F. L.; Schneider, J. P.; Pochan, D. J. Laterally Spaced Linear Nanoparticle Arrays Templated by Laminated β -Sheet Fibrils. *Adv. Mater.* **2008**, *20* (3), 447–451.
16. Veneziano, R.; Ratanalert, S.; Zhang, K.; Zhang, F.; Yan, H.; Chiu, W.; Bathe, M. Designer Nanoscale DNA Assemblies Programmed from the Top Down. *Science* **2016**, *352* (6293), 1534.
17. Jones, M. R.; Seeman, N. C.; Mirkin, C. A. Programmable Materials and the Nature of the DNA Bond. *Science* **2015**, *347* (6224), 840.
18. Zhang, X.; Lv, L.; Ji, L.; Guo, G.; Liu, L.; Han, D.; Wang, B.; Tu, Y.; Hu, J.; Yang, D.; et al. Self-Assembly of One-Dimensional Nanocrystal Superlattice Chains Mediated by Molecular Clusters. *J. Am. Chem. Soc.* **2016**, *138* (10), 3290–3293.

19. King, N. P.; Bale, J. B.; Sheffler, W.; McNamara, D. E.; Gonen, S.; Gonen, T.; Yeates, T. O.; Baker, D.; Methods, S. Accurate Design of Co-Assembling Multi-Component Protein Nanomaterials. *Nature* **2014**, *510* (7503), 103–108.
20. Pochan, D. J.; Chen, Z.; Cui, H.; Hales, K.; Qi, K.; Wooley, K. L. Toroidal Triblock Copolymer Assemblies. *Science* **2004**, *306*, 94–97.
21. Cui, H.; Chen, Z.; Zhong, S.; Wooley, K. L.; Pochan, D. J. Block Copolymer Assembly via Kinetic Control. *Science* **2007**, *317* (5838), 647–650.
22. Zhu, J.; Zhang, S.; Zhang, F.; Wooley, K. L.; Pochan, D. J. Hierarchical Assembly of Complex Block Copolymer Nanoparticles into Multicompartment Superstructures through Tunable Interparticle Associations. *Adv. Funct. Mater.* **2013**, *23* (14), 1767–1773.
23. Lee, S.; Leighton, C.; Bates, F. S. Sphericity and Symmetry Breaking in the Formation of Frank–Kasper Phases from One Component Materials. *Proc. Natl. Acad. Sci.* **2014**, *111* (50), 17723–17731.
24. Qiu, H.; Hudson, Z. M.; Winnik, M. A.; Manners, I. Multidimensional Hierarchical Self-Assembly of Amphiphilic Cylindrical Block Comicelles. *Science* **2015**, *347* (6228), 1329–1332.
25. Robertson, E. J.; Olivier, G. K.; Qian, M.; Proulx, C.; Zuckermann, R. N.; Richmond, G. L. Assembly and Molecular Order of Two-Dimensional Peptoid Nanosheets through the Oil–Water Interface. *Proc. Natl. Acad. Sci.* **2014**, *111* (37), 13284–13289.
26. Mannige, R. V; Haxton, T. K.; Proulx, C.; Robertson, E. J.; Battigelli, A.; Butterfoss, G. L.; Zuckermann, R. N.; Whitelam, S. Peptoid Nanosheets Exhibit a New Secondary-Structure Motif. *Nature* **2015**, *526* (7573), 415–420.
27. Knight, A. S.; Zhou, E. Y.; Francis, M. B.; Zuckermann, R. N. Sequence Programmable Peptoid Polymers for Diverse Materials Applications. *Adv. Mater.* **2015**, *27* (38), 5665–5691.
28. Jiao, F.; Chen, Y.; Jin, H.; He, P.; Chen, C.-L.; De Yoreo, J. J. Self-Repair and Patterning of 2D Membrane-Like Peptoid Materials. *Adv. Funct. Mater.* **2016**, *26* (48), 8960–8967.

29. Ma, X.; Zhang, S.; Jiao, F.; Newcomb, C. J.; Zhang, Y.; Prakash, A.; Liao, Z.; Baer, M. D.; Mundy, C. J.; Pfaendtner, J.; et al. Tuning Crystallization Pathways through Sequence Engineering of Biomimetic Polymers. *Nat. Mater.* **2017**, *16*, 767–774.
30. Boerneke, M. A.; Dibrov, S. M.; Hermann, T. Crystal-Structure-Guided Design of Self-Assembling RNA Nanotriangles. *Angew. Chemie Int. Ed.* **2016**, *55* (12), 4097–4100.
31. Loweth, C. J.; Caldwell, W. B.; Peng, X.; Alivisatos, a P.; Schultz, P. G. DNA-Based Assembly of Gold Nanocrystals. *Angew. Chemie Int. Ed.* **1999**, *38* (12), 1808–1812.
32. Suzuki, Y.; Endo, M.; Sugiyama, H. Lipid-Bilayer-Assisted Two-Dimensional Self-Assembly of DNA Origami Nanostructures. *Nat. Commun.* **2015**, *6*, 8052.
33. Yao, G.; Li, J.; Chao, J.; Pei, H.; Liu, H.; Zhao, Y.; Shi, J.; Huang, Q.; Wang, L.; Huang, W.; et al. Gold-Nanoparticle-Mediated Jigsaw-Puzzle-like Assembly of Supersized Plasmonic DNA Origami. *Angew. Chemie* **2015**, *127* (10), 3009–3012.
34. Brodin, J. D.; Auyeung, E.; Mirkin, C. A. DNA-Mediated Engineering of Multicomponent Enzyme Crystals. *Proc. Natl. Acad. Sci. U. S. A.* **2015**, *112* (15), 4564–4569.
35. Benenson, Y.; Paz-Elizur, T.; Adar, R.; Keinan, E.; Livneh, Z.; Shapiro, E. Programmable and Autonomous Computing Machine Made of Biomolecules. *Nature* **2001**, *414* (6862), 430–434.
36. Seelig, G.; Soloveichik, D.; Zhang, D. Y.; Winfree, E. Enzyme-Free Nucleic Acid Logic Circuits. *Science* **2006**, *314* (5805), 1585–1589.
37. Elbaz, J.; Lioubashevski, O.; Wang, F.; Remacle, F.; Levine, R. D.; Willner, I. DNA Computing Circuits Using Libraries of DNAzyme Subunits. *Nat. Nanotechnol.* **2010**, *5* (6), 417–422.
38. Wang, Y.; Ma, X.; Cui, G. Logical Computation Using Algorithmic Self-Assembly of DNA Sub-Tile. *J. Comput. Theor. Nanosci.* **2016**, *13* (6), 3959–3963.
39. Woolfson, D. N. The Design of Coiled-Coil Structures and Assemblies. *Adv. Protein Chem.* **2005**, *70*, 79–112.

40. Boyle, A. L.; Woolfson, D. N. Rational Design of Peptide-Based Biosupramolecular Systems. In *Supramolecular Chemistry: From Molecules to Nanomaterials*; John Wiley & Sons, Ltd: New York, 2012.
41. Kiick, K. L.; Tirrell, D. A. Protein Engineering by In Vivo Incorporation of Non-Natural Amino Acids: Control of Incorporation of Methionine Analogues by Methionyl-TRNA Synthetase. *Tetrahedron* **2000**, *56* (48), 9487–9493.
42. Radford, R. J.; Tezcan, F. A. A Superprotein Triangle Driven by Nickel(II) Coordination: Exploiting Non-Natural Metal Ligands in Protein Self-Assembly. *J. Am. Chem. Soc.* **2009**, *131* (26), 9136–9137.
43. Krueger, A. T.; Imperiali, B. Fluorescent Amino Acids: Modular Building Blocks for the Assembly of New Tools for Chemical Biology. *ChemBioChem* **2013**, *14* (7), 788–799.
44. Li, M.; Ethlers, M.; Schlesiger, S.; Zellermann, E.; Knauer, S. K.; Schmuck, C. Incorporation of a Non-Natural Arginine Analogue into a Cyclic Peptide Leads to Formation of Positively Charged Nanofibers Capable of Gene Transfection. *Angew. Chemie Int. Ed.* **2016**, *128* (2), 608–611.
45. Padilla, J. E.; Colovos, C.; Yeates, T. O. Nanohedra: Using Symmetry to Design Self Assembling Protein Cages, Layers, Crystals, and Filaments. *Proc. Natl. Acad. Sci. U. S. A.* **2001**, *98* (5), 2217–2221.
46. Yeates, T. O. Nanobiotechnology: Protein Arrays Made to Order. *Nat. Nanotechnol.* **2011**, *6* (9), 541–542.
47. Lai, Y.; Cascio, D.; Yeates, T. O. Structure of a 16-Nm Cage Designed by Using Protein Oligomers. *Science* **2012**, *336* (6085), 1129.
48. Zimenkov, Y.; Dublin, S. N.; Ni, R.; Tu, R. S.; Breedveld, V.; Apkarian, R. P.; Conticello, V. P. Rational Design of a Reversible PH-Responsive Switch for Peptide Self-Assembly. *J. Am. Chem. Soc.* **2006**, *128*, 6770–6771.
49. Sharp, T. H.; Bruning, M.; Mantell, J.; Sessions, R. B.; Thomson, A. R.; Zaccai, N. R. Cryo-Transmission Electron Microscopy Structure of a Gigadalton Peptide Fiber of de Novo Design. *Proc. Natl. Acad. Sci. U. S. A.* **2012**, *109* (33), 13266–13271.

50. Lanci, C.; MacDermaid, C.; Kang, S.; Acharya, R.; North, B.; Yang, X.; Qiu, X. J.; Degrado, W. F.; Saven, J. G. Computational Design of a Protein Crystal. *Proc. Natl. Acad. Sci. U. S. A.* **2012**, *109* (19), 7304–7309.
51. Xu, C.; Liu, R.; Mehta, A. K.; Guerrero-Ferreira, R. C.; Wright, E. R.; Dunin-Horkawicz, S.; Morris, K.; Serpell, L. C.; Zuo, X.; Wall, J. S.; et al. Rational Design of Helical Nanotubes from Self-Assembly of Coiled-Coil Lock Washers. *J. Am. Chem. Soc.* **2013**, *135* (41), 15565–15578.
52. Burgess, N. C.; Sharp, T. H.; Thomas, F.; Wood, C. W.; Thomson, A. R.; Zaccai, N.; Brady, R. L.; Serpell, L. C.; Woolfson, D. N. Modular Design of Self-Assembling Peptide-Based Nanotubes. *J. Am. Chem. Soc.* **2015**, *137* (33), 10554–10562.
53. King, N. P.; Sheffler, W.; Sawaya, M. R.; Vollmar, B. S.; Sumida, J. P.; André, I.; Gonen, T.; Yeates, T. O.; Baker, D. Computational Design of Self-Assembling Protein Nanomaterials with Atomic Level Accuracy. *Science* **2012**, *336* (6085), 1171–1174.
54. Gonen, S.; Dimairo, F.; Gonen, T.; Baker, D. Design of Ordered Two-Dimensional Arrays Mediated by Noncovalent Protein-Protein Interfaces. *Science* **2015**, *348* (6241), 1365–1368.
55. Zhong, S.; Cui, H.; Chen, Z.; Wooley, K. L.; Pochan, D. J. Helix Self-Assembly through the Coiling of Cylindrical Micelles. *Soft Matter* **2008**, *4* (1), 90–93.
56. Jonkheijm, P.; Schoot, P. van der; Schenning, A. P. H. J.; Meijer, E. W. Probing the Solvent-Assisted Nucleation Pathway in Chemical Self-Assembly. *Science* **2006**, *313* (5783), 80–83.
57. Lohr, A.; Lysetska, M.; Würthner, F. Supramolecular Stereomutation in Kinetic and Thermodynamic Self-Assembly of Helical Merocyanine Dye Nanorods. *Angew. Chemie - Int. Ed.* **2005**, *44* (32), 5071–5074.
58. Pashuck, E. T.; Stupp, S. I. Direct Observation of Morphological Transformation from Twisted Ribbons into Helical Ribbons. *J. Am. Chem. Soc.* **2010**, *132* (26), 8819–8821.
59. Zhang, S.; Greenfield, M. a; Mata, A.; Palmer, L. C.; Bitton, R.; Mantei, J. R.; Aparicio, C.; de la Cruz, M. O.; Stupp, S. I. A Self-Assembly Pathway to Aligned Monodomain Gels. *Nat. Mater.* **2010**, *9* (7), 594–601.

60. Brodin, J. D.; Carr, J. R.; Sontz, P. A.; Tezcan, F. A. Exceptionally Stable, Redox-Active Supramolecular Protein Assemblies with Emergent Properties. *Proc. Natl. Acad. Sci. U. S. A.* **2014**, *111* (8), 2897–2902.
61. Zhang, H. V.; Polzer, F.; Haider, M. J.; Tian, Y.; Villegas, J. A.; Kiick, K. L.; Pochan, D. J.; Saven, J. G. Computationally Designed Peptides for Self-Assembly of Nanostructured Lattices. *Sci. Adv.* **2016**, *2* (9), e1600307.
62. Korevaar, P. A.; Newcomb, C. J.; Meijer, E. W.; Stupp, S. I. Pathway Selection in Peptide Amphiphile Assembly. *J. Am. Chem. Soc.* **2014**, *136* (24), 8540–8543.
63. Fields, G. B.; Noble, R. L. Solid Phase Peptide Synthesis Utilizing 9-Fluorenylmethoxycarbonyl Amino Acids. *Int. J. Pept. Protein Res.* **1990**, *35* (3), 161–214.
64. Fischetti, R.; Stepanov, S.; Rosenbaum, G.; Barrea, R.; Black, E.; Gore, D.; Heurich, R.; Kondrashkina, E.; Kropf, A. J.; Wang, S.; et al. The BioCat Undulator Beamline 18ID: A Facility for Biological Non-Crystalline Diffraction and X-Ray Absorption Spectroscopy at the Advanced Photon Source. *J. Synchrotron Radiat.* **2004**, *11* (5), 399–405.
65. Petoukhov, M. V.; Franke, D.; Shkumatov, A. V.; Tria, G.; Kikhney, A. G.; Gajda, M.; Gorba, C.; Mertens, H. D. T.; Konarev, P. V.; Svergun, D. I. New Developments in the ATSAS Program Package for Small-Angle Scattering Data Analysis. *J. Appl. Crystallogr.* **2012**, *45* (2), 342–350.
66. Crick, F. H. C. The Fourier Transform of a Coiled-Coil. *Acta Crystallogr.* **1953**, *6* (8), 685–689.
67. Cooper, T. M.; Woody, R. W. The Effect of Conformation on the CD of Interacting Helices: A Theoretical Study of Tropomyosin. *Biopolymers* **1990**, *30* (7–8), 657–676.
68. Graddis, T. J.; Myszka, D. G.; Chaiken, I. M. Controlled Formation of Model Homo- and Heterodimer Coiled Coil Polypeptides. *Biochemistry* **1993**, *32* (47), 12664–12671.
69. Nelson, D. L.; Lehninger, A. L.; Cox, M. M. *Lehninger Principles of Biochemistry*, 4th editio.; W. H. Freeman: New York, NY, 2005.
70. Von Bergen, M.; Barghorn, S.; Biernat, J.; Mandelkow, E. M.; Mandelkow, E. Tau Aggregation Is Driven by a Transition from Random Coil to Beta Sheet Structure. *Biochim. Biophys. Acta - Mol. Basis Dis.* **2005**, *1739* (2), 158–166.

71. Wang, W. Protein Aggregation and Its Inhibition in Biopharmaceutics. *Int. J. Pharm.* **2005**, *289* (1–2), 1–30.
72. Chiti, F.; Dobson, C. M. Amyloid Formation by Globular Proteins under Native Conditions. *Nat. Chem. Biol.* **2009**, *5* (1), 15–22.
73. Tian, Y.; Zhang, H. V.; Kiick, K.; Saven, J. G.; Pochan, D. Transition from Disordered Aggregates to Ordered Lattices: Kinetic Control of the Assembly of a Computationally Designed Peptide. *Org. Biomol. Chem.* **2017**, *15* (29), 6109–6118.
74. Moyer, T. J.; Finbloom, J. A.; Chen, F.; Toft, D. J.; Cryns, V. L.; Stupp, S. I. PH and Amphiphilic Structure Direct Supramolecular Behavior in Biofunctional Assemblies. *J. Am. Chem. Soc.* **2014**, *136* (42), 14746–14752.
75. Chen, Y.; Gan, H. X.; Tong, Y. W. PH-Controlled Hierarchical Self-Assembly of Peptide Amphiphile. *Macromolecules* **2015**, *48* (8), 2647–2653.
76. Shao, H.; Parquette, J. R. Controllable Peptide-Dendron Self-Assembly: Interconversion of Nanotubes and Fibrillar Nanostructures. *Angew. Chemie - Int. Ed.* **2009**, *48* (14), 2525–2528.
77. Palmer, L. C.; Leung, C.-Y.; Kewalramani, S.; Kumthekar, R.; Newcomb, C. J.; Olvera De La Cruz, M.; Bedzyk, M. J.; Stupp, S. I. Long-Range Ordering of Highly Charged Self-Assembled Nanofilaments. *J. Am. Chem. Soc.* **2014**, *136* (41), 14377–14380.
78. Merg, A. D.; Boatz, J. C.; Mandal, A.; Zhao, G.; Mokashi-Punekar, S.; Liu, C.; Wang, X.; Zhang, P.; van der Wel, P. C. A.; Rosi, N. L. Peptide-Directed Assembly of Single-Helical Gold Nanoparticle Superstructures Exhibiting Intense Chiroptical Activity. *J. Am. Chem. Soc.* **2016**, *138* (41), 13655–13663.
79. Jacobs, W. M.; Frenkel, D. Self-Assembly of Structures with Addressable Complexity. *J. Am. Chem. Soc.* **2016**, *138* (8), 2457–2467.
80. Holland, V. F.; Lindenmeyer, P. H. Morphology and Crystal Growth Rate of Polyethylene Crystalline Complexes. *J. Polym. Sci.* **1962**, *57* (165), 589–608.
81. Li, D.; Nielsen, M. H.; Lee, J. R. I.; Frandsen, C.; Banfield, J. F.; De Yoreo, J. J. Direction-Specific Interactions Control Crystal Growth by Oriented Attachment. *Science* **2012**, *336* (6084), 1014–1018.

Chapter 3

NANOTUBES, PLATES, AND NEEDLES: PATHWAY-DEPENDENT SELF-ASSEMBLY PROCESS OF COMPUTATIONALLY DESIGNED PEPTIDES

3.1 Introduction

As discussed in **Chapter 1**, we take the approach of using computationally designed peptides combined with the control of the intermolecular interactions to build specific, programmable structures in a hierarchical fashion. The kinetic control of self-assembly processes with computationally-designed peptides remains largely unexplored. In this presented Ph.D. work, the computational design identified peptide molecules that can assemble into a desired coiled-coil building block and, subsequently, into desired inter-bundle nanostructures targeting desired assembled states.¹ Kinetic products from different assembly pathways are often in non-equilibrium states and their formation is sensitive to specific assembly solution conditions; this makes *a priori*, computational prediction and design of kinetically trapped products difficult. However, the manipulation of assembly pathways is productive in generating various hierarchical assembly products from a single, primary building block. In addition to earlier-mentioned synthetic polymer examples in **Chapter 1**, studies of conjugated molecules, such as π -conjugates,²⁻⁴ or polymer-peptide conjugates⁵⁻⁸ exhibit common, structural transitions when different intermolecular interactions are involved during an assembly process. For example, strong interactions such as hydrophobic interactions and π - π stacking occur and initially define a nanostructure. Then, subsequent, intermolecular reorganization can

occur, modulated by other interactions such as local steric effects, that produce, for example, more ordered intermolecular stacking^{2,5} or a variety of curved surfaces.^{3,6,8–}

¹¹ Similarly, due to the combination of hydrogen-bonding and chirality, peptides with β -sheet domains first fold and assemble into intermolecular β -sheet structures such as 1D ribbons or 2D laminates directed by hydrogen-bonding. Then, further driven by the minimization of hydrophobic faces exposed to aqueous solution, various types of curved surface such as twisted, helical, and even closed, tubular structures can form, even converting between structures in a kinetic manner.^{12,13}

In **Chapter 2**, we discussed the kinetically-controlled assembly process of computationally designed P422 sequence peptide, where kinetic traps can cause the formation of disordered aggregate structures. Additional manipulation, such as thermal annealing, is required to achieve the originally targeted, ordered assembly. In the work presented in this **Chapter 3**, shows that different assembly pathways using different pH conditions can result in unique, different ordered assemblies of a single type of computationally designed peptide. Specifically, solution pH control allows the reproducible formation of coiled-coil bundle building blocks that hierarchically assembled into regular, but uniquely different, peptide nanostructures spanning plates, remarkably uniform nanotubes, and needles.

3.2 Materials and Methods

3.2.1 Peptide Synthesis

Peptides synthesis was performed similar as described in **Chapter 2**.¹⁴

Peptide cleavage was performed similarly as described in **Chapter 2**.

3.2.2 Peptide Purification

Purification was performed similarly as described in **Chapter 2**.

Analytics was performed similarly as described in **Chapter 2**. Representative mass spectroscopy and chromatographic data are shown in **Figure 3.1** and **Figure 3.2**.

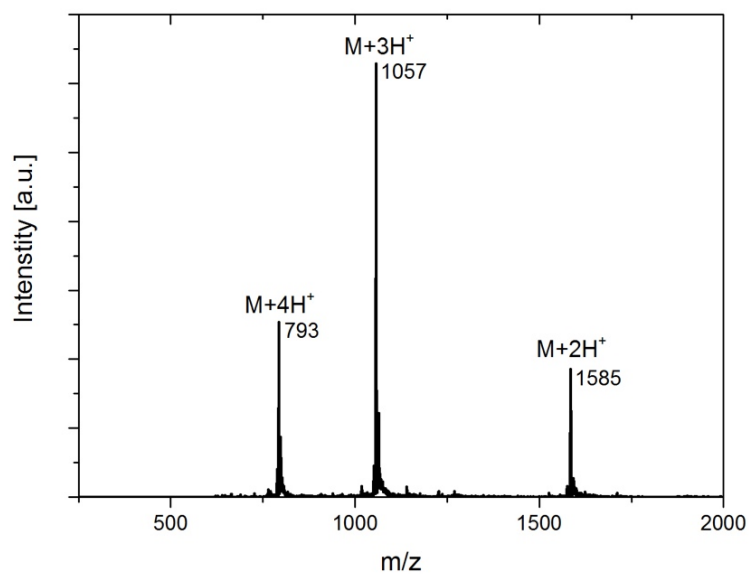


Figure 3.1 Representative ESI-mass spectrometry data for H-P222₉ peptides. Designed molecular weight: [M] 3168 Da. The accordingly calculated mass is: [M+2H⁺] 3170 Da, [M+3H⁺] 3171 Da, [M+4H⁺] 3172 Da. The experimental measured mass is: [M+2H⁺] 3170 Da, [M+3H⁺] 3171 Da, [M+4H⁺] 3172 Da.

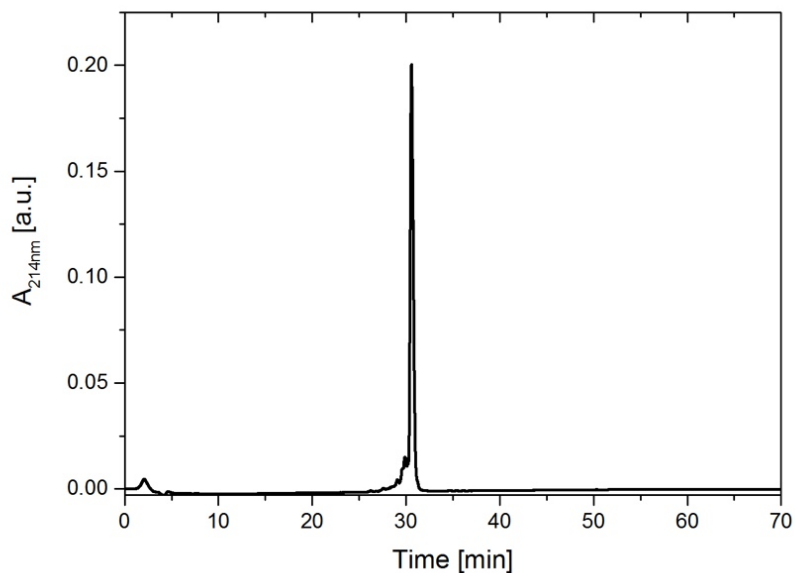


Figure 3.2 Representative analytical HPLC chromatographic data for H-P222_9 peptide. The single elution peak indicates the high purity of the peptide products.

3.2.3 Peptide Solution Self-assembly Experiments

The purified peptides were dissolved in buffer solutions to give a desired peptide concentration. Sodium acetate buffer pH 4.5, phosphate buffer pH 7.0 and borate buffer pH 10.0 were all 10mM, and no excess salt was added. The samples were heated to 90°C for 1 hour to assure complete dissolution of the peptides. All peptide self-assembly solutions were kept at room temperature during the course of the study. The assembly process was monitored with TEM, AFM and SAXS techniques.

3.2.4 Transmission Electron Microscopy

TEM sample grids preparation and images collection are as similar as being described in **Chapter 2**.

3.2.5 Cryogenic TEM (Cryo-TEM)

For cryo-TEM, lacey/carbon-coated 200 mesh copper grids (LC200-Cu, Electron Microscopy Sciences, Inc.) were used. The grids were freshly treated by glow discharge using a plasma cleaner (PDC-32G, Harrica Plasma, Inc.) before sample preparation. 3 μ L of sample was applied on to the grids, then blotted and plunged into liquid ethane cooled by liquid nitrogen using a Vitrobot vitrification system with blot force 0, blot time 1 second and blotted once. The grids were then kept in liquid nitrogen and quickly transferred to a Gatan 626 cryo-holder pre-cooled to below -170°C for TEM observation. The images were taken using TALOS microscope (FEI Company).

3.2.6 Scanning Transmission Electron Microscopy Mass-mapping Measurement

Microtubules formed by tubulin proteins (Cytoskeleton, Inc.) purified from bovine brain were used as structure standard materials for mass-mapping measurement. The carbon-coated 200 mesh copper grids (CF200-Cu, Electron Microscopy Sciences, Inc.) were freshly treated by glow discharge using a plasma cleaner (PDC-32G, Harrica Plasma, Inc.) before sample grid preparation. Firstly, 4 μ L of tubulin protein solution was applied on to the grids and blotted after 1 min incubation. Same amount of Milli-Q water drop was applied on to the grids, then immediately blotted for wash. This wash step was conducted three times. The grids containing tubulin proteins were firstly examined using microscope (TALOS, FEI) to

ensure the existence of protein microtubules. Then, 3 μ L of peptide nanotube solution was applied on to the same grids and blotted after 1 min incubation. Same wash step was conducted three times as well. The grids containing a mixture of protein microtubules and peptide nanotubes were subjected to microscope examination.

Grid was firstly examined under bright field mode to find the area of interest (AOI) that containing both protein microtubules and tubes (both appeared as dried out ribbons, but exhibited different contrast and width), and was adjusted to eccentric height, any astigmatism was also corrected as well. Then microscope was switched to STEM mode; and the following imaging was conducted by the use of high-angle annular dark field (HAADF) detector. A small part of the AOI was sacrificed for the focus adjustment. After focus adjustment, the imaging objects were brought into view for image collection. Single dark-field image was collected using 0.8 second dwell time setting. The collected dark-field STEM images intensity was analyzed using ImageJ. The intensity of select area is contributed by generally 3 components: $I_{assemblies}$ is from the object of your interest, such as protein microtubules or peptide tubes; I_{film} is from carbon support film of grid; I_{salts} is from residue salts remained from washing. Therefore, I_{film} and I_{salts} can be combined as $I_{background}$, and should be subtracted from $I_{assemblies}$ to evaluation the true intensity contribution from assembly structures. Tilted-beam dark field imaging was also conducted; however, the intensity is not good enough for high-quality imaging

3.2.7 Atomic Force Microscopy

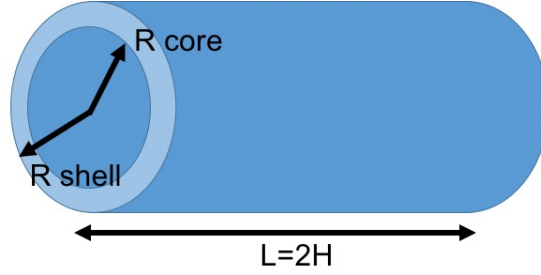
AFM measurement was conducted using the same instrument and AFM tip with similar procedure as described in **Chapter 2**.

3.2.8 Circular Dichroism

Secondary structure and coiled-coils were analyzed with the same method and procedures as described in **Chapter 2**.

3.2.9 Small Angle X-ray scattering

SAXS measurements were conducted at 5ID-D DND-CAT beamline at the Advanced Photon Source (APS) of Argonne National Laboratory (Argonne, IL). The beamline was operated at 17 keV corresponding to a wavelength of 0.7293 Å. A triple-detector setup was used to collect scattering data from small-angle, mid-angle and wide-angle regime simultaneously. The detector for small-angle scattering data collection was set at an 8507 mm sample distance to collect data from $2\theta = 0.015^\circ$ - 0.910° range. The detector for mid-angle scattering data collection was set at a 1013.6 mm sample distance to collect data from $2\theta = 0.872^\circ$ - 5.500° range. The detector for wide-angle scattering data collection was set at a 200.46 mm sample distance to collect data from $2\theta = 4.500^\circ$ - 30.000° range. Only small-angle scattering data was presented in this work. For measurement, 100 μ L of peptide assembly solution in buffer was transferred into quartz glass capillaries with a diameter of around 0.1 cm, which would be exposed in X-ray beam. 5 exposures of 1 sec were recorded. Scattering from buffer was recorded in the same way for background subtraction. The single spectra were averaged and subtracted for background using GSAS-II software package.¹⁵ Background subtracted SAXS curve was fit using the SasView software (www.sasview.org). A hollow cylinder model as in below was used for the form factor of a right circular hollow tube with a uniform scattering length density.¹⁶



The 1D scattering intensity is calculated in the following way:

$$P(q) = (scale)V_{shell}(\Delta\rho)^2 \int_0^1 \Psi^2 [q, R_{shell}(1-x^2)^{1/2}, R_{core}(1-x^2)^{1/2}] \left[\frac{\sin(qHx)}{qHx} \right]^2 dx$$

$$\Psi(q, y, z) = \frac{1}{1-\gamma^2} [\Lambda(qy) - \gamma^2 \Lambda(qz)]$$

$$\Lambda(a) = 2J_1(a)/a$$

$$\gamma = R_{core}/R_{shell}$$

$$V_{shell} = \pi(R_{shell}^2 - R_{core}^2)L$$

where scale is a scale factor based on peptide concentration, $J_1(x) = (\sin x - x \cos x)/x^2$ is the first order Bessel function, q is the scattering vector, R_{shell} is the tube shell radius, R_{core} is the tube core radius, L is the cylinder length.

3.3 Peptide Sequence

The computational design strategy is same as described in **Chapter 1** and **Chapter 2**. The sequence P222_9 investigated in this **Chapter 3** was designed based on the same homotetrameric coiled-coil bundle model, but differently, in the context of P222 lattice. The ionization state of the individual amino acid residues during the computational modeling was set according to neutral pH conditions. This coiled-coil bundle has a cylindrical shape with an estimated size of 4 nm in length and 2 nm in diameter. The sequence is DGRIEGM AEAIKKM AYNIADM AGRIWGE A-NH₂,

with estimated IEP of 7.13. Herein, we explored the assembly process for the N-terminus un-acetylated variant of this peptide sequence, denoted as H-P222_9 hereafter, in different assembly solution pH conditions.

3.4 Different Morphology Structures at Different pH Condition

The cast film transmission electron microscopy bright field data in **Figure 3.3** show assembly behavior of the same peptide sequence (H-P222_9) but reveal distinctly different nanoscale structures formed at pH 4.5, pH 7, and pH 10, respectively: nanoribbon-like structures (shown to be hollow nanotubes in situ, *vide infra*), 2D platelets and needle-like structures.

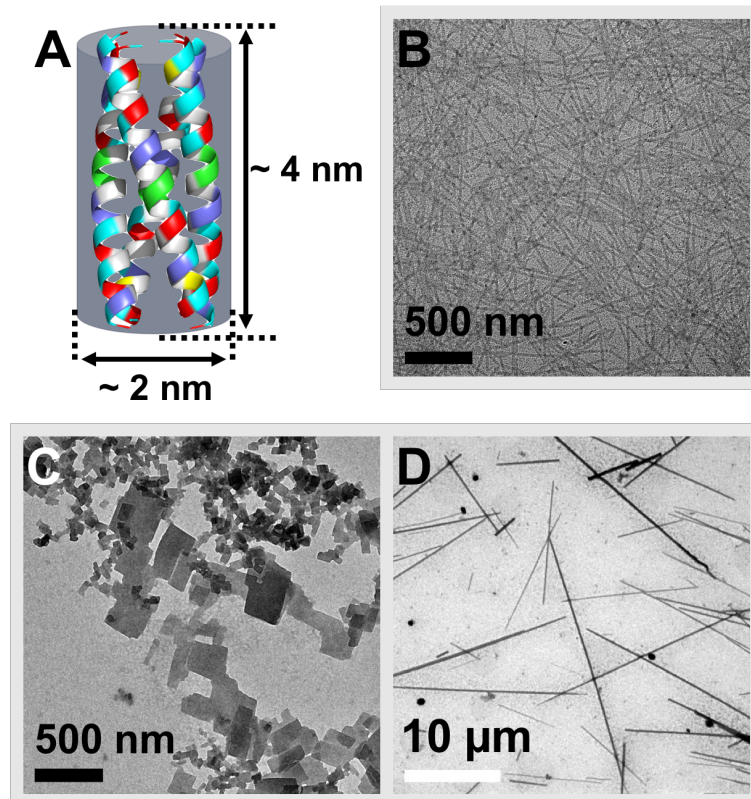


Figure 3.3 Designed H-P222_9 peptide coiled-coil bundle model and the TEM images of designed peptide assembled in aqueous solution with different pH values. **A:** The assembly building block is a cylinder-like homotetrameric coiled-coil bundle, with that is approximately 4 nm in length and 2 nm in diameter. The α -helices of designed sequence DGRIEGM AEAIKKM AYNIADM AGRIWGE A-NH₂ are represented by ribbon drawings (the exterior residues are colored according to amino acid properties: blue indicates basic residues, red indicates acidic residues, green indicates polar residues, and yellow indicates hydrophobic residues. Interior residues are colored grey). **B:** TEM image of 0.25 mM peptide assembled in 10 mM pH 4.5 sodium acetate buffer; observed are flattened assembled peptide nanotubes. **C:** TEM image of 1 mM peptide assembled in 10 mM pH 7 phosphate buffer; observed are 2D platelets. **D:** TEM image of 1 mM peptide assembled in 10 mM pH 10 borate buffer; observed are elongated, micrometer-long, needle-like structures.

Circular dichroism spectra of peptides in pH 4.5 and pH 10 buffers exhibit ellipticity minima typical for the α -helical conformation (**Figure 3.4**). Additionally, the ratios of

the two minima, $[\text{MRE}]_{225\text{nm}}/[\text{MRE}]_{210\text{nm}} = 1.11$ at pH 4.5 and $[\text{MRE}]_{222\text{nm}}/[\text{MRE}]_{208\text{nm}} = 0.99$ at pH 10, are both close to 1 and are thus indicative of a stabilized coiled-coil bundle at both pH conditions.^{17,18} Circular dichroism data could not be obtained in pH 7 buffer due to the solution turbidity caused by the fast assembly of the 2D plate nanostructure. However, the plate formation is consistent with the original bundle-based assembly design. Therefore, the designed peptide is able to form coiled-coil bundles at all three different pH values, which are thus indicated to serve as building blocks for the three different assembled structures. Further analysis from TEM images in **Figure 3.3B-D** reveal that the nanoribbons formed at pH 4.5 show high homogeneity with dimensions of $21.3 \text{ nm} \pm 2.8 \text{ nm}$ in width and an aspect ratio of over 100. The platelets and needle-like structures are consistent morphologies at pH 7 and pH 10, respectively, but are more heterogeneous in their dimensions. The lateral dimension of platelets varies from 50 nm to 500 nm, while the needle-like structures also have a broad distribution in width ranging between 100-250 nm. Both plates and needles show significant difference in thickness as observed from differences in TEM image contrast, the darker objects having larger thickness and exhibiting a larger mass-thickness contrast to the electron beam.

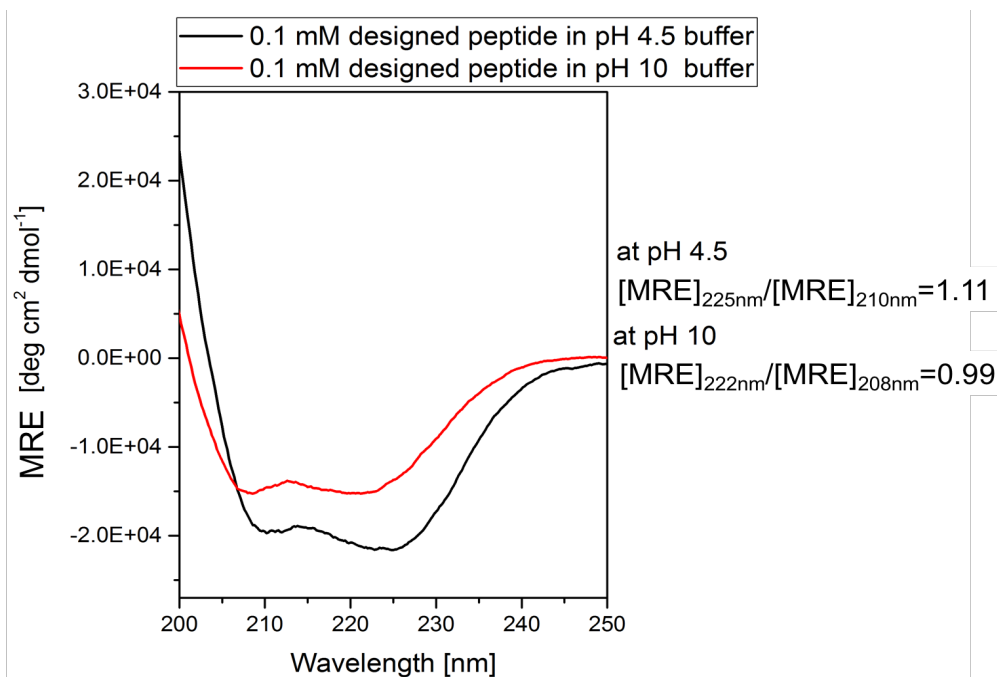


Figure 3.4 Circular dichroism spectroscopy data for H-P222_9 peptide measured at 20°C in pH 4.5 sodium acetate buffer and pH 10 borate buffer. Data is plotted with buffer background subtracted. Both spectrum show typical α -helical conformation. And at pH 4.5, the ratio of two ellipticity minima $[MRE]_{225nm}/[MRE]_{210nm} = 1.11$; at pH 10, the ratio of two ellipticity minima $[MRE]_{222nm}/[MRE]_{208nm} = 0.99$. The ratios are close to 1 indicating the stabilized coiled-coil formation in both pH conditions.

The corresponding atomic force microscopy (AFM) measurement results for the three assembled structures are shown in **Figure 3.5**, indicating morphologies that are consistent with the TEM results. The height scans of the flattened nanoribbon assemblies formed at pH 4.5 yield a narrow distribution of heights (4.4 nm with a standard deviation of 0.5 nm (**Figure 3.5D**)). The height scans for platelets and needle-like assemblies formed at pH 7 and pH 10 revealed much larger and varied thicknesses, varying from 17 nm to 33 nm for the platelets, and 50 nm to 200 nm for the needles (**Figure 3.5E and 3.5F**). Given that the estimated length of a coiled-coil

bundle in the z-direction is 4 nm (**Figure 3.3A**), it is reasonable that the observed nanoribbon structures could comprise one layer of assembled bundles with the bundle axis arranged perpendicularly to the AFM substrate or two layers of assembled bundles that lie flat on the AFM substrate. However, as will be seen, comparison with in situ cryo-TEM and SAXS data will show the ribbons to be dried tubes. The plate and needle-like structures formed at pH 7 and pH 10, respectively, clearly are made up of multiple layers of bundles stacking in the z-direction.

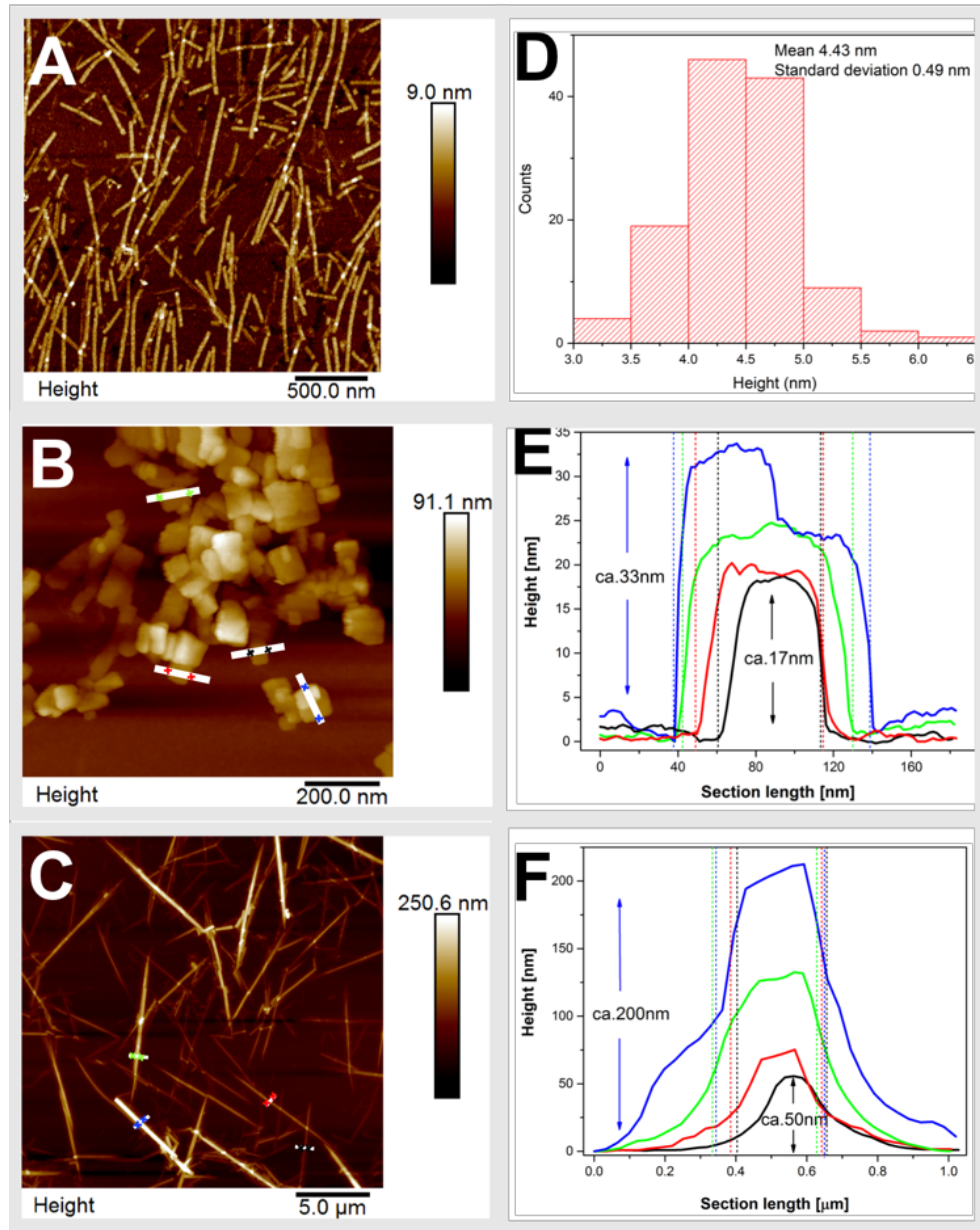


Figure 3.5 AFM of H-P222_9 peptide assembled in aqueous solution with different pH values. **A:** 0.25 mM peptide assembled in 10 mM pH 4.5 sodium acetate buffer. **B:** 1 mM peptide assembled in 10 mM pH 7 phosphate buffer. **C:** 1mM peptide assembled in 10mM pH 10 borate buffer. **D:** The corresponding height analysis histogram of the nanoribbon assemblies. **E:** The height scans of the platelet assemblies. **F:** The height scans of the needle-like assemblies.

3.5 Nanotube Structure Analysis

Because both conventional TEM and AFM detect structures in the dried state, cryogenic TEM and solution small-angle X-ray scattering (SAXS) were employed to observe in situ structure and whether or not the observed nanoribbons at pH 4.5 are due to drying and sample preparation on the solid substrates used in TEM and AFM. **Figure 3.6A** shows cryo-TEM observations of samples under the same pH 4.5 conditions as in **Figure 3.3B**. **Figure 3.6B** presents the SAXS results measured from the peptide assembly solution at the same pH condition (pH = 4.5).

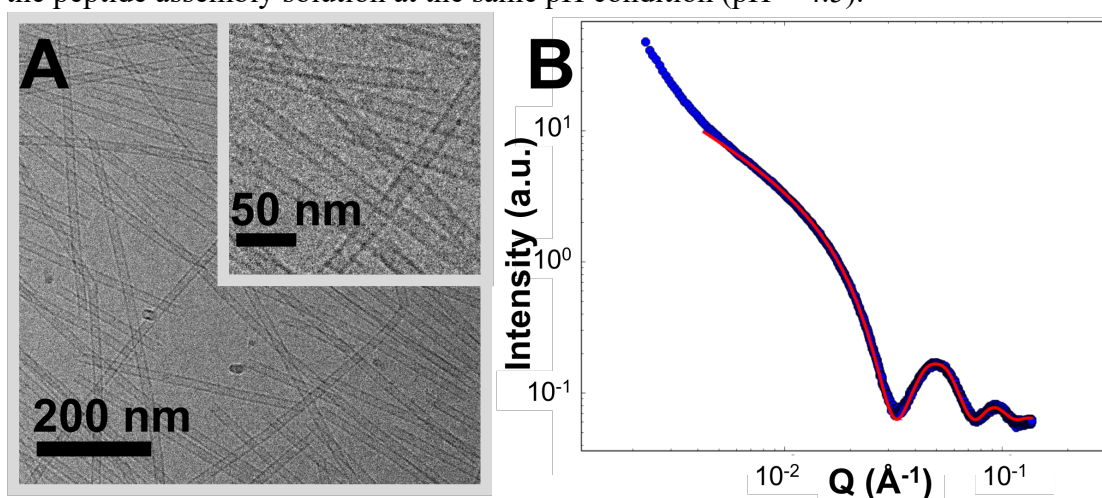


Figure 3.6 **A:** Cryo-TEM images of 0.2mM H-P222_9 peptide assembled in 10mM pH 4.5 sodium acetate buffer showing hollow nanotubes. Inset is higher magnification image showing tubes with tube diameter $13.3 \text{ nm} \pm 0.7 \text{ nm}$ and tube wall thickness $3.1 \text{ nm} \pm 0.5 \text{ nm}$. **B:** SAXS result measured from H-P222_9 peptide assembly solution at pH 4.5. The experimental data is plotted in blue, and the calculated curve using a hollow tube model is plotted in red.

3.5.1 TEM and SAXS Result and Analysis

Cryogenic conditions preserve the hydrated state of sample even under the electron microscope vacuum.^{19–24} As shown in **Figure 3.6A**, the nanostructure at pH 4.5 is clearly hollow nanotubes as indicated by the image contrast changing from tube

edge to center. From the average of measurements of the cryo-TEM images, the tube diameter was determined to be $13.3 \text{ nm} \pm 0.7 \text{ nm}$ (measured from wall center to wall center across the tube diameter), and the wall thickness $3.1 \text{ nm} \pm 0.5 \text{ nm}$. The histogram is shown in **Figure 3.7**.

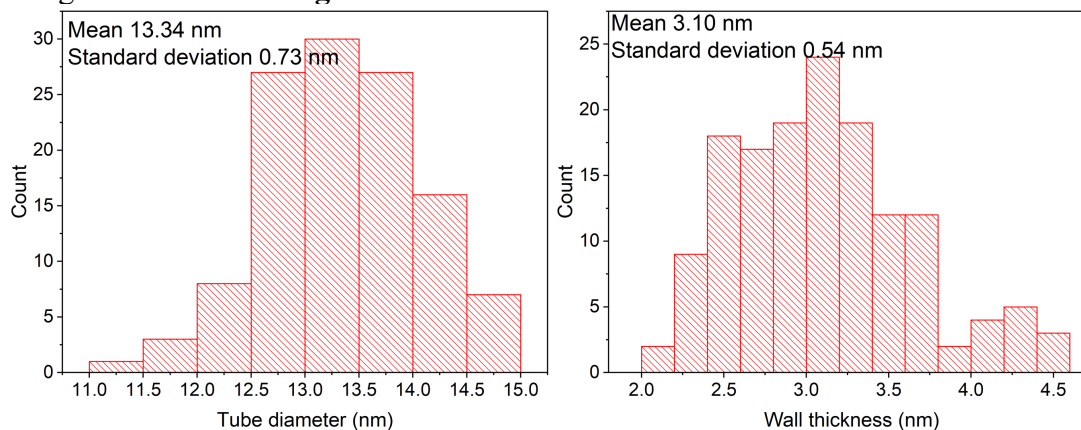


Figure 3.7 H-P222_9 peptide nanotube diameter and wall thickness measurement distribution. 10 different cryo-TEM images taken from the same samples were used for measurement in ImageJ. **Left:** The tube diameter was measured from wall center to wall center across the tube diameter. Total 119 different areas were measured giving the mean tube diameter value of 13.3 nm and standard deviation of 0.7 nm. **Right:** For nanotube wall thickness, total 146 different areas were measured giving the mean thickness value of 3.1 nm and standard deviation of 0.5 nm.

Given the similarity of the measured wall thickness value with the length of the designed bundle, the data are suggestive that the tube wall comprises a single layer of bundles. Further confirmation is obtained from the SAXS results shown in **Figure 3.6B**, where the scattering curve contains several, distinct intensity maxima and minima in the mid- to high- q region, a strong indication of ordered nanostructure. These oscillation peaks can be fit using a hollow cylindrical tube model with parameters obtained from the cryo-TEM results (tube width = $13.3 \text{ nm} \pm 0.7 \text{ nm}$; wall

thickness = $3.1 \text{ nm} \pm 0.5 \text{ nm}$; the outer radius of the tube, $R_{\text{shell}} = 8.2 \text{ nm} \pm 0.6 \text{ nm}$; the inner radius of the tube, $R_{\text{core}} = 5.1 \text{ nm} \pm 0.1 \text{ nm}$). As shown in **Figure 3.6B**, the red calculated curve determined with these values matches very well with the experimentally measured data. The tube dimensions calculated from the model fit to the SAXS data reveal $R_{\text{shell}} = 9 \text{ nm}$ and $R_{\text{core}} = 5.5 \text{ nm}$ (polydispersity was not included for calculation), values that are very close to those measured from cryo-TEM images. Therefore, the consistency of the scattering and microscopy data confirms the hollow tube structure with a wall structure consisting of a single layer of bundles.

Commonly reported self-assembled peptide nanotubes generally have three types of structures. One is the lipid-like bilayer hollow tube structures,²⁵ which is not an applicable structure model to the peptide nanotubes reported here due to the coiled-coil formation for our designed peptides. The other two are the helical wrapping of β -sheet^{6,8,26} or coiled-coil subunits,²⁷ and the end-to-end connected coiled-coils.^{28,29} Both of them are crystal-like, tight packing structure models. However, after careful evaluation of the high magnification cryo-TEM images of our peptide nanotubes, the nanotubes didn't exhibit surface morphology features that would lead to a possible helical wrapping or end-to-end connection structure. Therefore, we hypothesize that the bundles are packed in a looser manner within the nanotubes, as compared to the helical wrapping or end-to-end connection. Based on the results from cryo-TEM, SAXS and the individual bundle dimensions, two possible loosely packed bundle models within the peptide tube are proposed as shown in **Figure 3.8**.

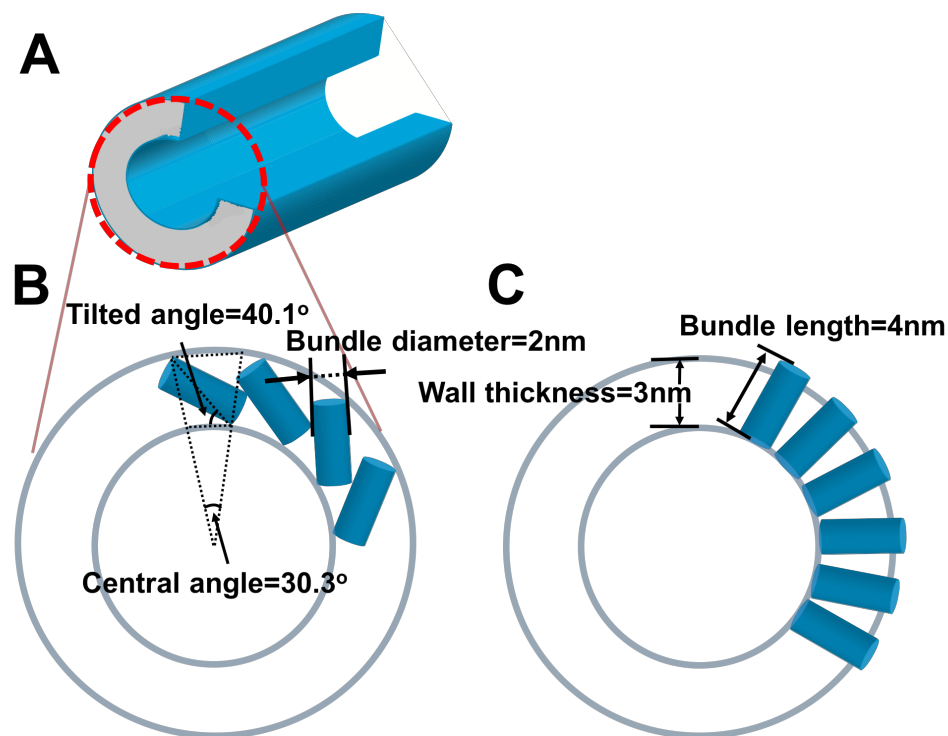


Figure 3.8 Possible structure models for peptide nanotubes formed at pH 4.5. **A, B:** Tilted single bundle-layered tube model. The tube wall is a single layer of peptide bundle. The cross-section schematic (**B**) reveals the bundles to be packed in a tilted angle to the tube wall. The tilted angle can be calculated as 40° . The corresponding central angle can be calculated as 30.3° . A single slice contains approximately 11 bundles. **C:** Perpendicular-packing tube model. Bundles are proposed as being packed perpendicularly to the tube wall. The wall thickness is approximately 3 nm according to TEM and SAXS results. The bundle length is approximately 4 nm according to design. A single cross-section contains approximately 16 bundles.

As mentioned above, the peptides adopt an α -helical secondary structure in pH 4.5 solutions, and concurrently assemble into coiled-coil bundles (CD data in **Figure 3.4**) prior to assembly into nanotubes. Considering the thin tube wall (approximately 3 nm) and the theoretically predicted bundle length (approximately 4 nm), the peptide tube wall is proposed as a single layer of peptide bundles, as shown in **Figure 3.8A-B**. The

first packing model assumes the tilted alignment of peptide bundles with respect to the tube wall, as shown in **Figure 3.8B**. The tilting could be caused by the repulsive interaction between positive charges located near the end of the bundles (the amine group at the uncapped N-terminus and arginine at position 3 are both positively charged). Based on the measured tube wall and bundle dimensions (wall thickness ≈ 3 nm, bundle length ≈ 4 nm), the tilted angle for the peptide bundles in the tube wall can be calculated as approximately 40° . One cross-sectional slice can accommodate approximately 11 bundles in the tilted model. More slices could stack beside one another along the tube axis forming the long aspect ratio nanotubes. Moreover, as coiled-coil bundles with anti-parallel organization, the bundle tilting offsets the bundle ends on the inner surface and outer surface of the peptide nanotube to alleviate the repulsive interactions of the positively charged ends. This model also explains the dried nanoribbon thickness measured via AFM: as peptide tubes dried and flattened, the tilted peptide bundles tend to lay down flat on the substrate, instead of standing straight. In this way, two layers of collapsed bundles produce a thickness of about 4 nm, which is close to the summation value of two bundle diameters. Similar tilted molecular arrangement has been suggested in lipid nanotube assemblies.^{30,31} Another possible perpendicular-packing tube model is illustrated in **Figure 3.8C**. This model assumes the perpendicular packing of peptide bundles to the tube wall, which would dictate that at the inner surface of the peptide tubes, the bundle-ends would be in a close contact. From a cross-sectional view of the tube, one cross-sectional slice can accommodate approximately 16 bundles restricted by the known tube dimension. However, for this model, a size discrepancy exists between the tube wall value (3 nm) and the bundle length value (4 nm). Another flaw is the close contact between bundles

at the inner tube surface. The separation among the bundle-ends in the outer surface of the peptide tubes was rationalized because of positively charged bundles ends repelling each other. But as coiled-coil bundles with anti-parallel organization, the same positive charge should exist at both bundle ends. This would disrupt the curvature formation and should disallow the inner tube surface having close contacting bundle packing. Therefore, the firstly described tilted-bundle tube model shown in **Figure 3.8B** is a more feasible model.

3.5.2 STEM Mass-Mapping Analysis

Since the structure of the assembly building block, the peptide coiled-coil bundle, is well-defined, the density of the assembled structure should provide an additional strategy to verify the bundle packing organization within the tubes. Scanning transmission electron microscopy (STEM) mass-mapping method^{32,33} is applied to evaluate the mass-per-length value of peptide nanotubes, with the use of microtubules formed by tubulin proteins (mass-per-length = 181.5 kDa/nm) as standard sample. The structure details of protein microtubules are described in **Figure 3.9**.

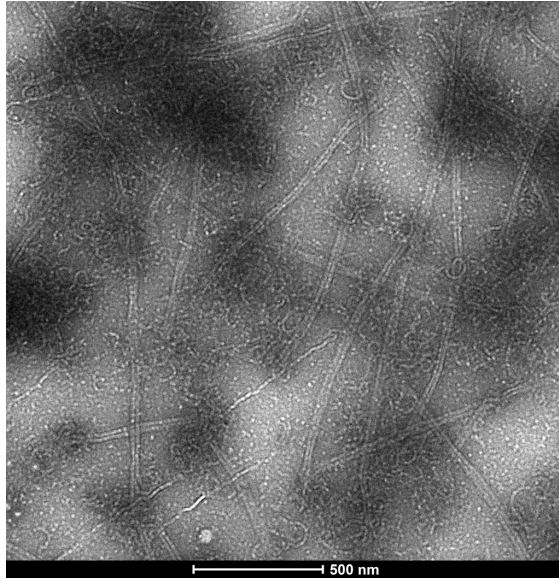


Figure 3.9 Negatively stained protein microtubules used as standard sample in STEM mass-mapping measurement. The microtubules are formed by the tubulin proteins (from Cytoskeleton, Inc.). Tubulin is composed of a heterodimer of two 55 kDa proteins. The microtubules formed from tubulin proteins have the mean diameter of 25 nm, and each micrometer of microtubule containing 1650 heterodimers (more information seen in Cytoskeleton, Inc. <https://www.cytoskeleton.com/tubulins/microtubules>). Therefore, the mass-per-length value of protein microtubules can be calculated as: $55 \times 2 \times 1650 \div 1000 = 181.5 \text{ kDa/nm}$.

The standard sample protein microtubules and the peptide nanotubes in the present work were applied to the same TEM grids for investigation. The areas containing both protein microtubules and peptide nanotubes were imaged under STEM mode and collected with the high-angle annular dark field (HAADF) detector, as shown in **Figure 3.10A**. The protein microtubules and peptide nanotubes are easily distinguished from each other. As indicated in **Figure 3.10A**, the brighter tube structures with larger width are from dried protein microtubules, the darker structures with smaller width are from dried peptide nanotubes. The lower intensity of peptide

nanotubes already indicates a loose-packing structure. The image intensity was analyzed using ImageJ, as indicated in **Figure 3.10A**. For protein microtubules, a box with dimension of $a \text{ nm} \times b \text{ nm}$ was drawn to include the whole section of protein microtubules ($a \text{ nm}$ in the direction of tube long axis) to obtain the intensity, $I_{standard}$. The same area box was also drawn in the nearby empty area to obtain the intensity of background, I_{bkg1} . For peptide nanotubes, a series of boxes with dimension of $c \text{ nm} \times d \text{ nm}$ were drawn to include whole sections of peptide nanotubes ($c \text{ nm}$ in the direction of nanotube long axis) to obtain the intensity of peptide nanotube, I_{tube} . The same area box was also drawn beside the peptide nanotube in the empty area to obtain the intensity of background, I_{bkg2} . The mass-per-length value of peptide nanotubes was calculated using the following equations:

$$\frac{I_{standard} - I_{bkg1}}{M_{standard}} = \frac{I_{tube} - I_{bkg2}}{M_{tube}}$$

$$M_{standard}(kDa) = 181.5 \left(\frac{kDa}{nm} \right) \times a (nm)$$

$$Mass \text{ per length}_{tube} = \frac{M_{tube}(kDa)}{c (nm)}$$

A minimum of 300 measurements from 10 different recorded STEM images were conducted to obtain statistically significant information of the mass-per-length value for the peptide nanotubes, as shown in **Figure 3.10B**.

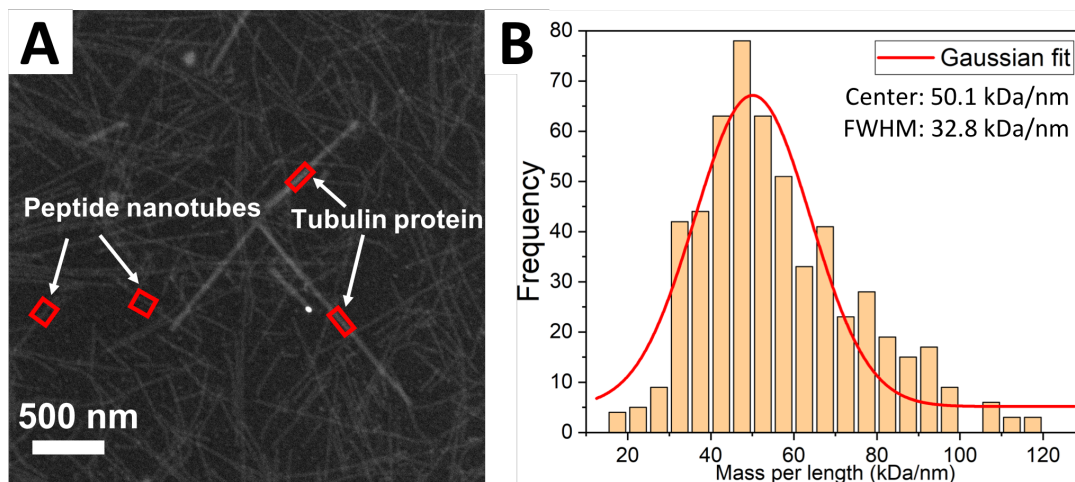


Figure 3.10 STEM mass-mapping results of peptide nanotubes with the use of protein microtubules as standard samples. **A:** As indicated, the relatively brighter 1D ribbon-like structures are the protein microtubules, while the relatively darker and more abundant 1D ribbon-like structures are the peptide nanotubes. In ImageJ, a box with dimension of $a \text{ nm} \times b \text{ nm}$ was drawn to include whole section of protein microtubules to obtain the intensity. A series of boxes with dimension of $c \text{ nm} \times d \text{ nm}$ was drawn to include whole section of peptide nanotube to obtain the intensity. **B:** Mass-per-length of peptide nanotube histogram obtained from STEM measurement, fitted to a single Gaussian peak (red curve) at 50.1 kDa/nm, with 32.8 kDa/nm full width at half maximum (FWHM).

The histogram of peptide nanotubes is fitted to a single Gaussian peak at approximately 50 kDa/nm, with FWHM at approximately 33 kDa/nm. The relatively large deviation arises largely from two factors: 1) The remaining salt residues from assembly buffer solution on the TEM grids could contribute to the intensity in STEM causing the inaccuracy in background subtraction. 2) The observed nanoribbon-like structures are the flattened nanotubes due to the drying effect discussed earlier. However, the flattening process may not be uniform, causing the peptide bundles to unevenly collapse, which could also contribute to the measurement error. For the two previously described bundle-packing models, shown in **Figure 3.8**, the mass-per-

length values can be calculated approximately as 70 kDa/nm for tilted-bundle model (**Figure 3.8B**) and 100 kDa/nm for the perpendicular-bundle model (**Figure 3.8C**). Considering the measured mass-per-length value 50 kDa/nm, the tilted-bundle model is more reasonable. The measured value (50 kDa/nm) is relatively small comparing to the theoretically calculated value (70 kDa/nm). This suggests the packing along the tube axis is possibly looser than the close-stacking of cross-sectional peptide tube slices depicted in **Figure 3.8B**. This is reasonable considering other positively charged regions along the bundles could also cause the separation of bundles (e.g., the lysines in position 12 and position 13). While the measurement error and resolution limitation does not allow the STEM mass-mapping to lead to a precise structure model, the results support our hypothesis about the loose-packing structure of peptide nanotubes.

3.5.3 Tube Formation Discussion

A hollow tube structure is an attractive structure in self-assembled materials due to the existence of internal channel that could provide avenues for transport of small molecules; selective transport should be possible on the basis of the identity of the peptides comprising the tube. As previously described, different from commonly reported peptide self-assembled nanotubes, the unique feature of the peptide nanotubes reported here is the assembly of the coiled-coil bundles into nanotubes when triggered by inter-bundle electrostatic repulsions under acidic solution conditions, although these coiled-coil bundles were designed to form 2D lattices at neutral pH.¹ These results underscore the highly sensitive nature of the assembly; it is likely that the specific distribution of positively charged amino acid residue patches along the bundle causes the formation of homogenous nanotubes. As is apparent from the sequence, DGRIEGM AEAIKKM AYNIADM AGRIWGE A-NH₂, the amine group of the un-

capped N-terminus and arginine at position 3 are positively charged. This positive patch is located near the end of the bundle, which almost certainly creates a repulsive force between the bundle-ends to produce the curvature for the tube formation. As described in **Figure 3.8B**, the bundles arrange in a tilted fashion within the tube wall in order to more homogeneously distribute the charge. The additional positively charged patch located in the middle part of the bundle (due to the lysine at position 12 and position 13) may further contribute to the repulsive forces, leading to further separation between the bundles in the wall and resulting in loose packing along the tube axis. Given that the bundles are organized in a highly homogenous nanotube structure, there must also exist interactions that keep bundles together. Considering the contacts shown in the tilted-bundle model shown in **Figure 3.8B**, it is possible that the arginine in position 3 forms hydrogen bonds and salt bridges with the aspartic acid in position 1 and glutamic acid in position 5. These attractive interactions may maintain the bundles in a tubular organization, while not solubilizing them.

To further elucidate the formation mechanism of the peptide nanotubes, the H-P222_9 peptide sequence was modified to create 3 variant sequences **AC**, **R3K** and **E5Q** as shown in **Table 3.1**.

Peptide	Sequence code
AC	Ac-DGRIE GMAEA IKKMA YNIAD MAGRI WGEA-NH₂
R3K	DGKIE GMAEA IKKMA YNIAD MAGRI WGEA-NH₂
E5Q	DGRIQ GMAEA IKKMA YNIAD MAGRI WGEA-NH₂

Table 3.1 The modified H-P222_9 sequences. **AC** is the original sequence with acetylated N-terminus. **R3K** is the original sequence with arginine in position 3 being substituted by lysine. **E5Q** is the original sequence with glutamic acid in position 5 being substituted by glutamine.

The assembled structures formed by these modified peptide sequences are shown in **Figure 3.11**. For the **AC** peptides, in contrast to the unmodified peptide where almost exclusively nanotubes have been observed at pH 4.5, a mixture of two-dimensional plates and nanotubes were observed at the same pH 4.5 by cryo-TEM (**Figure 3.11A**). The acetylation eliminated the positively charged amine group at N-terminus, which resulted in a reduction of the repulsive interaction between bundle ends and the corresponding loss of curvature and the resultant more two-dimensional plates. However, nanotubes still exist for the acetylated peptide at pH 4.5, suggesting that the charge of the amine groups at the N-terminus is not solely responsible for the curvature but that other charged amino acid residues (arginine 3) located near the end of the bundle also contribute.

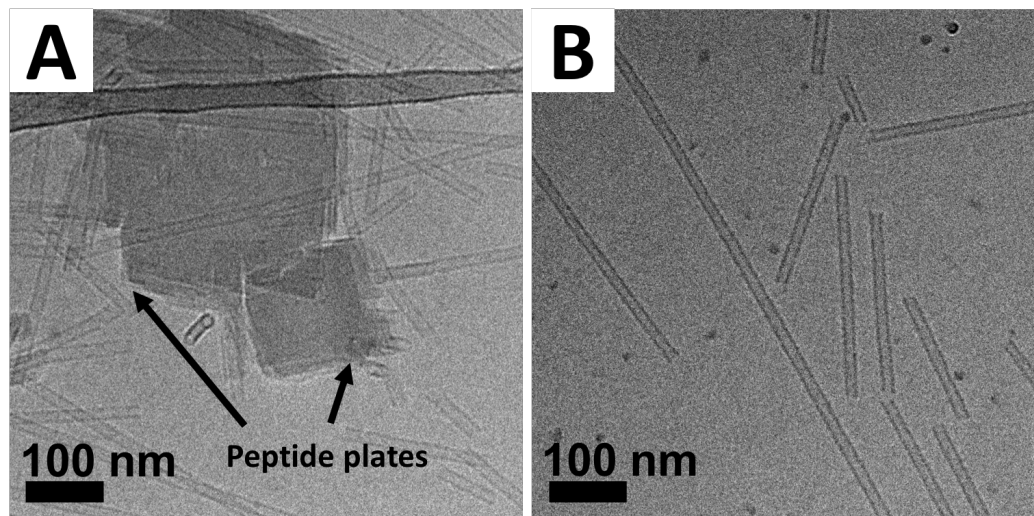


Figure 3.11 Cryo-TEM micrograph of modified sequences assembly structures. **A:** 0.2 mM **AC** sequence in 10 mM pH 4.5 sodium acetate buffer, assembled at room temperature for 24 hours. A mixture of two-dimensional plates and nanotubes can be observed. **B:** 0.2 mM **R3K** sequence in 10 mM pH 4.5 sodium acetate buffer, assembled at room temperature for 24 hours. Nanotubes are observed with width of 11.7 ± 1.1 nm and wall thickness of 4.0 ± 0.7 nm.

For the **R3K** sequence, in contrast, only nanotube structures were observed at pH 4.5, as shown in **Figure 3.11B**, which is similar to unmodified peptide. However, the dimensions of the tubes are slightly altered from the original sequence. From the average of measurements of the nanotubes cryo-TEM images (histogram shown in **Figure 3.12**), the **R3K** tube diameter was determined to be 11.7 ± 1.1 nm, and wall thickness 4.0 ± 0.7 nm (compared to the original H-P222_9 peptide sequence which produced nanotubes with a width of 13.3 ± 0.7 nm and wall thickness of 3.1 ± 0.5 nm). The replacement of the large, positively charged arginine by lysine, which has a lower pKa and a smaller functional group on the side chain, leads to a slightly smaller

nanotube but with a slightly thicker wall, indicating a reduction in the tilt angle of bundles and a correspondingly thicker tube wall. The reduced tilt angle also results in more tightly packed bundles, which results in higher curvature and smaller tube diameter, as shown in **Figure 3.13**.

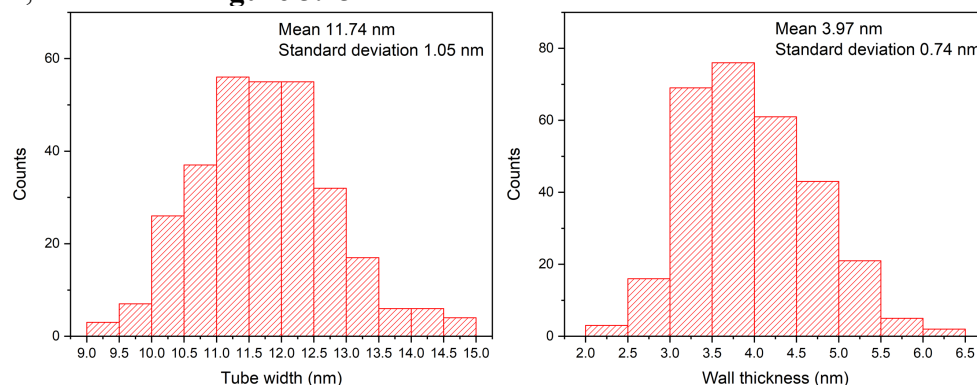


Figure 3.12 **R3K** peptide nanotube diameter and wall thickness measurement distribution for **Figure 3.11B**. 10 different cryo-TEM images taken from the same samples were used for measurement in ImageJ. Left: **R3K** peptide nanotube diameter distribution. The tube diameter was measured from wall center to wall center across the tube diameter. Total 296 different areas were measured giving the mean diameter value of 11.7 nm and standard deviation of 1.1 nm. Right: **R3K** peptide nanotube wall thickness distribution. Total 304 different areas were measured giving the mean thickness value of 4.0 nm and standard deviation of 0.7 nm.

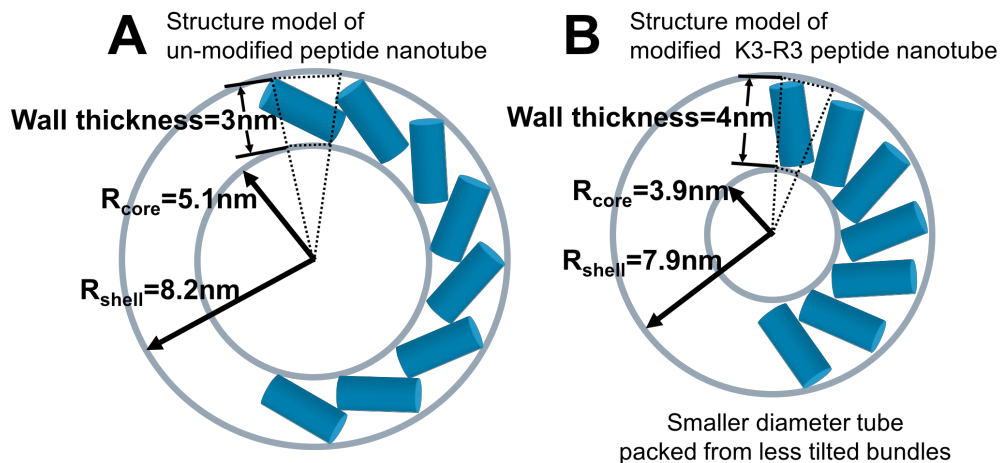


Figure 3.13 Comparison between nanotube structure models between un-modified H-P222_9 peptides and **R3K** modified peptides. **A**: The original tilted-bundle model of un-modified H-P222_9 peptide nanotubes, same as in **Figure 3.8B**, depicting the hollow tube with diameter $13.3 \text{ nm} \pm 0.7 \text{ nm}$ and tube wall thickness $3.1 \text{ nm} \pm 0.5 \text{ nm}$. **B**: The less tilted-bundle model of **R3K** modified peptide nanotubes, depicting the tube with diameter $11.7 \pm 1.1 \text{ nm}$ and wall thickness of 4.0 ± 0.7 . The bundles are less tilted, and packed more towards center, resulting in the thicker wall thickness and smaller tube diameter.

For **E5Q**, no assembled structures were observed after assembly at pH 4.5 (data not shown). The replacement of the negatively charged glutamic acid by the polar glutamine abolishes the formation of nanotubes, although CD spectroscopy indicates the formation of individual coiled-coil bundles (**Figure 3.14**). A salt bridge that possibly formed between negatively charged side chain of glutamic acid and other positively charged amino acid residues is a key interaction for tube organization, consistent with our previous hypothesis.

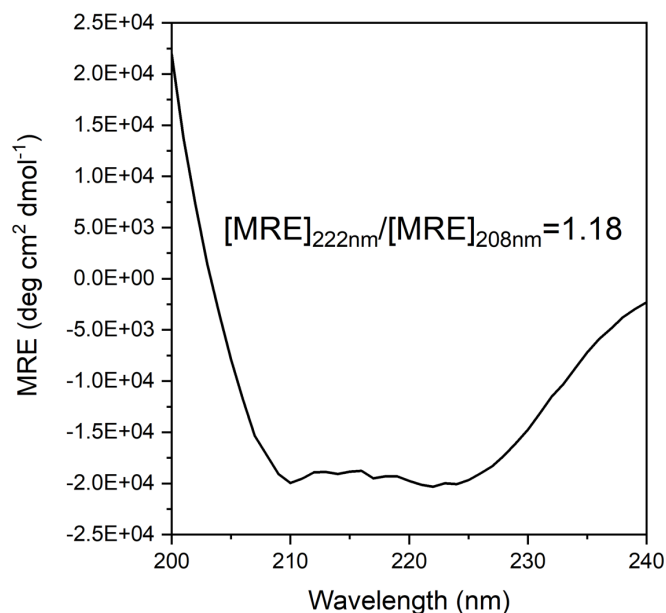


Figure 3.14 Circular dichroism spectroscopy data for the modified sequence **E5Q** measured at 20°C at pH 4.5. 0.1 mM concentration peptide in pH 4.5 10 mM sodium acetate buffer. Data is plotted with buffer background subtracted. The spectrum shows typical α -helical conformation. The ratio of two ellipticity minima $[MRE]_{222nm}/[MRE]_{208nm} = 1.18$. The ratio is close to 1 indicating the stabilized coiled-coil formation.

Moreover, the nanotube structures assembled from the original, un-modified H-P222_9 peptides were observed to be able to eventually convert to two-dimensional platelets with long-term aging (over 6 months) while being kept in the same acidic pH condition, as shown in **Figure 3.15**. The design of two-dimensional lattice structures is based on the neutral pH condition, and the estimated pI of this designed peptide (pI = 7.1) is also near neutral pH. The peptide assembles are able to reform platelets due to alleviation of significant electrostatic interactions that forced the formation of nanotubes. Results from all coiled-coil bundle assembly observed to date reveal that peptide bundle assembly occurs most effectively at a pH near the pI of the bundle

resulting in large, mature assemblies and thick plates when designed to form a two-dimensional lattice.³⁴ Therefore, the transition from tube to plate can be rationalized with the reorganization into more stable assembly products.

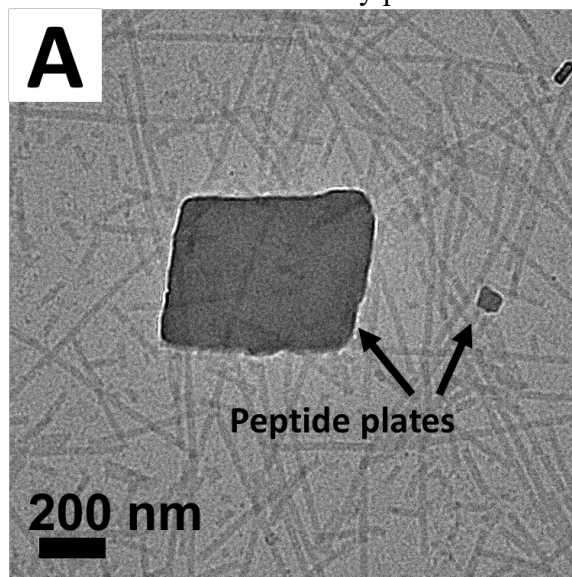


Figure 3.15 TEM image of 0.25 mM H-P222_9 peptide assembled in 10 mM pH 4.5 sodium acetate buffer, same condition as in **Figure 3.3B**, but with longer aging time (several months). Platelets can be observed. Image was taken under high defocused condition to reveal the tubes structure in background.

3.6 Needle-like Structure Analysis

For the needle-like structures that the peptides formed at pH 10 (as shown in **Figure 3.3D**), the high magnification image reveals the existence of orderly lattice strands within the assemblies, as shown in **Figure 3.16A**. Therefore, the needle-like structures are still composed of peptide bundle lattices but with a preferential growth direction. Similar to the discussion of nanotube formation, a driving force for preferential growth can also be rationalized by the charged state of the amino acids under basic conditions. When peptides are assembled at pH 10, the amine group at the

N-terminus become less protonated (and thus less charged), reducing the repulsive driving force for curvature and resulting in assemblies that tend to remain flat. Additionally, in the original bundle lattice design, two different bundle-bundle interfaces can be identified within the lattices, as shown in the inset model of **Figure 3.16A**. The specific interactions involved in the needle formation is in interface 2. At pH 7 the positively charged lysine at position 12 and position 13 were supposed to form a salt bridge with the negatively charged aspartic acid at position 20 between neighboring bundles to stabilize the interface 2, as drawn in **Figure 3.16B**. However, when the assembly pH was increased to 10 (near pKa of the lysine side chain), the reduced lysine charge weakens the salt bridge at the bundle-bundle interface 2, as drawn in **Figure 3.16B**. The destabilization of this interface could result in the preferential assembly of the peptides into elongated needle-like structures, as illustrated in **Figure 3.16C**. Importantly, the lattices did not completely disassociate into purely 1D assemblies, maintaining some growth in the y-direction and revealing that the bundle-bundle interface 2 for lattice assembly was not completely disassociated. Part of lysine side chains are still in charged state keeping the salt bridge interactions, and some other interactions at interface 2, such as π - π stacking from tyrosine in position 16, may also help to maintain certain stability for the needle formation process.

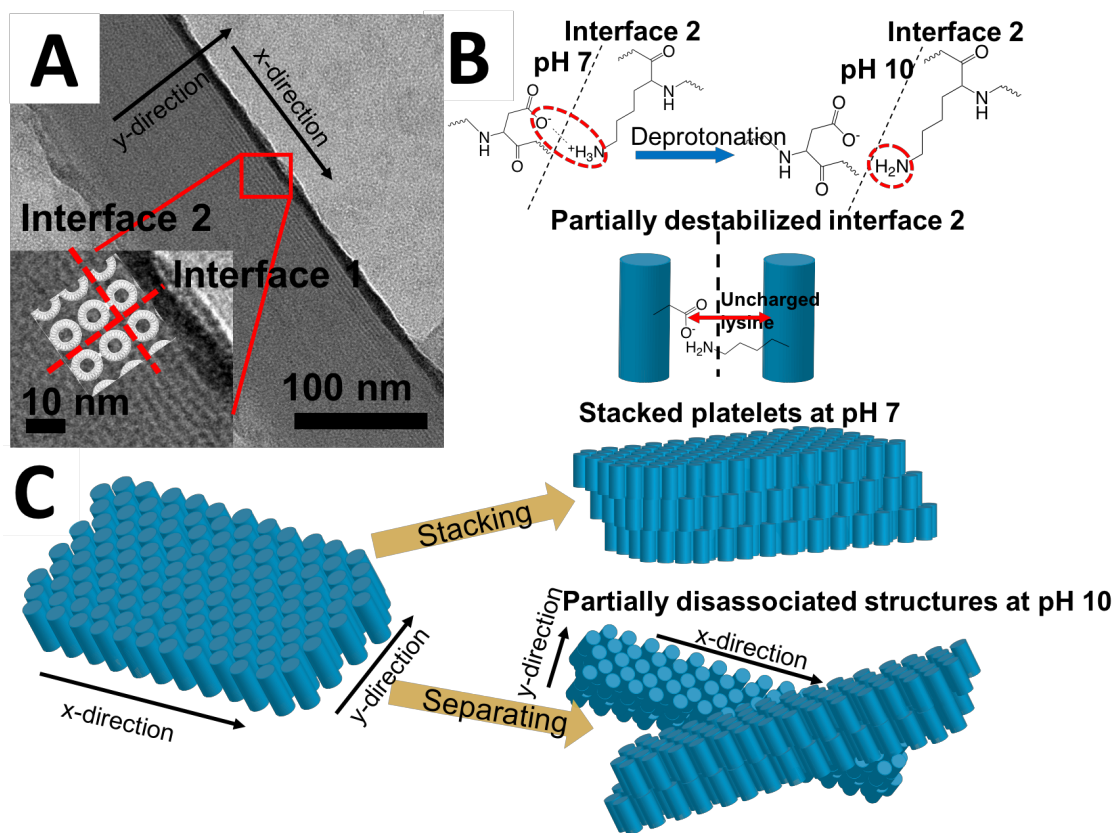


Figure 3.16 Schematic of needle-like structure formation process at pH 10. **A:** High-magnification TEM image of needle-like structure revealing the details of orderly spaced strands. Inset is the HRTEM showing the lattices superimposed with designed lattice model, viewing from coiled-coil bundle axis. Red dashed lines indicate the two bundle-bundle interfaces. **B:** At pH 7, at interface 2, lysine can form a salt bridge with aspartic acid. At pH 10, due to the partial deprotonation, salt bridge was weakened, partially destabilizing the designed bundle-bundle interface 2. **C:** The original design is for bundles to organize into two-dimensional lattices in both x- and y-directions, which is the case at pH 7. Two-dimensional plates were formed, even stacking in the z-direction. At pH 10, the partially destabilized interface 2 caused the assembly to preferentially form needle-like structures with preferential growth in x-direction.

3.7 Conclusion

The manipulation of the pH of peptide assembly solutions provided pathways of assembly to form a diverse set of self-assembled structures from a single de novo

designed peptide tetramer bundle. Nanotubes formed at low pH (4.5) are comprised of walls made from a single layer of peptide bundles in a tilted-alignment caused by repulsion of the positively charged N-terminus and amino acid residues located near the end of the bundle-bundle interfaces. At pH 7, which is near the pI of the peptide sequence, this repulsive interaction is weak, and the self-assembly process leads to the formation of two-dimensional platelets. At pH 10, the interaction along a bundle-bundle interface in the two-dimensional assembled state becomes weakened, causing some disassociation of this particular interface and resulting in needle-like structures. These three different nanostructures are able to form with the same designed peptide molecules and the same self-assembled tetrameric coiled-coil building blocks but with different inter-bundle interactions introduced by variations in solution pH. Computational design of the stable coiled-coil building blocks ensures a robust coiled-coil structure to form various inter-bundle assemblies under a variety of solution conditions, suggesting important opportunities to tailor the structures of this class of associating peptides.

REFERENCES

1. Zhang, H. V.; Polzer, F.; Haider, M. J.; Tian, Y.; Villegas, J. A.; Kiick, K. L.; Pochan, D. J.; Saven, J. G. Computationally Designed Peptides for Self-Assembly of Nanostructured Lattices. *Sci. Adv.* **2016**, *2* (9), e1600307.
2. Lohr, A.; Lysetska, M.; Würthner, F. Supramolecular Stereomutation in Kinetic and Thermodynamic Self-Assembly of Helical Merocyanine Dye Nanorods. *Angew. Chemie - Int. Ed.* **2005**, *44* (32), 5071–5074.
3. Tidhar, Y.; Weissman, H.; Wolf, S. G.; Gulino, A.; Rybtchinski, B. Pathway-Dependent Self-Assembly of Perylene Diimide/Peptide Conjugates in Aqueous Medium. *Chem. - A Eur. J.* **2011**, *17* (22), 6068–6075.
4. Hoeben, F. J. M.; Jonkheijm, P.; Meijer, E. W.; Albertus P. H. J. Schenning. About Supramolecular Assemblies of π -Conjugated Systems. *Angew. Chem. Int. Ed. Engl.* **2014**, *53* (46), 12537–12541.
5. Kühnle, H.; Börner, H. G. Biotransformation on Polymer-Peptide Conjugates: A Versatile Tool to Trigger Microstructure Formation. *Angew. Chemie - Int. Ed.* **2009**, *48* (35), 6431–6434.
6. Cui, H.; Cheetham, A. G.; Pashuck, E. T.; Stupp, S. I. Amino Acid Sequence in Constitutionally Isomeric Tetrapeptide Amphiphiles Dictates Architecture of One-Dimensional Nanostructures. *J. Am. Chem. Soc.* **2014**, *136*, 12461–12468.
7. Yu, Z.; Tantakitti, F.; Yu, T.; Palmer, L. C.; Schatz, G. C.; Stupp, S. I. Simultaneous Covalent and Noncovalent Hybrid Polymerizations. *Science* **2016**, *351* (6272), 497–502.
8. Merg, A. D.; Boatz, J. C.; Mandal, A.; Zhao, G.; Mokashi-Punekar, S.; Liu, C.; Wang, X.; Zhang, P.; van der Wel, P. C. A.; Rosi, N. L. Peptide-Directed Assembly of Single-Helical Gold Nanoparticle Superstructures Exhibiting Intense Chiroptical Activity. *J. Am. Chem. Soc.* **2016**, *138* (41), 13655–13663.
9. Zhong, S.; Cui, H.; Chen, Z.; Wooley, K. L.; Pochan, D. J. Helix Self-Assembly through the Coiling of Cylindrical Micelles. *Soft Matter* **2008**, *4* (1), 90–93.

10. Yan, X.; Cui, Y.; He, Q.; Wang, K.; Li, J.; Mu, W.; Wang, B.; Ou-yang, Z. C. Reversible Transitions between Peptide Nanotubes and Vesicle-like Structures Including Theoretical Modeling Studies. *Chem. - A Eur. J.* **2008**, *14* (19), 5974–5980.
11. Pashuck, E. T.; Stupp, S. I. Direct Observation of Morphological Transformation from Twisted Ribbons into Helical Ribbons. *J. Am. Chem. Soc.* **2010**, *132* (26), 8819–8821.
12. Aggeli, A.; Nyrkova, I. A.; Bell, M.; Harding, R.; Carrick, L.; McLeish, T. C. B.; Semenov, A. N.; Boden, N. Hierarchical Self-Assembly of Chiral Rod-like Molecules as a Model for Peptide β -Sheet Tapes, Ribbons, Fibrils, and Fibers. *Proc. Natl. Acad. Sci.* **2001**, *98* (21), 11857–11862.
13. Morris, K. L.; Zibae, S.; Chen, L.; Goedert, M.; Sikorski, P.; Serpell, L. C. The Structure of Cross- β Tapes and Tubes Formed by an Octapeptide, A β 1. *Angew. Chemie - Int. Ed.* **2013**, *52* (8), 2279–2283.
14. Fields, G. B.; Noble, R. L. Solid Phase Peptide Synthesis Utilizing 9-Fluorenylmethoxycarbonyl Amino Acids. *Int. J. Pept. Protein Res.* **1990**, *35* (3), 161–214.
15. Toby, B. H.; Von Dreele, R. B. GSAS-II: The Genesis of a Modern Open-Source All Purpose Crystallography Software Package. *J. Appl. Crystallogr.* **2013**, *46* (2), 544–549.
16. Kline, S. R. Reduction and Analysis of SANS and USANS Data Using IGOR Pro. *J. Appl. Crystallogr.* **2006**, *39* (6), 895–900.
17. Cooper, T. M.; Woody, R. W. The Effect of Conformation on the CD of Interacting Helices: A Theoretical Study of Tropomyosin. *Biopolymers* **1990**, *30* (7–8), 657–676.
18. Graddis, T. J.; Myszka, D. G.; Chaiken, I. M. Controlled Formation of Model Homo- and Heterodimer Coiled Coil Polypeptides. *Biochemistry* **1993**, *32* (47), 12664–12671.
19. Cui, H.; Hodgdon, T. K.; Kaler, E. W.; Abezgauz, L.; Danino, D.; Lubovsky, M.; Talmon, Y.; Pochan, D. J. Elucidating the Assembled Structure of Amphiphiles in Solution via Cryogenic Transmission Electron Microscopy. *Soft Matter* **2007**, *3* (8), 945–955.
20. Zhong, S.; Pochan, D. J. Cryogenic Transmission Electron Microscopy for Direct Observation of Polymer and Small-Molecule Materials and Structures in Solution. *Polym. Rev.* **2010**, *50* (3), 287–320.

21. Burrows, N. D.; Penn, R. L. Cryogenic Transmission Electron Microscopy: Aqueous Suspensions of Nanoscale Objects. *Microsc. Microanal.* **2013**, *19*, 1542–1553.
22. Friedrich, H.; Frederik, P. M.; De With, G.; Sommerdijk, N. A. J. M. Imaging of Self-Assembled Structures: Interpretation of TEM and Cryo-TEM Images. *Angew. Chemie - Int. Ed.* **2010**, *49* (43), 7850–7858.
23. Wirix, M. J. M.; Bomans, P. H. H.; Friedrich, H.; Sommerdijk, N. A. J. M.; De With, G. Three-Dimensional Structure of P3HT Assemblies in Organic Solvents Revealed by Cryo-TEM. *Nano Lett.* **2014**, *14* (4), 2033–2038.
24. Patterson, J. P.; Ianiro, A.; van Rijt, M.; Tuinier, R.; Esteves, C.; Sommerdijk, N. Studying Polymer Self-Assembly by Combined Cryogenic and Liquid Phase Transmission Electron Microscopy. *Microsc. Microanal.* **2016**, *22*, 14–15.
25. Vauthey, S.; Santoso, S.; Gong, H.; Watson, N.; Zhang, S. Molecular Self-Assembly of Surfactant-like Peptides to Form Nanotubes and Nanovesicles. *Proc. Natl. Acad. Sci.* **2002**, *99* (8), 5355–5360.
26. Wan, Y.; Wang, Z.; Sun, J.; Li, Z. Extremely Stable Supramolecular Hydrogels Assembled from Nonionic Peptide Amphiphiles. *Langmuir* **2016**, *32* (30), 7512–7518.
27. Egelman, E. H.; Xu, C.; DiMaio, F.; Magnotti, E.; Modlin, C.; Yu, X.; Wright, E.; Baker, D.; Conticello, V. P. Structural Plasticity of Helical Nanotubes Based on Coiled-Coil Assemblies. *Structure* **2015**, *23* (2), 280–289.
28. Xu, C.; Liu, R.; Mehta, A. K.; Guerrero-Ferreira, R. C.; Wright, E. R.; Dunin-Horkawicz, S.; Morris, K.; Serpell, L. C.; Zuo, X.; Wall, J. S.; et al. Rational Design of Helical Nanotubes from Self-Assembly of Coiled-Coil Lock Washers. *J. Am. Chem. Soc.* **2013**, *135* (41), 15565–15578.
29. Burgess, N. C.; Sharp, T. H.; Thomas, F.; Wood, C. W.; Thomson, A. R.; Zaccai, N.; Brady, R. L.; Serpell, L. C.; Woolfson, D. N. Modular Design of Self-Assembling Peptide-Based Nanotubes. *J. Am. Chem. Soc.* **2015**, *137* (33), 10554–10562.
30. Ji, Q.; Iwaura, R.; Kogiso, M.; Jung, J. H.; Yoshida, K.; Shimizu, T. Direct Sol-Gel Replication without Catalyst in an Aqueous Gel System: From a Lipid Nanotube with a Single Bilayer Wall to a Uniform Silica Hollow Cylinder with an Ultrathin Wall. *Chem. Mater.* **2004**, *16* (2), 250–254.

31. Yui, H.; Minamikawa, H.; Danev, R.; Nagayama, K.; Kamiya, S.; Shimizu, T. Growth Process and Molecular Packing of a Self-Assembled Lipid Nanotube: Phase-Contrast Transmission Electron Microscopy and XRD Analyses. *Langmuir* **2008**, *24* (3), 709–713.
32. Wall, J. S.; Hainfeld, J. F. Mass Mapping With The Scanning-Transmission Electron-Microscope. *Annu. Rev. Biophys. Biophys. Chem.* **1986**, *15*, 355–376.
33. Chen, B.; Thurber, K. R.; Shewmaker, F.; Wickner, R. B.; Tycko, R. Measurement of Amyloid Fibril Mass-per-Length by Tilted-Beam Transmission Electron Microscopy. *Proc. Natl. Acad. Sci. U. S. A.* **2009**, *106* (34), 14339–14344.
34. Tian, Y.; Zhang, H. V.; Kiick, K.; Saven, J. G.; Pochan, D. Transition from Disordered Aggregates to Ordered Lattices: Kinetic Control of the Assembly of a Computationally Designed Peptide. *Org. Biomol. Chem.* **2017**, *15* (29), 6109–6118.

Chapter 4

PEPTIDE-GOLD HYBRID MATERIALS DEVELOPMENT

4.1 Introduction

Nanomaterials possess unusual properties relative to their respective bulk state such as high catalytic activity^{1,2} and surface plasmon resonance.³ With these special properties, nanomaterials have great technological potential in the fields of chemical catalysis,² fuel cells,¹ molecular sensors,^{4,5} optics,^{6,7} surface-enhanced Raman spectroscopy,⁸ and enhanced imaging.⁹ Therefore, significant effort has been devoted to the study of nanomaterials regarding how to control the diameter, shape, and assembly of materials for desired properties. There usually are two strategies to produce nanomaterials. Top-down strategies, such as lithography, are expensive because of the need to pattern and grow materials at the nanometer scale. Bottom-up strategies, in contrast, are relatively less expensive and involve the reaction of precursor molecules or individual atoms to nucleate and grow into nanoparticles.¹⁰ In order to achieve high homogeneity of the nanoparticles formed via this chemical method, all of the particles in solution need to terminate growth at the same time.¹¹ Therefore, additive ligands are usually used in the synthesis of nanoparticles to passivate the surface growth. In the bottom-up production of gold nanoparticles, for example, there exist many, commonly used ligands such as ketones,¹⁰ amino acids,^{12,13} sulfur ligands,⁶ polyelectrolytes,^{10,11,14–16} surfactants,¹⁷ phosphines,^{18,19} ionic liquids,^{20–22} and solution ions, such as hydride and boride.^{23–27} Synthesis conditions can be controlled using a variety of conditions, including the choices of ligands, the

ratio of ligands to precursor molecules, the choice of reducing agents, and solution pH. Such variation of solution conditions allows control over the diameter distributions and shapes of nanoparticles,^{26–29} and examples include dendritic particles,¹ polyhedral particles,¹ nanoplates,³⁰ branched nanostructures,³⁰ nanorods,^{10,31} nanochains²² and a variety of anisotropic particles.^{7,10,11,15,16,31}

In addition to the control of individual nanoparticle structure, inter-particle interactions can be utilized to direct higher-order assembly of nanoparticles. For example, ligand-stabilized nanoparticles can pack into close-packed symmetries in which the inter-particle spacing can be adjusted by the alkyl chain length and branches of ligands.^{17,24,32} More specific organization of nanoparticles, such as directional end-to-end connection, can be achieved via the controlling of inter-particle polymer ligand interaction in certain solution conditions.³³ Peptides have been used to modify nanoparticles where the inter-particle assembly can be induced or disrupted depending on the formation or dissociation of inter-particle peptide coiled-coils.^{34–37} Other assembled structures, such as hollow capsids, have been formed from assembled cobalt nanoparticles directed by the hydrogen bonds of ligands.³⁸ One-dimensional nanoparticle chains were reported to have assembled with the guidance of oleylamine-ligated lead sulfate clusters.³⁹ More complicated and controllable nanoparticle assemblies can be constructed with pre-formed templates interacting with desired nanoparticle ligands or nanoparticle surfaces.^{40–44} For example, adenine-functionalized carbon nanotubes were reported to template the one-dimensional growth of silver nanoparticles through adenine-metal coordination.⁴⁵ Polymer self-assembled micelles,^{46,47} self-assembled lamellae⁴⁸ and polymer single crystals^{49,50} were reported to precisely guide the organization of nanoparticles through electrostatic interaction,

hydrogen bonding, gold-thiol bonds, gold-pyridine bonds, or other coordinate bonding. Thiol-functionalized DNA can be grafted on to gold nanoparticles through gold-thiol bonds and can be used to guide programmable and directional inter-particle assembly⁵¹⁻⁵³ or precisely controlled deposition of nanoparticles onto existing complex DNA scaffolds.^{54,55} Even without thiol-functionality, electrostatic interaction between DNA and inorganic precursor ions or nanoparticle ligands were reported to guide the patterning of inorganic species on DNA scaffolds.^{56,57} In nature, organisms can exhibit the ordered formation of inorganic species guided by proteins, also known as biomineralization.⁵⁸ Therefore, more assembled structures and choices of binding moieties can be explored with the use of proteins and peptides to template the formation of inorganic nanomaterials. For example, certain short peptide sequence, such as CALNN was rationally designed and identified as a highly effective binding ligand to gold nanoparticles.⁵⁹ Charged amino acid residues on self-assembled peptides, proteins and virus capsids can be used as generic binding sites for the formation of site-specific metallic nanoparticles.⁶⁰⁻⁶⁵ Nanoparticle-binding sites also can be created by conjugating peptide binding domains to alkyl chains. The self-assembled nanofibers from these amphiphilic molecules have successfully templated of a variety of different inorganic nanomaterials⁶⁶⁻⁶⁹ into tunable morphologies.⁷⁰⁻⁷² By deliberately modifying self-assembled peptide/protein structures with a short peptide sequence as an inorganic-binding epitope or single amino acid ligand such as cysteine, the inorganic species can be templated on these self-assembled structures and exhibit the same nanostructure as the biomolecular template.⁷³⁻⁷⁸ Therefore, via templated growth and assembly of inorganic nanoparticles, a path is provided from nanoparticles to ordered nanomaterials and potential nanodevices.

In this **Chapter 4**, we present the templated growth of gold nanomaterials on computationally designed self-assembled peptide nanostructures. Fundamental to this work is the peptide computational design which makes it possible to create peptide self-assembled nanostructures with desired shape and organization, thus allowing the programmable construction of inorganic nanomaterials. We investigated different gold nanoparticle growth pathways during the in-situ solution peptide-templated synthesis process as well as the adsorption of pre-made gold colloidal nanocrystals on pre-existing peptide templates. The peptide templates can effectively direct the organization of gold nanoparticles. Moreover, with the control of the underlying peptide assembly kinetics, various template morphologies can be formed that allow a variety of templated gold nanostructures to be produced.

4.2 Materials and Methods

4.2.1 Peptide Synthesis

Peptides were synthesized at a 0.1 mmol scale on an Automated microwave solid phase peptide synthesizer Liberty Blue (CEM Corporation). Standard Fmoc chemistry protocols were used.⁷⁹ Amino acids and rink amide resin were purchased from ChemPep Inc. Solvent dimethylformamide (DMF) and acetylation agent acetic anhydride were purchased from Fisher Scientific; both are certified ACS reagent grade with assay percent range $\geq 99.8\%$. Deprotection agent piperidine and activator N,N'-Diisopropylcarbodiimide (DIC) were purchased from Sigma-Aldrich; both are reagent grade with assay percent range $\geq 99\%$. Activator base ethyl(hydroxyimino) cyanoacetate (oxyma) was purchased from CEM corporation. All reagents were used

as received. Swelling step was performed for resin with 10 mL DMF for 5 min at room temperature. Deprotection was accomplished using 10 eqv. piperidine (20%-vol in DMF) with a two-step microwave heating program: 75°C-15s and 90°C-50s. Coupling was achieved using 5 eqv. oxyma (1 M in DMF), 5 eqv. DIC (0.5 M in DMF) and 5 eqv. amino acid (0.2 M in DMF) with a two-step microwave heating program: 75°C-15s and 90°C-110s. Final acetylation was performed using 5 eqv. acetic anhydride (10%-vol in DMF) with single step microwave heating program: 65°C-120s. Peptide cleavage was achieved by shaking in a cleavage cocktail of 9.5 mL trifluoroacetic acid (TFA), 2.5 mL triisopropylsilane, 2.5 mL 1,2-ethanedithiol, and 2.5 mL Milli-Q water for 2 hours. The peptide was then precipitated by adding the cleavage cocktail and cleaved peptide to diethyl ether. The mixture was centrifuged and washed and centrifuged three times with diethyl ether. The resulting peptide was dried in air, dissolved in water, and lyophilized.

4.2.2 Peptide Purification

Purification was performed similarly as described in **Chapter 2**.

The collected fractions were examined by Xevo G2-S QToF time of flight mass spectrometry (Waters Corporation). Injection was run through an UPLC system (Waters Corporation) using ACQUITY UPLC® Protein BEH C4 1.7 µm column (Waters Corporation), with gradient from 95% Milli-Q water (containing 0.2%-vol TFA)/5% acetonitrile (containing 0.2%-vol TFA) v/v to 5% Milli-Q water (containing 0.2%-vol TFA)/95% acetonitrile (containing 0.2%-vol TFA) v/v in 5min. Pure fractions were combined and lyophilized. TOF mass chromatographs and combined mass spectra are shown in **Figure 4.1** and **4.2**.

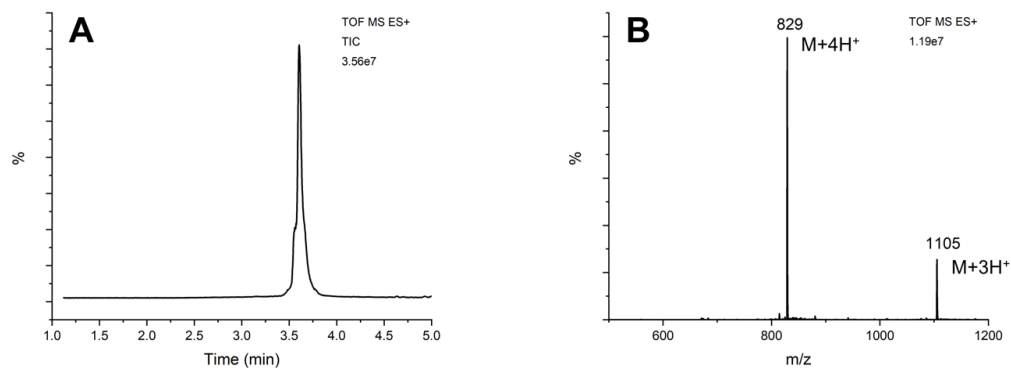


Figure 4.1 **A:** Time-of-flight mass chromatograph for Ac-C-P222 peptide. Peptides were eluted during the gradient of 95% solvent A to 5% solvent A in 5 min with first 0.5 min elution uncollected, in which solvent A is Milli-Q water containing 0.1%-vol TFA, solvent B is acetonitrile containing 0.1%-vol TFA. **B:** Combined mass spectrum of the major peak in mass chromatograph showing the m/z values. Designed molecular weight: [M] 3313 Da. The accordingly calculated mass is: [M+3H⁺] 3316 Da, [M+4H⁺] 3317 Da. The experimental measured mass is: [M+3H⁺] 3315 Da, [M+4H⁺] 3316 Da.

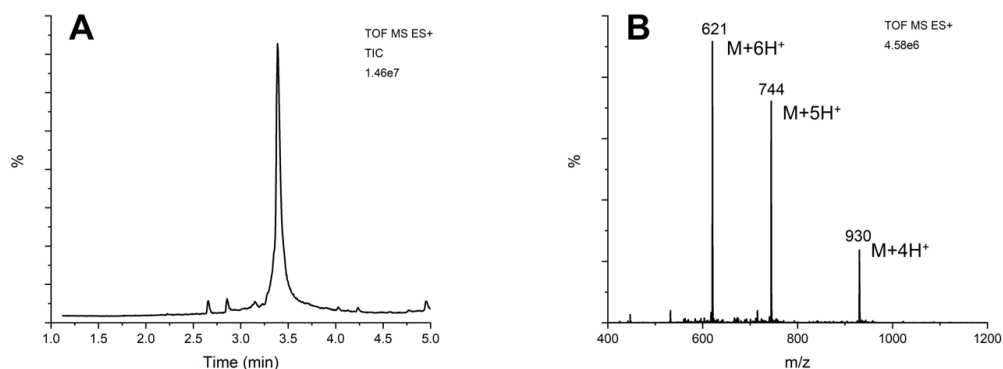


Figure 4.2 **A:** Time-of-flight mass chromatograph for Ac-C-P422 peptide. Peptides were eluted during the gradient of 95% solvent A to 5% solvent A in 5 min with first 0.5 min elution uncollected, in which solvent A is Milli-Q water containing 0.1%-vol TFA, solvent B is acetonitrile containing 0.1%-vol TFA. **B:** Combined mass spectrum of the major peak in mass chromatograph showing the m/z values. Designed molecular weight: [M] 3717 Da. The accordingly calculated mass is: [M+4H⁺] 3721 Da, [M+5H⁺] 3722 Da, [M+6H⁺] 3723 Da. The experimental measured mass is: [M+4H⁺] 3720 Da, [M+5H⁺] 3720 Da, [M+6H⁺] 3726 Da.

4.2.3 Peptide Solution Self-assembly Experiments

The purified peptides were dissolved in buffer solutions to give a desired peptide concentration. 2.5 eqv. tris(2-carboxyethyl)phosphine hydrochloride (TCEP, Sigma Aldrich) with respect to the amount of peptides was added to prevent di-sulfur bond formation. 50 mM sodium acetate buffer in pH 4.5 and 50 mM phosphate buffer in pH 7 were used without extra salt addition. The solution was heated to 90°C for 2 hours to assure complete dissolution of the peptides, then was let to cool ambiently to room temperature or incubated at 50°C to start assembly.

4.2.4 Templating of Gold Nanoparticles

Two strategies were applied for the gold nanoparticle templating purpose. The first strategy is in-situ solution synthesis with the use of chloroauric acid (HAuCl₄) and sodium borohydride (NaBH₄). Following the above described peptide self-assembly process, cysteine-modified peptide solution was first allowed to assemble at desired temperature for desired amount of time. Then, desired amount of HAuCl₄ solution (20 mM in DI water) and fresh NaBH₄ solution (20 mM in DI water) were successively added to peptide solution. Additional bis(p-sulfonatophenyl)phenylphosphane dehydrate (Sigma-Aldrich) was used for pH 7 condition for further gold particle stabilization purpose. The solution was gently mixed and kept at room temperatures for the growth of gold nanomaterials. The second strategy is to use pre-made gold colloidal nanocrystal solution for templating via a ligand-exchange mechanism. Commercially available 5 nm gold colloidal nanocrystal solution (stabilized suspension in 0.1 mM PBS, reactant free, Aldrich number 752568) was purchased from Sigma-Aldrich and used as received. Only Ac-C-P422 at pH 7 condition was investigated as templates due to the PBS buffer that the gold colloidal nanocrystals are dispersed in. Similarly, Ac-C-P422 peptide solution was firstly allowed to assemble for the formation of two-dimensional platelets at 50°C. Then same volume of pre-made gold colloidal nanocrystal solution was mixed with peptide solution and kept at room temperature for the adsorption of gold nanocrystals to the plates.

4.2.5 Transmission Electron Microscopy

TEM sample grid preparation and image collection were performed similarly as described in **Chapter 2**.

4.2.6 Cryogenic TEM (Cryo-TEM)

Cryo-TEM sample grid preparation and image collection were performed similarly as described in **Chapter 2**.

4.2.7 Circular Dichroism

Secondary structure and coiled-coils were analyzed with the same method and procedures as described in **Chapter 2**.

4.2.8 Gold Nanowires Deposition

Surface deposition method was applied for the fabrication of gold nanowire. A freshly Plasmon cleaned mica sheet was used a substrate. The mica sheet was firstly submerged into Ac-C-P222_9 peptide tube solution for peptide tubes to be deposited onto mica substrate. Then the mica sheet was submerged into 20 mM HAuCl₄ solution for 30 min for the AuCl₄⁻ to be absorbed onto peptide tubes. In the last step, the mica sheet was submerged into 20 mM NaBH₄ solution for 1 hour for reduction reaction. A red-ish thin layer was formed after these steps.

4.2.9 Atomic Force Microscopy

Atomic force microscopy was performed on a Bruker Multimode using Bruker ScanAsyst Air ultra-sharp tips with a nominal tip radius of 2 nm and a spring constant of 0.4 N/m. Samples were prepared by casting 15 μL of assembly solution on a freshly cleaved mica disc, the solution retained for 5 min on the disk, excess liquid blotted from the substrate with filter paper, and any remaining solution dried with application of compressed air. The instrument was operated in contact mode. Micrographs were recorded digitally using Bruker nanoscope software using 512 to 1024 lines at 0.5-1 Hz scan rate.

4.2.10 Wide and Small Angle X-ray scattering

SAXS measurements were conducted at 5ID-D DND-CAT beamline at the Advanced Photon Source (APS) of Argonne National Laboratory (Argonne, IL). The beamline was operated at 17 keV corresponding to a wavelength of 0.7293 Å. A triple-detector setup was used to collect scattering data from small-angle, mid-angle and wide-angle regime simultaneously. The detector for small-angle scattering data collection was set at an 8507 mm sample distance to collect data from $2\theta = 0.015^\circ$ - 0.910° range. The detector for mid-angle scattering data collection was set at a 1013.6 mm sample distance to collect data from $2\theta = 0.872^\circ$ - 5.500° range. The detector for wide-angle scattering data collection was set at a 200.46 mm sample distance to collect data from $2\theta = 4.500^\circ$ - 30.000° range. Only wide-angle scattering data was presented in this work. For measurement, 100 μ L of peptide assembly solution in buffer was transferred into quartz glass capillaries with a diameter of around 0.1 cm, which would be exposed in X-ray beam. 5 exposures of 1 sec were recorded. Scattering from buffer was recorded in the same way for background subtraction. The single spectra were averaged and subtracted for background using GSAS-II software package.⁸⁰

4.2.11 Ultraviolet-visible Spectroscopy (UV-vis)

UV-vis spectra of the in-situ solution gold nanoparticle synthesis process templated by Ac-C-P222 peptide were recorded using a Cary 60 UV-Vis spectrophotometry (Agilent Technologies). The sample solution was transferred into a quartz cuvette with 1mm path length (110-QS, Hellma, Inc.). Blank buffer solution with 0.5 mM TCEP was used for the background subtraction. Sample spectra were

recorded from 200-1000 nm at room temperature, every 30 min, with a scanning rate of 600 nm/min during the continuous monitoring process.

4.3 Peptide-mediated Gold Nanoparticle Structures

4.3.1 Cysteine-modified Peptide Assemblies

In **Chapter 2** and **Chapter 3**, we have demonstrated the designed P222_9 and P422_1 sequences (sequences details seen previous chapters) can assemble into one-dimensional nanotubes at pH 4.5 and two-dimensional plate-like lattice structures at pH 7, respectively. Here we add a single cysteine to the acetylated N-terminus of the sequences to introduce thiol groups into the peptide assemblies for the templating of gold (Au) nanomaterials. Therefore, two sequences (Ac-C-P222 (Ac-C DGRIE GMAEA IKKMA YNIAD MAGRI WGEA-NH₂) and Ac-C-P422 (Ac-C DQEIR QMAEW IKKMA QMIDK MAHRI DREA-NH₂)) were produced. The self-assembled structures of the cysteine-modified peptides examined by TEM are shown in **Figure 4.3**. The Ac-C-P222 assembled into nanotubes after being incubated in pH 4.5 buffer at room temperature for 18 hours, as previously observed for the P222_9 peptides. For Ac-C-P422, two-dimensional lattice structures can be observed after the incubation in pH 7 buffer, at 50°C for 7 hours, which are similar to the structures assembled from the P422_1 peptides.^{81,82} Therefore, these two types of peptide nanomaterials were used for further studies of templating.

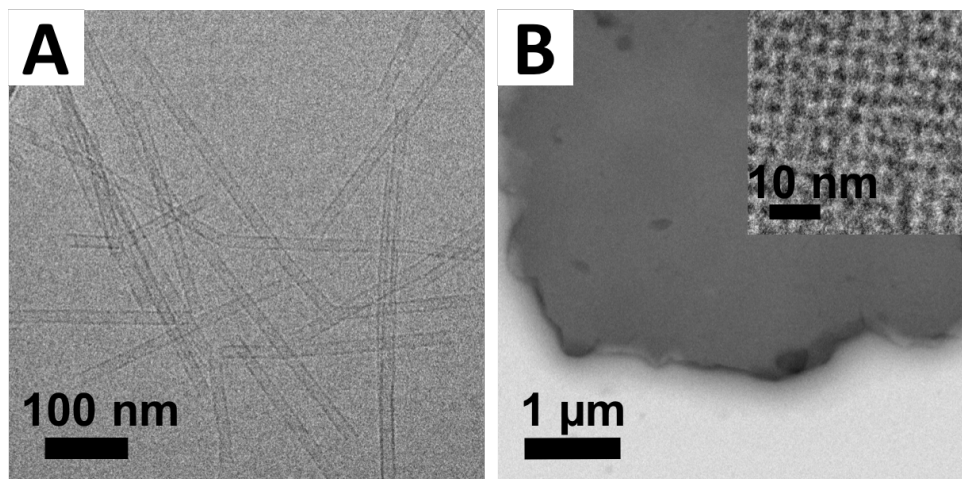


Figure 4.3 TEM micrographs of cysteine-modified peptide assemblies. **A:** Ac-C-P222 with 0.2 mM concentration, in 50 mM pH 4.5 buffer with 0.5 mM TCEP, assembled at room temperature for 18 hours. Hollow nanotubes can be observed under cryo-TEM. **B:** Ac-C-P422 with 0.5 mM concentration, in 50 mM pH 7 buffer with 1.25 mM TCEP, assembled at 50°C for 7 hours. Inset is the HRTEM image showing the lattice structures.

4.3.2 One-dimensional and Two-dimensional Gold Nanoparticle Arrays Templated by Peptide Assembly

Two strategies were applied for gold nanoparticle templating. The first strategy involved in-situ solution synthesis of inorganic particles with the use of chloroauric acid (HAuCl_4) and sodium borohydride (NaBH_4). The second strategy was to employ pre-made gold colloidal nanocrystals in solution for the templating of desired, inter-particle arrays via a particle-ligand exchange mechanism. For templating purposes, peptide solutions were allowed to assemble into desired template morphologies before the addition of gold species.

In the case of one-dimensional nanotube-templating, 0.2 mM Ac-C-P222 peptides were pre-assembled in pH 4.5 buffer at room temperature for 18 hours (one-dimensional nanotubes were formed similarly to those shown in **Figure 4.3A**). In-situ

gold nanoparticle synthesis was performed on the nanotubes by the successive addition of 2 equivalents HAuCl_4 and 2 equivalents NaBH_4 into the peptide nanotube suspension to reach the final concentration of 0.4 mM for each precursor reagent. Upon mixing of the gold synthesis reactants and the peptide nanotube templates, the solution exhibited a slow color transition from pale yellow to pink over a period of 12 hours. After 2 hours of room temperature growth, the templated gold nanoparticle morphology was examined via TEM. The results, shown in **Figure 4.4A-4.4C**, indicate the formation of gold nanoparticles and the ordered organization of gold nanoparticles into one-dimensional chain-like structures. In the case of two-dimensional templating of gold nanoparticles, 0.5 mM Ac-C-P422 peptides were pre-assembled in pH 7 buffer at 50°C for 6 hours (two-dimensional plate-like structures were formed similarly to those shown in **Figure 4.3B**). 10 equivalents HAuCl_4 , 10 equivalents NaBH_4 , and 5 equivalents bis(p-sulfonatophenyl)phenylphosphane dehydrate (for gold nanoparticle stabilization purposes) were added successively into solutions of pre-formed peptide plates to reach the final concentration of 5 mM for each precursor reagent and 2.5 mM for the stabilizing agent. Upon mixing, the color of the solution quickly turned red. After 24 hours of room temperature inorganic particle growth, TEM images indicated the formation of two-dimensional gold nanoparticle arrays as shown in **Figure 4.4D-4.4F**. For both cases, HAADF images were recorded as shown in **Figure 4.4C** and **4.4F** to reveal and confirm the formation of inorganic particles.

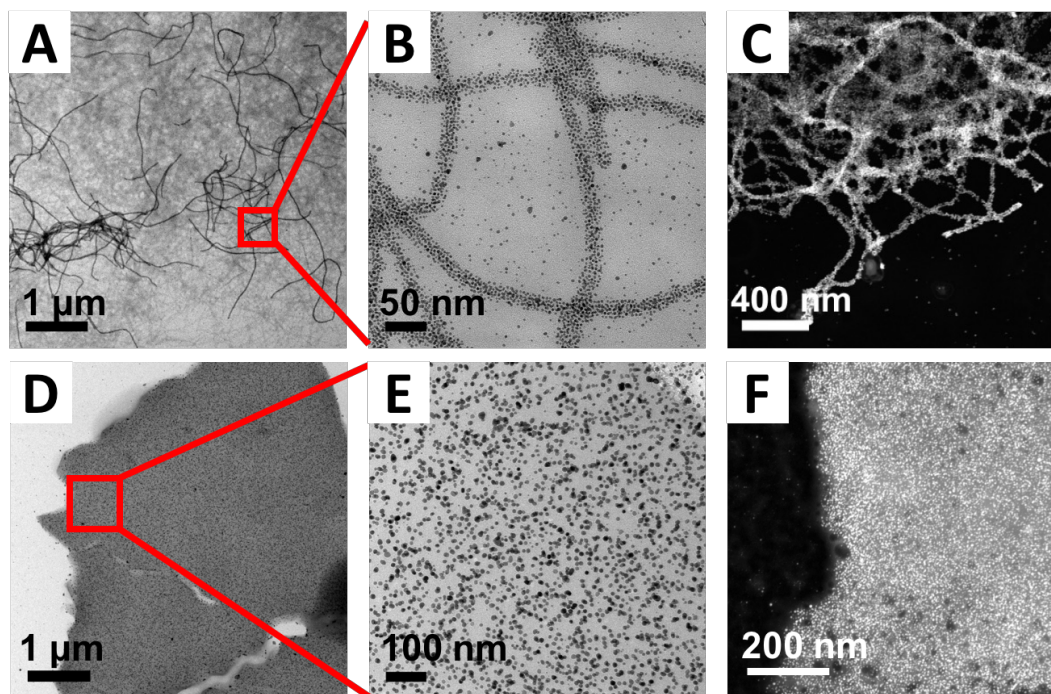


Figure 4.4 TEM images show the nanostructures of solution synthesized gold nanoparticles templated by cysteine-modified peptides. **A:** One-dimensional gold nanoparticle chains templated by peptide nanotubes in 50 mM pH 4.5 buffer with 0.2 mM Ac-C-P222 peptides, 0.4 mM HAuCl₄ and 0.4 mM NaBH₄, and incubated at room temperature for 2 hours. **B:** High magnification image showing individual gold nanoparticles. **C:** HAADF image with bright dots showing the inorganic nanoparticles. **D:** Two-dimensional gold nanoparticle arrays templated by peptide plates in 50 mM pH 7 buffer with 0.5 mM Ac-C-P422 peptides, 5 mM HAuCl₄, 5 mM NaBH₄ and 2.5 mM bis(*p*-sulfonatophenyl)phenylphosphane dehydrate and incubated at room temperature for 24 hours. **E:** High magnification image showing individual gold nanoparticles. **F:** HAADF image with bright dots showing the inorganic nanoparticles.

As a comparison study, assembled nanotubes and plates of the peptides without cysteine, P222_9 and P422_1, also were applied as templates for the solution synthesis of gold nanoparticles. The structures of synthesized gold nanoparticles examined by TEM are shown in **Figure 4.5**. The formed gold nanoparticles exhibit no

templated organization effect from the peptide assembled morphologies. Therefore, it is clear that inclusion of thiol-functionalization of the assemblies is critical as a binding site for gold nanoparticle nucleation and growth, yielding the templated particle arrays.

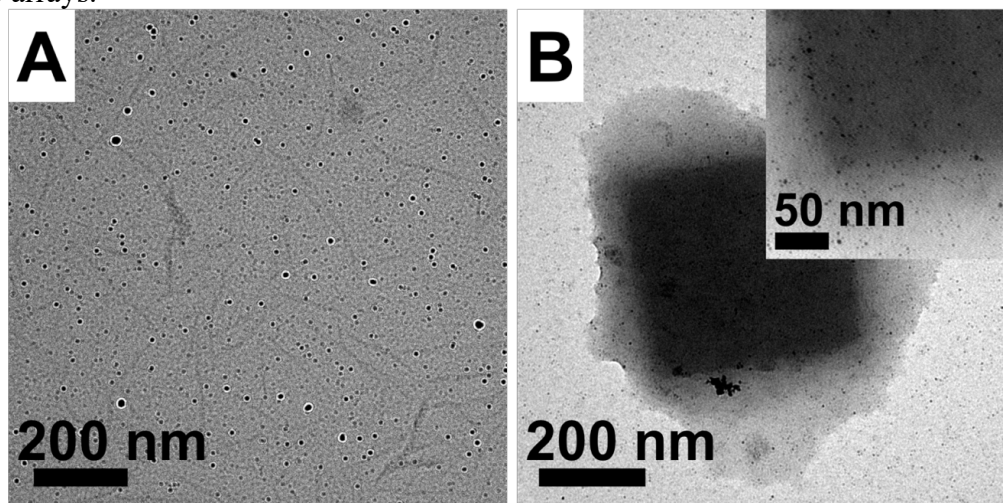


Figure 4.5 TEM images show the nanostructures of solution synthesized gold nanoparticles templated by non-cysteine peptides. **A:** Gold nanoparticles templated by peptide nanotubes in 50 mM pH 4.5 buffer with 0.2 mM P222_9, 0.4 mM HAuCl₄ and 0.4 mM NaBH₄. Image was taken under high defocus condition to reveal peptide nanotubes. The formed gold nanoparticles exhibit no templating effect. **B:** Gold nanoparticles templated by peptide plates in 50 mM pH 7 buffer with 0.5 mM P422_1, 5 mM HAuCl₄, 5 mM NaBH₄ and 2.5 mM bis(*p*-sulfonatophenyl)phenylphosphane dehydrate. Inset is the zoom-in image showing individual nanoparticles. The formed gold nanoparticles exhibit no templating effect.

In the absence of assembled peptide templates, solution synthesis produced irregular gold nanostructures, as shown in **Figure 4.6**. When HAuCl₄ reacted with an equal molar ratio of NaBH₄ (at a concentration of 1 mM) in either 50 mM pH 4.5 sodium acetate buffer or 50 mM pH 7 phosphate buffer, the color of the solution turned from pale yellow to deep purple/black immediately and produced irregular, so-

called “star gold” structures or network-like structures, as shown in **Figure 4.6A** and **4.6B**, respectively. NaBH_4 is a strong reducing agent, that is usually used as initial nucleation agent.²⁷ When gold is reduced for nucleation and growth with the assistance of NaBH_4 and no molecular ligands to stabilize forming particles, irregular structures as observed here are likely to be formed.⁸³

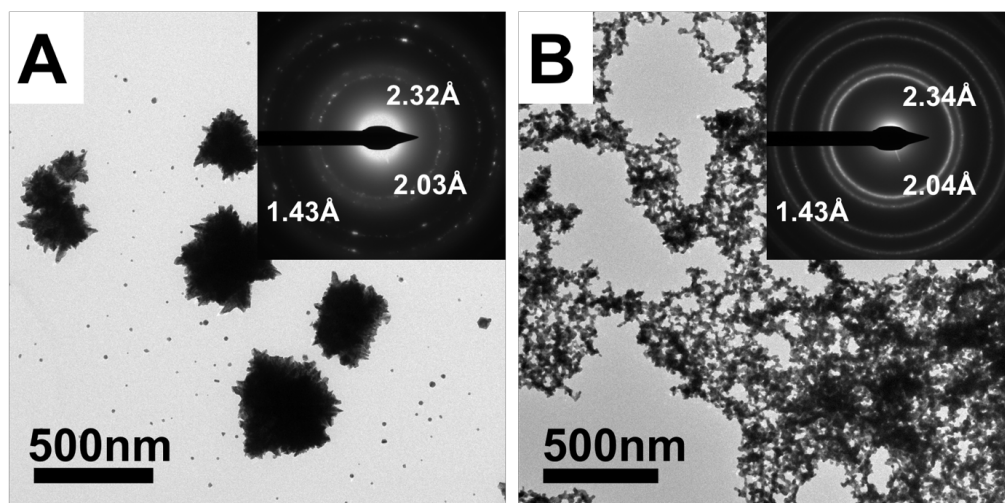


Figure 4.6 TEM images show the morphologies of un-templated growth of gold materials in solution. **A:** 1 mM HAuCl_4 in 50 mM pH 4.5 buffer and reduced by the same molar ratio of NaBH_4 and examined at 5 min time point. Inset is the electron diffraction pattern showing the crystalline gold. **B:** 1 mM HAuCl_4 in 50 mM pH 7 buffer and reduced by the same molar ratio of NaBH_4 and examined at 5 min time point. Inset is the electron diffraction pattern showing the crystalline gold.

When employing pre-made 5-nm gold colloidal nanocrystal (denoted as 5 nm AuNP hereafter) solutions for assembly, Ac-C-P422 platelets at pH 7 were used as templates because the received pre-made gold colloidal nanocrystals are dispersed in a pH 7 PBS buffer. The Ac-C-P422 peptides at 0.5 mM were pre-assembled in pH 7 buffer at 50°C for 6 hours to permit platelet formation. The same volume of 5 nm

AuNP solution was mixed with pre-assembled peptide solution and incubated at room temperature for 24 hours. A precipitate with red color formed gradually and the supernatant, which was initially light red, became colorless during incubation. The templated 5 nm AuNP morphology revealed by TEM micrographs in **Figure 4.7** shows that 5 nm AuNPs were adsorbed on the peptide plates in two-dimensional arrays. This templating process likely occurred via a ligand-exchange mechanism.²⁵ In this case, the peptide with the thiol-functionality can serve as the binding ligands for the 5 nm AuNPs and drive the ligand-exchange reaction.⁸⁴

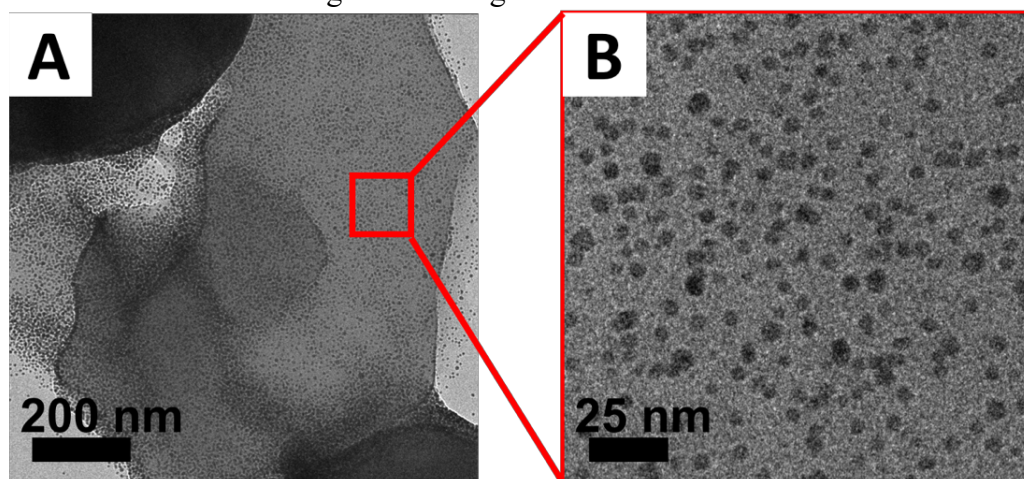


Figure 4.7 TEM images show the nanostructure of templated, pre-made 5 nm AuNPs. **A:** Two-dimensional 5 nm AuNP arrays templated by Ac-C-P422 peptide plates in 50 mM pH 7 buffer. The peptide plate solution and pre-made 5 nm AuNP solution were mixed and incubated at room temperature for 24 hours for examination. **B:** High magnification image showing individual 5 nm AuNPs.

4.3.3 Optical Property of Templated One-Dimensional Gold Nanoparticle Chain

As mentioned in the introduction, surface plasmon resonance (SPR) resulting from the collective oscillation of free conduction electrons, is an important feature of nanoparticles.¹¹ Colloidal gold nanoparticle solutions can exhibit different

characteristic colors from red to deep purple depending on the size of nanoparticles and the interparticle assembled state. Furthermore, the electromagnetic coupling between nanoparticles becomes more pronounced when the particle-particle distance is smaller than five times the particle radius, and this coupling can lead to a red-shift in the wavelength of the SPR peak.⁸⁵⁻⁸⁷ The plasmonic property has been utilized with gold nanoparticles in applications such as high sensitivity sensors,¹¹ enhanced imaging agents,⁹ surface-enhanced Raman spectroscopy,⁸ and plasmon solar cells.^{88,89}

For the above one-dimensional chain-like gold nanoparticle assemblies, gold nanoparticles were synthesized in situ, and the Ac-C-P222 nanotubes templated chains particles (shown in **Figure 4.4A-4.4C**). These colloidal solutions were stable and exhibited a pink color, indicative of the collective plasmon phenomena.^{3,11} The gold nanoparticle growth solution was incubated with Ac-C-P222 nanotubes for an extended time, and the nanostructure of the templated gold nanoparticles after 4 days of growth was examined by TEM, shown in **Figure 4.8A**. UV-Vis spectra were recorded to reveal the optical properties of ordered one-dimensional gold nanoparticle chains during the growth process (**Figure 4.8B**).

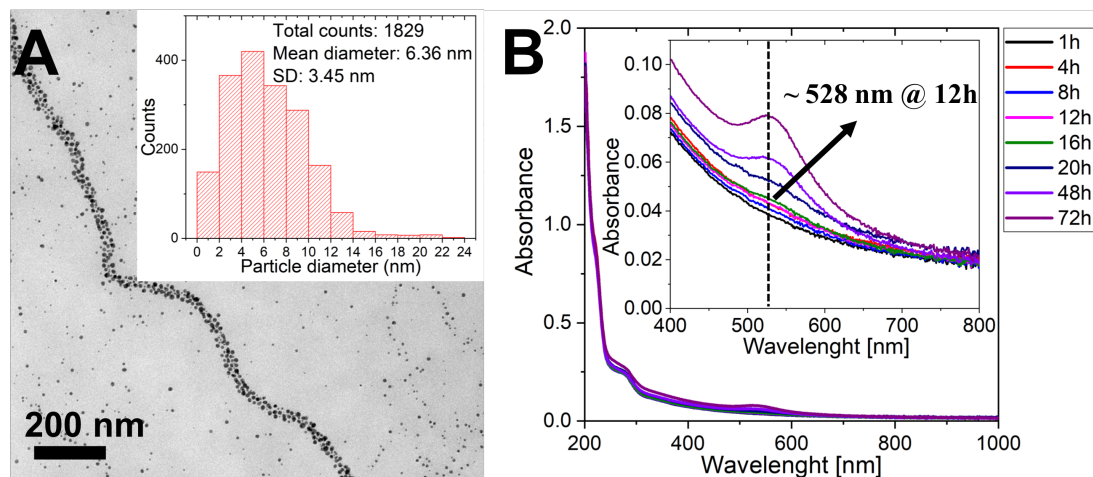


Figure 4.8 **A:** TEM image of peptide nanotube-templated growth of gold nanoparticle-chains (0.2 mM Ac-C-P222 nanotubes with 2eqv HAuCl₄ and 2eqv NaBH₄ with respect to the amount of peptides) after 4 days, inset is the gold nanoparticle diameter distribution width diameter of 6.4 nm \pm 3.4 nm. **B:** UV-Vis spectra recorded during gold nanoparticle growth process using 18 hour-assembled Ac-C-P222 peptide nanotubes as templates with 2eqv. HAuCl₄ and 2eqv. NaBH₄ with respect to the amount of peptides. The SPR peak at about 528 nm started to emerge at about 12 hours of gold nanoparticle growth.

The gold nanoparticles remain well organized in one-dimensional chain-like ensembles templated by the peptide nanotubes (**Figure 4.8A**, similar to **Figure 4.4A**) after 4 days of growth. The particle size analysis of the templated gold nanoparticles reveals the mean diameter of the gold nanoparticles to be 6.4 nm \pm 3.4 nm. (Histogram is shown in the inset of **Figure 4.8A**). Furthermore, the UV-Vis spectra exhibit SPR properties that are consistent with the close spacing of gold nanoparticles provided by the underlying peptide nanotube template (**Figure 4.8B**). During nanoparticle growth process, an SPR maximum at approximately 528 nm emerges beginning after at approximately 12 hours.¹¹ The intensity of this SPR peak continued to increase over the 72-hour time period. An SPR peak located at 528 nm usually corresponds to much

larger gold nanoparticles (diameter > 30 nm) than are observed in the TEM (diameter < 22 nm) (**Figure 4.8A**).³ Therefore, considering the much smaller gold nanoparticles observed in our study, the SPR peak at 528 nm is consistent with the coupling of the surface plasmons of closely packed, adjacent gold nanoparticles within the chain-like ensemble.^{51,90} Apart from this, the UV absorption features at approximately 219 nm and 280 nm persisted, indicative of little degradation of the peptide molecules throughout the reaction. As a comparison study, the UV-Vis spectra were monitored during gold nanoparticle synthesis using only HAuCl₄ and NaBH₄, in pH 4.5 buffer, in the absence of peptides (**Figure 4.9**). With no template present, only an absorption shoulder develops in the wavelength region of 500-550 nm; no distinctive SPR peak is observed.

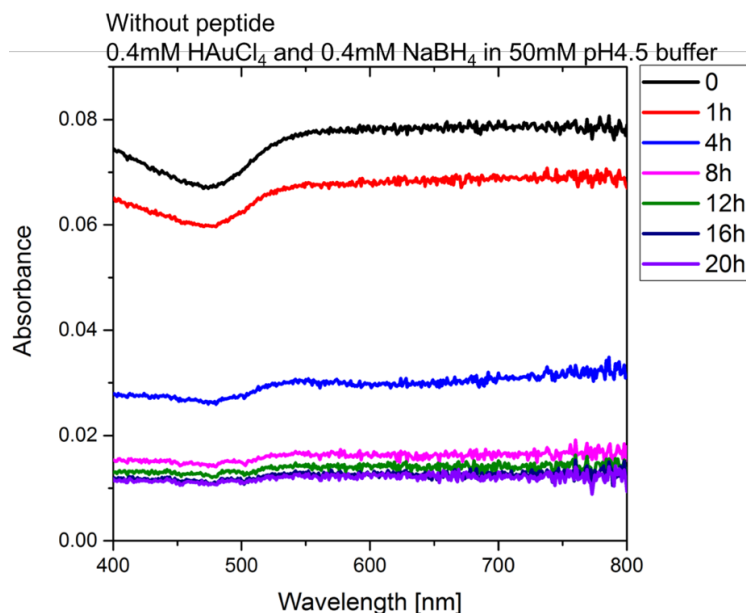


Figure 4.9 UV-Vis spectra recorded during gold nanoparticle synthesis process only using 0.4 mM H_{Au}Cl₄ and 0.4 mM NaBH₄, without peptide nanotubes as templates. No distinctive SPR peak is observed. Only an absorption shoulder appears in the wavelength region of 500nm-550nm.

4.3.4 Peptide Assembly Kinetic-Control of Gold Nanoparticle Organization

As discussed in **Chapter 2**, the assembled peptide morphologies used herein are strongly dependent on the kinetics of assembly.^{81,82} In a time-dependent, hierarchical manner, the designed peptides proceed through different assembly states: from random coils, to coiled-coil bundles, to inter-bundle morphologies. With knowledge of the assembly pathway of the peptides, gold precursor molecules or colloidal gold nanocrystal solution were introduced to the peptide templates at various peptide assembly time points to study the effect of different stages of peptide assembly on the type of gold nanostructures formed.

Ac-C-P222 was used first for the study of peptide assembly pathway effects on templated synthesis of gold nanoparticles. The peptide solution was first heated to 90°C for 2 hours to denature the peptides for a homogenous solution starting condition. In this stage, peptides existed in the form of dissolved random coils in solution (as shown by circular dichroism spectra in **Figure 4.10**, α -helical structures were mostly denatured after being incubated at 85°C for 30 min). After denaturing, the peptide solution was incubated at room temperature to start the isothermal peptide folding and assembly process. Gold precursor solutions (HAuCl₄ and NaBH₄) were added at three different peptide assembly time points: 1) 0 min at room temperature, at which point the peptides exist as denatured random coils (stage 1 in **Figure 4.11A**); 2) 10 min at room temperature, at which point the peptide coiled-coil bundles have been mostly formed while no significant peptide nanotubes are yet formed (stage 2 in **Figure 4.11A**), as shown by CD spectra in **Figure 4.10**, and 3) 18 hours, at which point well-assembled peptide nanotubes exist (stage 3 in **Figure 4.11A**). This last condition is the solution condition described in the previous section used to template the formation of one-dimensional gold chains. The gold nanostructures templated by

the peptides at different assembly stages were examined by TEM and are shown in **Figure 4.11B-4.11D**.

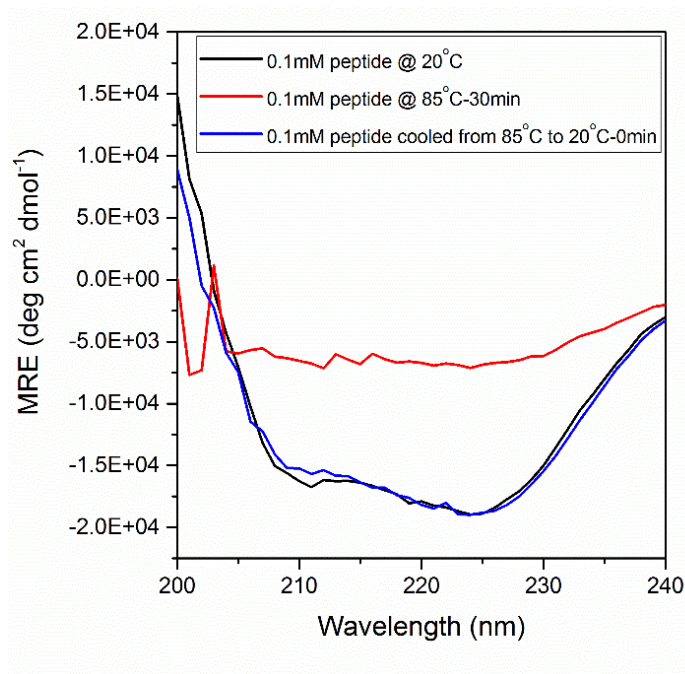


Figure 4.10 Circular dichroism spectroscopy data for Ac-C-P222 peptide with 0.1mM concentration measured at different temperatures in pH4.5 buffer condition containing 0.5mM TCEP. Data is plotted with buffer background subtracted. The spectrum measured at room temperature show typical α -helical conformation. The spectrum measured from 85°C-30min incubated the solution shows the melting of α -helical structures. The α -helical conformation can be recovered immediately once the solution is cooled, as shown by the spectrum measured from the solution cooled from 85°C to 20°C in time 0 point.

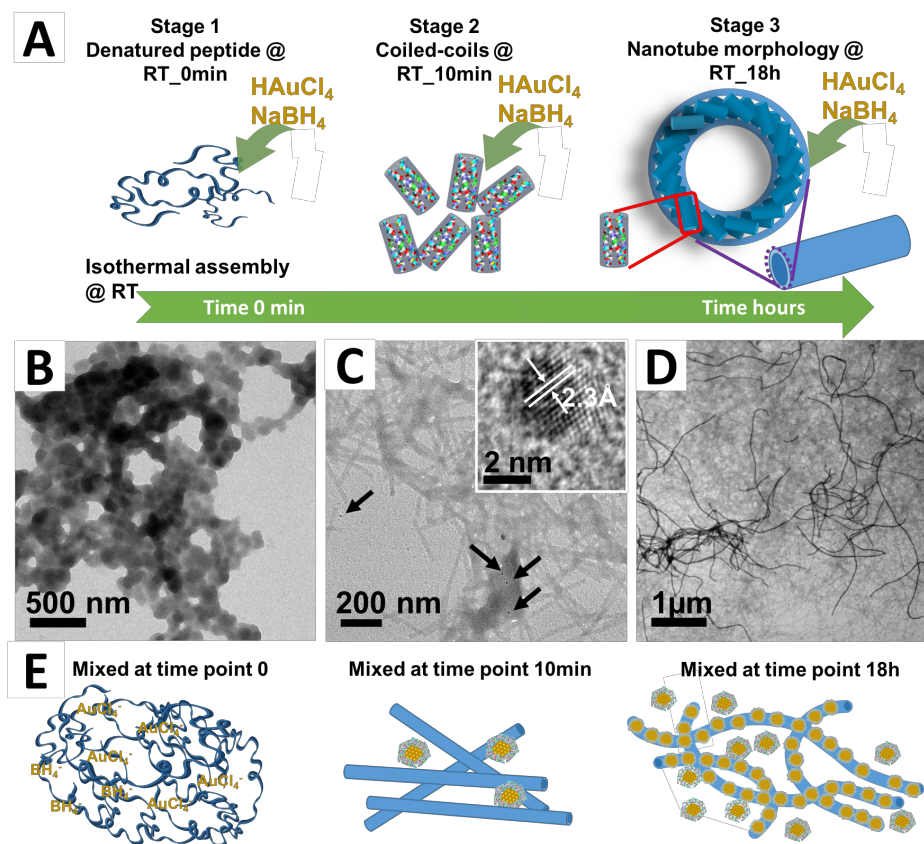


Figure 4.11 **A:** The schematic of the kinetic assembly process of Ac-C-P222. In stage 1, peptides exist as denatured random coils. In stage 2, peptides mainly exist as folded coiled-coil bundles, depicted by cylindrical ribbon-drawings. In stage 3, peptides mainly exist as assembled nanotube morphologies. **B:** TEM image showing the nanostructures formed from 2 eqv. gold precursor solution added at stage 1 of the peptide assembly process. The structure was examined 2 hours after mixing. **C:** TEM image showing the nanostructures formed from 2 eqv. gold precursor solution added at stage 2 of the peptide assembly process. The structure was examined after 24 hours from the point of mixing. Inset is the HR-TEM of an individual gold nanoparticle. **D:** TEM image showing the nanostructures formed from 2 eqv. gold precursor solution added at stage 3 of the peptide assembly process. The structure was examined after 2 hours from the point of mixing. **E:** The corresponding structure models illustrating the nanostructures formed in **B-D**, respectively. The sizes of objects are not in scale. After the attachment of gold nanoparticles, the peptide nanotubes exhibit more flexibility.

When gold precursor solution was mixed with denatured Ac-C-P222 (stage 1 in **Figure 4.11A**), white/yellow precipitate formed immediately, indicative of a disordered aggregate morphology (**Figure 4.11B**). This is likely from the interactions of the tetrachloroaurate anions with the positively charged peptides (Ac-C-P222 is expected to be positively charged at pH 4.5). When the AuNP precursor reagents were added to Ac-C-P222 solution at the time point of 10 minutes (stage 2 in **Figure 4.11A**), no precipitate formed. However, after 24 hours, only a few gold nanoparticles were observed, and most peptide nanotubes were devoid of gold nanoparticles (**Figure 4.11C**). This is due to the existence of coiled-coil bundles as the major specie in stage 2 when the gold precursors (HAuCl_4 and NaBH_4) were added to the solution. As shown by the cryo-TEM images in **Figure 4.12**, after 20 minutes of assembly only a limited number of short nanotubes were formed. Therefore, at the time point of 10 minutes peptide assembly, gold nuclei formed through a heterogeneous nucleation process mostly on the individual bundles. Bundles could act as surface passivation ligands and stabilize the gold nanoparticles, resulting in the formation of extremely small gold nanoparticles (not easily detectable under the TEM magnification for **Figure 4.11C**) not associated with any larger peptide template. When gold precursor solution was added to Ac-C-P222 solution at the time point of 18 hours (stage 3 in **Figure 4.11A**), well-assembled peptide nanotubes was the major template structure present, and gold nuclei formed on these one-dimensional peptide nanotubes giving the ordered gold nanoparticle chain structures as shown by **Figure 4.11D**. Another interesting structural feature that can be observed when comparing gold nanoparticle-attached peptide nanotubes with pure peptide nanotubes (**Figure 4.3C**) is that the gold functionalized peptide nanotubes exhibit more flexibility along the tube length. The

more flexible peptide nanotubes may be caused by local structural frustration and disruption when the gold nanoparticles are located within the tube wall and disrupt the bundle packing. The slightly disrupted packing seems to cause a local defect in tube wall providing for bends in the local tube morphology. The structure models of the in-situ synthesized gold nanoparticles mediated by Ac-C-P222 in different assembly stages is illustrated in **Figure 4.11E**.

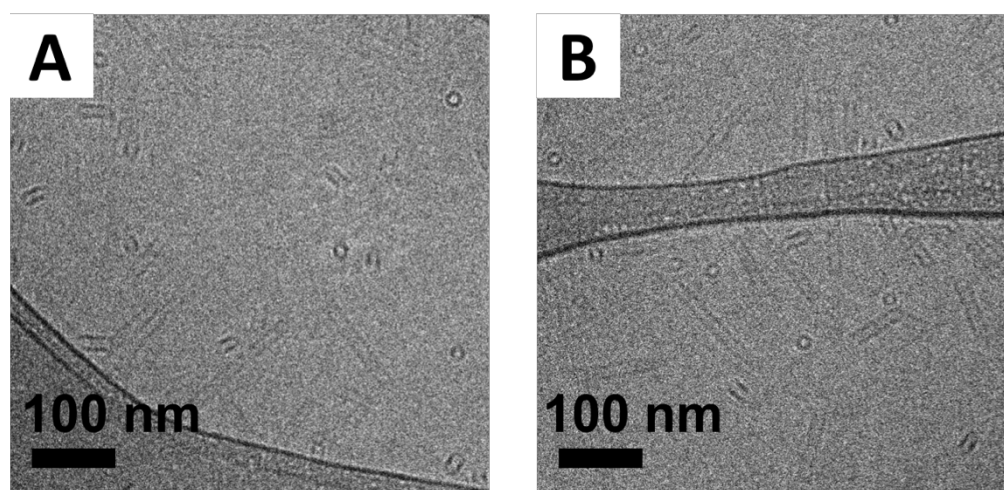


Figure 4.12 Cryo-TEM images show the morphology of Ac-C-P222 peptide assembly structures formed after 20 min of room temperature incubation. **A** and **B** were taken from different areas indicating the existence of only short peptide nanotubes. Individual un-assembled peptide coiled-coil bundles cannot be directly detected under TEM due to the small size and low electron density.

To study the peptide assembly pathway effects on the templated organization of pre-made colloidal 5 nm AuNPs, Ac-C-P422 in pH 7 buffer was used. The peptide solution was first thermally denatured at 90 °C for 2 hours, followed by 50°C isothermal incubation for peptide platelet formation. Peptides existed as random coils

at the higher temperature (as shown by circular dichroism spectra in **Figure 4.13**), while the refolding of α -helices and the formation of coiled-coil bundles was very rapid once the 50°C isothermal incubation started.⁸² During the assembly process of Ac-C-P422 peptide platelets, 5 nm AuNPs were added at two different time points of peptide assembly: 1) 0 min at 50°C (solution was just quenched to 50°C from 90°C) at which point all the peptides were still denatured and 2) 6 hours at 50°C incubation in which peptides existed in the state of well-assembled platelets.

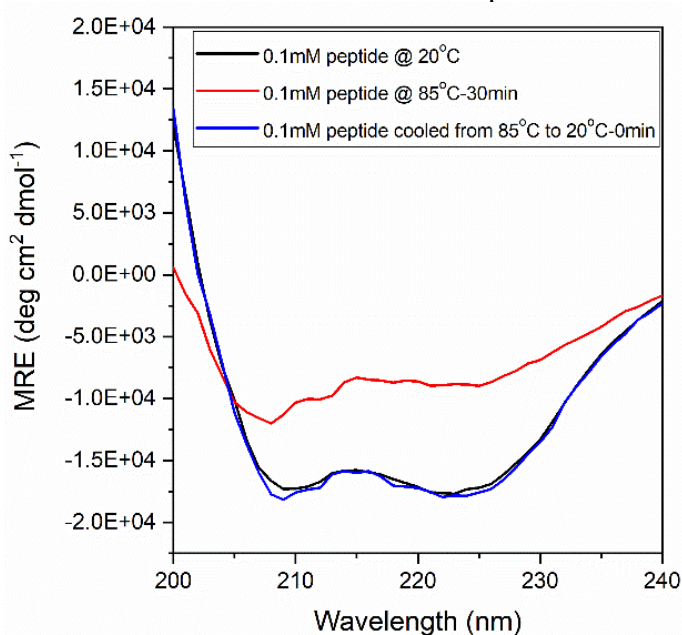


Figure 4.13 Circular dichroism spectroscopy data for Ac-C-P422 peptide with 0.1mM concentration measured at different temperatures in pH7 buffer condition containing 0.5mM TCEP. Data is plotted with buffer background subtracted. The spectrum measured at room temperature show typical α -helical conformation. The spectrum measured from 85°C-30min incubated the solution shows the melting of α -helical structures. The α -helical conformation can be recovered immediately once the solution is cooled, as shown by the spectrum measured from the solution cooled from 85°C to 20°C in time 0 point.

In **Figure 4.14**, the TEM images show the morphology of the 5 nm AuNPs organized by Ac-C-P422 from these two assembly stages with the structures observed after 24 hours from the 5 nm AuNP-peptide mixing. When the 5 nm AuNP colloidal solution was mixed with denatured peptides, two types of gold nanocrystal organizations were observed after 24 hours due to the lack of pre-existing ordered peptide template morphologies: 1) disordered, aggregated 5 nm AuNPs, as shown in the **area 1** of **Figure 4.14A** and **4.14B** or 2) the hexagonally packed 5 nm AuNPs, as shown in the **area 2** of **Figure 4.14A** and **4.14C**. It has been reported that peptide random coils and coiled-coils can be used as linkers to mediate the assembly of inorganic nanoparticles.^{34–36,91,92} The disordered, aggregated 5 nm AuNPs are most likely mediated by denatured peptide random coils, which displays a similar morphology as observed previously.³⁶ The hexagonally patterned 5 nm AuNPs are likely mediated by rigid peptide coiled-coil bundles. The distance between neighboring 5 nm AuNPs within the hexagonal pattern is $6.4 \text{ nm} \pm 1.8 \text{ nm}$, which is approximately twice the bundle length value. The theoretical neighboring AuNPs distance is approximately 8 nm, and drying of the sample may cause a slight shrinkage of the bundles. In such a system, the bundles form a shell outside of the 5 nm AuNPs, and the hexagonal pattern results from dense, close packing. This hexagonal dense packing is unique among reported work of using coiled-coils as inter-particle linkers. Previous reports demonstrated the successful construction of binary particle assemblies. However, no patterns with clear symmetries were observed.^{36,91} The coiled-coil-mediated 5 nm AuNP packing is similar to that observed with DNA-linked gold nanoparticles.⁵¹ When the 5 nm AuNP colloidal solution was mixed with well-assembled peptide

platelet solution, two-dimensional 5 nm AuNP arrays were formed as shown in **Figure 4.14D**.

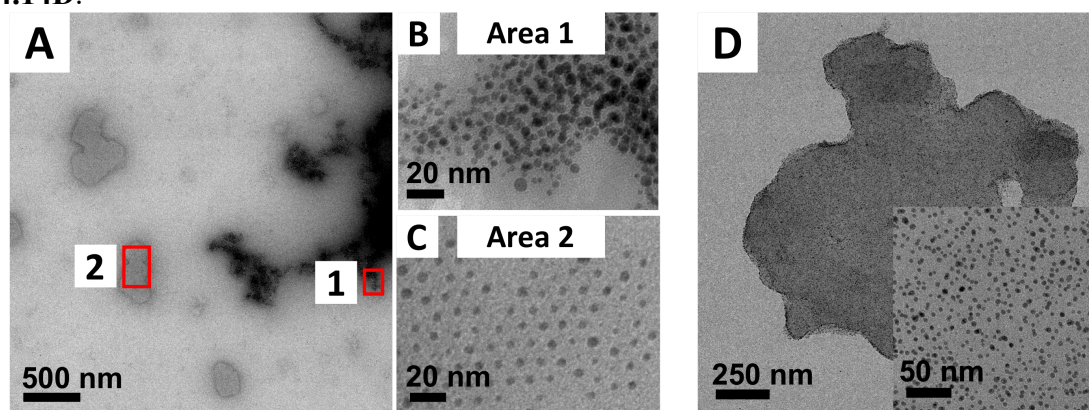


Figure 4.14 TEM images show the nanostructures of pre-made 5 nm AuNPs templated with Ac-C-P422 peptide assembled at different stages at 50°C in pH 7 buffer. **A**: 5 nm AuNP solution mixed with peptides in denatured state and examined after 24 hours from the mixing. **B**: High magnification image of indicated **area 1** in **A** showing disordered, aggregated 5 nm AuNPs. **C**: High magnification image of indicated **area 2** in **A** showing hexagonally packed 5 nm AuNP. **D**: 5 nm AuNP mixed with peptide solution after 6 hours of peptide plate-assembly at 50°C and evaluated after 24 hours from the mixing; two-dimensional 5 nm AuNP arrays can be observed. Inset is the high magnification image from plates showing the individual 5 nm AuNPs.

4.4 Fabrication of Gold Nanowires

Optical (SPR) properties that result from templated one-dimensional gold chains have motivated the development of simple fabrication methods for producing gold nanowires in this study. By using peptide nanotubes as a template, a solution-phase chemical deposition method has been developed based on the in-situ gold nanoparticle synthesis procedure described earlier. A mica sheet was used as a solid substrate to be exposed to three baths in succession: A) peptide solution of Ac-C-P222 nanotube, B) 20 mM H_{AuCl}₄ solution, and C) 20 mM NaBH₄ solution, for the coating

of peptide nanotubes and the subsequent gold formation. The process is illustrated in **Figure 4.15A**. AFM evaluation of the nanowire structures yielded measurements of nanowire height (**Figure 4.15B**), indicating an average height of $8.8 \text{ nm} \pm 1.3 \text{ nm}$ (**Figure 4.15C**). As demonstrated in **Chapter 3**, the average height of uncoated peptide nanotubes measured by AFM was $4.4 \text{ nm} \pm 0.5 \text{ nm}$, strongly suggesting that the increased height observed can be attributed to the nanotube gold coating. The results demonstrate a facile and effective process of reproducibly producing gold nanowires deposited on solid substrate. The high binding affinity of gold species to cysteine-modified peptides ensures the efficient coating of peptide tubes with gold. Further processing has the potential to control the orientation of nanowires and the thickness of the gold coating. Such control may allow modulation of electronic conductivity and SPR properties of the gold nanowires, which can be leveraged in functional devices such as solar cell and implantable electronic devices.

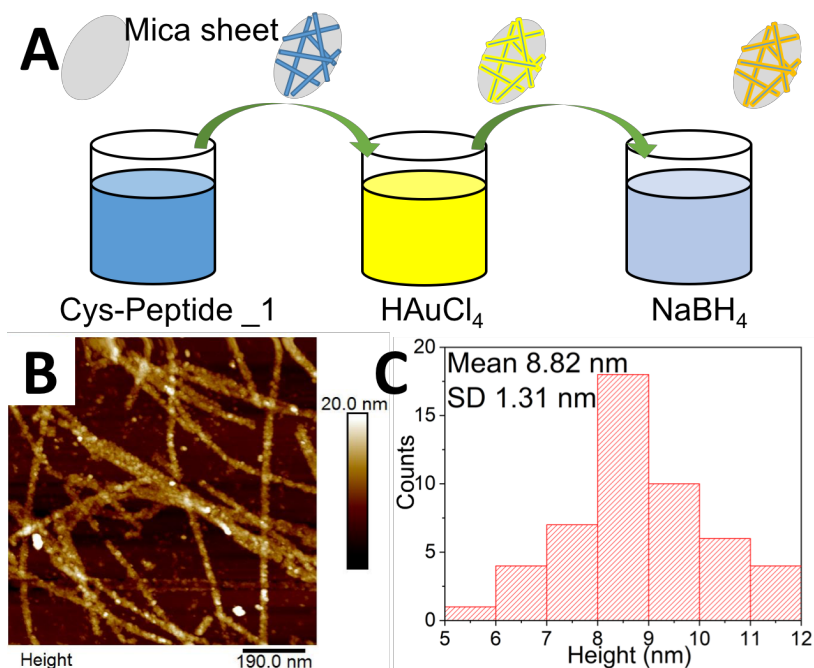


Figure 4.15 Gold nanowire deposition process. **A:** Three different baths including peptide solution, H_{Au}Cl₄, and NaBH₄ solution were exposed to a mica substrate successively for gold nanowires fabrication. **B:** AFM micrograph of the deposited gold nanowires on mica sheet. **C:** Height analysis reveals the average height as 8.8 nm with a standard deviation of 1.3 nm.

4.5 Conclusion

In this **Chapter 4**, we used computationally designed peptide sequences that can assemble into highly ordered nanostructures for gold nanoparticle templating applications. The designed, cysteine-modified peptides maintain self-assembled nanostructures and exhibit effective gold-binding, yielding one-dimensional and two-dimensional gold nanoparticle arrays. The kinetic features of the peptide assembly process also have been explored to direct the organization and growth of gold nanoparticles into various pathways. For the templated the one-dimensional gold nanoparticle chains, surface plasmon resonance properties are consistent with the

observed inter-particle distances. Furthermore, a deposition method was developed to deposit peptide-templated gold nanowires onto solid substrates in a scalable method. The gold nanowire deposition process gives the potential to allow the control of nanowire orientation and homogeneity. Processing methods such as electrospinning,⁹³ blade-coating,⁹⁴ and controlled evaporation^{95,96} can potentially be used to control the alignment of the peptide templates in the fabrication functional novel devices.

REFERENCES

1. Guo, S.; Wang, E. Noble Metal Nanomaterials: Controllable Synthesis and Application in Fuel Cells and Analytical Sensors. *Nano Today* **2011**, *6* (3), 240–264.
2. Narayanan, R.; El-Sayed, M. A. Catalysis with Transition Metal Nanoparticles in Colloidal Solution: Nanoparticle Shape Dependence and Stability. *J. Phys. Chem. B* **2005**, *109* (26), 12663–12676.
3. Link, S.; El-Sayed, M. A. Size and Temperature Dependence of the Plasmon Absorption of Colloidal Gold Nanoparticles. *J. Phys. Chem. B* **1999**, *103* (21), 4212–4217.
4. Elghanian, R.; Storhoff, J. J.; Mucic, R. C.; Letsinger, R. L.; Mirkin, C. A. Selective Colorimetric Detection of Polynucleotides Based on the Distance-Dependent Optical Properties of Gold Nanoparticles. *Science* **1997**, *277* (5329), 1078–1081.
5. Lertvachirapaiboon, C.; Baba, A.; Ekgasit, S.; Thammacharoen, C.; Shinbo, K.; Kato, K.; Kaneko, F. Gold Nanoparticles Synthesis Used for Sensor Applications. *Int. Symp. Electr. Insul. Mater.* **2011**, 395–397.
6. Daniel, M. C.; Astruc, D. Gold Nanoparticles: Assembly, Supramolecular Chemistry, Quantum-Size-Related Properties, and Applications Toward Biology, Catalysis, and Nanotechnology. *Chem. Rev.* **2004**, *104* (1), 293–346.
7. Murphy, C. J.; Tapan K. Sau; Anand M. Gole; Christopher J. Orendorff; Jinxin Gao; Linfeng Gou; Hunyadi, S. E.; Li, T. Anisotropic Metal Nanoparticles: Synthesis, Assembly, and Optical Applications. *J. Phys. Chem. B* **2005**, *109*, 13857–13870.
8. Vianna, P. G.; Grasseschi, D.; Costa, G. K. B.; Carvalho, I. C. S.; Domingues, S. H.; Fontana, J.; De Matos, C. J. S. Graphene Oxide/Gold Nanorod Nanocomposite for Stable Surface-Enhanced Raman Spectroscopy. *ACS Photonics* **2016**, *3* (6), 1027–1035.

9. El-Sayed, I. H.; Huang, X.; El-Sayed, M. A. Surface Plasmon Resonance Scattering and Absorption of Anti-EGFR Antibody Conjugated Gold Nanoparticles in Cancer Diagnostics: Applications in Oral Cancer. *Nano Lett.* **2005**, *5* (5), 829–834.
10. Pérez-Juste, J.; Pastoriza-Santos, I.; Liz-Marzán, L. M.; Mulvaney, P. Gold Nanorods: Synthesis, Characterization and Applications. *Coord. Chem. Rev.* **2005**, *249* (17–18), 1870–1901.
11. Eustis, S.; El-Sayed, M. A. Why Gold Nanoparticles Are More Precious than Pretty Gold: Noble Metal Surface Plasmon Resonance and Its Enhancement of the Radiative and Nonradiative Properties of Nanocrystals of Different Shapes. *Chem. Soc. Rev.* **2006**, *35* (3), 209–217.
12. Selvakannan, P.; Mandal, S.; Phadtare, S.; Pasricha, R.; Sastry, M. Capping of Gold Nanoparticles by the Amino Acid Lysine Renders Them Water-Dispersible. *Langmuir* **2003**, *19* (21), 3545–3549.
13. Bhargava, S. K.; Booth, J. M.; Agrawal, S.; Coloe, P.; Kar, G. Gold Nanoparticle Formation during Bromoaurate Reduction by Amino Acids. *Langmuir* **2005**, *21* (6), 5949–5956.
14. Mayer, A. B. R.; Mark, J. E. Comparisons between Cationic Polyelectrolytes and Nonionic Polymers for the Protection of Palladium and Platinum Nanocatalysts. *J. Polym. Sci. Part A Polym. Chem.* **1997**, *35* (15), 3151–3160.
15. Xu, X.; Cortie, M. B. Shape Change and Color Gamut in Gold Nanorods, Dumbbells, and Dog Bones. *Adv. Funct. Mater.* **2006**, *16* (16), 2170–2176.
16. Jiao, Z.; Xia, H.; Tao, X. Modulation of Localized Surface Plasmon Resonance of Nanostructured Gold Crystals by Tuning Their Tip Curvature with Assistance of Iodide and Silver(I) Ions. *J. Phys. Chem. C* **2011**, *115* (16), 7887–7895.
17. Diroll, B. T.; Jishkariani, D.; Cargnello, M.; Murray, C. B.; Donnio, B. Polycatenar Ligand Control of the Synthesis and Self-Assembly of Colloidal Nanocrystals. *J. Am. Chem. Soc.* **2016**, *138* (33), 10508–10515.
18. Warner, M. G.; Reed, scott m.; Hutchison, J. E. Small, Water-Soluble, Ligand-Stabilized Gold Nanoparticles Synthesized by Interfacial Ligand Exchange Reactions. *Chem. Mater.* **2000**, *12* (9), 3316–3320.

19. Woehrle, G. H.; Warner, M. G.; Hutchison, J. E. Ligand Exchange Reactions Yield Subnanometer, Thiol-Stabilized Gold Particles with Defined Optical Transitions. *J. Phys. Chem.* **2002**, *106*, 9979–9981.
20. Kim, K.-S.; Demberelnyamba, D.; Lee, H. Size-Selective Synthesis of Gold and Platinum Nanoparticles Using Novel Thiol-Functionalized Ionic Liquids. *Langmuir* **2004**, *20* (3), 556–560.
21. Bouvy, C.; Baker, G. A.; Yin, H.; Dai, S. Growth of Gold Nanosheets and Nanopolyhedra in Pyrrolidinium-Based Ionic Liquids: Investigation of the Cation Effect on the Resulting Morphologies. *Cryst. Growth Des.* **2010**, *10* (3), 1323–1331.
22. Chirea, M.; Freitas, A.; Vasile, B. S.; Ghitulica, C.; Pereira, C. M.; Silva, F. Gold Nanowire Networks: Synthesis, Characterization, and Catalytic Activity. *Langmuir* **2011**, *27*, 3906–3913.
23. Merga, G.; Saucedo, N.; Cass, L. C.; Puthussery, J.; Meisel, D. “Naked” Gold Nanoparticles: Synthesis, Characterization, Catalytic Hydrogen Evolution, and SERS. *J. Phys. Chem. C* **2010**, *114* (35), 14811–14818.
24. Fink, J.; Kiely, C. J.; Bethell, D.; Schiffrin, D. J. Self-Organization of Nanosized Gold Particles. *Chem. Mater.* **1998**, *10* (3), 922–926.
25. Ansar, S. M.; Ameer, F. S.; Hu, W.; Zou, S.; Pittman, C. U.; Zhang, D. Removal of Molecular Adsorbates on Gold Nanoparticles Using Sodium Borohydride in Water. *Nano Lett.* **2013**, *13* (3), 1226–1229.
26. Deraedt, C.; Salmon, L.; Gatard, S.; Ciganda, R.; Hernandez, R.; Ruiz, J.; Astruc, D. Sodium Borohydride Stabilizes Very Active Gold Nanoparticle Catalysts. *Chem. Commun.* **2014**, *50* (91), 14194–14196.
27. Kimling, J.; Maier, M.; Okenve, B.; Kotaidis, V.; Ballot, H.; Plech, A. Turkevich Method for Gold Nanoparticle Synthesis Revisited. *J. Phys. Chem. B* **2006**, *110* (32), 15700–15707.
28. Jana, N. R.; Peng, X. Single-Phase and Gram-Scale Routes toward Nearly Monodisperse Au and Other Noble Metal Nanocrystals. *J. Am. Chem. Soc.* **2003**, *125* (47), 14280–14281.
29. Wang, S.; Qian, K.; Bi, X.; Huang, W. Influence of Speciation of Aqueous HAuCl_4 on the Synthesis, Structure, and Property of Au Colloids. *J. Phys. Chem. C* **2009**, *113* (16), 6505–6510.

30. Grzelczak, M.; Pérez-Juste, J.; Mulvaney, P.; Liz-Marzán, L. M. Shape Control in Gold Nanoparticle Synthesis. *Chem. Soc. Rev.* **2008**, *37* (9), 1783–1791.
31. Jana, N. R. Gram-Scale Synthesis of Soluble, near-Monodisperse Gold Nanorods and Other Anisotropic Nanoparticles. *Small* **2005**, *1* (8–9), 875–882.
32. Ye, X.; Zhu, C.; Ercius, P.; Raja, S. N.; He, B.; Jones, M. R.; Hauwiler, M. R.; Liu, Y.; Xu, T.; Alivisatos, A. P. Structural Diversity in Binary Superlattices Self-Assembled from Polymer-Grafted Nanocrystals. *Nat. Commun.* **2015**, *6*, 10052.
33. Nie, Z.; Fava, D.; Kumacheva, E.; Zou, S.; Walker, G. C.; Rubinstein, M. Self-Assembly of Metal-Polymer Analogues of Amphiphilic Triblock Copolymers. *Nat. Mater.* **2007**, *6* (8), 609–614.
34. Aili, D.; Enander, K.; Rydberg, J.; Nesterenko, I.; Björefors, F.; Baltzer, L.; Liedberg, B. Folding Induced Assembly of Polypeptide Decorated Gold Nanoparticles. *J. Am. Chem. Soc.* **2008**, *130* (17), 5780–5788.
35. Aili, D.; Enander, K.; Baltzer, L.; Liedberg, B. Assembly of Polypeptide-Functionalized Gold Nanoparticles through a Heteroassociation-and Folding-Dependent Bridging. *Nano Lett.* **2008**, *8* (8), 2473–2478.
36. Stevens, M. M.; Flynn, N. T.; Wang, C.; Tirrell, D. A.; Langer, R. Coiled-Coil Peptide-Based Assembly of Gold Nanoparticles. *Adv. Mater.* **2004**, *16* (11), 915–918.
37. Eibling, M. J.; Macdermaid, C. M.; Qian, Z.; Lanci, C. J.; Park, S. J.; Saven, J. G. Controlling Association and Separation of Gold Nanoparticles with Computationally Designed Zinc-Coordinating Proteins. *J. Am. Chem. Soc.* **2017**, *139* (49), 17811–17823.
38. Nonappa; Haataja, J. S.; Timonen, J. V. I.; Malola, S.; Engelhardt, P.; Houbenov, N.; Lahtinen, M.; Häkkinen, H.; Ikkala, O. Reversible Supracolloidal Self-Assembly of Cobalt Nanoparticles to Hollow Capsids and Their Superstructures. *Angew. Chemie Int. Ed.* **2017**, *129* (23), 6573–6577.
39. Zhang, X.; Lv, L.; Ji, L.; Guo, G.; Liu, L.; Han, D.; Wang, B.; Tu, Y.; Hu, J.; Yang, D.; et al. Self-Assembly of One-Dimensional Nanocrystal Superlattice Chains Mediated by Molecular Clusters. *J. Am. Chem. Soc.* **2016**, *138* (10), 3290–3293.

40. Ofir, Y.; Samanta, B.; Rotello, V. M. Polymer and Biopolymer Mediated Self-Assembly of Gold Nanoparticles. *Chem. Soc. Rev.* **2008**, *37* (9), 1814–1825.
41. Storhoff, J. J.; Mirkin, C. A. Programmed Materials Synthesis with DNA. *Chem. Rev.* **1999**, *99* (7), 1849–1862.
42. Shenhar, R.; Norsten, T. B.; Rotello, V. M. Polymer-Mediated Nanoparticle Assembly: Structural Control and Applications. *Adv. Mater.* **2005**, *17* (6), 657–669.
43. Gao, X.; Matsui, H. Peptide-Based Nanotubes and Their Applications in Bionanotechnology. *Adv. Mater.* **2005**, *17* (17), 2037–2050.
44. Chen, C. L.; Rosi, N. L. Peptide-Based Methods for the Preparation of Nanostructured Inorganic Materials. *Angew. Chemie - Int. Ed.* **2010**, *49* (11), 1924–1942.
45. Singh, P.; Lamanna, G.; Ménard-Moyon, C.; Toma, F. M.; Magnano, E.; Bondino, F.; Prato, M.; Verma, S.; Bianco, A. Formation of Efficient Catalytic Silver Nanoparticles on Carbon Nanotubes by Adenine Functionalization. *Angew. Chemie - Int. Ed.* **2011**, *50* (42), 9893–9897.
46. Cui, H.; Chen, Z.; Zhong, S.; Wooley, K. L.; Pochan, D. J. Block Copolymer Assembly via Kinetic Control. *Science* **2007**, *317* (5838), 647–650.
47. Qiu, H.; Gao, Y.; Boott, C. E.; Gould, oliver e c; Harniman, R. L.; Miles, M. J.; Webb, S. E. D.; Winnik, M. A.; Manners, I. Uniform Patchy and Hollow Rectangular Platelet Micelles from Crystallizable Polymer Blends. *Science* **2016**, *352* (6286), 697–701.
48. Li, W.; Wang, K.; Zhang, P.; He, J.; Xu, S.; Liao, Y.; Zhu, J.; Xie, X.; Nie, Z. Self-Assembly of Shaped Nanoparticles into Free-Standing 2D and 3D Superlattices. *Small* **2016**, *12* (4), 499–505.
49. Qi, H.; Mei, S.; Zhou, T.; Dong, B.; Li, C. Y. Nanoparticle-Decorated Polymer Single Crystals for Nanoscale Materials. *ACS Symp. Ser.* **2016**, *1224*, 79–90.
50. Mei, S.; Qi, H.; Zhou, T.; Li, C. Y. Precisely Assembled Cyclic Gold Nanoparticle Frames via 2D Polymer Single Crystal Templating. *Angew. Chemie Int. Ed.* **2017**, *56* (44), 13645–13649.

51. Mirkin, C. A.; Letsinger, R. L.; Mucic, R. C.; Storhoff, J. J. A DNA-Based Method for Rationally Assembling Nanoparticles into Macroscopic Materials. *Nature* **1996**, *382* (6592), 607–609.
52. Mirkin, C. A. Programming the Assembly of Two- and Three-Dimensional Architectures with DNA and Nanoscale Inorganic Building Blocks. *Inorg. Chem.* **2000**, *39* (11), 2258–2272.
53. Jones, M. R.; Seeman, N. C.; Mirkin, C. A. Programmable Materials and the Nature of the DNA Bond. *Science* **2015**, *347* (6224), 840.
54. Loweth, C. J.; Caldwell, W. B.; Peng, X.; Alivisatos, a P.; Schultz, P. G. DNA-Based Assembly of Gold Nanocrystals. *Angew. Chemie Int. Ed.* **1999**, *38* (12), 1808–1812.
55. Yao, G.; Li, J.; Chao, J.; Pei, H.; Liu, H.; Zhao, Y.; Shi, J.; Huang, Q.; Wang, L.; Huang, W.; et al. Gold-Nanoparticle-Mediated Jigsaw-Puzzle-like Assembly of Supersized Plasmonic DNA Origami. *Angew. Chemie* **2015**, *127* (10), 3009–3012.
56. Braun, E.; Eichen, Y.; Sivan, U.; Ben-Yoseph, G. DNA-Templated Assembly and Electrode Attachment of a Conducting Silver Wire. *Nature* **1998**, *391* (6669), 775–778.
57. Warner, M. G.; Hutchison, J. E. Linear Assemblies of Nanoparticles Electrostatically Organized on DNA Scaffolds. *Nat. Mater.* **2003**, *2* (4), 272–277.
58. Janairo, J. I. B. *Peptide-Mediated Biomineralization*; Springer, Singapore, **2016**.
59. Lévy, R.; Thanh, N. T. K.; Christopher Doty, R.; Hussain, I.; Nichols, R. J.; Schiffrin, D. J.; Brust, M.; Fernig, D. G. Rational and Combinatorial Design of Peptide Capping Ligands for Gold Nanoparticles. *J. Am. Chem. Soc.* **2004**, *126* (32), 10076–10084.
60. Shenton, W.; Mann, S.; Douglas, T.; Young, M.; Stubbs, G. Inorganic-Organic Nanotube Composites from Template Mineralization of Tobacco Mosaic Virus. *Adv. Mater.* **1999**, *11* (3), 253–256.
61. Shenton, W.; Pum, D.; Sleytr, U. B.; Mann, S. Synthesis of Cadmium Sulphide Superlattices Using Bacterial S-Layers. *Nature* **1997**, *389* (6651), 585–587.

62. Scheibel, T.; Parthasarathy, R.; Sawicki, G.; Lin, X.-M.; Jaeger, H.; Lindquist, S. L. Conducting Nanowires Built by Controlled Self-Assembly of Amyloid Fibers and Selective Metal Deposition. *Proc. Natl. Acad. Sci. U. S. A.* **2003**, *100* (8), 4527–4532.
63. Dujardin, E.; Peet, C.; Stubbs, G.; Culver, J. N.; Mann, S. Organization of Metallic Nanoparticles Using Tobacco Mosaic Virus Templates. *Nano Lett.* **2003**, *3* (3), 413–417.
64. Lamm, M. S.; Sharma, N.; Rajagopal, K.; Beyer, F. L.; Schneider, J. P.; Pochan, D. J. Laterally Spaced Linear Nanoparticle Arrays Templated by Laminated β -Sheet Fibrils. *Adv. Mater.* **2008**, *20* (3), 447–451.
65. Sharma, N.; Top, A.; Kiick, K. L.; Pochan, D. J. One-Dimensional Gold Nanoparticle Arrays by Electrostatically Directed Organization Using Polypeptide Self-Assembly. *Angew. Chemie* **2009**, *121*, 7212–7216.
66. Hartgerink, J. D.; Beniash, E.; Stupp, S. I. Self-Assembly and Mineralization of Peptide-Amphiphile Nanofibers. *Science* **2001**, *294* (5547), 1684–1688.
67. Li, L. S.; Stupp, S. I. One-Dimensional Assembly of Lipophilic Inorganic Nanoparticles Templated by Peptide-Based Nanofibers with Binding Functionalities. *Angew. Chemie - Int. Ed.* **2005**, *44* (12), 1833–1836.
68. Sone, E. D.; Stupp, S. I. Bioinspired Magnetite Mineralization of Peptide-Amphiphile Nanofibers. *Chem. Mater.* **2011**, *23* (8), 2005–2007.
69. Pazos, E.; Sleep, E.; Rubert Pérez, C. M.; Lee, S. S.; Tantakitti, F.; Stupp, S. I. Nucleation and Growth of Ordered Arrays of Silver Nanoparticles on Peptide Nanofibers: Hybrid Nanostructures with Antimicrobial Properties. *J. Am. Chem. Soc.* **2016**, *138* (17), 5507–5510.
70. Chen, C. L.; Zhang, P.; Rosi, N. L. A New Peptide-Based Method for the Design and Synthesis of Nanoparticle Superstructures: Construction of Highly Ordered Gold Nanoparticle Double Helices. *J. Am. Chem. Soc.* **2008**, *130* (41), 13555–13557.
71. Merg, A. D.; Boatz, J. C.; Mandal, A.; Zhao, G.; Mokashi-Punekar, S.; Liu, C.; Wang, X.; Zhang, P.; van der Wel, P. C. A.; Rosi, N. L. Peptide-Directed Assembly of Single-Helical Gold Nanoparticle Superstructures Exhibiting Intense Chiroptical Activity. *J. Am. Chem. Soc.* **2016**, *138* (41), 13655–13663.

72. Mokashi-Punekar, S.; Merg, A. D.; Rosi, N. L. Systematic Adjustment of Pitch and Particle Dimensions within a Family of Chiral Plasmonic Gold Nanoparticle Single Helices. *J. Am. Chem. Soc.* **2017**, *139* (42), 15043–15048.
73. Ramin Djalali; Yung-fou Chen; Matsui, H. Au Nanowire Fabrication from Sequenced Histidine-Rich Peptide. *J. Am. Chem. Soc.* **2002**, *124* (46), 13660–13661.
74. McMillan, R. A.; Paavola, C. D.; Howard, J.; Chan, S. L.; Zaluzec, N. J.; Trent, J. D. Ordered Nanoparticle Arrays Formed on Engineered Chaperonin Protein Templates. *Nat. Mater.* **2002**, *1* (4), 247–252.
75. Yu, L.; Banerjee, I. A.; Matsui, H. Direct Growth of Shape-Controlled Nanocrystals on Nanotubes via Biological Recognition. *J. Am. Chem. Soc.* **2003**, *125* (48), 14837–14840.
76. Mo, X.; An, Y.; Yun, C. S.; Yu, S. M. Nanoparticle-Assisted Visualization of Binding Interactions between Collagen Mimetic Peptide and Collagen Fibers. *Angew. Chemie - Int. Ed.* **2006**, *45* (14), 2267–2270.
77. Mcmillan, R. A.; Howard, J.; Zaluzec, N. J.; Kagawa, H. K.; Mogul, R.; Li, Y.-F.; Paavola, C. D.; Trent, J. D. A Self-Assembling Protein Template for Constrained Synthesis and Patterning of Nanoparticle Arrays. *J Am Chem Soc* **2005**, *127* (9), 2800–2801.
78. Glover, D. J.; Giger, L.; Kim, S. S.; Naik, R. R.; Clark, D. S. Geometrical Assembly of Ultrastable Protein Templates for Nanomaterials. *Nat. Commun.* **2016**, *7*, 11771.
79. Fields, G. B.; Noble, R. L. Solid Phase Peptide Synthesis Utilizing 9-Fluorenylmethoxycarbonyl Amino Acids. *Int. J. Pept. Protein Res.* **1990**, *35* (3), 161–214.
80. Toby, B. H.; Von Dreele, R. B. GSAS-II: The Genesis of a Modern Open-Source All Purpose Crystallography Software Package. *J. Appl. Crystallogr.* **2013**, *46* (2), 544–549.
81. Zhang, H. V.; Polzer, F.; Haider, M. J.; Tian, Y.; Villegas, J. A.; Kiick, K. L.; Pochan, D. J.; Saven, J. G. Computationally Designed Peptides for Self-Assembly of Nanostructured Lattices. *Sci. Adv.* **2016**, *2* (9), e1600307.

82. Tian, Y.; Zhang, H. V.; Kiick, K.; Saven, J. G.; Pochan, D. Transition from Disordered Aggregates to Ordered Lattices: Kinetic Control of the Assembly of a Computationally Designed Peptide. *Org. Biomol. Chem.* **2017**, *15* (29), 6109–6118.
83. Pong, B. K.; Elim, H. I.; Chong, J. X.; Ji, W.; Trout, B. L.; Lee, J. Y. New Insights on the Nanoparticle Growth Mechanism in the Citrate Reduction of Gold(III) Salt: Formation of the Au Nanowire Intermediate and Its Nonlinear Optical Properties. *J. Phys. Chem. C* **2007**, *111* (17), 6281–6287.
84. Ghadiri, M. R.; Soares, C.; Choi, C. A Convergent Approach to Protein Design - Metal Ion-Assisted Spontaneous Self-Assembly of a Polypeptide into a Triple-Helix Bundle Protein. *J. Am. Chem. Soc.* **1992**, *114* (3), 825–831.
85. Kumar, A.; Pattarkine, M.; Bhadbhade, M.; Mandale, A. B.; Ganesh, K. N.; Datar, S. S.; Dharmadhikari, C. V.; Sastry, M. Linear Superclusters of Colloidal Gold Particles by Electrostatic Assembly on DNA Templates. *Adv. Mater.* **2001**, *008* (5), 341–344.
86. Lin, S.; Li, M.; Dujardin, E.; Girard, C.; Mann, S. One-Dimensional Plasmon Coupling by Facile Self-Assembly of Gold Nanoparticles into Branched Chain Networks. *Adv. Mater.* **2005**, *17* (21), 2553–2559.
87. Ghosh, S. K.; Pal, T. Interparticle Coupling Effect on the Surface Plasmon Resonance of Gold Nanoparticles: From Theory to Applications. *Chem. Rev.* **2007**, *107* (11), 4797–4862.
88. Qiao, L.; Wang, D.; Zuo, L.; Ye, Y.; Qian, J.; Chen, H.; He, S. Localized Surface Plasmon Resonance Enhanced Organic Solar Cell with Gold Nanospheres. *Appl. Energy* **2011**, *88* (3), 848–852.
89. Su, Y. H.; Ke, Y. F.; Cai, S. L.; Yao, Q. Y. Surface Plasmon Resonance of Layer-by-Layer Gold Nanoparticles Induced Photoelectric Current in Environmentally-Friendly Plasmon-Sensitized Solar Cell. *Light Sci. Appl.* **2012**, *1*, e14.
90. Mucic, R. C.; Storhoff, J. J.; Mirkin, C. A.; Letsinger, R. L. DNA-Directed Synthesis of Binary Nanoparticle Network Materials. *J. Am. Chem. Soc.* **1998**, *120* (48), 12674–12675.
91. Slocik, J. M.; Tam, F.; Halas, N. J.; Naik, R. R. Peptide-Assembled Optically Responsive Nanoparticle Complexes. *Nano Lett.* **2007**, *7* (4), 1054–1058.

92. Wagner, S. C.; Roskamp, M.; Cölfen, H.; Böttcher, C.; Schlecht, S.; Kokscha, B. Switchable Electrostatic Interactions between Gold Nanoparticles and Coiled Coilpeptides Direct Colloid Assembly. *Org. Biomol. Chem.* **2009**, *7* (1), 46–51.
93. Singh, G.; Bittner, A. M.; Loscher, S.; Malinowski, N.; Kern, K. Electrospinning of Diphenylalanine Nanotubes. *Adv. Mater.* **2008**, *20* (12), 2332–2336.
94. Dörfling, B.; Vohra, V.; Dao, T. T.; Garriga, M.; Murata, H.; Campoy-Quiles, M. Uniaxial Macroscopic Alignment of Conjugated Polymer Systems by Directional Crystallization during Blade Coating. *J. Mater. Chem. C* **2014**, *2* (17), 3303–3310.
95. Lin, Y.; Su, Z.; Xiao, G.; Balizan, E.; Kaur, G.; Niu, Z.; Wang, Q. Self-Assembly of Virus Particles on Flat Surfaces via Controlled Evaporation. *Langmuir* **2011**, *27* (4), 1398–1402.
96. Wang, Z.; Bao, R.; Zhang, X.; Zhang, X.; Ou, X.; Lee, C. S.; Chang, J. C. One-Step Self-Assembly, Alignment, and Patterning of Organic Semiconductor Nanowires by Controlled Evaporation of Confined Microfluids. *Angew. Chemie - Int. Ed.* **2011**, *50* (12), 2811–2815.

Chapter 5

INTERACTIONS BETWEEN GOLD PRECURSOR ANIONS AND POSITIVELY CHARGED CYSTEINE CONTAINING PEPTIDE SCAFFOLDS DURING THE TEMPLATED AQUEOUS SYNTHESIS

5.1 Introduction

As discussed in **Chapter 4**, templating methods, combined with colloidal nanoparticle synthesis chemistry, provide the facile strategy of producing highly ordered inorganic and composite nanomaterials through the templated organization/assembly of individual nanoparticles.¹ The use of additive ligands to control the synthesis process of nanoparticles can be claimed as the most fundamental templating method. In the synthesis of gold nanoparticles, a variety of ligands, such as sulfur ligands,² amino acids,^{3,4} polyelectrolytes,⁵⁻⁹ surfactants,¹⁰ phosphine,^{11,12} and ionic liquid,¹³⁻¹⁵ have been explored to produce gold nanoparticles with tunable sizes¹⁶⁻¹⁹ and shapes.^{33,34} Higher order hierarchical structures of nanoparticles can be achieved through inter-particle interactions that are mediated by the particle surface ligands. For example, the simplest steric effect can lead to the dense packing of nanoparticles in which the spacing can be controlled by the chain length of ligands.^{10,24,25} More complicated nanostructures can be produced by the incorporation of more specific inter-particle interactions. For example, hollow capsids composed of cobalt nanoparticles were assembled directed by hydrogen-bonding among the ligands.²⁶ One-dimensional Fe₃O₄ nanoparticle chains were reported to have assembled with the guidance of oleylamine-ligated lead sulfate clusters.²⁷ Binary gold nanoparticle assemblies were reported to have assembled under the control of coiled-

coil pairing of peptide ligands.²⁸⁻³⁰ Programmable inorganic nanoparticle lattices were reported to have been produced via the base-pairing interaction of designable DNA ligands.³¹⁻³³ Moreover, inspired by the biomineralization process in nature,³⁴ with the use of pre-formed materials as scaffolds, inorganic nanoparticles can be selectively attached to the binding sites producing the inorganic and composite nanomaterials inheriting the same structure feature of scaffolds.³⁵⁻³⁹ In this process, the key driving force is the interaction between particles and the scaffolds. A type of generic interaction is the electrostatic interaction that exists between inorganic species and the scaffolds. For example, the chargeable poly(acrylic acid) corona in self-assembled block co-polymer micelles has shown the strong binding affinity to counter ion-coated gold nanoparticles. This affinity has produced the orderly stacked gold nanoparticles.⁴³ Charged DNA scaffolds were reported to have been used to adsorb oppositely charged inorganic precursor anions and nanoparticles producing linear inorganic nanoparticle arrays and nanowires.^{40,41} Acidic and basic amino acid residues in proteins and virus capsids were also reported to have shown strong electrostatic binding affinity to inorganic species for the formation of scaffold-organized 1D and 2D inorganic nanoparticle arrays.⁴²⁻⁴⁸ Other than generic electrostatic interactions, more specific interactions between certain molecular groups and inorganic species also have been identified. For example, the mostly utilized specific bonding is the thiol-gold bonding interaction. Thiol-functionalized DNA molecules were reported to have been grafted onto gold nanoparticles, and directed the specific decoration of nanoparticles on DNA scaffolds.^{49,50} With a similar mechanism, thiol-functionalized polymer single crystals⁴⁵ and thiol-functionalized peptide scaffolds⁵¹⁻⁵⁴ were also reported to have exhibited obvious specific binding to gold species. Besides gold, the thiol group was reported

to have binding affinity to other types of noble metals such as silver and platinum.^{52,55} The imidazole group in histidine is identified as an important moiety for the templating of inorganic nanoparticles on peptide scaffolds.^{54,56–59} Although the binding mechanism of histidine to inorganic species is the general electrostatic interaction, specific coordinations between imidazole and metal ions can be formed.⁶⁰ Therefore, histidine as binding moiety is listed separately. The bonding between aromatic groups and metallic species also has been largely explored. For example, pyridine-gold bonds were reported to have directed the 1D and 2D organizations of gold nanoparticles on peptide nanofibers and polymer single crystals.^{61,62} The fluorenylmethoxycarbonyl (Fmoc-) group was used in the synthesis of 1D silver nanoparticle arrays on peptide fiber scaffolds.⁶³ Certain short peptide sequences containing aromatic amino acid residues such as phenylalanine, tyrosine, and tryptophan have been identified as effective metal binding sequences and used to guide the specific decoration or synthesis of inorganic nanoparticles on scaffolds.^{64–66} Other specific bondings, such as adenine-metal coordination,⁶⁷ hydrogen bonding with silica particles⁴⁴ and more, are continuously being reported, which enriches the toolbox that can be used in the templating study of nanoparticles. However, in most of the reported studies, only one type of interaction was utilized and investigated for each templating system. This may not be sufficient for the more complicated templating materials, such as DNA and peptides, that can contain aromatic, charged and thiol-functionality at the same time. In **Chapter 4**, we demonstrated examples of the successful use of thiol-functionalized, self-assembled Ac-C-P222 nanotubes as scaffolds to template the solution synthesis of ordered gold nanoparticle arrays. In addition to the desired thiol-gold bonding, due to the acidic condition used for peptide self-assembly, the positive

charges that peptides carry could impose strong electrostatic interactions to the precursor anions (chloroauric acid and sodium borohydride) used in the synthesis. Therefore, in this work, further investigation was conducted about the effect of precursor molecule ratio on the synthesized gold nanomaterials morphology, the precursor molecule addition order on gold nanoparticle growth pathways, and the selective peptide-metallic binding effect in order to discuss the inorganic anion-peptide and gold-peptide interactions during the templating synthesis process.

5.2 Materials and Methods

5.2.1 Peptide Synthesis

Peptides were synthesized as described in **Chapter 4**.

5.2.2 Peptide Purification

Purification was performed as described in **Chapter 3**.

5.2.3 Peptide Solution Self-assembly Experiments

The self-assembly process is the same as described in **Chapter 4**.

5.2.4 Templating of Gold Nanoparticles

In-situ templating synthesis of gold nanoparticle method was used as described in **Chapter 4**.

5.2.5 Transmission Electron Microscopy

TEM sample grids preparation and images collection are as similar as being described in **Chapter 2**.

5.2.6 Cryogenic TEM (Cryo-TEM)

Cryo-TEM sample preparation and images collection are as similar as being described in **Chapter 3**.

5.2.7 Wide and Small Angle X-ray scattering

WAXS/SAXS measurements were conducted as described in **Chapter 4**.

5.3 Stoichiometry Effect

In **Chapter 4**, we have demonstrated the cysteine containing Ac-C-P222 peptide (Ac- C DGRIE GMAEA IKKMA YNIAD MAGRI WGEA-NH₂) can be used to effectively template the in-situ solution synthesis of gold nanoparticles. The peptide itself can firstly adopt α -helical secondary-structure in aqueous condition for the formation of homotetrameric coiled-coil bundle structure and then can further assemble into hollow tubular structure with width of 13.0 ± 0.8 nm and wall thickness of 3.2 ± 0.4 nm, in acidic buffer (50mM pH 4.5 sodium acetate buffer), as shown in **Figure 4.3A**.⁶⁸ When these cysteine-containing peptide nanotubes were applied as scaffolds for the templated solution synthesis of gold nanoparticles using chloroauric acid (HAuCl₄) and sodium borohydride (NaBH₄) as precursor molecules, clear one-dimensional chain-like organization of gold nanoparticles can be observed under TEM after 2 hours of incubation, as shown in **Figure 4.4A**. To explore the effect of precursor molecule ratio on the morphology of gold nanomaterials, the amount of precursor molecules was varied from 1-equivalent to 3-equivalents with respect to the peptide concentration. After the sequential addition of HAuCl₄ and NaBH₄ to peptide nanotube suspensions, and 2 hours of incubation, the gold nanomaterials morphology was examined by TEM, as shown in **Figure 5.1**.

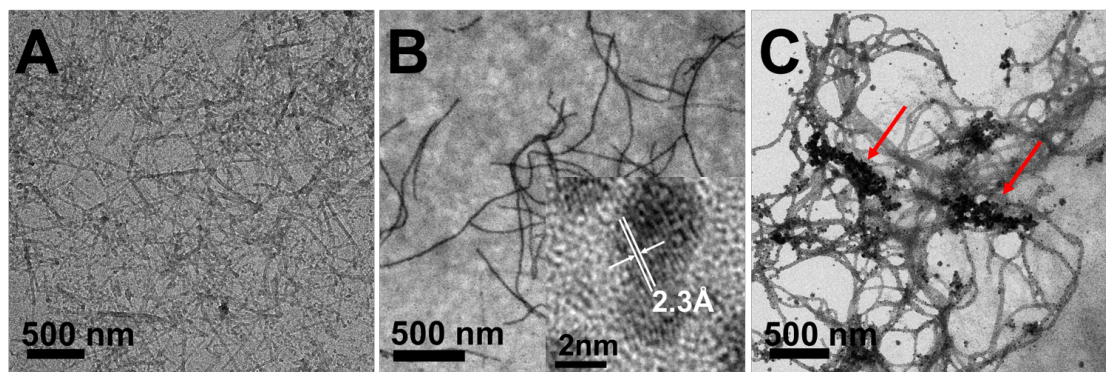


Figure 5.1 TEM images of Ac-C-P222 peptide nanotube templated solution synthesis of gold nanoparticles with different precursor molecule ratio. **A:** 0.2 mM peptide nanotubes with 0.5 mM TCEP, 0.2 mM H_{AuCl}₄ and 0.2 mM NaBH₄ in 50 mM pH 4.5 buffer were used as growth solution and incubated for 2 hours. (Molar ratio of peptide: H_{AuCl}₄: NaBH₄=1: 1: 1). **B:** 0.2 mM peptide nanotubes with 0.5 mM TCEP, 0.4 mM H_{AuCl}₄ and 0.4 mM NaBH₄ in 50 mM pH 4.5 buffer were used as growth solution and incubated for 2 hours. (Molar ratio of peptide: H_{AuCl}₄: NaBH₄=1: 2: 2). Inset is HR-TEM of individual gold nanoparticle showing gold (111) crystal plane with 2.3 Å spacing. **C:** 0.2 mM peptide nanotubes with 0.5 mM TCEP, 0.6 mM H_{AuCl}₄ and 0.6 mM NaBH₄ in 50 mM pH 4.5 buffer were used as growth solution and incubated for 2 hours. (Molar ratio of peptide: H_{AuCl}₄: NaBH₄=1: 3: 3).

The 2-equivalents precursor molecule amount is the optimal templating growth condition; clear one-dimensionally organized gold nanoparticle chains can be observed in **Figure 5.1B**. The lower or higher molar ratio resulted in undesired gold nanomaterials morphology. As shown by **Figure 5.1A**, the incubation of peptide nanotubes with 1eqv. of H_{AuCl}₄ and 1eqv. of NaBH₄ did not yield significant formation of gold nanoparticles; no obvious particles could be seen with TEM and no diffraction peaks could be obtained by solution WAXS (data not shown). When the amount of precursor molecules was increased to 3 equivalents (molar ratio of peptide: H_{AuCl}₄: NaBH₄=1: 3: 3), inhomogeneous gold nanoparticle growth is observed as indicated by red arrows in **Figure 5.1C**. When the amount of precursor molecule was

further increased to 5 equivalents, even elongated rod shape gold nanoparticles and continuous gold nanowires could be observed, as shown in **Figure 5.2**.

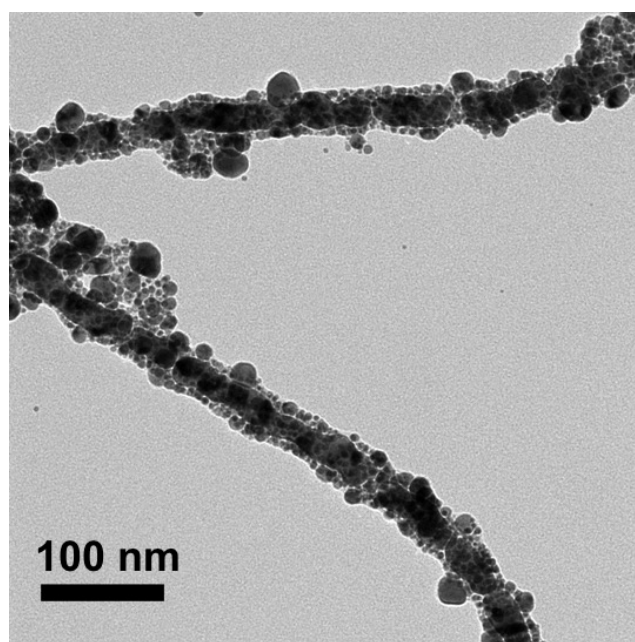


Figure 5.2 TEM image shows the formation of continuous gold nanowire structures from the solution condition containing 0.2 mM Ac-C-P222 peptide nanotubes, 0.5 mM TCEP, 1 mM H_{AuCl}₄ and 1 mM NaBH₄, and incubated for growth for 2 hours. (Molar ratio of peptide: H_{AuCl}₄: NaBH₄=1: 5: 5)

Combining the gold nanoparticle growth observation under different precursor molecules ratio conditions, we can conclude that a critical molar ratio of precursor molecules vs. peptides is needed for the formation of gold nanoparticles, which is determined by the number of positive amino acid residues each peptide carries. In our studied cases, the critical molar ratio of H_{AuCl}₄: NaBH₄: peptide is 2: 2: 1. In this Ac-C-P222 peptide sequence used for templating, there are four positively charged amino acid residues (arginine at position 4, lysine at position 13, lysine at position 14 and arginine at position 25) that can pair with precursor anions. In the ideal ion-pairing condition, each peptide molecule can pair with exact 2eqv. of AuCl₄⁻ and 2eqv. of BH₄⁻ (total 4 equivalents anions). In the actual situation, because peptide molecules

are folded and assembled into nanotubes, certain charged residues may not be accessible. Therefore, each peptide molecule accommodates less than total 4 equivalents anions. For the 2-equivalent precursor molecule condition, 2eqv. of AuCl_4^- anions firstly pair with positively charged peptides forming a complex structure that is similar to a ligand-stabilized complex.⁶⁹ Then the sequentially added 2eqv. of BH_4^- will not be completely restricted by ion-pairing with peptides but still can react with AuCl_4^- for gold nucleation and growth. The reduced Au^0 can be coordinated with cysteine residues through thiol-gold bonding for the formation of ordered one-dimensional chains. When the amount of precursor molecules is decreased to 1-equivalent condition, the positively charged peptides are in large excess and can bind with most of the AuCl_4^- and BH_4^- anions through ion-pairing interaction.⁶⁹ We hypothesize that the formed peptide- BH_4^- complex reduced the reducibility of BH_4^- hindering the formation of gold nanoparticles. However, the formation of gold nanoparticles in this solution condition containing only 1-equivalent precursor molecules can be triggered by extra UV radiation. The photo-reduced gold nanoparticles can be observed by dark field TEM as shown in **Figure 5.3**. This proves that the loss of reducibility of BH_4^- is responsible for the lack of gold nanoparticle formation; AuCl_4^- anions are still present in the solution. In high precursor molecules ratio conditions, there are not sufficient peptides to coordinate and control the growth of gold nanoparticles from being coalesced. Moreover, it is known that initially formed gold nanoparticles can catalyze the gold reduction reaction for the formation of large gold nanoparticles, elongated rods and wires.⁵ Therefore, the gold nanoparticles that nucleated on the site of peptide nanotubes can recruit excess AuCl_4^- for the further growth into elongated gold nanorods and gold nanowires structures.

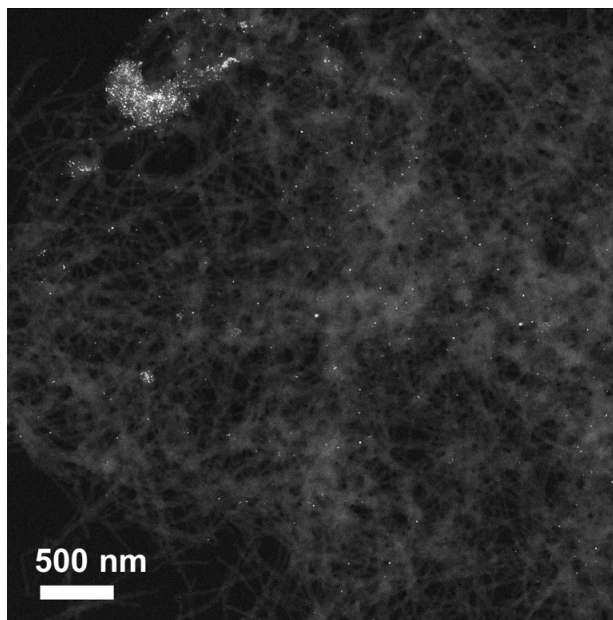


Figure 5.3 HAADF image of UV photo-induced formation of gold nanoparticles. In 0.2 mM Ac-C-P222 peptide nanotube solution with 0.5 mM TCEP, 1eqv. of HAuCl_4 (20 mM in DI water) and 1eqv. of NaBH_4 (20 mM in DI water) were added successively, to reach the final concentration of 0.2 mM for each precursor molecule. The solution was then radiated under UV lamp with wavelength of 365 nm, 20.1 mW/cm^2 for 7 hours. Bright particles in the image indicate the existence of inorganic gold nanoparticles.

5.4 Addition Order Effect of Precursor Molecules

In the previously described gold solution synthesis process, precursor solutions were added successively to peptide nanotube solutions in the order of HAuCl_4 first and NaBH_4 second. We then examined the effect of the addition order of precursor molecules on the growth pathway of gold nanoparticles. 2eqv. of NaBH_4 was firstly added to the Ac-C-P222 peptide nanotube solutions then followed by 2eqv. of HAuCl_4 . The solution was incubated at room temperature for gold nanoparticle

growth. The resulting nanostructure morphology was examined by TEM, as shown in **Figure 5.4A**.

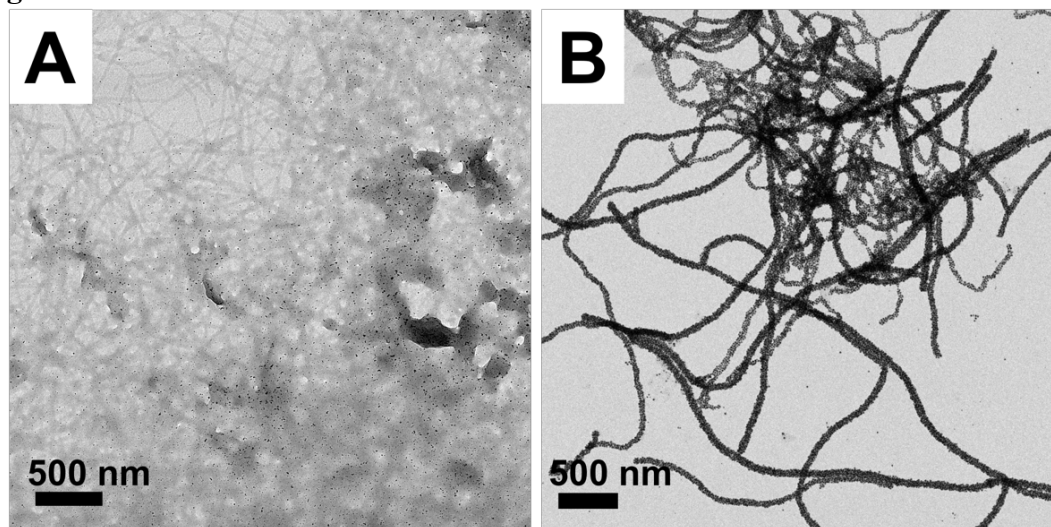


Figure 5.4 TEM images show the gold nanoparticle growth on Ac-C-P222 peptide tubes with precursor molecules in the addition order of NaBH_4 as the first and HAuCl_4 as the second added. **A:** In 0.2 mM peptide nanotube solution containing 0.5 mM TCEP, NaBH_4 and HAuCl_4 were successively added to reach the final concentration of 0.4 mM for each precursor molecules. The solution was incubated for 7 hours. **B:** In 0.2 mM peptide nanotube solution containing 0.5 mM TCEP, NaBH_4 and HAuCl_4 were successively added to reach the final concentration of 0.4 mM for each precursor molecules. The solution was then radiated under UV lamp with wavelength of 365 nm, 20.1 mW/cm² for 7 hours. Gold nanoparticles were formed in one-dimensional organization.

Compared with the result of the same 2-equivalents precursor molecule condition but in different addition order shown in **Figure 5.1B**, the formation of gold nanoparticles was hindered when NaBH_4 was firstly mixed with peptides. The few observed gold nanoparticles did not appear to have significant templating order. As discussed in the previous section, when BH_4^- is firstly presented in the solution, peptide- BH_4^- complex structures can be formed through ion-pairing interaction. This decreases the reducibility of NaBH_4 in solution which inhibits the formation of gold nanoparticles.

Although our solution condition is acidic, NaBH_4 could be consumed by reacting with water. However, during the solution addition process, no incubation time is allowed between two additions. Also, as shown in **Figure 5.4A**, a certain amount of gold nanoparticles can be spotted which proves that NaBH_4 has not completely reacted with water. Therefore, we believe that the interaction between BH_4^- anions and positively charged peptides is the cause of the suppressed gold formation results. Furthermore, the unreacted HAuCl_4 can be reduced via UV photo-reduction giving the one-dimensional templated gold chain organization, which can be clearly observed under TEM as shown in **Figure 5.4B**. If the amount of firstly added NaBH_4 was further increased to 5 equivalents, the reduction of the following added HAuCl_4 can be further hindered resulting in the observation of salt clusters from unreacted HAuCl_4 under TEM as shown in **Figure 5.5A** (spherical structures with the diameters of 100-200 nm). This is because 5 eqv. of NaBH_4 is in excess to peptides. Therefore, most of the positively charged sites of peptides will be occupied by BH_4^- anions. The following added HAuCl_4 will remain unbound and unreacted in solution which can form salt clusters while being dried during TEM sample preparation. Similar unreacted HAuCl_4 salt clusters can be observed by TEM in the early growth stage of gold nanoparticles in the solution condition that HAuCl_4 was firstly added, as shown in **Figure 5.6**. These salt clusters can react with further added NaBH_4 and disappear giving the formation of gold nanoparticles, as shown by TEM image in **Figure 5.5B**. From these results, it can be concluded that in our studied case, pre-incubation of NaBH_4 with peptide templates will inhibit the formation of gold nanoparticles and decrease the templating order. This has not been commonly observed or discussed in the field of peptide templating. On the contrary, it has been reported that in certain specific cases, the pre-incubation of NaBH_4 with protein cage scaffolds can promote the templated growth.⁵⁴ The uniqueness of our system is that acidic conditions make the peptide side chains mostly in a positively charged state. This brings more complex ion-pairing interactions to the system in addition to the desired thiol-gold bonding. Therefore, as being discussed here, more attention should be paid in the choice of precursor molecule ratio and addition order to achieve optimal templating result.

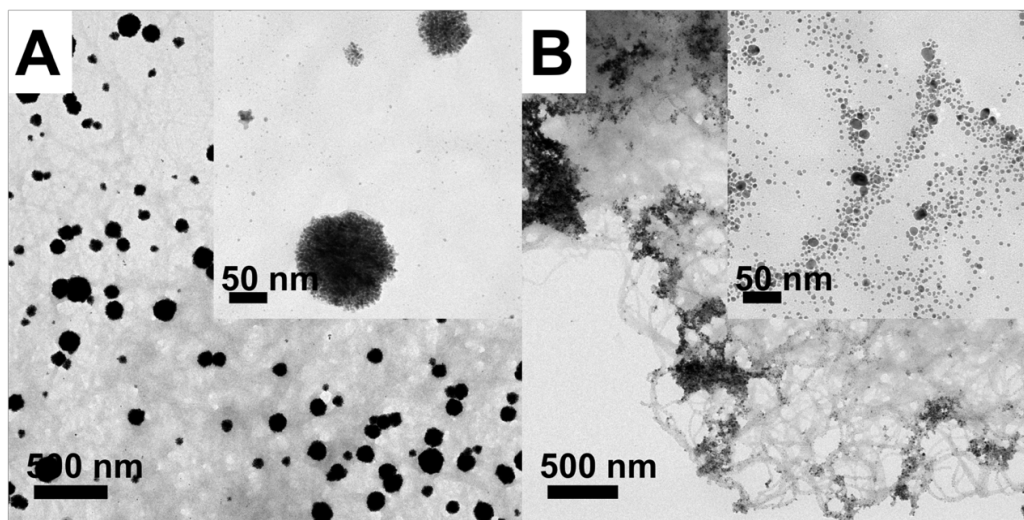


Figure 5.5 TEM images show the gold nanoparticle growth on Ac-C-P222 peptide tubes with precursor molecules in the addition order of NaBH_4 as the first and HAuCl_4 as the second. **A:** In 0.2 mM peptide nanotube solution containing 0.5 mM TCEP, NaBH_4 and HAuCl_4 were successively added to reach the final concentration of 1 mM for each precursor molecule. The solution was then incubated for growth for 2 hours. Spherical clusters are observed along with peptide nanotubes. Inset is the high magnification image of spherical clusters revealing the clustered structures. **B:** To the same solution shown in **A**, extra 5eqv. of NaBH_4 with respect to peptide concentration was added and incubated for 2 hours. Spherical clusters disappeared after the extra addition of NaBH_4 . Gold nanoparticles formed. Inset is the high magnification image showing the individual gold nanoparticles organized into one-dimensional structures templated by peptide nanotubes.

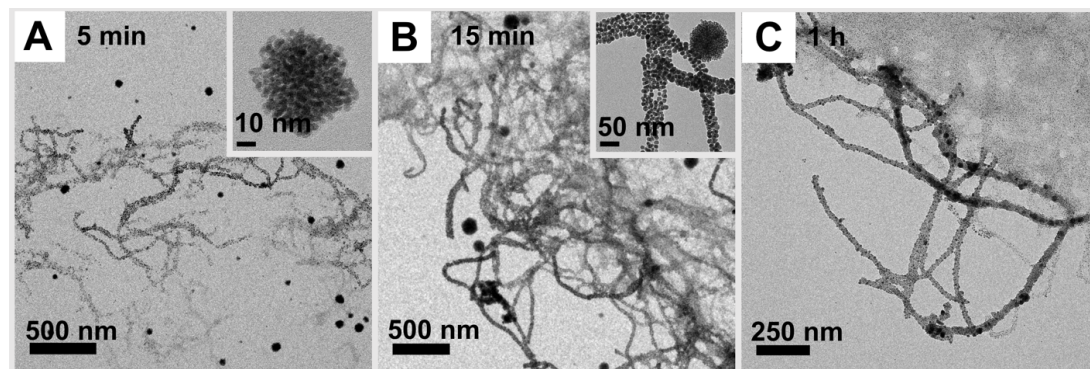


Figure 5.6 TEM images show the time-dependent growth process of gold nanoparticles on Ac-C-P222 peptide tubes in 5-equivalent condition. 0.2mM cysteine modified peptide solution was firstly assembled in 50mM pH 4.5 buffer with 2 eqv. TCEP for 18hours. 5 eqv. of HAuCl_4 solution and 5 eqv. of NaBH_4 with respect to peptide concentration were successively added to the solution for the growth of gold nanomaterials. **A:** After 5min of growth, some gold nanoparticles organized in one-dimension were observed. Spherical salt clusters from not yet reacted HAuCl_4 were observed as well. Inset is the high magnification image of cluster structure. **B:** After 15min of growth, more gold nanoparticles organized in one-dimension were observed. Spherical salt clusters were reduced. Inset is high magnification image showing the cluster structure and the templated gold nanoparticles. **C:** After 1h of growth, all the salt clusters disappeared, forming gold nanoparticles.

A two-step addition procedure of precursor molecules is proposed to further prove our hypothesis about the interactions between precursor anions and positively charged peptides. In the first step, 1-equivalent NaBH_4 was added to the peptide nanotube solution. Successively, 5-equivalents HAuCl_4 were added to the same peptide solution. The solution was then incubated at room temperature for 2 hours and examined by TEM. In the second step, an additional 4-equivalents NaBH_4 were added to the same incubated solution, and examined by TEM after 5 min. The nanostructure morphology revealed by TEM is shown in **Figure 5.7**. After the first step addition of 1-equivalent NaBH_4 and 5-equivalent HAuCl_4 , no significant formation of gold nanoparticles can be observed; salt clusters from unreacted HAuCl_4 are exhibited as shown in **Figure 5.7A**. This meets the expectation that the firstly added BH_4^- anions

should be bound to peptide and, therefore, have lost the reducibility. The following added AuCl_4^- anions can bind to the remaining charged sites on peptide templates that remain unreacted. And, since the amount of 5-equivalents HAuCl_4 is in excess, the unbound HAuCl_4 forms salt clusters during the drying process of TEM sample preparation. After the second step addition of an extra 4-equivalents NaBH_4 , the orderly templated one-dimensional gold nanoparticles formed very efficiently even only being incubated for 5 min as shown in **Figure 5.7B**. This is because the additional 4-equivalents of NaBH_4 reduced the unreacted HAuCl_4 that was bound on the peptide templates during the first step. Since most of the positively charged sites on peptides were occupied in the first step, the NaBH_4 added in the second step can remain unbound and, therefore, has high reactivity. Zeta-potential change of peptide solution during this multi-step addition process was also measured to confirm the adsorption of precursor anions to positively charged peptides. The zeta-potential value of pure peptide nanotubes in 50 mM pH 4.5 buffer is +44.98 mV. This meets our expectation that due to the acidic condition, peptides will carry positive charges. After the first step addition of 1-equivalent NaBH_4 and 5-equivalent HAuCl_4 , the zeta-potential value dropped to +12.62 mV. This is showing the adsorption of anions to peptides. After the second step addition of extra 4-equivalent NaBH_4 , the solution became ruby-red with flocculation. This is no long a stable colloidal solution, which is indicative of the further decrease of zeta potential (the acquired zeta potential is +5.47 mV).

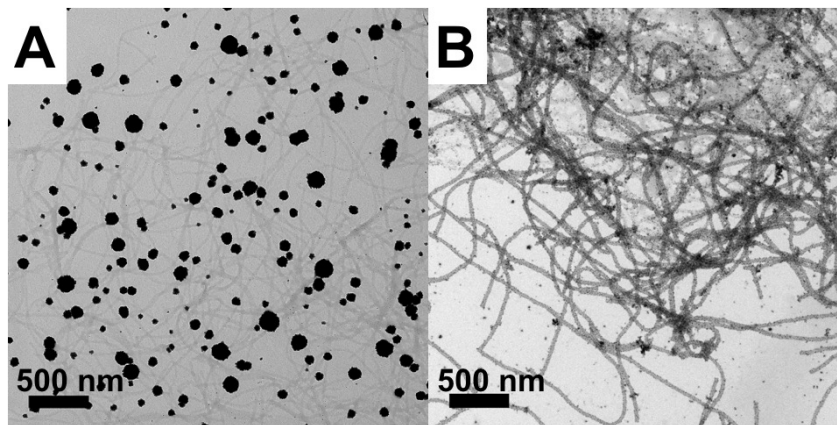


Figure 5.7 TEM images show the gold nanoparticle growth result on Ac-C-P222 peptide nanotubes through a multi-step addition procedure of precursor molecules. **A:** In 0.2 mM peptide nanotube solution containing 0.5 mM TCEP, 1eqv. of NaBH_4 and 5eqv. of HAuCl_4 with respect to peptide concentration were added successively and incubated for growth for 2 hours. (Molar ratio of peptide: NaBH_4 : HAuCl_4 =1: 1: 5) Salt clusters are observed along with peptide nanotubes. **B:** To the same solution, extra 4eqv. of NaBH_4 with respect to peptide concentration was added, and incubated for 5 min. One-dimensional gold nanoparticle arrays can be observed.

5.5 Binding Selectivity to inorganic Species

As can be seen from above, the gold precursor anions have strong binding affinity to positively charged peptide side chains. The formed gold nanoparticles have clear binding effect to cysteine-modified peptide templates through thiol-gold bonding as shown in **Figure 5.1B**. Cryo-TEM images were also taken, shown in **Figure 5.8**, to confirm the one-dimensionally organized gold nanoparticles are not due to the drying accumulation effect, but is because of thiol-gold bonding.

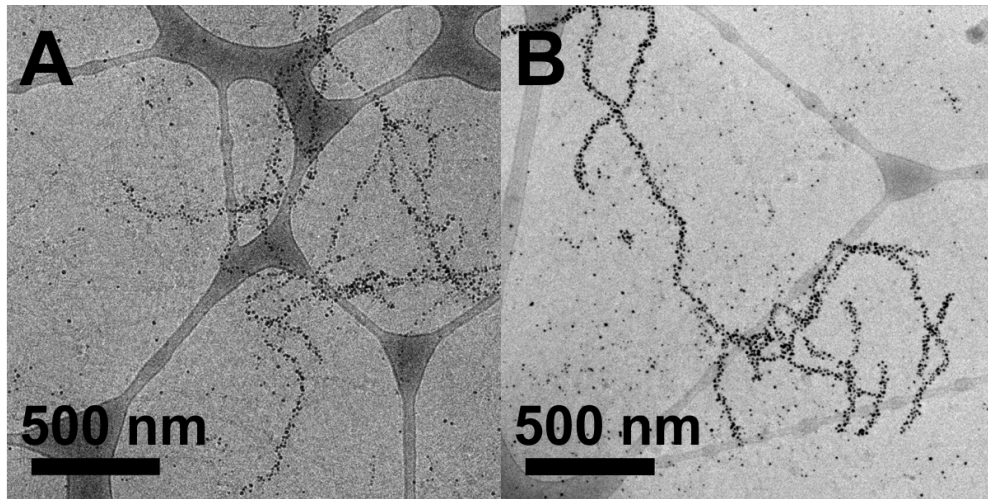


Figure 5.8 Cryo-TEM images of Ac-C-P222 peptide nanotube templated solution synthesis of gold nanoparticles. 0.2 mM cysteine-modified peptide nanotubes with 0.5 mM TCEP, 0.4 mM HAuCl₄ and 0.4 mM NaBH₄ were used as growth solution and incubated for 4 days for imaging. **A** and **B** are taken from the same sample in different areas, showing the peptide nanotubes attached with gold nanoparticles. This confirms the one-dimensional organization of gold nanoparticles is from the bonding between cysteine and peptides, not due to drying accumulation effect.

Moreover, to further evaluate the selective binding affinity of peptide scaffolds to the inorganic species, non-cysteine containing H-P222 peptide nanotubes were investigated for the gold nanoparticle binding, and, cysteine containing Ac-C-P222 peptide nanotubes were investigated for the silver gold nanoparticle binding. The selective binding morphology results are revealed by TEM and shown in **Figure 5.9**.

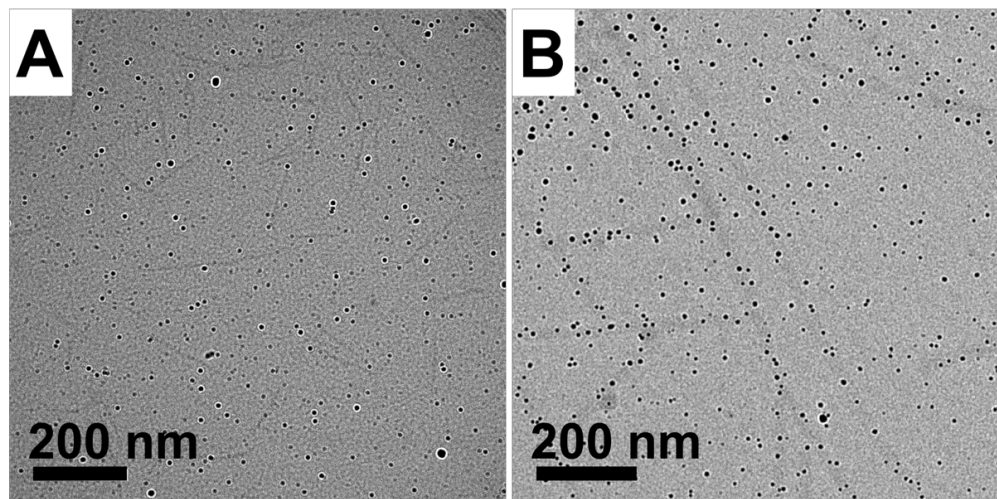


Figure 5.9 TEM images show the growth of gold nanoparticles on non-cysteine containing H-P222 peptide tubes and the growth of silver nanoparticles on cysteine containing Ac-C-P222 peptide tubes. **A:** In 0.2 mM H-P222 peptide nanotube solution, 5eqv. of HAuCl_4 and 5eqv. of NaBH_4 with respect to peptide concentration were added successively and incubated for 2 hours. **B:** In 0.2 mM Ac-C-P222 peptide nanotube solution containing 0.5 mM TCEP, 5eqv. of AgNO_3 and 5eqv. of NaBH_4 with respect to peptide concentration were added successively and incubated for 2 hours. Both images were taken under highly defocused condition to reveal the tubes. Therefore, the observed widths of tubes are not accurate.

As shown in **Figure 5.9A**, after 2 hours of incubation of gold precursor molecules with H-P222 peptide nanotubes, significant amount of gold nanoparticles was observed. However, these gold nanoparticles do not appear to display any obvious templating effect. They are observed being randomly distributed among the imaging area. There are reported examples that the templated growth of inorganic nanoparticles can be achieved just via electrostatic interactions.⁴²⁻⁴⁸ In our studied case, the electrostatic interactions play an important role in the adsorption of precursor anions to peptide scaffolds. However, after the reduction of gold, it seems a strong binding moiety such as cysteine is needed for the templating purpose. This may be because of

the steric effect that the peptide molecules are packed within the nanotubes in which the space is limited for the gold nanoparticle growth. While cysteine is exposed on the surface of nanotubes, according to the nanotube model described in **Chapter 3**, without space restriction, reduced Au⁰ can migrate to the nanotube surface, bind with thiol groups and further grow into large nanoparticles. The binding result of silver nanoparticles to Ac-C-P222 peptide nanotubes is shown in **Figure 5.9B**. Significant amount of silver nanoparticles were observed as well. But the spatial distribution of silver nanoparticles is random without obvious templating order indicating no strong binding affinity of cysteine to silver nanoparticles in our case. The binding affinity can be quantified by calculating the loading percentage of nanoparticles on peptide nanotubes, as well as in empty area, as shown by **Figure 5.10**. Within the nanotubes, ~10% of the nanotube area is occupied by silver nanoparticles. In empty area, using the same area calculation method, ~10% of the empty area is occupied by silver nanoparticle. No significant difference exists between nanotubes and empty area indicates that the Ac-C-P222 nanotube does not exhibit strong binding affinity to silver nanoparticles. As comparison, the loading percentage of gold nanoparticles on Ac-C-P222 nanotubes is calculated to be ~32%, as shown by **Figure 5.11**. The much denser loading confirms the selective binding affinity of Ac-C-P222 nanotubes to gold.

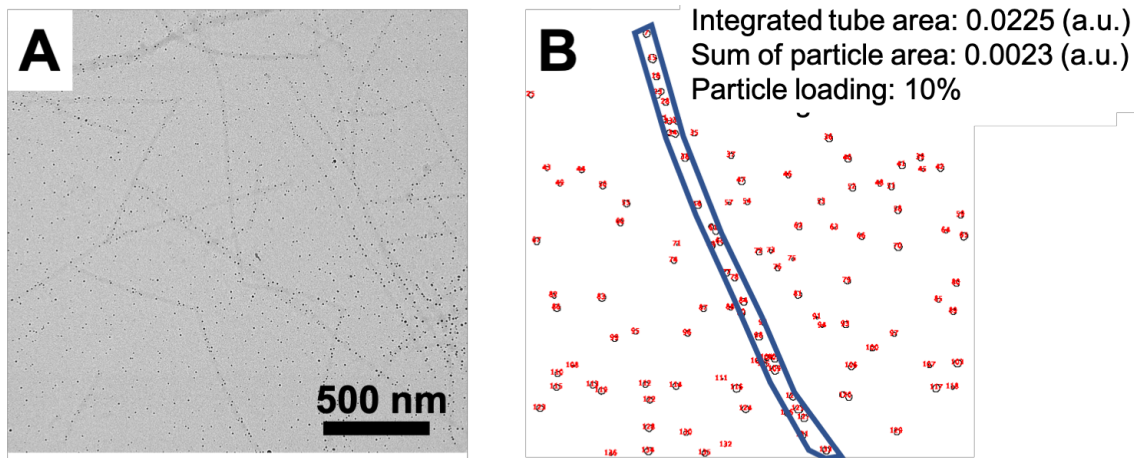


Figure 5.10 The loading percentage calculation of Ag nanoparticles on peptide nanotubes. **A:** The original TEM image of Ag nanoparticles synthesized with Ac-C-P222 nanotubes as templates. The image was taken from the same sample shown in **Figure 5.9**. **B:** The image with particle area information extracted from **A** using ImageJ. The red outlines indicate the areas of Ag nanoparticles. The blue outline indicates the area of the peptide nanotube, which can be calculated in ImageJ as A_{tube} . Within the nanotube area, the area summation of the silver nanoparticles can be calculated as A_{particle} . Therefore, the loading percentage can be calculated as $A_{\text{particle}}/A_{\text{tube}}*100\%$.

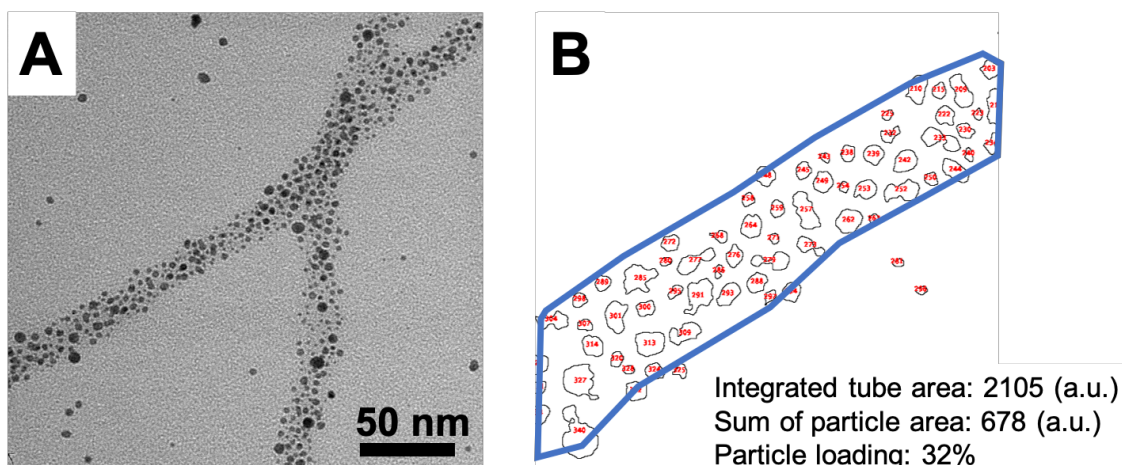


Figure 5.11 The loading percentage calculation of Au nanoparticles on peptide nanotubes. **A:** The original TEM image of Au nanoparticles synthesized with Ac-C-P222 nanotubes as templates. The image was taken from the same sample shown in **Figure 4.4B** in **Chapter 4**. **B:** The image with particle area information extracted from **A** using ImageJ. The red outlines indicate the areas of Au nanoparticles. The blue outline indicates the area of the peptide nanotube, which can be calculated in ImageJ as A_{tube} . Within the nanotube area, the area summation of the silver nanoparticles can be calculated as A_{particle} . Therefore, the loading percentage can be calculated as $A_{\text{particle}}/A_{\text{tube}}*100\%$.

Although, it has been reported in the literature that cysteine exhibits binding affinity to silver nanoparticles as well.^{52,55} In our studied case, due to the acidic solution condition, peptides carry positive charges. This is not facilitating the adsorption of Ag^+ cations to templating scaffolds, which may be the reason of the hindered templating effect. Therefore, the results indicate that the adsorption of inorganic precursor anions and the strong binding moiety in the scaffolds are both important for the ordered templating synthesis.

5.6 Conclusion

In this **Chapter 5**, we examined the electrostatic interactions between inorganic species and peptide templating scaffolds in addition to the desired thiol-gold bonding. Due to the charged nature of this studied peptide sequence, precursor anions can be bound to peptides during the gold nanoparticle synthesis process, which can result in successful templating or hinder the formation of gold nanoparticles depending on stoichiometry and addition order of precursor molecules. The adsorption of gold precursor anions to peptide scaffolds through the ion-pairing is facilitating the templated growth of gold nanoparticles. However, the ion-pairing between the reductant anions and peptides reduces the reducibility of reductants hindering the formation of nanoparticles.

REFERENCES

1. Dickerson, M. B.; Sandhage, K. H.; Naik, R. R. Protein- and Peptide-Directed Syntheses of Inorganic Materials. *Chem. Rev.* **2008**, *108* (11), 4935–4978.
2. Daniel, M. C.; Astruc, D. Gold Nanoparticles: Assembly, Supramolecular Chemistry, Quantum-Size-Related Properties, and Applications Toward Biology, Catalysis, and Nanotechnology. *Chem. Rev.* **2004**, *104* (1), 293–346.
3. Selvakannan, P.; Mandal, S.; Phadtare, S.; Pasricha, R.; Sastry, M. Capping of Gold Nanoparticles by the Amino Acid Lysine Renders Them Water-Dispersible. *Langmuir* **2003**, *19* (21), 3545–3549.
4. Bhargava, S. K.; Booth, J. M.; Agrawal, S.; Coloe, P.; Kar, G. Gold Nanoparticle Formation during Bromoaurate Reduction by Amino Acids. *Langmuir* **2005**, *21* (6), 5949–5956.
5. Mayer, A. B. R.; Mark, J. E. Comparisons between Cationic Polyelectrolytes and Nonionic Polymers for the Protection of Palladium and Platinum Nanocatalysts. *J. Polym. Sci. Part A Polym. Chem.* **1997**, *35* (15), 3151–3160.
6. Eustis, S.; El-Sayed, M. A. Why Gold Nanoparticles Are More Precious than Pretty Gold: Noble Metal Surface Plasmon Resonance and Its Enhancement of the Radiative and Nonradiative Properties of Nanocrystals of Different Shapes. *Chem. Soc. Rev.* **2006**, *35* (3), 209–217.
7. Xu, X.; Cortie, M. B. Shape Change and Color Gamut in Gold Nanorods, Dumbbells, and Dog Bones. *Adv. Funct. Mater.* **2006**, *16* (16), 2170–2176.
8. Jiao, Z.; Xia, H.; Tao, X. Modulation of Localized Surface Plasmon Resonance of Nanostructured Gold Crystals by Tuning Their Tip Curvature with Assistance of Iodide and Silver(I) Ions. *J. Phys. Chem. C* **2011**, *115* (16), 7887–7895.
9. Pérez-Juste, J.; Pastoriza-Santos, I.; Liz-Marzán, L. M.; Mulvaney, P. Gold Nanorods: Synthesis, Characterization and Applications. *Coord. Chem. Rev.* **2005**, *249* (17–18), 1870–1901.

10. Diroll, B. T.; Jishkariani, D.; Cargnello, M.; Murray, C. B.; Donnio, B. Polycatenar Ligand Control of the Synthesis and Self-Assembly of Colloidal Nanocrystals. *J. Am. Chem. Soc.* **2016**, *138* (33), 10508–10515.
11. Warner, M. G.; Reed, scott m.; Hutchison, J. E. Small, Water-Soluble, Ligand-Stabilized Gold Nanoparticles Synthesized by Interfacial Ligand Exchange Reactions. *Chem. Mater.* **2000**, *12* (9), 3316–3320.
12. Woehrle, G. H.; Warner, M. G.; Hutchison, J. E. Ligand Exchange Reactions Yield Sudnanometer, Thiol-Stabilized Gold Particles with Defined Optical Transitions. *J. Phys. Chem.* **2002**, *106*, 9979–9981.
13. Kim, K.-S.; Dembereinyamba, D.; Lee, H. Size-Selective Synthesis of Gold and Platinum Nanoparticles Using Novel Thiol-Functionalized Ionic Liquids. *Langmuir* **2004**, *20* (3), 556–560.
14. Bouvy, C.; Baker, G. A.; Yin, H.; Dai, S. Growth of Gold Nanosheets and Nanopolyhedra in Pyrrolidinium-Based Ionic Liquids: Investigation of the Cation Effect on the Resulting Morphologies. *Cryst. Growth Des.* **2010**, *10* (3), 1323–1331.
15. Chirea, M.; Freitas, A.; Vasile, B. S.; Ghitulica, C.; Pereira, C. M.; Silva, F. Gold Nanowire Networks: Synthesis, Characterization, and Catalytic Activity. *Langmuir* **2011**, *27*, 3906–3913.
16. Kimling, J.; Maier, M.; Okenve, B.; Kotaidis, V.; Ballot, H.; Plech, A. Turkevich Method for Gold Nanoparticle Synthesis Revisited. *J. Phys. Chem. B* **2006**, *110* (32), 15700–15707.
17. Jana, N. R.; Peng, X. Single-Phase and Gram-Scale Routes toward Nearly Monodisperse Au and Other Noble Metal Nanocrystals. *J. Am. Chem. Soc.* **2003**, *125* (47), 14280–14281.
18. Wang, S.; Qian, K.; Bi, X.; Huang, W. Influence of Speciation of Aqueous H₂AuCl₄ on the Synthesis, Structure, and Property of Au Colloids. *J. Phys. Chem. C* **2009**, *113* (16), 6505–6510.
19. Deraedt, C.; Salmon, L.; Gatard, S.; Ciganda, R.; Hernandez, R.; Ruiz, J.; Astruc, D. Sodium Borohydride Stabilizes Very Active Gold Nanoparticle Catalysts. *Chem. Commun.* **2014**, *50* (91), 14194–14196.
20. Guo, S.; Wang, E. Noble Metal Nanomaterials: Controllable Synthesis and Application in Fuel Cells and Analytical Sensors. *Nano Today* **2011**, *6* (3), 240–264.

21. Grzelczak, M.; Pérez-Juste, J.; Mulvaney, P.; Liz-Marzán, L. M. Shape Control in Gold Nanoparticle Synthesis. *Chem. Soc. Rev.* **2008**, *37* (9), 1783.
22. Jana, N. R. Gram-Scale Synthesis of Soluble, near-Monodisperse Gold Nanorods and Other Anisotropic Nanoparticles. *Small* **2005**, *1* (8–9), 875–882.
23. Murphy, C. J.; Tapan K. Sau; Anand M. Gole; Christopher J. Orendorff; Jinxin Gao; Linfeng Gou; Hunyadi, S. E.; Li, T. Anisotropic Metal Nanoparticles: Synthesis, Assembly, and Optical Applications. *J. Phys. Chem. B* **2005**, *109*, 13857–13870.
24. Fink, J.; Kiely, C. J.; Bethell, D.; Schiffrin, D. J. Self-Organization of Nanosized Gold Particles. *Chem. Mater.* **1998**, *10* (3), 922–926.
25. Ye, X.; Zhu, C.; Ercius, P.; Raja, S. N.; He, B.; Jones, M. R.; Hauwiller, M. R.; Liu, Y.; Xu, T.; Alivisatos, A. P. Structural Diversity in Binary Superlattices Self-Assembled from Polymer-Grafted Nanocrystals. *Nat. Commun.* **2015**, *6*, 10052.
26. Nonappa; Haataja, J. S.; Timonen, J. V. I.; Malola, S.; Engelhardt, P.; Houbenov, N.; Lahtinen, M.; Häkkinen, H.; Ikkala, O. Reversible Supracolloidal Self-Assembly of Cobalt Nanoparticles to Hollow Capsids and Their Superstructures. *Angew. Chemie Int. Ed.* **2017**, *129* (23), 6573–6577.
27. Zhang, X.; Lv, L.; Ji, L.; Guo, G.; Liu, L.; Han, D.; Wang, B.; Tu, Y.; Hu, J.; Yang, D.; et al. Self-Assembly of One-Dimensional Nanocrystal Superlattice Chains Mediated by Molecular Clusters. *J. Am. Chem. Soc.* **2016**, *138* (10), 3290–3293.
28. Stevens, M. M.; Flynn, N. T.; Wang, C.; Tirrell, D. A.; Langer, R. Coiled-Coil Peptide-Based Assembly of Gold Nanoparticles. *Adv. Mater.* **2004**, *16* (11), 915–918.
29. Slocik, J. M.; Tam, F.; Halas, N. J.; Naik, R. R. Peptide-Assembled Optically Responsive Nanoparticle Complexes. *Nano Lett.* **2007**, *7* (4), 1054–1058.
30. San, B. H.; Li, Y.; Tarbet, E. B.; Yu, S. M. Nanoparticle Assembly and Gelatin Binding Mediated by Triple Helical Collagen Mimetic Peptide. *ACS Appl. Mater. Interfaces* **2016**, *8* (31), 19907–19915.

31. Mirkin, C. A.; Letsinger, R. L.; Mucic, R. C.; Storhoff, J. J. A DNA-Based Method for Rationally Assembling Nanoparticles into Macroscopic Materials. *Nature* **1996**, 382 (6592), 607–609.
32. Brodin, J. D.; Auyeung, E.; Mirkin, C. A. DNA-Mediated Engineering of Multicomponent Enzyme Crystals. *Proc. Natl. Acad. Sci. U. S. A.* **2015**, 112 (15), 4564–4569.
33. Jones, M. R.; Seeman, N. C.; Mirkin, C. A. Programmable Materials and the Nature of the DNA Bond. *Science* **2015**, 347 (6224), 840.
34. Janairo, J. I. B. *Peptide-Mediated Biomineralization*; Springer, Singapore, **2016**.
35. Ofir, Y.; Samanta, B.; Rotello, V. M. Polymer and Biopolymer Mediated Self-Assembly of Gold Nanoparticles. *Chem. Soc. Rev.* **2008**, 37 (9), 1814–1825.
36. Storhoff, J. J.; Mirkin, C. A. Programmed Materials Synthesis with DNA. *Chem. Rev.* **1999**, 99 (7), 1849–1862.
37. Shenhar, R.; Norsten, T. B.; Rotello, V. M. Polymer-Mediated Nanoparticle Assembly: Structural Control and Applications. *Adv. Mater.* **2005**, 17 (6), 657–669.
38. Gao, X.; Matsui, H. Peptide-Based Nanotubes and Their Applications in Bionanotechnology. *Adv. Mater.* **2005**, 17 (17), 2037–2050.
39. Chen, C. L.; Rosi, N. L. Peptide-Based Methods for the Preparation of Nanostructured Inorganic Materials. *Angew. Chemie - Int. Ed.* **2010**, 49 (11), 1924–1942.
40. Braun, E.; Eichen, Y.; Sivan, U.; Ben-Yoseph, G. DNA-Templated Assembly and Electrode Attachment of a Conducting Silver Wire. *Nature* **1998**, 391 (6669), 775–778.
41. Warner, M. G.; Hutchison, J. E. Linear Assemblies of Nanoparticles Electrostatically Organized on DNA Scaffolds. *Nat. Mater.* **2003**, 2 (4), 272–277.
42. Shenton, W.; Mann, S.; Douglas, T.; Young, M.; Stubbs, G. Inorganic-Organic Nanotube Composites from Template Mineralization of Tobacco Mosaic Virus. *Adv. Mater.* **1999**, 11 (3), 253–256.

43. Shenton, W.; Pum, D.; Sleytr, U. B.; Mann, S. Synthesis of Cadmium Sulphide Superlattices Using Bacterial S-Layers. *Nature* **1997**, *389* (6651), 585–587.
44. Scheibel, T.; Parthasarathy, R.; Sawicki, G.; Lin, X.-M.; Jaeger, H.; Lindquist, S. L. Conducting Nanowires Built by Controlled Self-Assembly of Amyloid Fibers and Selective Metal Deposition. *Proc. Natl. Acad. Sci. U. S. A.* **2003**, *100* (8), 4527–4532.
45. Meegan, J. E.; Aggeli, A.; Boden, N.; Brydson, R.; Brown, A. P.; Carrick, L.; Brough, A. R.; Hussain, A.; Ansell, R. J. Designed Self-Assembled β -Sheet Peptide Fibrils as Templates for Silica Nanotubes. *Adv. Funct. Mater.* **2004**, *14* (1), 31–37.
46. Zhou, Y.; Kogiso, M.; He, C.; Shimizu, Y.; Koshizoki, N.; Shimizu, T. Fluorescent Nanotubes Consisting of CdS-Embedded Bilayer Membranes of a Peptide Lipid. *Adv. Mater.* **2007**, *19* (8), 1054–1058.
47. Lamm, M. S.; Sharma, N.; Rajagopal, K.; Beyer, F. L.; Schneider, J. P.; Pochan, D. J. Laterally Spaced Linear Nanoparticle Arrays Templated by Laminated β -Sheet Fibrils. *Adv. Mater.* **2008**, *20* (3), 447–451.
48. Jun, J. M. V.; Altoe, M. V. P.; Aloni, S.; Zuckermann, R. N. Peptoid Nanosheets as Soluble, Two-Dimensional Templates for Calcium Carbonate Mineralization. *Chem. Commun.* **2015**, *51* (50), 10218–10221.
49. Loweth, C. J.; Caldwell, W. B.; Peng, X.; Alivisatos, a P.; Schultz, P. G. DNA-Based Assembly of Gold Nanocrystals. *Angew. Chemie Int. Ed.* **1999**, *38* (12), 1808–1812.
50. Yao, G.; Li, J.; Chao, J.; Pei, H.; Liu, H.; Zhao, Y.; Shi, J.; Huang, Q.; Wang, L.; Huang, W.; et al. Gold-Nanoparticle-Mediated Jigsaw-Puzzle-like Assembly of Supersized Plasmonic DNA Origami. *Angew. Chemie* **2015**, *127* (10), 3009–3012.
51. Mo, X.; An, Y.; Yun, C. S.; Yu, S. M. Nanoparticle-Assisted Visualization of Binding Interactions between Collagen Mimetic Peptide and Collagen Fibers. *Angew. Chemie - Int. Ed.* **2006**, *45* (14), 2267–2270.
52. Kasotakis, E.; Mossou, E.; Adler-Abramovich, L.; Mitchell, E. P.; Forsyth, V. T.; Gazit, E.; Mitraki, A. Design of Metal-Binding Sites onto Self-Assembled Peptide Fibrils. *Pept. Sci.* **2009**, *92* (3), 164–172.
53. Hamley, I. W. Peptide Nanotubes. *Angew. Chemie - Int. Ed.* **2014**, *53* (27), 6866–6881.

54. Zhou, Z.; Bedwell, G. J.; Li, R.; Palchoudhury, S.; Prevelige, P. E.; Gupta, A. Pathways for Gold Nucleation and Growth over Protein Cages. *Langmuir* **2017**, *33* (23), 5925–5931.
55. Li, G.; Wang, Y.; Wang, L.; Song, A.; Hao, J. Hydrogels of Super-Long Helices to Synthesize Hybrid Ag-Helical Nanomaterials. *Langmuir* **2016**, *32* (46), 12100–12109.
56. Ramin Djalali; Yung-fou Chen; Matsui, H. Au Nanowire Fabrication from Sequenced Histidine-Rich Peptide. *J. Am. Chem. Soc.* **2002**, *124* (46), 13660–13661.
57. Sharma, N.; Top, A.; Kiick, K. L.; Pochan, D. J. One-Dimensional Gold Nanoparticle Arrays by Electrostatically Directed Organization Using Polypeptide Self-Assembly. *Angew. Chemie* **2009**, *121*, 7212–7216.
58. Brodin, J. D.; Carr, J. R.; Sontz, P. A.; Tezcan, F. A. Exceptionally Stable, Redox-Active Supramolecular Protein Assemblies with Emergent Properties. *Proc. Natl. Acad. Sci. U. S. A.* **2014**, *111* (8), 2897–2902.
59. Kracht, S.; Messerer, M.; Lang, M.; Eckhardt, S.; Lauz, M.; Grobóty, B.; Fromm, K. M.; Giese, B. Electron Transfer in Peptides: On the Formation of Silver Nanoparticles. *Angew. Chemie Int. Ed.* **2015**, *54*, 2912–2916.
60. Deschamps, P.; Kulkarni, P. P.; Gautam-Basak, M.; Sarkar, B. The Saga of Copper(II)-L-Histidine. *Coord. Chem. Rev.* **2005**, *249* (9–10), 895–909.
61. Li, L. S.; Stupp, S. I. One-Dimensional Assembly of Lipophilic Inorganic Nanoparticles Templated by Peptide-Based Nanofibers with Binding Functionalities. *Angew. Chemie - Int. Ed.* **2005**, *44* (12), 1833–1836.
62. Mei, S.; Qi, H.; Zhou, T.; Li, C. Y. Precisely Assembled Cyclic Gold Nanoparticle Frames via 2D Polymer Single Crystal Templating. *Angew. Chemie Int. Ed.* **2017**, *56* (44), 13645–13649.
63. Hu, Y.; Xu, W.; Li, G.; Xu, L.; Song, A.; Hao, J. Self-Assembled Peptide Nanofibers Encapsulated with Superfine Silver Nanoparticles via Ag + Coordination. *Langmuir* **2015**, *31* (31), 8599–8605.
64. Naik, R. R.; Stringer, S. J.; Agarwal, G.; Jones, S. E.; Stone, M. O. Biomimetic Synthesis and Patterning of Silver Nanoparticles. *Nat. Mater.* **2002**, *1* (3), 169–172.
65. Slocik, J. M.; Stone, M. O.; Naik, R. R. Synthesis of Gold Nanoparticles Using Multifunctional Peptides. *Small* **2005**, *1* (11), 1048–1052.

66. Chen, C. L.; Zhang, P.; Rosi, N. L. A New Peptide-Based Method for the Design and Synthesis of Nanoparticle Superstructures: Construction of Highly Ordered Gold Nanoparticle Double Helices. *J. Am. Chem. Soc.* **2008**, *130* (41), 13555–13557.
67. Singh, P.; Lamanna, G.; Ménard-Moyon, C.; Toma, F. M.; Magnano, E.; Bondino, F.; Prato, M.; Verma, S.; Bianco, A. Formation of Efficient Catalytic Silver Nanoparticles on Carbon Nanotubes by Adenine Functionalization. *Angew. Chemie - Int. Ed.* **2011**, *50* (42), 9893–9897.
68. Zhang, H. V.; Polzer, F.; Haider, M. J.; Tian, Y.; Villegas, J. A.; Kiick, K. L.; Pochan, D. J.; Saven, J. G. Computationally Designed Peptides for Self-Assembly of Nanostructured Lattices. *Sci. Adv.* **2016**, *2* (9), e1600307.
69. Slocik, J. M.; Wright, D. W. Biomimetic Mineralization of Noble Metal Nanoclusters. *Biomacromolecules* **2003**, *4* (5), 1135–1141.

Chapter 6

CONCLUSIONS AND PERSPECTIVE

6.1 Conclusions

This Ph.D. dissertation is based on a collaborative materials research project with the goal of establishing computational design methodology for a programmable peptide self-assembly system. The peptide self-assembly system features the anti-parallel, homotetrameric coiled-coil bundle composed of α -helical 29-mer synthetic peptides as the fundamental assembly building block. The higher order, programmable self-assembly structures can be assembled from the coiled-coils by the variation of only certain exterior amino acid residues with the targeting of predetermine structures (monolayer of lattices with certain space group symmetries, P622, P222 and P422). The formation of coiled-coil bundles and the higher order assembly structures are confirmed experimentally and characterized in detail as described in this Ph.D. dissertation as well as in the Ph.D. dissertation by Michael Haider (University of Delaware, 2018). Due to the robust design of the hydrophobic bundle core, the coiled-coil bundles can keep intact in a variety of solution conditions (pH = 4.5, 7, 8, 10; temperature = 30°C, 40°C, 50°C, 60°C) other than the neutral pH, room temperature condition in which the computational designing is based. The inter-bundle interactions are therefore controlled by different solution conditions and utilized in the kinetic controlling of the self-assembly process of the coiled-coil bundles.

The solution pH and temperature-dependent assembly behavior of designed P422_1 sequence peptide was thoroughly investigated by the methods of microscopy

and X-ray scattering and discussed in **Chapter 2**. A sequence isoelectric point (pI) related rule is established for the rational explanation and prediction of peptide assembly behavior in different pH conditions. The examined N-terminus acetylated P422_1 sequence exhibits fast assembly kinetics in a solution condition of pH 7 and pH 8, which are near the pI of this sequence. This is due to the overall neutral net charge the peptide coiled-coil bundles carry determined by the solution pH. Therefore, there are less electrostatic interactions involved to disrupt the self-assembly of coiled-coil bundles. The fast assembly kinetics can cause the assembly structures being trapped in metastable states as revealed by the slow assembly structure morphology transition from initially formed disordered aggregates to the ordered lattices over the period of 8 weeks. The thermal annealing method (assembly solution temperature = 40°C or 50°C) is applied to accelerate the lattices formation to a period of several hours. As the net charge of peptide coiled-coil bundles increases when peptides are assembled in solution pH conditions that are much deviated from the pI of the sequence, the assembly kinetic behavior is significantly altered. In the condition of pH = 10, due to the increased negative net charge carried by the peptide bundles, the self-assembly process is slowed by the inter-bundle electrostatic interactions. In the condition of pH = 4.5, the even more significant positive net charge that the peptide bundles carry completely disrupts the inter-bundle assembly process. Therefore, peptides exist as soluble coiled-coil bundles in solution instead of forming higher order self-assembled lattices.

Based on a similar inter-bundle interaction controlling strategy, the self-assembled structures from designed P222_9 sequence peptides in different solution pH conditions (pH = 4.5, 7 and 10) are characterized and discussed in **Chapter 3**. The

peptides also exhibit fast assembly kinetics at pH 7 which is close to the pI of the sequence, and form two-dimensional platelets. More diverse nanostructures are observed when peptides are assembled in very different solution pH conditions. At pH 4.5, uniform nanotubular structures with the diameter of around 13 nm are observed. At pH 10, anisotropic needle-like structures with length over several micrometers are observed. Based on the circular dichroism analysis, the peptide coiled-coil structures exist in all of the three pH conditions and act as basic assembly building blocks for the higher order self-assembled structures. The self-assembled peptide nanotubes are thoroughly analyzed by cryo-TEM, solution small-angle X-ray scattering, STEM mass-mapping and site-specific amino acid substitution. A monolayer of tilted-arranged peptide coiled-coil bundles is proposed as the structure model of peptide nanotubes. The positively charged portion (induced by acidic assembly condition, pH = 4.5) in the exterior part of the bundle is proposed to be the reason to cause the tilted arrangement of the bundles for the formation of curved surface.

Based on the developed nanostructures, one-dimensional nanotubes assembled from designed P222_9 sequence at pH 4.5, and two-dimensional platelets assembled from designed P422_1 sequence at pH 7, the templating application of these nanostructures is demonstrated in **Chapter 4**. Cysteine with the thiol-functional group is used as a binding site for gold nanoparticles. Therefore, cysteine-modified peptides, Ac-C-P222 and Ac-C-P422, were synthesized. The cysteine-modified peptides assemble into similar nanostructures compared to the un-modified peptides and were used as templates for gold nanoparticles. Both the in-situ solution gold nanoparticles synthesis and the ligand-exchange process using premade 5 nm Au nanocrystals produced orderly templated gold nanoparticles, including one-dimensional gold

nanoparticle chains and two-dimensional gold nanoparticle arrays based on different templates. The optical property of one-dimensional gold nanoparticle chains was probed using UV-vis spectroscopy. The enhanced plasmonic properties were observed due to the coupling effect of the closely arranged neighboring gold nanoparticles templated by peptide nanotubes. A facile surface deposition method was developed, based on the solution templated gold nanoparticle synthesis process, for the fabrication of solid-state gold nanowires.

In **Chapter 5**, the solution templating process of gold nanoparticles on Ac-C-P222 peptide nanotubes formed at pH 4.5 was investigated in detail. Due to the positively charged nature of peptide nanotube scaffolds, multiple interactions, including gold-thiol bonding and electrostatic interactions between peptides and precursor anions are involved during this process. The synergic effect of these interactions determines the proper amount of precursor molecules and the addition order for the optimal formation of templated gold nanoparticles. The Ac-C-P222 peptide contains 4 positively charged amino acid residues that can bind with precursor anions (AuCl_4^- and BH_4^-) via ion-pairing interactions in acidic condition. Therefore, the addition of 2-equivalent of HAuCl_4 and NaBH_4 results in the most homogenous formation of templated 1D chain-like gold nanoparticles. The excessive addition of precursor reagents gives the formation of aggregated gold nanoparticles. The insufficient addition of precursor reagents hinders the formation of gold nanoparticles due to the precursor anions being bound by excess peptides. Due to the strong electrostatic interactions between precursors anions and peptides, when NaBH_4 is firstly added to the peptide templates suspension solution, precursor anions are bound by the peptides thus losing the reducibility. In this specific case, the first addition of

precursor reagents is required to be HAuCl_4 for the efficient formation of gold nanoparticles. Furthermore, Ac-C-P222 peptide nanotubes exhibit strong binding selectivity to gold nanoparticles synthesized using anionic HAuCl_4 while less binding affinity to silver nanoparticles synthesized using cationic AgNO_3 .

6.2 Prospective

6.2.1 Co-assembly of multiple peptides

In **Chapter 3** and **Chapter 4**, it was demonstrated that two peptides H-P222_9 (DGRIE GMAEA IKKMA YNIAD MAGRI WGEA-NH₂) and Ac-C-P222 (Ac- C DGRIE GMAEA IKKMA YNIAD MAGRI WGEA-NH₂) both can assemble into homogenous nanotubes in acidic conditions. The morphologies of nanotubes assembled from each peptide are shown by cryo-TEM images in **Figure 6.1**.

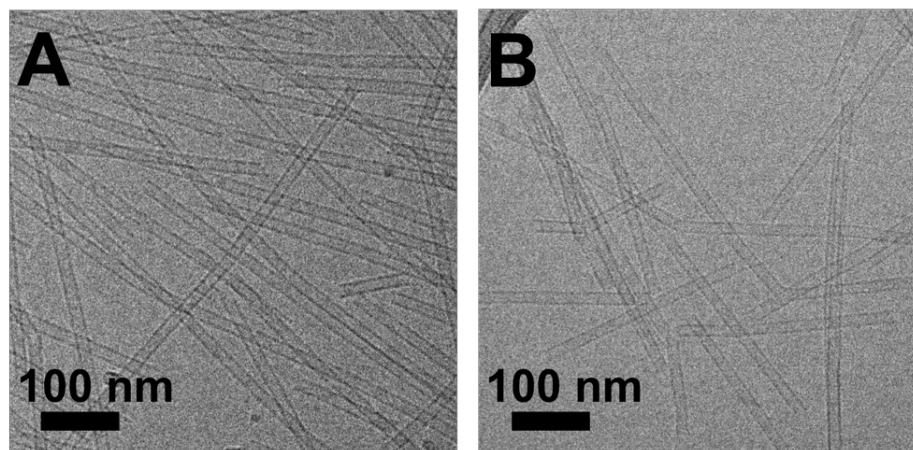


Figure 6.1 **A:** Cryo-TEM images of 0.2mM H-P222_9 peptide assembled in 10mM pH 4.5 buffer at room temperature for 18 hours. The tube diameter measured from wall center to wall center in TEM images is $13.3 \text{ nm} \pm 0.7 \text{ nm}$. The wall thickness measured from TEM images is $3.1 \text{ nm} \pm 0.5 \text{ nm}$. **B:** Cryo-TEM images of 0.2mM Ac-C-P222 peptide assembled in 50 mM pH 4.5 buffer with additional 2.5 TCEP at room temperature for 18 hours. The tube diameter measured from TEM is $13.0 \pm 0.8 \text{ nm}$, and wall thickness is $3.2 \pm 0.4 \text{ nm}$.

As shown in **Figure 6.1**, the nanotubes assembled individually from these two peptides have almost identical morphology; micrometer-long, rigid nanotubes of similar size. Although partially broken points can be spotted, no branches can be observed. Serendipitously, it was found that the co-assembly of these two molecules yields the unusual branched nanotube structures composed of Y- and T-junctions, as revealed by cryo-TEM images in **Figure 6.2-6.4**.

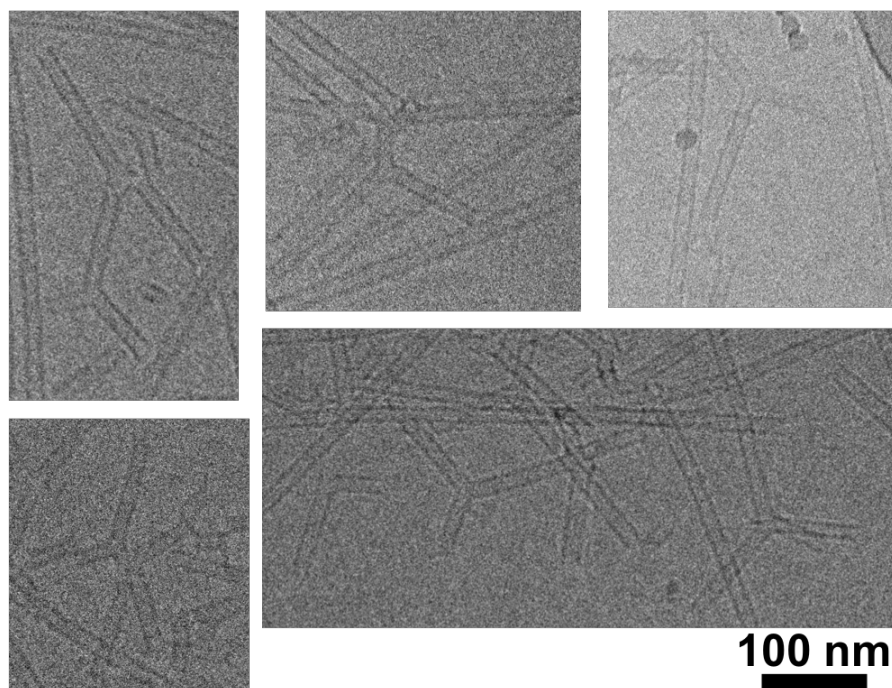


Figure 6.2 Cryo-TEM images of branched nanotubes co-assembled from H-P222_9 and Ac-C-P222 peptides. 0.2 mM H-P222_9 and 0.2 mM Ac-C-P222 peptides firstly were allowed to self-assemble in pH 4.5 buffer individually. After 5 min of separate assembly, solutions were mixed for co-assembly. Nanostructures were examined after 18 hours of co-assembly.

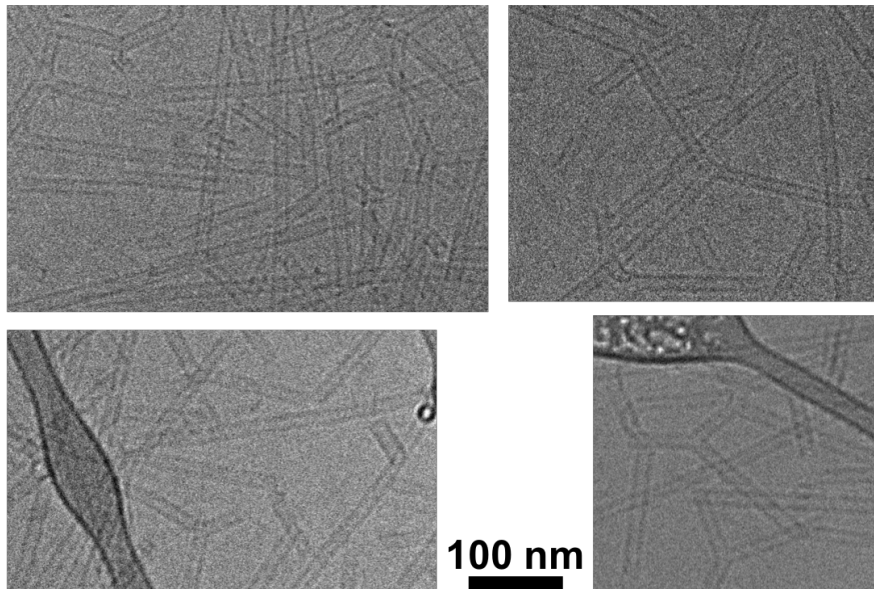


Figure 6.3 Cryo-TEM images of branched nanotubes co-assembled from H-P222_9 and Ac-C-P222 peptides. 0.2 mM H-P222_9 and 0.2 mM Ac-C-P222 peptides firstly were allowed to self-assemble in pH 4.5 buffer individually. After 30 min of separate assembly, solutions were mixed for co-assembly. Nanostructures were examined after 18 hours of co-assembly.

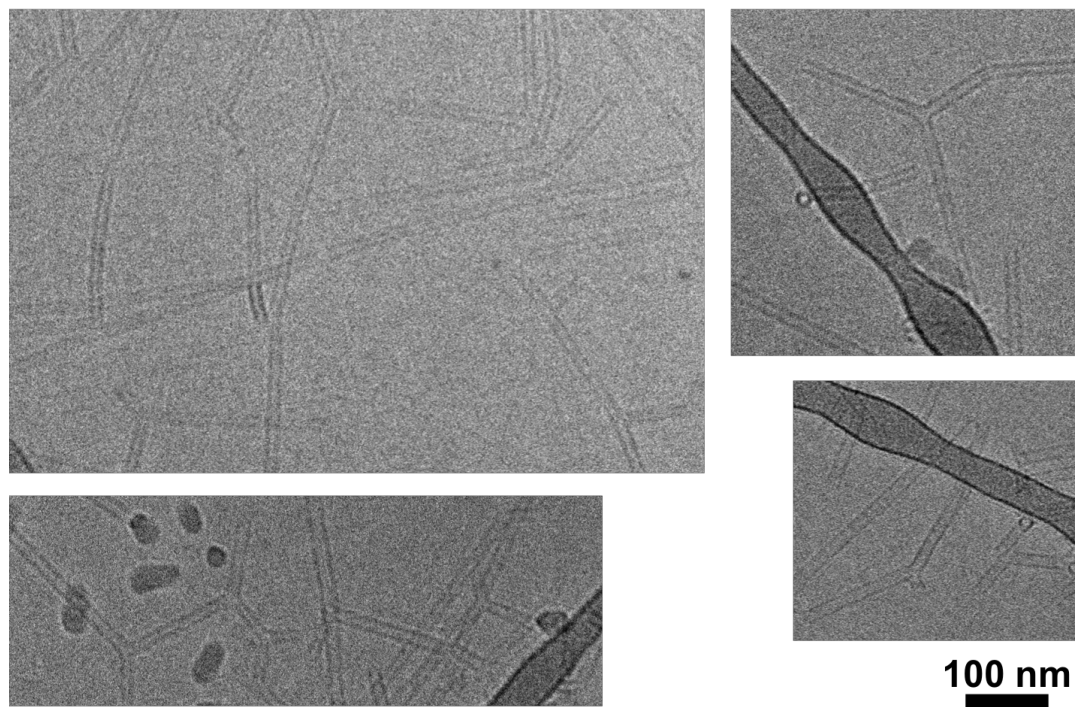


Figure 6.4 Cryo-TEM images of branched nanotubes co-assembled from H-P222_9 and Ac-C-P222 peptides. 0.2 mM H-P222_9 and 0.2 mM Ac-C-P222 peptides firstly were allowed to self-assemble in pH 4.5 buffer individually. After 3 hours of separate assembly, solutions were mixed for co-assembly. Nanostructures were examined after 18 hours of co-assembly.

In the co-assembly experiment, the H-P222_9 and Ac-C-P222 peptides were firstly allowed to assemble individually. As discussed in the previous chapters, the peptide self-assembly process is a time-dependent kinetic process. In the initial separate assembly stage, two peptides each can form coiled-coil bundles, and short nanotubes. After the mixing of two initially assembled peptides, the co-assembly produced the clear branches in the nanotubes. Furthermore, by comparing the morphologies of the branched nanotubes in **Figure 6.2-6.4**, the co-assembly of the longest separately assembled sample (3 hours of separate-assembly, shown in **Figure**

6.4) produced the longest nanotubes between the junction points. And the co-assembly of the shortest separately assembled sample (5 min of separate-assembly, shown in **Figure 6.2**) produced mostly the branches and the shortest nanotubes between the junction points. We hypothesize that the junctions occur when short nanotubes of each molecule assembled during the initial separate-assembly stage attempt to fuse into longer nanotubes. The possible assembly kinetic difference between two nanotubes causes the imperfect fusing thus leading to the formation of junctions.

From the observation of the branched nanotubes formation, the structure itself is an attractive research object. In the example of self-assembled polymers and surfactants, branched cylindrical micelles composed of Y-junctions and bi-continuous cylindrical micelles have been observed in some cases such as PS-*b*-PAA (polystyrene-*b*-poly(acrylic acid)), and PB-*b*-PEO (poly (1,2-butadiene)-*b*-poly(ethylene oxide)) existing between the cylindrical and bilayer phases.¹⁻³ Due to the surface curvature changes in the junction regions, the energy barrier is usually higher for the formation of junctions than the formation of end-capping micelles or toroid micelles. Certain molecule composition, such as bi-arm or tri-arm or mixture surfactants,^{4,5} or additives,⁶ or solvent condition^{1-3,5} are required to make the branched morphology a more energy-favored state. Crystallization-driven self-assembly method also has been applied to co-assemble two types of cylindrical micelle seeds with different crystalline core sizes so that the micelles with smaller core sizes can be attached to thicker core creating branches.⁷ Branched, hollow tubes are ubiquitous morphologies in nature and inorganic materials, such as vesicular, carbon nanotubes,⁸⁻¹¹ which have important impact in materials transporting. Such branched morphology is less common in self-assembled soft materials systems. Bilayer branched nanotubes

assembled from PS₂₄₀-*b*-PEO₁₅ (polystyrene-*b*-poly(ethylene oxide)) have been reported in the late 90s by Eisenberg et al.¹² Due to the small weight of hydrophilic PEO domain, the more flat bilayer structure lowers the energy barrier for the formation of the junctions. And, the junctions reflect the transition morphology from tubes to vesicles due to the co-existence of vesicles and vesicle-capped tubes. Biomacromolecules, such as polynucleotides and polypeptides offer more designing and controlling opportunities to self-assemble complex nanomaterials due to their shape and sequence-specificities. Branches in self-assembled biomacromolecular nanofibers and nanorods can be deliberately induced using conformational flexible molecules¹³ or junction molecules.¹⁴⁻¹⁶ In the aspect of hollow nanotubes, although great efforts have been devoted to produce various examples of DNA¹⁷⁻¹⁹ or peptide-based nanotubes, the branched morphology is rarely observed. This is because for most cases of DNA- and peptide-based nanotubes, the tube formation is from the helical-wrapping or curling-and-closure of layered structures. Thus, molecules within the tubes are in a very ordered, crystalline-like packing manner that allows little structure frustration or defects for branches to exist. Zhang research group at MIT has reported the observation of branched tube structures assembled from short surfactant-like peptides. The structure defects in the bilayer nanotubes are believed to be the cause of tube fusing.^{20,21} To the best of our knowledge, the branched structure presented here is the first example in mono-layer peptide nanotubes. An even more attractive point is that there is only one amino acid residue difference within the two peptides used in the co-assembly process. Such small difference in molecular structure causes the possible difference in assembly kinetics. This is a significant advantage of using sequence-specific peptides in the study of molecular self-assembly. The site-

specific modification of peptide molecules can be achieved precisely, which allows the opportunity of detailed interpretation of the assembly behavior from the molecular level. Future research effort is worthy of investment in this direction.

6.2.2 Novel materials development

As a researcher in the field of Materials Science, the ultimate goal of studying self-assembly is to develop novel materials. In the Ph.D. work presented in this dissertation, initial effort has been devoted to demonstrate the proof-of-concept for peptide-based materials development. As demonstrated in **Chapter 4**, self-assembled peptide nanotubes are used as templates for the fabrication of solid-state gold nanowires. Moreover, the abundant functional groups in the side chains of the peptide assemblies give more opportunities for the further functionalization. As being reported by other groups, glutaraldehyde has been largely utilized as the cross-linking agent in peptides and proteins for protein-based materials development.^{22,23} Inspired by these works, a similar strategy was applied in our study to covalently cross-link the self-assembled peptide nanotubes to improve the nanomaterial's stability. The obtained preliminary results are shown in **Figure 6.5**.

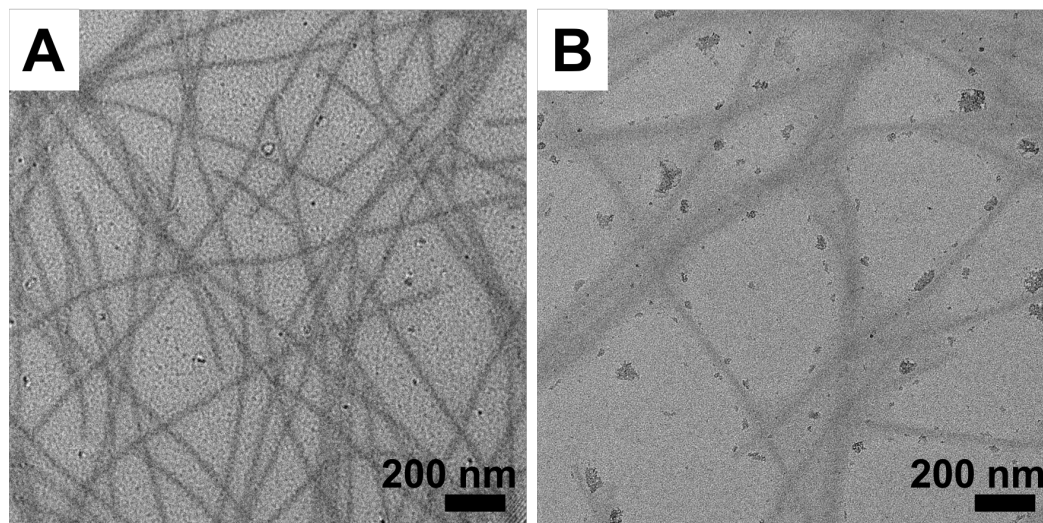


Figure 6.5 TEM images of glutaraldehyde cross-linked H-P222_9 nanotubes. **A:** Peptide nanotubes assembled from H-P222_9 and cross-linked by glutaraldehyde in pH 4.5 buffer. **B:** The cross-linked nanotubes from **A** mixed with DMF. The morphology is showing the nanotube structures are able to maintain themselves in the polar solvent.

As shown in **Figure 6.5A**, the reaction of cross-linking agent glutaraldehyde with the self-assembled peptide nanotubes does not have significant effect on the morphology of peptide nanotubes. The stability of cross-linked peptide nanotubes is tested by mixing the peptide nanotube suspension solution with the same amount (volume) of DMF (dimethylformamide), which can often disrupt the secondary-structures and assembled-structures of peptides.²⁴ After 1 day of incubation with peptide nanotube suspension solution and DMF solvent, as shown in **Figure 6.5B**, most of the nanotube morphology was maintained. It is likely that the glutaraldehyde cross-linked the primary amine groups in the side chains of self-assembled peptide nanotubes resulting in the more stable structures. This reveals a great opportunity in our studied case to fabricate more stable materials with potential application properties. For example, as shown in **Figure 6.2-6.4**, the branched nanotubes can be constructed by the co-

assembly of two tube-former peptides. With the glutaraldehyde cross-linking modification, the inter-connected structural features of the branched nanotubes can be maintained with improved mechanical property. The resulted materials can possibly possess foam-like porous structures with potential applications as filtering materials, catalysts carriers and a cell-growth medium.

6.2.3 Conclusion

The Ph.D. work presented in this dissertation just scratched the surface of two focused fields in the study of self-assembly. One is to understand the self-assembly behavior from the molecular structure level. Another is to develop novel materials based on control of the self-assembly process of molecules. The presented studies have revealed the delicate mechanisms governing the inter- and intra-molecular interactions during the self-assembly process, as well as shown the fine and high-quality self-assembled nanostructures. Future research also should be based on these two aspects with the ultimate goal of developing robust methods to achieve the high complexity and programmability in the self-assembly process. Automated fabrication is the future for the industrial manufacturing. Therefore, the robust, reproducible, large-scale and efficient application of automated molecular self-assembly will be an important factor to revolutionize the future of manufacturing.

REFERENCES

1. Zhang, L.; Eisenberg, A. Thermodynamic vs Kinetic Aspects in the Formation and Morphological Transitions of Crew-Cut Aggregates Produced by Self-Assembly of Polystyrene-*b*-Poly(Acrylic Acid) Block Copolymers in Dilute Solution. *Macromolecules* **1999**, *32* (7), 2239–2249.
2. Jain, S.; Bates, F. S. On the Origins of Morphological Complexity in Block Copolymer Surfactants. *Science* **2003**, *300* (5618), 460–464.
3. Jain, S.; Bates, F. S. Consequences of Nonergodicity in Aqueous Binary PEO-PB Micellar Dispersions. *Macromolecules* **2004**, *37* (4), 1511–1523.
4. Danino, D.; Talmon, Y.; Levy, H.; Beinert, G.; Zana, R. Branched Threadlike Micelles in an Aqueous Solution of a Trimeric Surfactant. *Science* **1995**, *269* (5229), 1420–1421.
5. Lin, Z. Branched Worm-like Micelles and Their Networks. *Langmuir* **1996**, *12* (7), 1729–1737.
6. Zhang, M.; Wang, M.; He, S.; Qian, J.; Saffari, A.; Lee, A.; Kumar, S.; Hassan, Y.; Guenther, A.; Scholes, G.; et al. Sphere-to-Wormlike Network Transition of Block Copolymer Micelles Containing CdSe Quantum Dots in the Corona. *Macromolecules* **2010**, *43* (11), 5066–5074.
7. Qiu, H.; Du, V. A.; Winnik, M. A.; Manners, I. Branched Cylindrical Micelles via Crystallization-Driven Self-Assembly. *J. Am. Chem. Soc.* **2013**, *135* (47), 17739–17742.
8. He, L.; Lu, J. Q.; Jiang, H. Controlled Carbon-Nanotube Junctions Self-Assembled from Graphene Nanoribbons. *Small* **2009**, *5* (24), 2802–2806.
9. Yun, S. H.; Wu, J. Z.; Dibos, A.; Zou, X.; Karlsson, U. O. Self-Assembled Boron Nanowire Y-Junctions. *Nano Lett.* **2006**, *6* (3), 385–389.
10. Wei, D.; Liu, Y.; Cao, L.; Fu, L.; Li, X.; Wang, Y.; Yu, G.; Zhu, D. A New Method to Synthesize Complicated Multibranched Carbon Nanotubes with Controlled Architecture and Composition. *Nano Lett.* **2006**, *6* (2), 186–192.

11. Bandaru, P. R. Electrical Characterization of Carbon Nanotube Y-Junctions: A Foundation for New Nanoelectronics. *J. Mater. Sci.* **2007**, *42* (5), 1809–1818.
12. Yu, K.; Eisenberg, A. Bilayer Morphologies of Self-Assembled Crew-Cut Aggregates of Amphiphilic PS-*b*-PEO Diblock Copolymers in Solution. *Macromolecules* **1998**, *31* (11), 3509–3518.
13. Zhang, C.; Su, M.; He, Y.; Zhao, X.; Fang, P. -a.; Ribbe, A. E.; Jiang, W.; Mao, C. Conformational Flexibility Facilitates Self-Assembly of Complex DNA Nanostructures. *Proc. Natl. Acad. Sci.* **2008**, *105* (31), 10665–10669.
14. Boer, D. R.; Kerckhoffs, J. M. C. A.; Parajo, Y.; Pascu, M.; Usón, I.; Lincoln, P.; Hannon, M. J.; Coll, M. Self-Assembly of Functionalizable Two-Component 3D DNA Arrays through the Induced Formation of DNA Three-Way-Junction Branch Points by Supramolecular Cylinders. *Angew. Chemie Int. Ed.* **2010**, *49* (13), 2336–2339.
15. Ryadnov, M. G.; Woolfson, D. N.; Chem, A.; Ed, I. Introducing Branches into a Self-Assembling Peptide Fiber. *Angew. Chem. Int. Ed. Engl.* **2003**, *42* (26), 3021–3023.
16. Matsuura, K. Construction of Spherical Virus-Inspired Peptide Nanoassemblies. *Polym. J.* **2012**, *44* (6), 469–474.
17. Liu, D.; Park, S. H.; Reif, J. H.; LaBean, T. H. DNA Nanotubes Self-Assembled from Triple-Crossover Tiles as Templates for Conductive Nanowires. *Proc. Natl. Acad. Sci.* **2004**, *101* (3), 717–722.
18. Liu, H.; Chen, Y.; He, Y.; Ribbe, A. E.; Mao, C. Approaching the Limit: Can One DNA Oligonucleotide Assemble into Large Nanostructures? *Angew. Chemie - Int. Ed.* **2006**, *45* (12), 1942–1945.
19. Lo, P. K.; Karam, P.; Aldaye, F. A.; McLaughlin, C. K.; Hamblin, G. D.; Cosa, G.; Sleiman, H. F. Loading and Selective Release of Cargo in DNA Nanotubes with Longitudinal Variation. *Nat. Chem.* **2010**, *2* (4), 319–328.
20. Santoso, S.; Hwang, W.; Hartman, H.; Zhang, S. Self-Assembly of Surfactant-like Peptides with Variable Glycine Tails to Form Nanotubes and Nanovesicles. *Nano Lett.* **2002**, *2* (7), 687–691.
21. Vauthey, S.; Santoso, S.; Gong, H.; Watson, N.; Zhang, S. Molecular Self-Assembly of Surfactant-like Peptides to Form Nanotubes and Nanovesicles. *Proc. Natl. Acad. Sci.* **2002**, *99* (8), 5355–5360.

22. Vilenchik, L. Z.; Griffith, J. P.; Clair, N. St.; Navia, M. A.; Margolin, A. L. Protein Crystals as Novel Microporous Materials. *J. Am. Chem. Soc.* **1998**, *120* (18), 4290–4294.
23. Häring, D.; Schreier, P. Cross-Linked Enzyme Crystals. *Curr. Opin. Chem. Biol.* **1999**, *3* (1), 35–38.
24. Brodin, J. D.; Carr, J. R.; Sontz, P. A.; Tezcan, F. A. Exceptionally Stable, Redox-Active Supramolecular Protein Assemblies with Emergent Properties. *Proc. Natl. Acad. Sci. U. S. A.* **2014**, *111* (8), 2897–2902.

Appendix

PERMISSION LETTERS

A. American Chemical Society Publications License



Title: Sequence and Structural Duality: Designing Peptides to Adopt Two Stable Conformations

Author: Maya J. Pandya, Eleonora Cerasoli, Abbey Joseph, et al

Publication: Journal of the American Chemical Society

Publisher: American Chemical Society

Date: Dec 1, 2004

Copyright © 2004, American Chemical Society

Home **Create Account** **Help**

LOGIN

If you're a **copyright.com user**, you can login to RightsLink using your copyright.com credentials. Already a **RightsLink user** or want to [learn more?](#)

PERMISSION/LICENSE IS GRANTED FOR YOUR ORDER AT NO CHARGE

This type of permission/license, instead of the standard Terms & Conditions, is sent to you because no fee is being charged for your order. Please note the following:

- Permission is granted for your request in both print and electronic formats, and translations.
- If figures and/or tables were requested, they may be adapted or used in part.
- Please print this page for your records and send a copy of it to your publisher/graduate school.
- Appropriate credit for the requested material should be given as follows: "Reprinted (adapted) with permission from (COMPLETE REFERENCE CITATION). Copyright (YEAR) American Chemical Society." Insert appropriate information in place of the capitalized words.
- One-time permission is granted only for the use specified in your request. No additional uses are granted (such as derivative works or other editions). For any other uses, please submit a new request.

If credit is given to another source for the material you requested, permission must be obtained from that source.

BACK

CLOSE WINDOW

Copyright © 2018 Copyright Clearance Center, Inc. All Rights Reserved. [Privacy statement](#). [Terms and Conditions](#). Comments? We would like to hear from you. E-mail us at customer@copyright.com



Title: Nanotubes, Plates, and Needles: Pathway-Dependent Self-Assembly of Computationally Designed Peptides
Author: Yu Tian, Frank B. Polzer, Huixi Violet Zhang, et al
Publication: Biomacromolecules
Publisher: American Chemical Society
Date: Nov 1, 2018
Copyright © 2018, American Chemical Society

LOGIN
If you're a **copyright.com user**, you can login to RightsLink using your copyright.com credentials. Already a **RightsLink user** or want to [learn more?](#)

PERMISSION/LICENSE IS GRANTED FOR YOUR ORDER AT NO CHARGE

This type of permission/license, instead of the standard Terms & Conditions, is sent to you because no fee is being charged for your order. Please note the following:

- Permission is granted for your request in both print and electronic formats, and translations.
- If figures and/or tables were requested, they may be adapted or used in part.
- Please print this page for your records and send a copy of it to your publisher/graduate school.
- Appropriate credit for the requested material should be given as follows: "Reprinted (adapted) with permission from (COMPLETE REFERENCE CITATION). Copyright (YEAR) American Chemical Society." Insert appropriate information in place of the capitalized words.
- One-time permission is granted only for the use specified in your request. No additional uses are granted (such as derivative works or other editions). For any other uses, please submit a new request.

BACK

CLOSE WINDOW

Copyright © 2018 [Copyright Clearance Center, Inc.](#) All Rights Reserved. [Privacy statement](#). [Terms and Conditions](#). Comments? We would like to hear from you. E-mail us at customer care@copyright.com

B. Royal Society of Chemistry License

Royal Society of Chemistry LICENSE TERMS AND CONDITIONS

Nov 13, 2018

This is a License Agreement between Yu Tian ("You") and Royal Society of Chemistry ("Royal Society of Chemistry") provided by Copyright Clearance Center ("CCC"). The license consists of your order details, the terms and conditions provided by Royal Society of Chemistry, and the payment terms and conditions.

All payments must be made in full to CCC. For payment instructions, please see information listed at the bottom of this form.

License Number	4467101428422
License date	Nov 12, 2018
Licensed content publisher	Royal Society of Chemistry
Licensed content title	Organic
Licensed content date	Jan 1, 2003
Type of Use	Thesis/Dissertation
Requestor type	Author of requested content
Format	Print, Electronic
Portion	chapter/article
The requesting person/organization is:	Yu Tian/University of Delaware
Title or numeric reference of the portion(s)	Chapter 2. (Efforts in nonmaterial construction via ...complex nanostructure with simple building blocks.)
Title of the article or chapter the portion is from	Kinetically controlled peptide self-assembly process for the formation of two-dimensional nanostructures
Editor of portion(s)	N/A
Author of portion(s)	Yu Tian
Volume of serial or monograph.	N/A
Issue, if republishing an article from a serial	N/A
Page range of the portion	
Publication date of portion	December 2018
Rights for	Main product
Duration of use	Life of current edition
Creation of copies for the disabled	no
With minor editing privileges	no
For distribution to	United States
In the following language(s)	Original language of publication
With incidental promotional use	no
The lifetime unit quantity of new product	Up to 499

Title Programmable nano materials development via kinetically controlled self-assembly of computationally designed peptidesa

Institution name other

Expected presentation date Dec 2018

Billing Type Invoice

Billing Address Yu Tian
201 DuPont Hall, University of Delaware

NEWARK, DE 19716
United States
Attn: Yu Tian

Total (may include CCC user fee) 0.00 USD

Terms and Conditions

TERMS AND CONDITIONS

The following terms are individual to this publisher:

None

Other Terms and Conditions:

STANDARD TERMS AND CONDITIONS

1. Description of Service; Defined Terms. This Republication License enables the User to obtain licenses for republication of one or more copyrighted works as described in detail on the relevant Order Confirmation (the "Work(s)"). Copyright Clearance Center, Inc. ("CCC") grants licenses through the Service on behalf of the rightsholder identified on the Order Confirmation (the "Rightsholder"). "Republication", as used herein, generally means the inclusion of a Work, in whole or in part, in a new work or works, also as described on the Order Confirmation. "User", as used herein, means the person or entity making such republication.

2. The terms set forth in the relevant Order Confirmation, and any terms set by the Rightsholder with respect to a particular Work, govern the terms of use of Works in connection with the Service. By using the Service, the person transacting for a republication license on behalf of the User represents and warrants that he/she/it (a) has been duly authorized by the User to accept, and hereby does accept, all such terms and conditions on behalf of User, and (b) shall inform User of all such terms and conditions. In the event such person is a "freelancer" or other third party independent of User and CCC, such party shall be deemed jointly a "User" for purposes of these terms and conditions. In any event, User shall be deemed to have accepted and agreed to all such terms and conditions if User republishes the Work in any fashion.

3. Scope of License; Limitations and Obligations.

3.1 All Works and all rights therein, including copyright rights, remain the sole and exclusive property of the Rightsholder. The license created by the exchange of an

Order Confirmation (and/or any invoice) and payment by User of the full amount set forth on that document includes only those rights expressly set forth in the Order Confirmation and in these terms and conditions, and conveys no other rights in the Work(s) to User. All rights not expressly granted are hereby reserved.

3.2 General Payment Terms: You may pay by credit card or through an account with us payable at the end of the month. If you and we agree that you may establish a standing account with CCC, then the following terms apply: Remit Payment to: Copyright Clearance Center, 29118 Network Place, Chicago, IL 60673-1291. Payments Due: Invoices are payable upon their delivery to you (or upon our notice to you that they are available to you for downloading). After 30 days, outstanding amounts will be subject to a service charge of 1-1/2% per month or, if less, the maximum rate allowed by applicable law. Unless otherwise specifically set forth in the Order Confirmation or in a separate written agreement signed by CCC, invoices are due and payable on "net 30" terms. While User may exercise the rights licensed immediately upon issuance of the Order Confirmation, the license is automatically revoked and is null and void, as if it had never been issued, if complete payment for the license is not received on a timely basis either from User directly or through a payment agent, such as a credit card company.

3.3 Unless otherwise provided in the Order Confirmation, any grant of rights to User (i) is "one-time" (including the editions and product family specified in the license), (ii) is non-exclusive and non-transferable and (iii) is subject to any and all limitations and restrictions (such as, but not limited to, limitations on duration of use or circulation) included in the Order Confirmation or invoice and/or in these terms and conditions. Upon completion of the licensed use, User shall either secure a new permission for further use of the Work(s) or immediately cease any new use of the Work(s) and shall render inaccessible (such as by deleting or by removing or severing links or other locators) any further copies of the Work (except for copies printed on paper in accordance with this license and still in User's stock at the end of such period).

3.4 In the event that the material for which a republication license is sought includes third party materials (such as photographs, illustrations, graphs, inserts and similar materials) which are identified in such material as having been used by permission, User is responsible for identifying, and seeking separate licenses (under this Service or otherwise) for, any of such third party materials; without a separate license, such third party materials may not be used.

3.5 Use of proper copyright notice for a Work is required as a condition of any license granted under the Service. Unless otherwise provided in the Order Confirmation, a proper copyright notice will read substantially as follows: "Republished with permission of [Rightsholder's name], from [Work's title, author, volume, edition number and year of copyright]; permission conveyed through Copyright Clearance Center, Inc. " Such notice must be provided in a reasonably legible font size and must be placed either immediately adjacent to the Work as used (for example, as part of a

by-line or footnote but not as a separate electronic link) or in the place where substantially all other credits or notices for the new work containing the republished Work are located. Failure to include the required notice results in loss to the Rightsholder and CCC, and the User shall be liable to pay liquidated damages for each such failure equal to twice the use fee specified in the Order Confirmation, in addition to the use fee itself and any other fees and charges specified.

3.6 User may only make alterations to the Work if and as expressly set forth in the Order Confirmation. No Work may be used in any way that is defamatory, violates the rights of third parties (including such third parties' rights of copyright, privacy, publicity, or other tangible or intangible property), or is otherwise illegal, sexually explicit or obscene. In addition, User may not conjoin a Work with any other material that may result in damage to the reputation of the Rightsholder. User agrees to inform CCC if it becomes aware of any infringement of any rights in a Work and to cooperate with any reasonable request of CCC or the Rightsholder in connection therewith.

4. Indemnity. User hereby indemnifies and agrees to defend the Rightsholder and CCC, and their respective employees and directors, against all claims, liability, damages, costs and expenses, including legal fees and expenses, arising out of any use of a Work beyond the scope of the rights granted herein, or any use of a Work which has been altered in any unauthorized way by User, including claims of defamation or infringement of rights of copyright, publicity, privacy or other tangible or intangible property.

5. Limitation of Liability. UNDER NO CIRCUMSTANCES WILL CCC OR THE RIGHTSHOLDER BE LIABLE FOR ANY DIRECT, INDIRECT, CONSEQUENTIAL OR INCIDENTAL DAMAGES (INCLUDING WITHOUT LIMITATION DAMAGES FOR LOSS OF BUSINESS PROFITS OR INFORMATION, OR FOR BUSINESS INTERRUPTION) ARISING OUT OF THE USE OR INABILITY TO USE A WORK, EVEN IF ONE OF THEM HAS BEEN ADVISED OF THE POSSIBILITY OF SUCH DAMAGES. In any event, the total liability of the Rightsholder and CCC (including their respective employees and directors) shall not exceed the total amount actually paid by User for this license. User assumes full liability for the actions and omissions of its principals, employees, agents, affiliates, successors and assigns.

6. Limited Warranties. THE WORK(S) AND RIGHT(S) ARE PROVIDED "AS IS". CCC HAS THE RIGHT TO GRANT TO USER THE RIGHTS GRANTED IN THE ORDER CONFIRMATION DOCUMENT. CCC AND THE RIGHTSHOLDER DISCLAIM ALL OTHER WARRANTIES RELATING TO THE WORK(S) AND RIGHT(S), EITHER EXPRESS OR IMPLIED, INCLUDING WITHOUT LIMITATION IMPLIED WARRANTIES OF MERCHANTABILITY OR FITNESS FOR A PARTICULAR PURPOSE. ADDITIONAL RIGHTS MAY BE REQUIRED TO USE ILLUSTRATIONS, GRAPHS, PHOTOGRAPHS, ABSTRACTS, INSERTS OR OTHER PORTIONS OF THE WORK (AS OPPOSED TO THE ENTIRE WORK) IN A MANNER CONTEMPLATED BY USER; USER UNDERSTANDS AND AGREES THAT NEITHER CCC NOR THE RIGHTSHOLDER MAY HAVE SUCH ADDITIONAL RIGHTS TO GRANT.

7. Effect of Breach. Any failure by User to pay any amount when due, or any use by User of a Work beyond the scope of the license set forth in the Order Confirmation and/or these terms and conditions, shall be a material breach of the license created by the Order Confirmation and these terms and conditions. Any breach not cured within 30 days of written notice thereof shall result in immediate termination of such license without further notice. Any unauthorized (but licensable) use of a Work that is terminated immediately upon notice thereof may be liquidated by payment of the Rightsholder's ordinary license price therefor; any unauthorized (and unlicensable) use that is not terminated immediately for any reason (including, for example, because materials containing the Work cannot reasonably be recalled) will be subject to all remedies available at law or in equity, but in no event to a payment of less than three times the Rightsholder's ordinary license price for the most closely analogous licensable use plus Rightsholder's and/or CCC's costs and expenses incurred in collecting such payment.

8. Miscellaneous.

8.1 User acknowledges that CCC may, from time to time, make changes or additions to the Service or to these terms and conditions, and CCC reserves the right to send notice to the User by electronic mail or otherwise for the purposes of notifying User of such changes or additions; provided that any such changes or additions shall not apply to permissions already secured and paid for.

8.2 Use of User-related information collected through the Service is governed by CCC's privacy policy, available online here: <http://www.copyright.com/content/cc3/en/tools/footer/privacypolicy.html>.

8.3 The licensing transaction described in the Order Confirmation is personal to User. Therefore, User may not assign or transfer to any other person (whether a natural person or an organization of any kind) the license created by the Order Confirmation and these terms and conditions or any rights granted hereunder; provided, however, that User may assign such license in its entirety on written notice to CCC in the event of a transfer of all or substantially all of User's rights in the new material which includes the Work(s) licensed under this Service.

8.4 No amendment or waiver of any terms is binding unless set forth in writing and signed by the parties. The Rightsholder and CCC hereby object to any terms contained in any writing prepared by the User or its principals, employees, agents or affiliates and purporting to govern or otherwise relate to the licensing transaction described in the Order Confirmation, which terms are in any way inconsistent with any terms set forth in the Order Confirmation and/or in these terms and conditions or CCC's standard operating procedures, whether such writing is prepared prior to, simultaneously with or subsequent to the Order Confirmation, and whether such writing appears on a copy of the Order Confirmation or in a separate instrument.

8.5 The licensing transaction described in the Order Confirmation document shall be governed by and construed under the law of the State of New York, USA, without regard to the principles thereof of conflicts of law. Any case, controversy, suit, action,

or proceeding arising out of, in connection with, or related to such licensing transaction shall be brought, at CCC's sole discretion, in any federal or state court located in the County of New York, State of New York, USA, or in any federal or state court whose geographical jurisdiction covers the location of the Rightsholder set forth in the Order Confirmation. The parties expressly submit to the personal jurisdiction and venue of each such federal or state court. If you have any comments or questions about the Service or Copyright Clearance Center, please contact us at 978-750-8400 or send an e-mail to info@copyright.com.

v 1.1

Questions? customercare@copyright.com or +1-855-239-3415 (toll free in the US) or +1-978-646-2777.